UNRAVELING GALAXY EVOLUTION USING NUMERICAL SIMULATIONS

By

Claire Kopenhafer

A DISSERTATION

Submitted to
Michigan State University
in partial fulfillment of the requirements
for the degree of

Astronomy and Astrophysics—Doctor of Philosophy
Computational Mathematics, Science and Engineering—Dual Major

2022

ABSTRACT

One of the primary concerns in galaxy evolution is how galaxies form their stars: what keeps that star formation going over cosmic time, and what causes it to stop in a processes called "quenching". Galaxies with mass similar to our own Milky Way occupy a sweet spot between abundance and brightness that makes them easy to find in the sky, and such galaxies also populate a transitionary regime in behavior that make them interesting for studying galaxy evolution. Numerical modeling—from semi-analytic models to numerical simulations—are valuable tools for understanding the multiple intersecting physical processes that drive galaxy evolution. These processes act both within and around individual galaxies such that numerical models must necessarily encompass a range of spatial and temporal scales. Multiple approaches are commonly used in order for this modeling to be physically insightful. *In this dissertation I will present my efforts to unravel the mechanisms of galaxy evolution affect Milky Way-like galaxies using a variety of numerical models.*

Addressing the issue of what causes galaxies to stop forming stars, I first investigate an unusual population of galaxies called the "breakBRDs" (Tuttle and Tonnesen 2020). Within the dominant framework for galaxy quenching, galaxies first stop forming stars in their centers and later in their outskirts. This is the "inside-out" quenching paradigm. The breakBRD galaxies possess observational markers that run counter to this narrative. We used the IllustrisTNG cosmological simulation (Pillepich et al. 2018b) to find a set of simulated galaxies that are analogous to the observed breakBRDs in order to better understand their evolution. We found that the breakBRD analogues are galaxies that ultimately become fully quenched, but found no clear cause for the "outside-in" modality. This is not the dominant channel for quenching in the IllustrisTNG simulation, but roughly 10% of quiescent galaxies with $10 < \log_{10}(M_*/\mathrm{M}_\odot) < 11$ had centrally-concentrated star formation similar to the breakBRD analogues.

As to what keeps galaxies forming their stars, I used a set of idealized simulations of Milky Way-like galaxies to study the interactions of the circumgalactic medium (CGM) and its host galaxy. The CGM is an extended volume of gas that accounts for about half of the baryonic matter in a galaxy's dark matter halo. This gas is also "multiphase," containing gas at a wide range of densities

and temperatures. It may therefore function as a reservoir from which gas may cool, condense, and accrete onto the host galaxy where it can eventually drive star formation and stellar feedback primarily via Type II supernovae. This cycle of condensation and feedback may self-regulate the overall star formation rate of a galaxy. Our idealized simulations include both the CGM and explicit formation of stars but find that stellar feedback can drive outflows that disrupt the CGM with large, hot, low-density cavities. This is true even after we adjust the stellar feedback efficiency to accommodate the "settling" of the initial conditions. We therefore conclude that the picture of star formation self-regulation in Milky Way-like galaxies is missing physical processes at the edge of the galaxy halo that work in tandem with accretion of CGM gas and stellar feedback.

The CGM is typically observed via absorption spectra that contain features from numerous metal ions. In order to better compare the simulated CGM with observations, most simulations need to be post-processed to derive similar information as that extracted from spectra. Therefore, I also present preliminary work quantifying the uncertainties inherent to this post-processing. The results herein focus on the assumption that metals in the CGM follow the abundance pattern of our Sun, which is not physically well-reasoned. We derive plausible alternative abundance patterns using chemical evolution modeling and apply these to a post-processing of the FOGGIE cosmological zoom simulations (Peebles 2020; Simons et al. 2020). We find that adopting a non-Solar abundance affects the column density of CGM absorbers of about ± 1 dex.

Finally, I present future research directions for all the projects described herein. These include investigating the CGM of the breakBRD analogues from IllustrisTNG, outlining additions to our idealized galaxy simulations that may address the issue of disruptive outflows, and both scaling up our existing uncertainty quantification project as well as including the additional source of uncertainty, ionizing radiation.

This dissertation is dedicated to my past self, whose dreams brought me here.

ACKNOWLEDGEMENTS

Thank you to Michigan State University for being my academic home for both my undergraduate degree and for my graduate program. My graduate research has been made possible by the Department of Energy Computational Science Fellowship program (DE-FG02-97ER25308) and NSF grant 1908109. Computing resources for the projects herein have been provided by the Extreme Science and Engineering Discovery Environment (XSEDE) under allocation TGAST090040, the Michigan State University High Performance Computing Center (operated by the Institute for Cyber-Enabled Research), the Quest high performance computing facility at Northwestern University (jointly supported by the Office of the Provost, the Office for Research, and Northwestern University Information Technology), and computing facilities supported by the Scientific Computing Core at the Flatiron Institute (a division of the Simons Foundation). Work in Chapter 2 was initiated at the Kavli Summer Program in Astrophysics held at the Center for Computational Astrophysics of the Flatiron Institute in 2018, co-funded by the Kavli Foundation and the Simons Foundation.

Software resources include (in no particular order): Astropy (Astropy Collaboration et al. 2018), FSPS (Conroy, Gunn, and White 2009; Conroy and Gunn 2010), python-fsps (Foreman-Mackey, Sick, and Johnson 2014), NumPy (Harris et al. 2020), SciPy (Virtanen et al. 2020), Matplotlib (Hunter 2007), Pandas (McKinney 2010), yt (Turk et al. 2011), and GNU parallel (Tange 2020).

Thank you to the Physics of Atomic Nuclei summer program and to the folks at the Shodor Education Foundation for helping set me on the path to this graduate degree. Thanks especially to Zach Constan, Michael Kilburn, and Aaron Weeden.

Many thanks to the Department of Energy Computational Science Graduate Fellowship for its strong community of both fellows and alumni, and for its financial and professional support. Particular thanks to fellow MSU graduate student Zane Crawford, and to CSGF alumni Sarah Richardson.

As part of my CSGF fellowship, I was able to spend a summer practicum at Sandia National Laboratory. Thank you to Kristian Beckwith, Patrick Knapp, Kyle Cochrane, and Raymond Clay III for both making my time there so scientifically enriching and for showing me what working

outside of an academic institution could be like, especially on a interdisciplinary team.

Thank you to the Kavli Summer Program in Astrophysics for accepting me to the 2018 school on galaxy formation and to the Flatiron Institute's Center for Computational Astrophysics for hosting. This program was an incredible opportunity to meet both fellow graduate students and members of the academic community whose names I had seen on the papers I was reading. Special thanks to collaborators Cassi Lochhaas, Tjitske Starkenburg, and Stephanie Tonnesen who I met at the KSPA and who helped me grow as a researcher. Thanks also to the CSGF for letting me miss the annual summer meeting to attend this school.

Thank you also to fellow members of the FOGGIE collaboration, including Molly Peeples and Jason Tumlinson for being such excellent team leaders and inspiring scientists, and to Chris Howk and Nicolas Lehner for inviting me to give the astronomy seminar at Notre Dame.

Endless thanks to Jessie Micallef and Vashti Sawtelle for joining me in the dream of hosting an American Physical Society Conference for Undergraduate Women in Physics at MSU, and to the hardworking students, post-docs, faculty, and staff on our organizing. Thank you also to all of our conference presenters and to all of our attendees for making it such a successful event.

Thank you to my fellow graduate students past and present, including Huei Sears, Adam Kawash, Justin Grace, Mike Pajkos, Brandon Barker, Teresa Panurach, Forrest Glines, Carl Fields, Jessica Maldonado, CJ Llorente, and Kristen Dage for the friendship and support.

Thank you to the members of my committee—Mark Voit, Laura Chomiuk, Wolfgang Kerzendorf, and Kendall Mahn—for the personal and professional guidance. Additional thanks to faculty members Ed Brown, Morten Hjorth-Jensen, Johannes Pollanen, and Danny Caballero, and to Kim Crosslan for being a wonderful provider of hugs as well as for keeping our department functioning.

Very special thanks to my parents for their never ending support of my goals, to Mathew McPeak for being such a wonderful partner, and to Kayla Walker for being an excellent partner (in crime).

Finally, so many thanks to Brian O'Shea, for being an advisor, mentor, and friend for many years. Thank you for your guidance and support.

TABLE OF CONTENTS

KEY TO ABBREVIATIONS

AGB Asymptotic Giant Branch

AGN Active Galactic Nucleus; pl. Active Galactic Nuclei

AMR Adaptive Mesh Refinement

bBRDa BreakBRD Analogues

B/T Bulge (to) Total (ratio)

CIC Cloud-In-Cell

CIE Collisional Ionization Equilibrium

CFL Courant-Friedrichs-Lewy

CGM Circumgalactic Medium

CMB Cosmic Microwave Background

CMD Color Magnitude Diagram

COS *Cosmic Origins Spectrograph*

DR Data Release

EOS Equation of State

EUV Extreme Ultraviolet

FFT Fast Fourier Transform

GMC Giant Molecular Cloud

ICM Intracluster Medium

IGM Intergalactic Medium

IMF Initial Mass Function

IR Infrared

ISM Interstellar Medium

KS Kolmogorov–Smirnov

LOS Line of Sight

MAD Median Absolute Deviation

NFW Navarro, Frenk, and White

NUV Near Ultraviolet

PIE Photoionization Equilibrium

SAM Semi-Analytic Model

SED Spectral Energy Distribution

SDSS Sloan Digital Sky Survey

SFH Star Formation History

SFMS Star-Forming Main Sequence; alt. Star-Formation Main Sequence

SFR Star Formation Rate

SMHM Stellar Mass (to) Halo Mass (relationship)

SNe Supernovae; sing. Supernova (SN)

SNR Supernova Remnant

SPH Smoothed Particle Hydrodynamics

SPS Stellar Population Synthesis

sSFR Specific Star Formation Rate

UV Ultraviolet

UVB (metagalactic) Ultraviolet Background (radiation)

ΛCDM "Lambda" Cold Dark Matter, where Λ is the cosmological constant

CHAPTER 1

INTRODUCTION

The deep field images from the Hubble Space Telescope and JW Space Telescope[1] demonstrate a universe full of galaxies that range in size, shape, and color. Studying galaxy evolution can reveal how this diversity came to be. This evolution is shaped by a wide range of intersecting physical processes that span many orders of magnitude in both physical and temporal scale—from the formation of a single star to the interactions between whole galaxies. This makes for multiple interesting research avenues under the galaxy evolution umbrella. Such breadth also means that there is a large amount of background context that one should ideally be familiar with. The goal of this chapter is to provide this context assuming the reader has a basic familiarity with astrophysical concepts. Each of the following chapters will come with its own introduction that will provide more specific context for the work described therein.

The practice of astrophysics can also be divided into two or three approaches: observation, theory, and computation (where "computation" may or may not be considered part and parcel of "theory"). The works in this dissertation use computational models to advance our theoretical understanding of galaxy evolution. The computer models in question, as well as the numerical methods used to calculate them, have been built up over decades of work and are relatively standardized across the astrophysical community. I would therefore be remiss to not to include an overview of these techniques.

The structure of this chapter is as follows. In Section 1.1 I will introduce the major galactic components whose processes and interactions have a major impact on the evolution of galaxies. Section 1.2 will highlight some of the observational evidence that provides clues for the mechanisms by which galaxies evolve. Section 1.3 will cover how we model galaxies and their components using computers.

[1] I elect to not spell out the full name of this telescope because of its namesake's involvement in the removal of LGBTQ+ people from the federal government, a campaign known as the "Lavendar Scare." See https://astrobites.org/2021/12/19/jwst_renaming/ for more.

1.1 The Components of Galaxies

A galaxy's evolution is the result of several interacting physical processes both inside and outside of the galaxy itself. For the purposes of this dissertation, it will be helpful to think of galaxies in terms of four major components: dark matter, gas and plasma, stars, and supermassive black holes. This is not an exhaustive list; indeed, a different dissertation on galaxies might put more emphasis on dust, magnetic fields, and/or cosmic rays. While these other factors will certainly come into play within the chapters that follow, for now our story of galaxy evolution will focus on the four major factors listed above.

1.1.1 Dark Matter

Dark matter is the gravitational "glue" that holds a galaxy together in a system called a "halo." While the halo also contains the galaxy's gas, stars, and supermassive black hole, the dark matter dominates the system by mass and therefore dominates its dynamics. Dark matter halos are gravitationally bound, approximately stable structures where the random motions of the constituent particles support the system against its own self-gravity (Benson 2010). This definition depends on the assumption that dark matter is a particle. Indeed, galaxy evolution is typically framed by the cold dark matter paradigm with an additional cosmological constant (ΛCDM; see the reviews of Benson 2010; Frenk and White 2012). This paradigm successfully describes the large scale structure of the universe (Seljak et al. 2005; Percival et al. 2007; Ferramacho, Blanchard, and Zolnierowski 2009; Sánchez et al. 2009 as reviewed by Benson 2010) and observations of the cosmic microwave background (CMB; Hinshaw et al. 2013; Planck Collaboration et al. 2020).

Fluctuations within the CMB tell us about perturbations in the dark matter density that seeded the formation of today's galaxies. Under our current understanding of the early universe (see e.g. Benson 2010; Wechsler and Tinker 2018), quantum-scale density fluctuations were expanded to cosmological scales by inflation. Unlike baryonic matter, cold dark matter exerts no pressure and so has no restoring force against gravitational collapse. These perturbations are therefore able to grow, first linearly and then nonlinearly. As described in Benson (2010), simple analytic models (e.g.

Gunn 1977; Shaw and Mota 2008), empirical measurements (e.g. Hamilton et al. 1991; Peacock and Dodds 1996; Smith et al. 2003; Heitmann et al. 2009), and N-body simulations (e.g. Klypin and Shandarin 1983; Springel et al. 2005; Heitmann et al. 2010) have been able to understand the nonlinear growth regime, painting a picture of halos connected by filaments and sheets of dark matter. These structures collectively form the "cosmic web," which is consistent with large-scale galaxy and quasar clustering observed by, e.g., the Sloan Digital Sky Survey (SDSS; Tegmark et al. 2004).

The mass distribution of these halos can be analytically described through the formalism first laid out in Press and Schechter (1974) as recounted by the reviews of Benson (2010) and Frenk and White (2012). The number of halos per unit volume with mass between M and $M + \delta M$, or $\delta M(\mathrm{d}n/\mathrm{d}M)$, can be written as

$$\frac{\mathrm{d}n}{\mathrm{d}M} = f\left(\sigma(M)\right) \frac{\bar{\rho}}{M} \frac{\mathrm{d}\ln\sigma^{-1}}{\mathrm{d}M}. \tag{1.1}$$

where $\bar{\rho}$ is the mean density of the universe and $\sigma(M)$ is the root mean square amplitude of smoothed density fluctuations (Jenkins et al. 2001). The form of $f(\sigma)$ has been subject to much research, but the most accurate fit to N-body simulations was presented by Tinker et al. (2008). Fluctuations on the smallest scales collapse first, decoupling from cosmological expansion and becoming virialized. This state is so named for the virial theorem for bound systems

$$\langle \mathrm{KE} \rangle + \frac{1}{2}\langle \mathrm{PE} \rangle = 0 \tag{1.2}$$

where $\langle \mathrm{KE} \rangle$ and $\langle \mathrm{PE} \rangle$ are the time-averaged kinetic and (gravitational) potential energies, respectively. By convention, $\langle \mathrm{PE} \rangle < 0$. Note that the zero on the right hand side of Equation 1.2 is not obvious for galaxies, as they are not closed systems and the present form necessarily ignores any boundary terms that capture infalling dark matter.

Indeed, the transition between a halo and the background dark matter distribution is smooth, which makes it difficult to define the "edge" of the halo (e.g. Diemer, More, and Kravtsov 2013; Deason et al. 2020). The most common definition is the "virial radius" r_{vir}, which is the radius within which the virial theorem holds. In practice, approximations of the virial radius are used

instead. The most common approximation is r_{200}, though this quantity has competing definitions (Deason et al. 2020): either the radius within which the mean density is 200 times the critical density (e.g. Navarro, Frenk, and White 1996) or within which the mean density is 200 times the mean cosmic value (e.g Diemand, Kuhlen, and Madau 2007). Throughout this work I adopt the former definition. The critical density[2] is defined as

$$\rho_{\rm crit}(z) = \frac{3H(z)^2}{8\pi G} \tag{1.3}$$

where the Hubble parameter H is a function of redshift z. The approximate virial radius r_{200}, and by extension the approximate virial mass $M_{200} \approx M_{\rm vir}$, are therefore defined via

$$200\rho_{\rm crit} = \frac{3}{4}\frac{M_{200}}{\pi r_{200}^3}. \tag{1.4}$$

The value $200\rho_{\rm crit}$ is rounded from the $187\rho_{\rm crit}$ suggested by spherical models for halo collapse and early N-body simulations (e.g. Cole and Lacey 1996; Bryan and Norman 1998), though as Benson (2010) and Frenk and White (2012) note in their reviews halos are not spherical but instead are better described by triaxial ellipsoids. It should also be noted that the smaller r_{500} is commonly used for galaxy clusters (Evrard, Metzler, and Navarro 1996; Voit 2005) and in general the dark matter distribution can extend beyond $r_{\rm vir}$ (Trevisan, Mamon, and Stalder 2017; Wechsler and Tinker 2018). Still, the virial radius and its approximation r_{200} dominate the literature as the nominal boundary for a dark matter halo.

The internal density structure of dark matter halos follows a nearly-universal profile. The first of these profiles was laid out in Navarro, Frenk, and White (1996) and is now known as an "NFW profile":

$$\rho(r) = \frac{\rho_s}{(r/r_s)(1+(r/r_s))^2} \tag{1.5}$$

where ρ_s and r_s are the characteristic density and radius, respectively. Alternatively, the scale radius may be replaced by the concentration $c = r_{200}/r_s$, which typically has values of around

[2]The critical density is the average density (on the scales of hundreds of Mpc) of baryons, dark matter, and dark energy that would result in a flat universe. Here it is expressed as a mass density but it can also be expressed as an energy density.

~ 10. This profile is accurate to within 10–20% (Benson 2010; Frenk and White 2012). At the expense of a third free parameter, the Einasto profile provides greater accuracy (Einasto 1965; Retana-Montenegro et al. 2012):

$$\rho(r) = \rho_{-2} \exp\left(-2n\left[\left(\frac{r}{r_{-2}}\right)^{1/n} - 1\right]\right) \tag{1.6}$$

where ρ_{-2} and r_{-2} are the density and radius at which $\rho(r) \propto r^{-2}$. The parameter n controls how the logarithmic slope varies with radius, with

$$-\frac{\mathrm{d}\ln\rho}{\mathrm{d}\ln r} \propto r^{1/n}, \tag{1.7}$$

and n typically has values around ~ 5 (Retana-Montenegro et al. 2012).

Dark matter halos grow hierarchically via mergers (Frenk et al. 1985, 1988). Most of these mergers are "minor", which Frenk and White (2012) define as having a mass ratio less than 1:10.[3] The future merger of the Milky Way and Andromeda is an example of a major merger with a mass ratio of about 1:2 depending on estimates of the halo mass. Larger halos can also accrete diffuse dark matter not associated with a non-linearly collapsing structure. Both minor mergers and accretion lead to a general picture "inside-out" halo growth where less-bound dark matter is gradually added outside a strongly bound core (ibid.).[4] The effect of mergers on gas and stars will be covered in Sections 1.1.2 and 1.1.3.

Early improvements to cosmological N-body simulations revealed that dark matter halos could contain smaller virialized "subhalos." These structures orbit in the gravitational potential of their host halo and can also be the cause of minor mergers (see the reviews of Benson 2010; Wechsler and Tinker 2018). These subhalos can also host galaxies of their own, leading to the designation "central" for the galaxies that form at the core of the host halo and "satellite" for those in its subhalos. Indeed, satellites may in turn have satellites of their own, such as the Large Magellanic Cloud around our own Milky Way. Dark matter (sub)halos and the galaxies they contain can be roughly

[3]Definitions for major and minor mergers vary. Benson (2010) use a ratio of 1:4 as the cutoff, while in Section 2.4.2.3 we adopt 1:3.

[4]This is not to be confused with the "inside-out" *stellar* growth that will come up in Section 1.1.3.

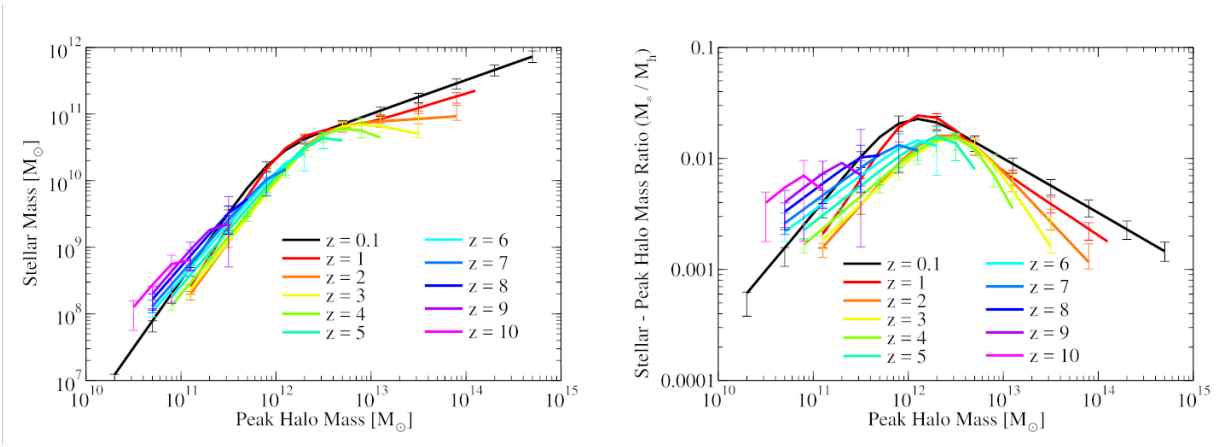

Figure 1.1 Stellar mass (left) and stellar mass fraction (right; written $M_*/M_{\rm h}$ where $M_{\rm h} \sim M_{\rm vir}$) as a function of peak historical dark matter halo mass. These relationships are shown as they evolve with redshift (colored lines), where the present day is $z = 0$ (black). "Peak historical halo mass" refers to the maximum dark matter mass attained by a halo before a given redshift. Though dark matter halos tend to grow with decreasing redshift, this definition is robust to stochastic variation. The high redshift curves cutoff at smaller halo masses because larger halos have not had time to form, while at all redshifts the cutoff at the low mass end is due to observational detection limits. Today's $M_{\rm vir} \sim 10^{12}$ M$_\odot$ halos have about $10^{10.5}$ M$_\odot$ of stars. Reproduced from Behroozi et al. (2019).

categorized based on their halo mass: halos with $10^8 < M_{\rm vir} < 10^{11}$ M$_\odot$ host dwarf galaxies,[5] those with $10^{11} < M_{\rm vir} < 10^{13}$ M$_\odot$ host your "average" individual galaxy including the so-called L^* galaxies with $M_{\rm vir} \sim 10^{12}$ M$_\odot$, galaxy groups typically live in halos with $10^{13} < M_{\rm vir} < 10^{14}$ M$_\odot$, and galaxy clusters occupy the universe's largest structures with $M_{\rm vir} > 10^{14}$ M$_\odot$.

Galaxies can also be segregated into these same general categories using their stellar mass. The relationship connecting galaxy stellar mass to dark matter halo mass is known as the "stellar mass-halo mass" (SMHM) relation.[6] As seen in Figure 1.1, this relationship is not linear. This Figure shows both the stellar mass and the stellar mass fraction ($M_*/M_{\rm vir}$) as functions of halo mass. For $M_{\rm vir} \lesssim 10^{12}$ M$_\odot$, the stellar mass fraction $M_*/M_{\rm vir}$ increases with halo mass. Yet at $M_{\rm vir} \gtrsim 10^{12}$ M$_\odot$, the mass fraction *decreases* with increasing halo mass (e.g. Behroozi, Wechsler,

[5] A halo with $M_{\rm vir} \sim 10^8$ M$_\odot$ should have a virial temperature (Section 1.1.2) of roughly 10^4 K. After cosmic reionization, the radiation background is able to heat gas to about this temperature. This should greatly reduce the ability of very small dark matter halos to cool and form stars (Somerville and Davé 2015).

[6] Sometimes written as the stellar-to-halo mass relation (SHMR), as in the review by Wechsler and Tinker (2018). Understanding the SMHM relation depends on a variety of modeling techniques and assumptions which are discussed in that review.

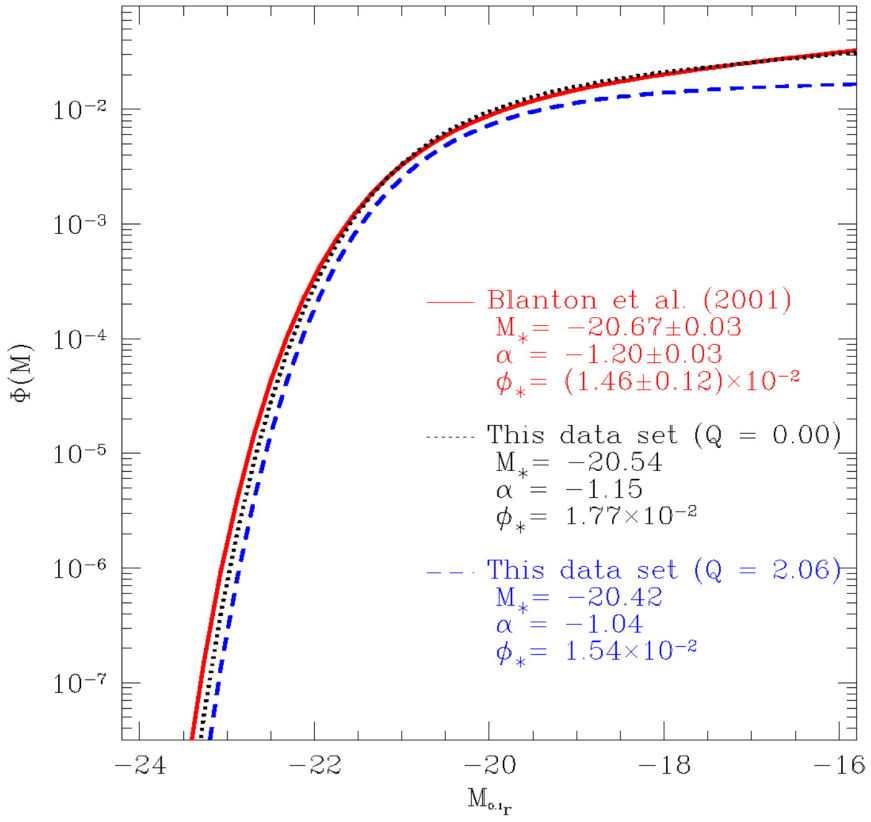

Figure 1.2 Best-fit Schechter luminosity functions from Blanton et al. (2001) (solid red line) and Blanton et al. (2003) (black dotted and blue dashed lines). The dashed model allows for luminosity evolution. The functions are presented in units of absolute magnitude, such that brighter galaxies have lower values (see Section 1.2.1 for more on magnitudes). The parameter M_* is written as M^* in the text and is equivalent to L^* when using these units. The parameter ϕ_* specifies the normalization. Reproduced from Blanton et al. (2003).

and Conroy 2013b; Behroozi et al. 2019, and references therein). As seen on the left of Figure 1.1, the total stellar mass continues to increase with halo mass in this regime albeit less quickly than in smaller halos. The L^* galaxies with $M_{\rm vir} \sim 10^{12}$ $M_\odot$ represent the peak of galaxy star formation efficiency (Behroozi, Wechsler, and Conroy 2013a) and the transition point of the SMHM relation. The variation in the SMHM above and below the characteristic L^* mass is a strong demonstration of how the "galaxy-halo connection" impacts the evolution of the galaxy itself (Wechsler and Tinker 2018).

The L^* galaxies are of particular interest within this dissertation. They are named for the galaxy luminosity function first proposed by Schechter (1976) where the number of galaxies per

unit volume $\phi(L) \propto L^{\alpha} \exp(-L/L^{*})$ with $\alpha \sim -1$ (Longair 1998). In this form, L^{*} functions as a scale radius defining the "knee" of the distribution. An example of luminosity functions fit to SDSS data are shown in Figure 1.2 where the luminosity is expressed as the absolute magnitude M. Brighter galaxies have lower absolute magnitudes (see Section 1.2.1). Galaxies with the lowest luminosities (highest magnitudes and by extension, lowest stellar and dark matter halo masses) are the most populous. For low luminosities ($L < L^{*}$ and $M > M^{*}$), $\phi(L)$ is relatively flat as the luminosity increases. At high luminosities and masses ($L > L^{*}$ and $M < M^{*}$), $\phi(L)$ drops sharply. The largest galaxies contain the most stars and are therefore quite bright, but are overall few in number. Small galaxies dominate the halo mass function but are overall dimmer. The L^{*} galaxies therefore dominate the luminosity density of the nearby, low-redshift universe as they exist at a sweet-spot of halo number density and halo luminosity. This makes them relatively easy to study (e.g. Robotham et al. 2013) and, as discussed previously, these galaxies and their halos represent a transition point in galaxy behavior. The additional consequences of this transition mass will be discussed more in Sections 1.1.2 and 1.2.2.

1.1.2 Gas

Astronomers tend to refer to neutral gas and both partially and fully ionized plasmas as simply "gas." Benson (2010) gives a good overview of the pre-galactic evolution of gas. Baryons in the early, pre-galaxy universe are expected to be approximately uniformly distributed following the dark matter distribution. By-and-large, baryons are expected to trace dark matter structures even as halos and the cosmic web form, concentrating in the gravitational potential wells of these structures. Gas is primarily funneled into halos along dark matter filaments. The amount of gas a halo accretes depends on the depth of the halo's potential well (and by extension, its total mass and density profile) as well as the pressure of the gas. Unlike with dark matter, a gas's own thermal pressure will halt collapse unless the gas can cool.

When talking about gas bound to dark matter halos, it is important to understand another virial

quantity, the virial temperature:

$$T_{\rm vir} = \frac{2}{3}\frac{GM_{\rm vir}}{r_{\rm vir}}\frac{\mu m_{\rm H}}{k_{\rm B}} \tag{1.8}$$

where $m_{\rm H}$ is the mass of hydrogen, $k_{\rm B}$ is the Boltzmann constant, and μ is the mean molecular weight ($\mu \approx 0.6$ for fully ionized primoridal gas). This is the temperature required to fulfill the virial condition (Equation 1.2) assuming all of the kinetic energy is in the form of thermal particle motions and not turbulence or bulk fluid motions.

Also important to our discussion are two timescales, the cooling time and the freefall time. The cooling time is the timescale on which gas at a given temperature would radiate away all of its thermal energy (see the review of Donahue and Voit 2022). The cooling rate, expressed as Λ, is a complicated function of density, temperature, and metallicity.[7] If the internal energy density is u, the rate of energy loss per unit time is $\dot{u} = -n_e n_i \Lambda(T, Z, n, z)$ where Z is the metallicity, z is the redshift, and n_e, n_i, and n are the electron, ion, and total densities respectively. The cooling rate Λ will be discuessed more in Section 1.3.2.3. Gas with temperatures near 10^6 K, which is the virial temperature for L^* halos, is almost completely ionized such that $u = 3P/2$ where $P = 3nk_{\rm B}T$ is the gas pressure. The cooling time is then

$$t_{\rm cool} = \frac{3nk_{\rm B}T}{2n_e n_i \Lambda(T, Z, n)}. \tag{1.9}$$

As noted by Donahue and Voit (ibid.), the assumption that $u = 3P/2$ is particularly nice when we are also considering the adiabatic invariant $K \equiv k_{\rm B}Tn_e^{-2/3}$—commonly called the gas "entropy"—because $\mathrm{d}\ln K/\mathrm{d}t = -1/t_{\rm cool}$. The adiabatic invariant K is related to the specific entropy per particle via $\mathrm{d}s = 3/2\,\mathrm{d}\ln K$. This relation is independent of the normalization of K, so $K \equiv k_{\rm B}Tn_e^{-2/3}$ is chosen due to its suitability for X-ray measurements of the intracluster medium (ICM; ibid.). This expression for the entropy K will come up often in Chapter 3.

The other important timescale is the freefall time, which approximates the time it would take a test particle to fall to the center of the dark matter potential from a distance r when ignoring fluid

[7] Astronomers collectively refer to all elements heavier than helium as "metals." When the mass fraction of metals is expressed relative to the metal mass fraction of the Sun (which is approximately 0.022), we refer to this as the "metallicity." By definition, the metallicity of the Sun is 1 $Z_\odot$.

effects such as drag. Generally, $t_{\rm ff} = \sqrt{2r/g}$, where g is the gravitational acceleration. If we treat the mass enclosed ($M_{\rm enc}$) by a sphere of radius r as a point mass, we can approximate the freefall time as

$$t_{\rm ff} \approx \sqrt{\frac{2r^3}{GM_{\rm enc}(r)}}. \tag{1.10}$$

Gas will accrete supersonically if it is moving faster than the sound speed corresponding to the virial temperature, leading to an accretion shock (Binney 1977). It is important to note that these shocks are *not* spherical as gas accretion is not isotropic. Where this shock forms depends on the difference between the cooling and freefall times. If the cooling time is long compared to the freefall time, the shock forms near or slightly inside the virial radius (Bertschinger 1985; Tozzi and Norman 2001; Voit et al. 2003; Benson 2010). This shock heats the accreting gas to the virial temperature, and is known as "hot-mode" accretion. Gas accreted in the manner is expected to form a hydrostatically supported atmosphere where its pressure obeys the equilibrium equation[8]

$$\frac{{\rm d}P}{{\rm d}r} = -\frac{GM(r)}{r^2}\rho(r). \tag{1.11}$$

Gas will then gradually fall to the center of the dark matter halo's gravitational potential as it cools and loses pressure support (Benson 2010).

On the other hand, if the cooling time of accreting gas is shorter than the freefall time the shock forms at smaller radii and closer to the nascent galaxy (Rees and Ostriker 1977; White and Frenk 1991). This means that for small halos, gas accretes without being shock-heated to the virial temperature. It instead accretes through filaments in a process dubbed "cold-mode" accretion, approaching the center of the dark matter halo with speeds near the freefall velocity. This gas will still be heated at some point nearer the halo center, but presumably it will be able to cool more efficiently due to the higher density of gas accumulated near the center.

Based on an analysis of shock-front stability (Birnboim and Dekel 2003), shocks will only form near the virial radius in halos with $10^{11} < M_{\rm vir} < 10^{12}$ $\rm M_\odot$ depending on the gas metallicity.

[8]The assumption of hydrostatic equilibrium, which is also called "hydrodynamic" equilibrium in astronomy literature, is typically accompanied by the assumption of spherical symmetry. This is why Equation 1.11 is written in terms of the scalar radial distance r and not the vector position $\mathbf{r}$.

Though the transition between accretion modes is gradual, simulations have confirmed the existence of a transitional halo mass in this range (Kereš et al. 2005; Dekel et al. 2009). Recall from Section 1.1.1 that this halo mass corresponds to L^* galaxies as well as a peak in star formation efficiency.

Once gas has reached sufficient densities at the center of the dark matter halo, it can form stars. This is of course a vast oversimplification, but it is beyond the scope of this dissertation to discuss the formation of the first stars (dubbed "Population Three" or Pop III stars; see Bromm and Yoshida 2011 for a review) and the earliest, high-redshift galaxies. What is important, however, is how stars (and black holes) affect the evolution of a galaxy. The hot and cold accretion modes described above cannot be the full story, or galaxies would be "self-similar" just like their host halos. They would not show the variety we will discuss in Section 1.2 nor the variable star formation efficiency that gives rise to the SMHM relation described in Section 1.1.1 (see Donahue and Voit 2022 and the references therein).

In addition to stars, gas that collects at the center of a halo's potential well makes up the interstellar medium (ISM). Recall from the beginning of this section that what astronomers collectively refer to as "gas" actually spans a wide range of phases, from neutral atomic and molecular gas to fully ionized plasma. This loose language is advantageous because of the wide ranges of densities and temperatures that astrophysical fluids can occupy. The ISM is a well-studied example of this. Going forward, we will use Roman numeral notation for ionization states. Within this notation, H I is neutral hydrogen, while H II is fully ionized. A label such as O VI indicates that five electrons have been removed from oxygen.

ISM gas tends to occupy the following density and temperature phases, as identified by Draine (2011): the hot ionized medium (temperature $T \gtrsim 10^{5.5}$ K and hydrogen number density $n \sim 4 \times 10^{-3}$ cm^{-3}), which has been shock-heated by supernovae and accounts for about half of the disk by volume; the warm ionized medium ($T \sim 10^4$ K and $n \sim 10^{-1}$ cm^{-3}), which is primarily composed of diffuse H II that has been ionized by starlight;[9] the warm neutral medium ($T \sim 10^{3.7}$ K and $n \sim 10^{-1}$ cm^{-3}), which accounts for approximately 40% of the disk by volume; the cold neutral

[9]When dense clouds of H II are found near the young stars responsible for their ionization they are simply called "H II regions" and are considered separately from the warm ionized medium.

medium ($T \sim 10^2$ K and $n \sim 10^1$ cm^{-3}), which is predominantly atomic gas; diffuse molecular gas ($T \sim 50$ K and $n \sim 10^2$ cm^{-3}), which is similar to the cold neutral medium but dense enough that H_2 self-shielding prevents H_2 in the cloud interior from being photo-dissociated; and dense molecular gas ($10 \lesssim T \lesssim 50$ K and $10^3 \lesssim n \lesssim 10^6$ cm^{-3}), within which the giant molecular clouds (GMCs) that give birth to stellar populations can be found. Draine (2011) introduces these phases in the context of the Milky Way but they extend to the ISMs of other galaxies as well. The relationship between these phases can be understood through the three-phase model of McKee and Ostriker (1977). In this model, the cold neutral medium and molecular gas are distributed as clouds embedded in the hot ionized medium. Warm gas—both the ionized and neutral—envelopes these clouds.

Beyond gas, the ISM also contains "dust": small solid particles usually less than 1 μm in size (Draine 2011). Dust can absorb and scatter ultraviolet (UV) and visible light from stars, causing an apparent reddening. This removal of bluer wavelengths is called "extinction." Dust grains can also polarize starlight. Depending on the grain's structure, they may become partially or fully aligned with the ISM's large-scale magnetic field. Polarization due to dust grains is therefore an important way of inferring the structure of galactic magnetic fields.

Intriguingly, the ISM's thermal and (turbulent) kinetic energy densities are roughly on par with the energy densities of both magnetic fields and cosmic rays (ibid.). For cosmic rays, this energy density is dominated by protons with ~ 1 GeV of kinetic energy (that is, protons whose kinetic energy is roughly on par with their rest mass energy). Zweibel (2013) provide a review of cosmic rays physics in our galaxy. Within a few kpc of our Sun, the root mean square magnetic field strength is about 5 μG. At these field strengths the cosmic ray gyroradius is less than 10^{12} cm and so, from the perspective of galaxies, cosmic rays can be treated as streaming along magnetic field lines. While cosmic rays themselves are highly relativistic, their net motion along field lines can be much slower. They are also well-confined, with 1 GeV cosmic rays residing in the galaxy for ~ 10 Myr—which is 2–3 orders of magnitude larger than the light travel time across the Milky Way disk. Cosmic rays and magnetic fields can both exert pressure on the surrounding gas in addition

to the gas's own thermal pressure.

The ISM can be thought of as an "machine" that turns gas into stars, but this machine must be continually supplied with gas in order to continue running. The Milky Way, for example, is currently forming stars at a rate of roughly 1.5–2 $M_\odot$ yr^{-1} (Chomiuk and Povich 2011; Licquia and Newman 2015) and has roughly 5×10^9 $M_\odot$ of gas in its ISM (based on Peeples et al. 2014; see Section 3.3.1). Assuming the Milky Way is able to maintain its current star formation rate, this is only enough fuel for a few billion more years of star formation. Our own Sun is almost five billion years old, and cosmically speaking, galaxy star formation rates tended to be higher in the past (peaking around redshift $z = 2$). This is strong evidence that the Milky Way ISM is accreting gas in order to maintain its observed star formation rate.

Critical to this continued feeding is the circumgalactic medium (CGM). Accreting gas in the Milky Way and other galaxies must, by geometric construction, pass through or originate from the CGM. This includes the gas that accretes along dark matter filaments as well as that stripped from any satellites. The CGM itself can be a considerable source of gas that accretes into the ISM, as it accounts for roughly half of the expected baryonic content of the entire system (Werk et al. 2014; Tumlinson, Peeples, and Werk 2017). It has therefore become an essential component of theories for the long-term regulation of star formation (see the review by Donahue and Voit 2022).

Like the ISM, the CGM contains a mixture of gas phases, though generally at much higher temperatures and lower densities. For example, the "warm" phase of the ISM has a temperature of roughly 10^4 K. Gas at this temperature can also be found in the CGM, but in that context, such gas is considered "cold." Also like the ISM, the CGM consists of colder, dense gas structures embedded within hotter diffuse gas. For the CGM, this hot gas is at the virial temperature. In Milky Way-like L^* galaxies at $z \sim 0$, $T_{\rm vir} \sim 10^6$ K. The CGM of individual galaxies is generally less well-studied than the ISM, receiving intensive focus only in the last decade or so with the advent of the Hubble Space Telescope's *Cosmic Origins Spectrograph* (COS; Tumlinson, Peeples, and Werk 2017). It's corollary in clusters, the ICM, is hot enough to be observed in X-ray emission,

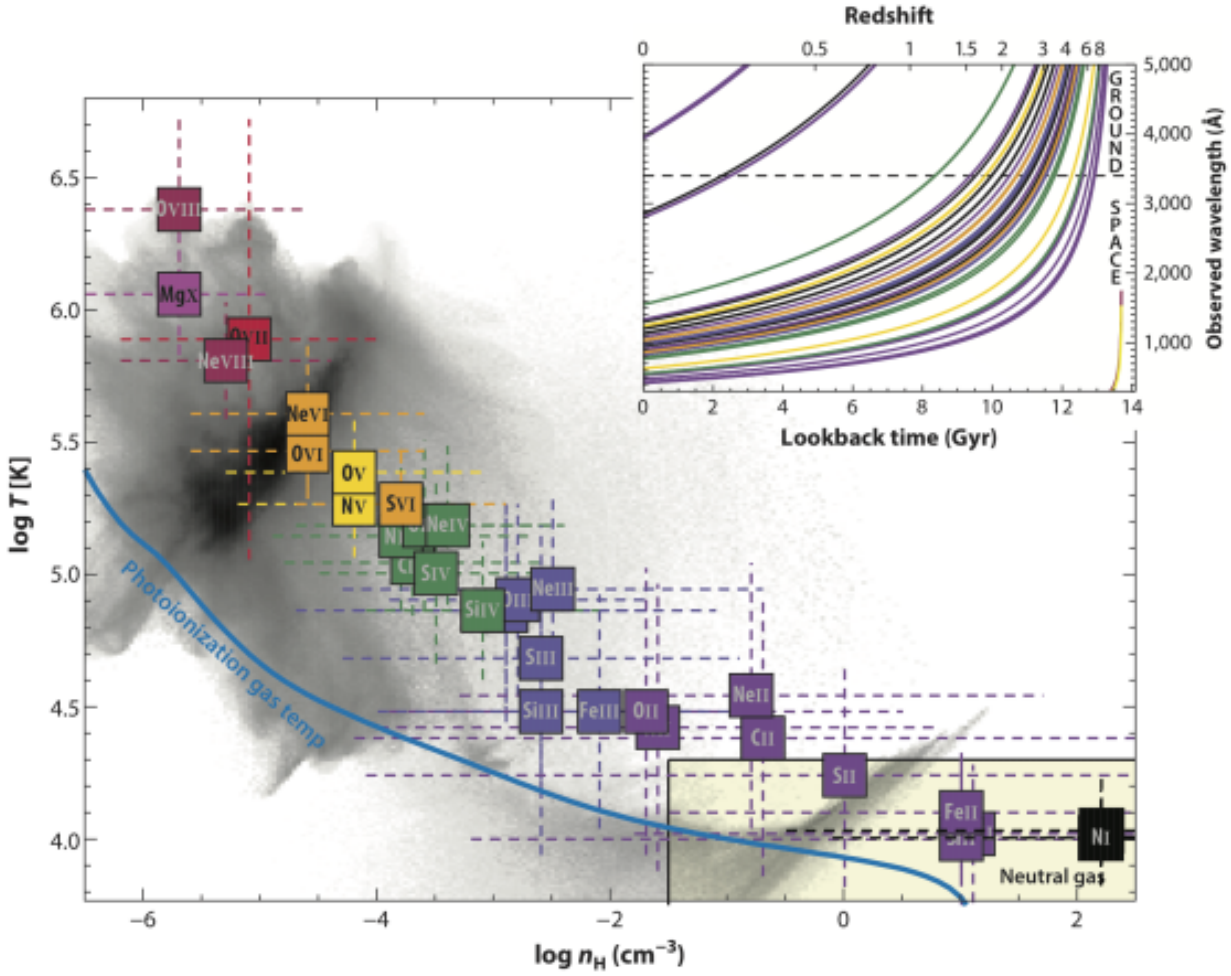

Figure 1.3 The density-temperature phase structure (grayscale) of a $z = 0$ galaxy from the EAGLE simulation with $M_* = 2.5 \times 10^{10}$ $M_\odot$. This phase distribution has been overlaid with colored markers for various metal ions and their absorption lines. These markers are colored according to ionization state. The position of each box is set by its peak ionization fraction in collisional and photoionization equilibrium models (for the temperature and density axes, respectively). The ranges mark where the ionization fraction is over half its maximum (i.e. the absorption line's full width at half maximum). The inset gives an idea of which ionization states must be observed from space given the redshift of the absorbing object. Reproduced from Tumlinson, Peeples, and Werk (2017); see references therein.

but the CGM of smaller systems is not observable in emission due to its low density.[10] It must therefore be observed via absorption spectra. Additionally, the metal ions which can trace the underlying density, temperature, and metallicity of the CGM produce absorption features that are primarily observed in the UV, which requires the use of space telescopes due to the ability of Earth's atmosphere to absorb UV light. These relatively recent technological advances mean that the CGM's gas phases are not delineated as explicitly as in the ISM, though Figure 1.3 shows the range of densities and temperatures expected within the CGM based on the EAGLE simulation (Schaye et al. 2015; gray shading) and ionic absorption line diagnostics (colored boxes).

Because of the extremely low densities in the CGM (compared to the ISM), its gas is usually unobservable in emission without stacking together multiple galaxy observations (Tumlinson, Peeples, and Werk 2017). The exception is the ICM, which is the CGM equivalent for galaxy clusters. The virial temperature of this gas ($T_{\rm vir} \sim 10^8$ K) is such that the hot phase is observable in X-rays (see e.g. the review by Donahue and Voit 2022). But for individual galaxies on the scale of the Milky Way, CGM gas can only be observed via absorption lines. Typically this is accomplished by using quasars (see Section 1.1.4) as a "backlight" (e.g. the studies by Bordoloi et al. 2014; Werk et al. 2014; Lehner et al. 2018; Lofthouse et al. 2020; McCabe et al. 2021) though other backlights include the galaxy itself (a technique known as "down-the-barrel" spectroscopy; see Tumlinson, Peeples, and Werk 2017) and halo stars within our own Milky Way (Bish et al. 2021). The metal absorption lines found within these spectra reveal that CGM gas is a complex mixture of densities and temperatures as demonstrated by Figure 1.3, giving rise to the moniker that the CGM is a "multiphase medium."

Like the ISM, the CGM likely contains magnetic fields and cosmic rays. Indeed, simulations show that cosmic rays can help drive galactic outflows (e.g. Salem and Bryan 2014; Simpson et al. 2016; Brüggen and Scannapieco 2020). They also provide a form of non-thermal pressure support, allowing more cold gas to be found at large distances from the galaxy (e.g. Butsky and Quinn

[10]The ICM has only recently been earnestly connected to the CGM of lower mass halos. The Milky Way was known to have a "hot halo" similar to the ICM as far back as 1956 but studying this halo gas in other galaxies has only become possible with COS (see the history given by Donahue and Voit 2022).

2018; Ji et al. 2020). Simulations with magnetic fields also slow the speed of galactic outflows and generally make the CGM pressure smoother (van de Voort et al. 2021).

As discussed in Section 1.1.1, dark matter halos primarily grow via mergers. These mergers affect the gas within galaxies as well. Mergers that add a large amount of gas to the larger "primary" galaxy are known as "wet" mergers. Such mergers may result in a burst of star formation in the primary galaxy. The alternative are "dry" mergers which do not add much in the way of gas. Section 1.1.1 also introduced the idea of subhalos, which may contain satellite galaxies. For example, the Milky Way contains several satellite galaxies, the largest of which are the Large and Small Magellanic Clouds. When moving through the CGM/ICM of their host, these satellites are likely to experience ram pressure and therefore become stripped of weakly gravitationally bound gas.

1.1.3 Stars

Galaxies are most readily identified in observations by their stellar content. In the 1920s there was a debate over whether the so-called "spiral nebulae" of the Messier catalog, such as the neighboring Andromeda galaxy (M31), were features within our own Milky Way or distant "island universes." The debate was eventually settled thanks to the work of Henrietta Swan Leavitt and Edwin Hubble. Leavitt discovered that the period of a Cepheid variable star's brightness fluctuations were correlated with its average intrinsic luminosity (Leavitt and Pickering 1912). Knowledge of the intrinsic luminosity allows one to estimate the object's distance. In 1924, Hubble discovered Cepheid variable stars in Andromeda and other spiral nebulae and, using Leavitt's discovery, was able to show that these objects must exist outside the Milky Way (Hubble 1925). Our modern study of galaxies had begun.

For the purposes of galaxy evolution, stars perform two necessary functions for the system. First, given that stars are hot, gravitationally-bound balls of plasma, they act as a "sink" for gas within the galaxy's interstellar medium (ISM). Earlier I likened the galaxy ISM as a machine that turns gas into stars. The exact details of this conversion are the subject of a rich field of research in its own right, but the general picture is as follows: whole populations of stars form within giant

molecular clouds (GMCs), which are turbulent complexes of dust and dense cold gas (usually molecular hydrogen with $n \sim 10^2$ cm^{-3} and $T \sim 10$ K; see Section 1.1.2). Fragmentation within GMCs drives gas to higher and higher densities until protostars form.

The first attempt at characterizing when gas is able to collapse into a protostar was Jeans (1902). Ignoring effects such as radiation, turbulence, magnetic fields, and boundary pressure from the surrounding ISM, the "Jeans criterion" is derived assuming a sphere of uniform density and temperature in virial equilibrium (Equation 1.2). Given an initial density ρ_0 and temperature T for the cloud, the minimum cloud mass for collapse is given by

$$M_{\rm J} = \left(\frac{5k_{\rm B}T}{G\mu m_{\rm H}}\right)^{3/2}\left(\frac{3}{4\pi\rho_0}\right)^{1/2}. \tag{1.12}$$

Alternatively, the Jeans criterion can be formulated in terms of a minimum cloud radius

$$R_{\rm J} = \left(\frac{15k_{\rm B}T}{4\pi G\mu m_{\rm H}\rho_0}\right)^{1/2}. \tag{1.13}$$

While a simple estimate, the Jeans criterion was used in several early numerical recipes for star formation as a means of ensuring that a parcel of gas was unstable against collapse (see Section 1.3.2.4).

The resulting zero-age main sequence mass of stars formed within a GMC can be statistically described by an initial mass function (IMF). Prominent examples of attempts to determine the IMF include Salpeter and Hoffman (1995), Kroupa (2001), and Chabrier (2003). This distribution function is often assumed to be universal across space and cosmic time. The IMF is also an important component of stellar population synthesis (SPS). SPS is a technique that traces the evolution of one or more individual stellar populations—each born from a separate GMC—in order to model e.g. a galaxy's spectral energy distribution (SED)[11] or the elemental yields of supernovae. Examples of SPS codes include FSPS (Conroy, Gunn, and White 2009; Conroy and Gunn 2010), Starburst99 (Leitherer et al. 1999), and SYGMA (Ritter et al. 2018b).

[11]While an SED and a spectrum both break down light in terms of wavelength or frequency, the independent variable for an SED is energy whereas for (emission or absorption) spectra it is typically flux or intensity. These two quantities are of course not unrelated.

On the scale of whole galaxies (as opposed to that of protostars within GMCs), the star formation rate is often related to the gas density via a power law. Typically, it is the *surface* density of these quantities (denoted Σ with dimensions of mass per area) that is related, such that $\Sigma_{\rm SFR} \propto \Sigma_{\rm gas}^{n}$ (Schmidt 1959, 1963). Kennicutt (1989) determined that $n \approx 1.4$ based on globally-averaged $\Sigma_{\rm SFR}$ and $\Sigma_{\rm gas}$, thus giving us the famed Kennicutt-Schmidt star formation law. Star-forming spiral galaxies consistently fall on this relation (e.g. de los Reyes and Kennicutt 2019; Sánchez 2020).

Modern instrumentation has allowed for investigation of the "resolved" Kennicutt-Schmidt law; that is, the relationship between $\Sigma_{\rm SFR}$ and $\Sigma_{\rm gas}$ within and throughout an individual galaxy. By also considering the surface density of stars Σ_{*}, researchers are able to investigate a trifecta of resolved relationships: the Kennicutt-Schmidt relation between $\Sigma_{\rm SFR}$ and $\Sigma_{\rm gas}$ (or more commonly, the surface density of molecular hydrogen $\Sigma_{\rm mol}$), the star formation main sequence which relates $\Sigma_{\rm SFR}$ to Σ_{*} (see also Sections 1.2.1 and 1.2.2), and the molecular gas main sequence relating $\Sigma_{\rm mol}$ and Σ_{*}. Studies of these relations hope to uncover information about what regulates star formation within galaxies. Data from the PHANGS and ALMaQUEST surveys show that the resolved relationship vary among even star-forming galaxies (Ellison et al. 2021; Popesso et al. 2022). Both Ellison et al. (2021) and Baker et al. (2022) find the ALMaQUEST data suggest that a galaxy's resolved star formation main sequence is a result of the other "more fundamental" relationships with $\Sigma_{\rm mol}$. Barrera-Ballesteros et al. (2021) reformulated the canonical Kennicutt-Schmidt star formation law so that $\Sigma_{\rm SFR}$ depends on both Σ_{*} and $\Sigma_{\rm mol}$, while Sánchez et al. (2021) suggest the three relations outlined above are projections of a more fundamental plane. Still other work, like Bacchini et al. (2020), work to establish *volumetric* star formation laws which depend on the three-dimensional density ρ. They find that such laws perform better in low density environments and may be more fundamental than the laws based on surface densities.

Stars in regular massive galaxies ($M_{\rm vir} \gtrsim 10^{11}$ M$_{\odot}$) are largely divided into two morphological components: a disk and a spheroid (the latter is sometimes called a "bulge," particularly when accompanying a disk). These two components are also kinematically distinct. Disks are rotationally supported with velocities that are a relatively flat function of radius, while stars in spheroids have

more isotropically distributed velocities. Spiral galaxies have prominent disks but also may have notable bulges, just like our own Milky Way. Elliptical galaxies are, on the other hand, primarily spheroid-dominated.[12] The division between disk- and spheroid- dominated is somewhat arbitrary, as galaxies exist on a continuum. Metrics for characterizing this continuum include bulge-to-disk and bulge-to-total mass ratios, the ratio of the radius containing 90% of starlight to that containing 50%, and the so-called "Sérsic index" n obtained by fitting a Sérsic profile to the galaxy's light profile (Somerville and Davé 2015). Though the metrics and their values vary across the literature, the division is nevertheless important for the picture of galaxy evolution, as we will see in Section 1.2.1. Generally, galaxies are believed to form "inside-out," as stars in bulges tend to be older and lower in heavy element content.[13] The spheroidal component is largely believed to be formed from stars acquired during galaxy mergers,[14] while disks are understood to be forming their stars "in situ" from gas already present in the galaxy.

The second function of stars is as a source of energy and chemically-enriched matter. Generally, the process of returning energy and mass is known as "feedback." Stellar feedback is primarily a form of negative feedback, in that it disrupts future star formation by destroying molecular clouds and heating gas. The review from Somerville and Davé (ibid.) cite observed examples of this negative feedback. Within molecular clouds, only about 1% of the gas mass is converted into stars over the cloud's freefall time as defined by the mean cloud density. This inefficiency has been attributed to turbulence within molecular clouds that is driven by stellar feedback (Krumholz, Dekel, and McKee 2012). On galaxy scales, it was recognized early on that supernova explosions

[12]The spheroid-dominated ellipticals can also be referred to as "early-type" galaxies since the disk/spheroid morphological dichotomy maps onto the "Hubble sequence," which is a morphological classification system and early model for the evolution of galaxies. Within this system, disk-dominated galaxies may be also be called "late-types." While the Hubble sequence runs counter to the modern narrative of morphological evolution (see Section 1.2.1), the names persist.

[13]The metallicity of a star is often assumed to match the metal content of the gas from which it formed. Since heavy elements are produced in stars and returned to the gas by winds and supernovae, metallicity is often used as a proxy for stellar generations.

[14]This is at least true for "classical" bulges; there are also "psuedobulges." Even the nomenclature "spheroidal" can be somewhat fraught, as there are spheroidal and dwarf spheroidal galaxies that are not quite the same thing as the "spheroids" talked about here. Like Somerville and Davé (2015), we use "spheroidal" in the sense of classic giant elliptical galaxies. Any references to "bulges" should be understood to reference classical bulges; i.e., those that structurally similar to classic giant ellipticals except that they embedded in a disk (Kormendy and Ho 2013).

could prevent star formation by both heating and removing ISM gas (White and Rees 1978; Dekel and Silk 1986; White and Frenk 1991). Gas removal occurs via large scale outflows, signs of which are ubiquitously observed in galaxies that are actively forming stars (see the review of Veilleux, Cecil, and Bland-Hawthorn 2005). These outflows may then go on to enrich the CGM (e.g. Peeples et al. 2014). Feedback from stars may also work to encourage star formation as a form of positive feedback by compressing gas within star forming regions (e.g. Cosentino et al. 2022), but this is effect is subdominant.

The most dramatic sources of stellar feedback sources are supernovae. Of primary concern are the Type II "core-collpase" and Type Ia supernovae. A Type II supernova can occur at the end of a massive ($\gtrsim 8$ $M_\odot$) star's life when fusion within its core is no longer able to support the star against gravity. More massive stars burn through their fuel faster and therefore have shorter lifespans, with the first Type II supernova detonating ~ 3.5 Myr after a stellar population forms (assuming a fully sampled IMF; (Maeder and Meynet 1989; Ekström et al. 2012). Canonically, a Type II supernova releases on the order of 10^{51} ergs of energy into the surrounding ISM. Since stellar fusion is the source of all elements other than the hydrogen, helium, and small amount of lithium created shortly after the Big Bang, some fraction of these elements are also released during a supernova. The phases of a supernova explosion will be discussed in Section 1.3.2.4 when we consider numerical models for these events.

Though the exact ignition mechanism is uncertain, Type Ia supernovae are almost certainly the result of binary white dwarf systems. Since these compact objects are formed at the end of a low-mass star's life, there is a time delay on the order of gigayears before feedback from Type Ia supernovae are important for galaxies. In quiescent galaxies with little active star formation (and therefore few Type II supernovae), their impact can be quite significant (e.g. Voit and Donahue 2011). They input a similar amount of energy as Type II supernovae but over an extended timescale (see the review by Donahue and Voit 2022).

Stars need not explode to exert feedback on their environments. Massive stars, such as those in the OB spectral class or in the asymptotic giant branch (AGB) phase of evolution, can dump

momentum and enriched matter into their surroundings via line-driven winds. Radiation can also exert pressure on nearby gas and dust and heat said material by creating photoionized bubbles (see the overview in Keller, Kruijssen, and Chevance 2022). While the mass, momentum, and/or energy that may be injected by these processes is orders of magnitudes less than that injected by supernovae, these processes can occur sooner after star formation and therefore disrupt nearby star-forming gas (Hopkins, Quataert, and Murray 2012b; Chevance et al. 2022; Keller, Kruijssen, and Chevance 2022).

1.1.4 Supermassive Black Holes

Central supermassive black holes (SMBHs) are believed to be a ubiquitous feature of galaxies or, at the very least, the massive ones ($M_{\rm vir} > 10^{11}$ $M_\odot$). These black holes tend to have masses $M_{\rm BH} \gtrsim 10^6$ $M_\odot$, far exceeding the mass of black holes we expect from the death of a single star in the few tens of $M_\odot$. As SMBHs draw material into their potential wells, it will tend to form a disk due to angular momentum conservation. As this gas dissipates its angular momentum and accretes onto the SMBH, it will heat up and begin to radiate. When the accretion disk radiates particularly strongly, we refer to it as an active galactic nucleus (AGN). The strongest AGN are known as "quasars" and they can often serve as "backlights" for absorption spectra (see Section 1.1.2).

The origin of SMBHs remains uncertain (Somerville and Davé 2015 and references therein). They may be the result of the first generation of stars, the so-called "Pop III" stars that are completely lacking in metals. These stars are theorized to be generally more massive than the enriched stars we see today. Another option is the "direct collapse" theory, where a large amount of gas with little to no angular momentum is able to collapse into a black hole without first forming a star (see Wise et al. 2019 for a feasibility study of this mechanism in simulations). Whatever the formation mechanism, it must be able to explain the existence of quasars at very high redshift, including the most distant ever found at $z = 7.64$ (Yang et al. 2021).

The AGN that result from SMBH growth have implications for the entire host galaxy, despite the SMBH itself only having an immediate sphere of influence on the the order of 1–100 pc

(Kormendy and Ho 2013). Indeed, the energy released while growing an SMBH must exceed the binding energy of the host galaxy (Silk and Rees 1998, as reviewed by Somerville and Davé 2015). The mechanism by which this energy couples to the gas, as well as the efficiency of this coupling, is an open area of research beyond the scope of this dissertation. Like with stars in Section 1.1.3, we consider these energy injection modes to be a form of "feedback." Feedback from AGN is especially important in galaxies with $M_{\rm vir} \gtrsim 10^{12}$ $M_\odot$ because of the relative inefficiency of stellar feedback at these masses (see e.g. the review by Donahue and Voit 2022).

The strongest evidence for a link between the evolution of an SMBH and its host galaxy comes from two very tight correlations with the mass of the black hole $M_{\rm BH}$. These correlated quantities are the the mass of the stellar bulge $M_{\rm bulge}$ (see Section 1.1.3) and the bulge's velocity dispersion σ. Each side of these two relationships, $M_{\rm BH}$–$M_{\rm bulge}$ and $M_{\rm BH}$–σ, describe the depth of the gravitational potential well of either the SMBH or the center of its host galaxy. These relations therefore say something about how gas accretes onto the SMBH. Kormendy and Ho (2013) provide a review of this and other less tight correlations. They note that while these relationships are often used as evidence for "co-evolution" between the SMBH and its host, that co-evolution actually has two forms. In its weak form, the SMBH co-evolves with the galaxy because the galaxy affects how gas accretes onto and grows the SMBH. The strong form of co-evolution sees the SMBH also affecting the host galaxy through AGN feedback.

The review from Somerville and Davé (2015) provides a brief overview of AGN feedback from the perspective of galaxy evolution. This feedback could take the form of thermal energy injection (e.g. gas heating), kinetic energy injection (e.g. winds), or pure radiation that can ionize and photodissociate gas. AGN observations are associated with hot bubbles, broad spectrum electromagnetic radiation, and both relativistic jets and nonrelativistic winds and outflows. What on galaxy scales might be considered thermal or kinetic feedback are likely in and of themselves the result of radiation on smaller scales, such as gas heating via photon scattering or winds driven by radiation pressure. Importantly, AGN feedback is observed to occur in two different "modes." The first is the radiatively-efficient "quasar" or "bright" mode, associated with high accretion rates. The

second is the radiatively-*inefficient* "radio" or "jet" mode (Somerville and Davé 2015). This latter mode lacks the typical radiative signatures such as bright UV, X-ray, and infrared (IR) emission. It is detectable only in the radio as highly collimated relativistic jets. Father out from the galaxy, within the CGM or ICM, these jets overlap with hot bubbles seen in X-ray emission. Exactly how these bubbles are heated is uncertain, but they are certainly hot enough and diffuse enough to rise buoyantly through the surrounding gas.

1.2 Hallmarks of Galaxy Evolution

The constancy of the speed of light means that looking into distant space also means that we are looking back in time. Without this fact we would likely know very little about how galaxies change over time. Still, galaxies evolve on timescales far longer than a human lifetime. We instead must piece together their stories by studying large samples across cosmic time. The next two sections will discuss some of the clues that piece such stories together.

1.2.1 The Galaxy Bimodality

Galaxies broadly fall into two categories: blue, actively star-forming, spiral-armed disk galaxies and red, "quiescent" elliptical galaxies with minimal star formation. The most primitive indicator of this bimodality (in terms of observable quantities) comes from galaxy color magnitude diagrams (CMDs; e.g. Baldry et al. 2004), which plot the colors of galaxies against their total brightness as measured in magnitudes.[15]

Magnitudes are a system for quantifying brightness that has its roots in ancient Greece. In the original system, magnitudes were used to rank-order classes of stars by how bright they appeared to the unaided eye. The brightest stars were of the first magnitude, the second brightest second magnitude, and so on. In the modern era, astronomical objects can have fractional and even negative magnitudes. The system's rank-order origins mean that smaller values correspond to brighter objects. Additionally, since the human eye responds logarithmically to brightness, magnitudes

[15]While brightness and luminosity have the same dimensionality (energy per time, with a possible additional dependence on frequency or wavelength), the technical distinction is that luminosity measures the energy output at the source, while brightness is measured at the observer.

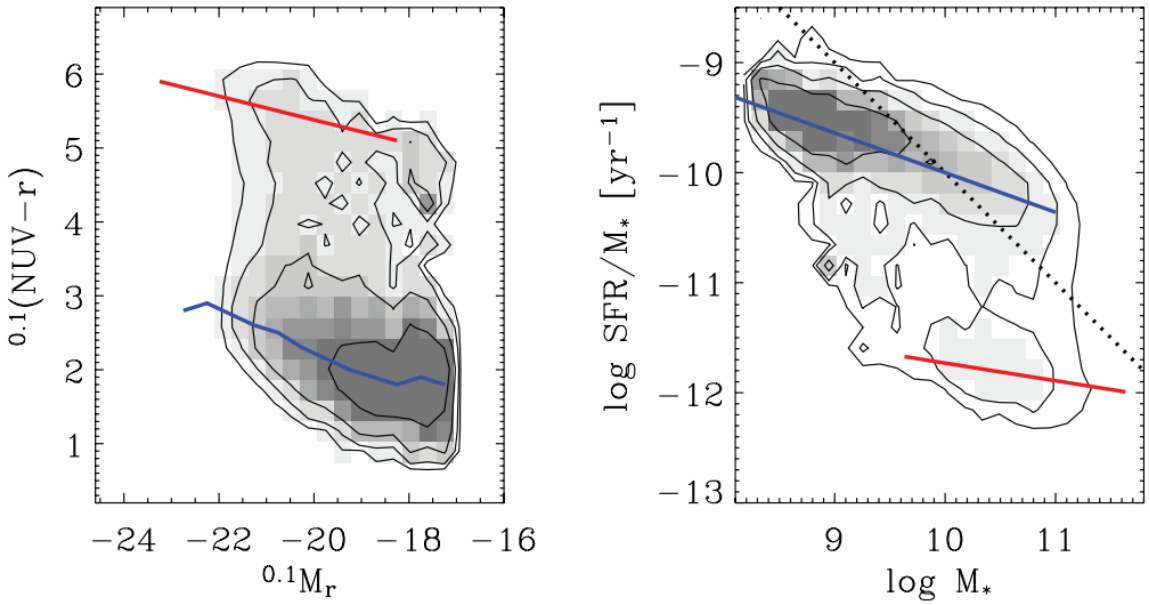

Figure 1.4 Distributions of galaxy (NUV-r) color vs. M_r magnitude (left) and specific star formation rate vs. stellar mass (right) for galaxies at $z \sim 0.1$. The magnitudes in the left panel have been adjusted to the galaxy rest-frame and used to infer the physical quantities in the right panel. Higher $^{0.1}$(NUV-r) is a more "red" color, while lower $^{0.1}M_r$ is brighter. The blue and red lines highlight trends in these bimodal distributions; the relations on the left are from Wyder et al. (2007) and the blue line on the right is from Salim et al. (2007). Contours enclose 38%, 68%, 87%, and 95% of the distribution while the dotted line corresponds to an SFR of 1 $M_\odot yr^{-1}$. Reproduced from Schiminovich et al. (2007).

remain a logarithmic system: a star of magnitude 1 is 2.5 times brighter than magnitude 2 and so on. The brightness of an object can be reported as observed, in which case it is the "apparent" magnitude (denoted m), but the apparent brightness of an object also depends on its distance. "Absolute" magnitudes (denoted M) compensate for this by adjusting objects to be at a uniform distance of 10 pc. In this way, absolute magnitudes facilitate easier comparisons between objects but require an estimate of their distances. The magnitude of an object is typically measured through a filter that transmits a knowable range of wavelengths. The difference between two filters—a logarithmic ratio of fluxes—quantifies an object's color.

An example of a CMD is shown on the left of Figure 1.4, reproduced from Schiminovich et al. (2007). The galaxies in this distribution lie at a redshift of roughly $z \sim 0.1$. The y-axis of the CMD shows the (NUV-r) color where the near ultraviolet (NUV) and r-band absolute magnitudes

have first been corrected for the median galaxy redshift, $z = 0.1$. This correction is indicated using a superscript prefix (see Blanton et al. 2003 for more on this correction). Higher $^{0.1}$(NUV-r) is a more "red" color. The x-axis is the r-band absolute magnitude, again corrected to the galaxy's rest frame. Values to the left are brighter. Red and blue lines mark the "ridge" of the red and blue sequences from Wyder et al. (2007).

Galaxies with bluer colors such as (NUV-r) are dominated by young stars, which burn both brighter and hotter (therefore appearing bluer). Such stars must be "young" compared to the galaxy's overall stellar population because these bright, hot stars live comparably short lives. If these stars were to die off without being replaced, the cooler, redder, lower mass stars that likely formed alongside them (see the discussion on IMFs in Section 1.1.3) would begin to dominate the galaxy's light. Therefore, for a galaxy to be so dominated by young stars that it appears "blue," it must be actively forming stars. By the same token, a galaxy that appears redder is not actively forming stars, instead allowing its older stars to dominate its light. This is the origin of one of the correlations laid out at the beginning of this section: "blue" galaxies are star-forming, while "red" galaxies are "dead."[16]

The star formation rate (SFR) of a galaxy can be estimated from its color while its total stellar mass can be inferred from its absolute magnitude using a mass-to-light calibration. This was the approach used by Schiminovich et al. (2007). In more recent times, it is more common to use multiple filters or even spectroscopy measurements to construct as spectral energy distribution (SED). A model for the galaxy's star formation history (SFH) and total stellar mass can be fit to this SED using stellar population synthesis (SPS), which is a technique for modeling the light from mock stellar populations of arbitrary age and total mass. This SED-fitting approach is the most popular way of estimating information about a galaxy's stellar populations (Somerville and Davé 2015; see e.g. Sánchez et al. 2021; Sherman et al. 2021 for some more recent applications). Nonetheless, the work of Schiminovich et al. (2007) provides an instructive example because the authors show both the CMD and the inferred stellar mass and star formation rate (SFR) for the same

[16] "Red and dead" is a common colloquialism among astronomers.

dataset.

The latter can be seen on the right of Figure 1.4. On this panel, the blue line is a fit to the star-forming main sequence (SFMS) from Salim et al. (2007) while the red line roughly marks the quiescent sequence. I will discuss the SFMS more in Section 1.2.2. The y-axis of the right-hand panel shows the specific star formation rate (sSFR), which is the galaxy's SFR divided by its stellar mass. The sSFR is useful for comparing the vigor with which galaxies form stars across a range of galaxy masses (both stellar and, by proxy, halo). When viewed in terms of sSFR and stellar mass, the galaxy's color and star formation bimodality becomes more apparent. Importantly, the red and dead galaxies tend to be found at higher stellar masses.

Recall from Section 1.1.1 that a galaxy's halo and stellar mass are believed to grow hierarchically over time. The tendency of red, quiescent galaxies to have higher stellar masses implies a sequence for galaxy evolution: lower mass, star-forming galaxies transition into quiescent galaxies as they grow in mass through a process called "quenching."[17] This is supported by estimates of the "quenched fraction," which is the fraction of galaxies at a given stellar mass that are quiescent. This fraction tends to increase with stellar mass (e.g. Behroozi et al. 2019). The number and mass density of quiescent galaxies has been increasing since $z \sim 2$ whereas the same densities of star-forming galaxies have remained relatively constant or even decreased (Bell et al. 2004, 2007; Faber et al. 2007; Brammer et al. 2011; Muzzin et al. 2013). These observations imply that, as cosmic time progresses, more and more star-forming galaxies are quenching (Somerville and Davé 2015). In Figure 1.4, between the SFMS and "red cloud" around sSFR $\sim 10^{-11}$ yr^{-1} is a region of parameter space called the "green valley." The relative dearth of galaxies in this region, which is believed to be the transition between active and quenched star formation, indicates that the process of quenching is quick.

As outlined in Sections 1.1.2 and 1.1.3, a galaxy needs gas if it's going to form stars. Indeed, more massive quiescent galaxies tend to have a lower fraction of cold gas in their ISMs (Catinella

[17] Both "quiescent" and "quenched" are adjectives commonly used to describe a galaxy as having little-to-no star formation. They may be used interchangeably. "Quenching" may also be used as a verb to describe the process of reaching this low-star formation state.

et al. 2010; Saintonge et al. 2011; Young et al. 2011; Serra et al. 2012 as reviewed by Naab and Ostriker 2017). The act of quenching, then, seems to be related to a lack of gas from which to form stars; yet, this opens up a whole host of further questions. Man and Belli (2018) explore this topic in detail, noting that not only must something interrupt star formation but that the quiescent state must be maintained. After all, Section 1.1.2 mentioned several ways that galaxies are able to *supply* themselves with gas. Quenching must interrupt this process and do so for an extended period of time.

Man and Belli (ibid.) identify many avenues which are able to disrupt the star formation process. Gas may be ejected from the ISM by particularly strong feedback, or cold gas may be rapidly consumed by a particularly efficient burst of star formation before it can be replenished. While both of these can deplete the ISM's gas supply, they are not long term effects. ISM gas can also be prevented from forming stars if it has a large amount of turbulence. When the molecular gas fraction is already low, large-scale shearing from the motion of the stellar bulge (see Section 1.1.3) can drive turbulence, as can stellar bars. This process is called "morphological quenching." Gas external to the galaxy—whether in the CGM or IGM—is also unlikely to be able to reach the ISM of a quenched galaxy. With "cosmological starvation," a reduced amount of gas accretes onto the dark matter halo. This is the only quenching mechanism that cannot be caused by some kind of feedback. Alternatively, gas that does accrete (or which may already be in the CGM) may be unable to cool and reach the ISM. Given that this gas naturally tends to cool (as discussed in Section 1.1.2), something must be actively adding energy. With the exception of cosmological starvation, AGN are capable of contributing to all of these avenues for quenching. Though the exact mechanism for quenching is uncertain (and may be variable), the community generally accepts that AGN and their feedback are an essential element. This is supported by both observations (e.g. Salim et al. 2007) and simulation results (e.g. Weinberger et al. 2018).

The bimodality in galaxy color and sSFR implies a transition from star-forming to quiescence within galaxies, but we have not yet addressed the accompanying bimodality in morphology. In Section 1.1.3, we discussed how stars in a galaxy largely belong to either a disk-like component

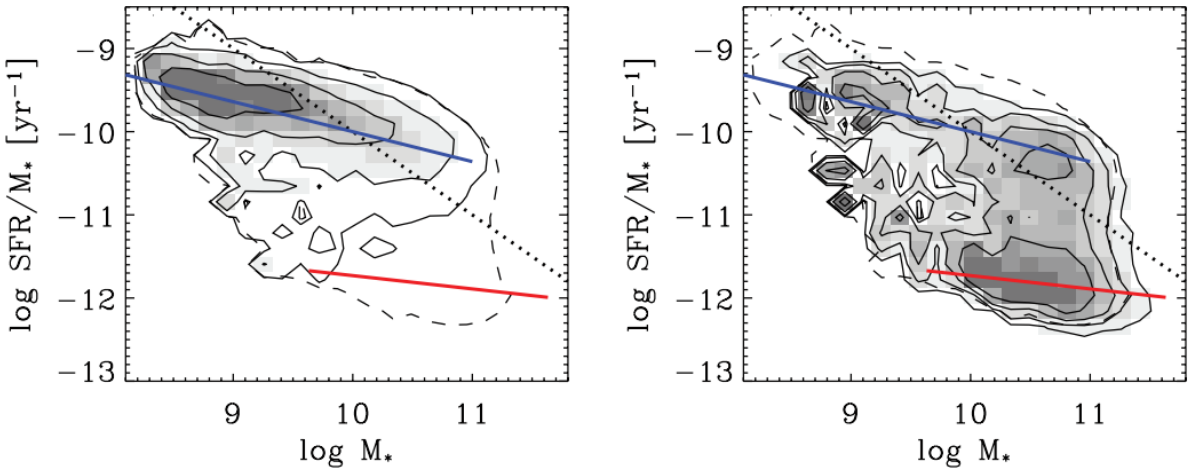

Figure 1.5 Distributions of galaxy specific star formation rate vs. stellar mass as in Figure 1.4, but with the galaxy population split on a Sérsic of $n = 2.4$. The left panel shows disk-dominated galaxies ($n < 2.4$) and the right spheroid-dominated ($n > 2.4$). Solid lines are the same as in Figure 1.4, and solid contours enclose 38%, 68%, 87%, and 95% of each subset. The black dashed line replicates the 95% contour for the entire population from Figure 1.4. Reproduced from Schiminovich et al. (2007).

or a spheroidal bulge. Interestingly, star-forming galaxies tend to be dominated by the former morphology and quiescent galaxies the latter. For a demonstration of this we once again turn to Schiminovich et al. (2007). In Figure 1.5 we see the same population of galaxies as in Figure 1.4 but split by a Sérsic index of $n = 2.4$. As mentioned in Section 1.1.3, fitting a Sérsic profile is one way of quantifying how centrally concentrated a galaxy's light is. A lower Sérsic n indicates a more extended and disk-like stellar profile. The left panel of Figure 1.5 shows stellar mass vs. sSFR for disk-dominated galaxies while the right shows the spheroid-dominated population. The disk galaxies almost entirely fall along the star forming main sequence, while the spheroids are dominated by quiescent galaxies. Indeed, the fraction of spheroid-dominated galaxies increases with stellar mass (Somerville and Davé 2015).

Collectively, these correlations imply that galaxies evolve morphologically in addition to quenching. Debates over the process(es) by which this occurs are largely beyond the scope of this dissertation, but some relevant material is covered in Section 2.2.

1.2.2 Scaling Relations

Galaxies demonstrate a number of correlations between their global properties that have relatively little scatter. These correlations are referred to as "scaling relations." We have already encountered a few examples of these relations, such as the stellar mass-halo mass relation from Section 1.1.1, the black hole $M_{\rm BH}$-σ relation in Section 1.1.4, and the original "global" Kennicutt-Schmidt star formation law in Section 1.2.1. In this section I will briefly introduce other common instances of scaling relations. The existence of such relations as well as their shape, scatter, and evolution give important clues for galaxy evolution and provide useful benchmarks against which to compare theoretical predictions. An example of this was seen in Section 1.1.3. In the present section I will first consider the star forming main sequence (SFMS; see Section 1.2.1) in more detail before introducing other widely known scaling relations.

As seen in Section 1.2.1, a considerable number of all galaxies tend to cluster along a linear relationship in $\log(\dot{M}_*)$–$\log(M_*)$ space. This clustering defines the SFMS, which can be more formally described through a fit (e.g. Salim et al. 2007; Lee et al. 2015) or by using the ridge-line of the distribution (e.g. Renzini and Peng 2015; Sherman et al. 2021). Importantly, the SFMS evolves over the history of the universe. While the SFMS can be detected out to at least redshift $z \sim 6$ (Steinhardt et al. 2014; Salmon et al. 2015 as reviewed by Somerville and Davé 2015; see also Popesso et al. 2022), the normalization of the SFMS has declined since $z \sim 2$ (Speagle et al. 2014; Popesso et al. 2022). This is accompanied by an overall decrease since the peak in cosmic star formation rate density since $z \sim 2$, an era sometimes referred to as "cosmic noon." Sherman et al. (2021) find that the slope of the SFMS remains roughly constant to either side of cosmic noon despite an overall increase in quiescent and quenching galaxies towards $z = 0$. This increase was discussed in Section 1.2.1 as well, but the constancy of the SFMS's slope suggests this relation encodes something fundamental about how galaxies form their stars. Perhaps, as discussed in Section 1.1.3 with recent investigations of the resolved Kennicutt-Schmidt relation, the SFMS encodes the results of fundamental processes within galaxies that hold constant over cosmic time. Or perhaps, as alluded to in Section 1.1.2, it's an important clue to how the CGM is able to regulate

a galaxy's gas supply (see Section 3.2 for more details).

Popesso et al. (2022) compiled a wide variety of SFMS studies from $0 \leq z \lesssim 6$ and fit this data with the functional form used by Lee et al. (2015):

$$\dot{M}_*(M_*) = \max(\dot{M}_*)/(1 + M_*/M_0)^{-\gamma} \tag{1.14}$$

where γ is the power-law index at low stellar masses, M_0 is the turnover mass, and $\max(\dot{M}_*)$ is the asymptote at high stellar mass. The advantage of this form over a traditional power law fit to $\dot{M}_*$ is that it captures the flattening of the SFMS at higher stellar mass. Their SFMS data is dominated by central galaxies, allowing M_0 to be translated into a host halo mass (see Section 1.1.1). The resulting halo mass corresponds to the transitional mass between cold and hot accretion modes discussed in Section 1.1.2. Therefore, Popesso et al. (2022) propose that the flattening of the SFMS occurs because galaxies at the turnover mass transition to inefficient disk-feeding, as gas accreted onto the halo via hot mode must first cool before it can reach this disk and fuel star formation—and hot gas in such galaxies generally has a very long cooling time due to the high virial temperature. This connection to the transitional L^* halo mass first introduced in Section 1.1.1 shows how star formation within a galaxy can be impacted by the host dark matter halo despite the vast range of scales between the two.

The decrease in the SFMS's normalization is accompanied by an observed decrease in the amount of cold gas since $z \sim 2$ (see Somerville and Davé 2015; Naab and Ostriker 2017 and references therein). Indeed, the mean cold gas fraction of the ISM also scales negatively with the stellar mass (Baldry, Glazebrook, and Driver 2008; Peeples and Shankar 2011 as reviewed by Somerville and Davé 2015). This reinforces the idea that galaxy quenching involves some degree of gas removal, as discussed in Section 1.2.1. In that section I also briefly described that quenching is accompanied by a morphological transformation. Somerville and Davé (ibid.) also note in their review that the correlation between quiescence and structural properties such as spheroid fraction, (spheroid) velocity dispersion, and central density is even stronger than the relationship between quiescence and stellar mass (Bell et al. 2012; Cheung et al. 2012; Bluck et al. 2014; Lang et al. 2014).

In fact, stellar mass (and by extension, luminosity) correlate with structural properties in both disk-dominated and spheroidal galaxies. Like the SFMS, the slope, scatter, and evolution of these "structural" scaling relations, as Somerville and Davé (2015) refer to them, encode information about the formation history of galaxies. Some of these relationships are well known in astrophysics, such as the Tully-Fisher and Faber-Jackson relations between luminosity and velocity (Faber and Jackson 1976; Tully and Fisher 1977). The former applies to disks, whose velocity is characterized by the maximum $v_{\max}$ of its rotation curve $v(r)$. The Faber-Jackson relation applies to spheroids, whose velocity is less ordered and instead characterized by the velocity dispersion σ. The size of a spheroid-dominated galaxy is characterized by its half-light or "effective" radius r_e (that is, the radius enclosing half of its total luminosity) while the size of a disk galaxy is described by its "scale radius" r_s which comes from the exponential nature of their light profile. These sizes also have scaling relationships with the total luminosity and stellar mass (Kormendy 1977; Shen et al. 2003; Courteau et al. 2007; Bernardi et al. 2010 as reviewed by Somerville and Davé 2015). Similar to the resolved star formation relations discussed in Section 1.1.3, the relationships between stellar mass, velocity, and size form a fundamental plane of which these individual relations are projections (Djorgovski and Davis 1987; Faber et al. 1987; Bender, Burstein, and Faber 1992; Burstein et al. 1997 as in Somerville and Davé 2015).

1.3 Numerical Models of Galaxies

Astrophysics is one of the first fields to leverage the power of supercomputers (see the Introduction of Thornton 1970). Indeed, computer models have revolutionized our ability to study galaxy evolution from a theoretical perspective. There are two main categories of numerical models used for this aim: semi-analytic models and numerical simulations. A comprehensive review of these two approaches and their pitfalls was provided by Somerville and Davé (2015). I will give a brief introduction to semi-analytic models in Section 1.3.1 before giving a technical overview of the methods used in numerical simulations in Section 1.3.2.

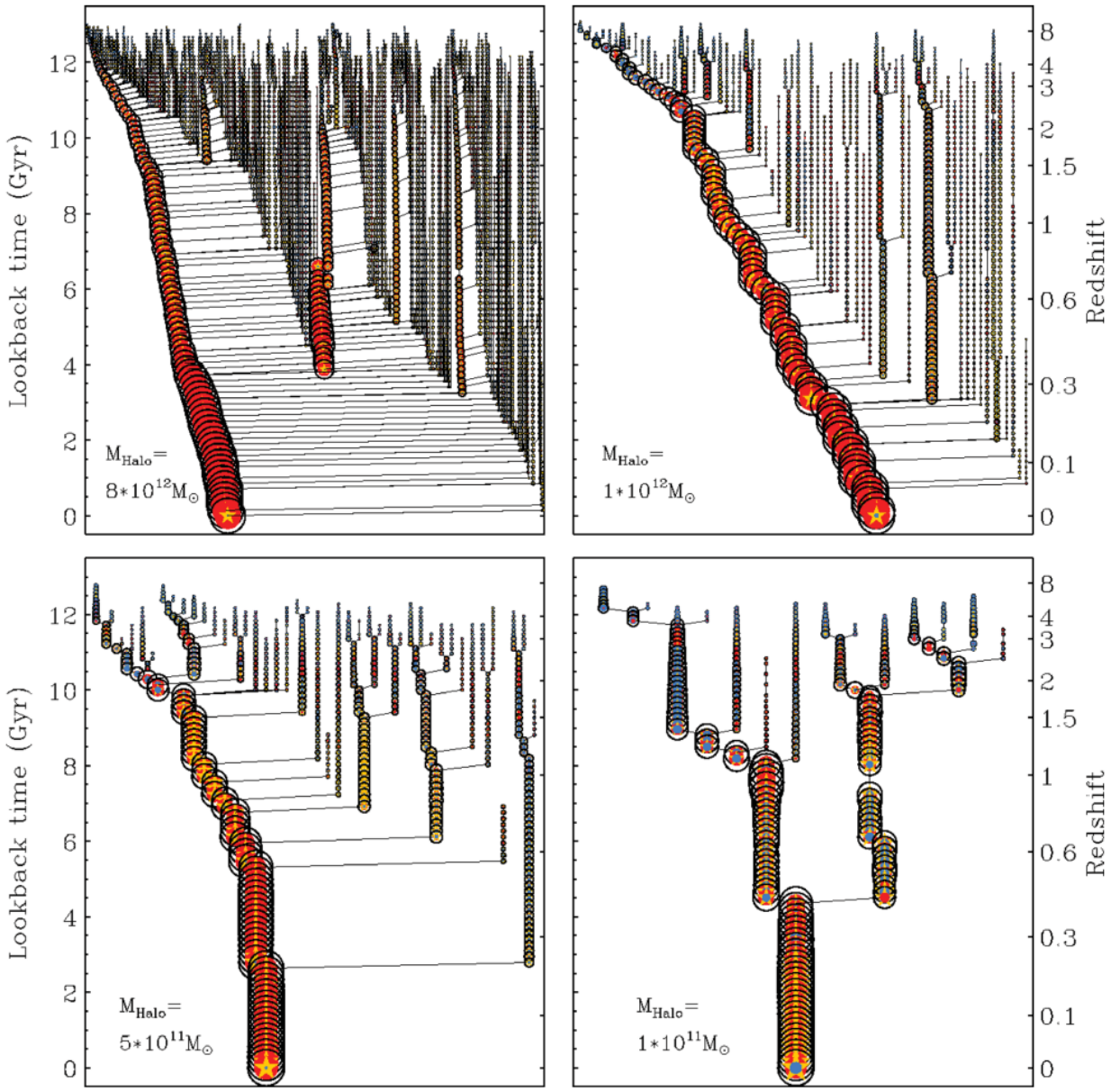

Figure 1.6 Examples of merger trees with galaxies modelled by a SAM. The final mass of each halo is written in the bottom left corner, while the y-axis shows the age of the universe in both redshift and lookback time. Symbols represent dark matter (black open circles), stars (yellow filled stars), hot gas (red filled circles), and cold gas (blue filled circles). Symbol size is proportional to the mass of each component, normalized to the final halo mass. See original text for more details. Reproduced from Hirschmann et al. (2012).

1.3.1 Semi-Analytic Models

Semi-analytic models (SAMs) are those models that use straightforward ordinary differential equations to description the evolution of bulk galaxy properties over time. While these equations are simple to write down, they can be quite numerous and come with a number of free parameters. Typical bulk properties of interest include the galaxy's stellar and gas masses, which may be further broken into phases. Typical SAMs may track the accretion of gas onto dark matter halos, star formation out of cold ISM gas, and removal of ISM gas due to feedback (either depositing it into the CGM or removing it from the halo entirely). For instance, star formation can be related to the mass of cold ISM gas via

$$\dot{M}_* = \epsilon_* \frac{M_{\rm cold}}{\tau_*} \tag{1.15}$$

where $\dot{M}_*$ is the time derivative of the stellar mass, ϵ_* is the global star formation efficiency, and τ_* a global star formation timescale (see Somerville and Davé 2015 for more details). Through these kinds of relations, galaxies can be "painted" over a dark matter halo and its merger history. An example of halo merger histories (called "merger trees" because of their hierarchical nature) and the resulting galaxies from a SAM from Hirschmann et al. (2012) are shown in Figure 1.6. The symbol sizes are proportional to the mass of the components: dark matter in black, stellar mass as a yellow star, and hot and cold gas in red and blue circles respectively. Halo mergers are indicated with black lines.

The merger trees and halo growth histories used by SAMs can be generated semi-analytically or extracted from an N-body dark matter simulation (see Section 1.3.2.2). When generated semi-analytically, they are typically assembled by sampling Press-Schechter distributions (e.g. Lacey and Cole 1993; see Somerville and Davé 2015 and Section 1.1.1). For dark matter simulations, a dedicated "halo-finding" algorithm must be used to associate individual N-body particles into halos. Examples include the SUBFIND, FOF (short for "friend-of-friends"), and ROCKSTAR algorithms (Springel et al. 2005; Dolag et al. 2009; Behroozi, Wechsler, and Wu 2013). These algorithms have difficulty detecting (sub)halos below $\sim$ 30–40 particles (Knebe et al. 2011a) so SAMs usually implement a recipe for halo mergers once a subhalo can no longer be identified

within its host. Usually these recipes include a burst of star formation and some kind of morphological transformation (though generally only for major mergers), such as moving stars from a disk component to a spheroidal one (Somerville and Davé 2015).

Both SAMs and the more fundamental numerical simulations that I will discuss in the next section rely on simple parameterized models to encapsulate processes that are under-resolved or poorly understood. Equation 1.15 is one such example for a SAM: choices must be made as to the parameters ϵ_* and τ_*. Yet because SAMs treat galaxies in a macroscopic way, with bulk quantities traced for distinct components, they are significantly more computationally efficient than numerical simulations. This allows them to be coupled to Markov-chain Monte Carlo techniques for performing Bayesian parameter inference, revealing parameter degeneracies when fitting to observed or simulated data (e.g. Henriques et al. 2009; Lu et al. 2011 as reviewed in Somerville and Davé 2015, and Côté et al. 2018).

1.3.2 Numerical Simulations

At first glance, the term "numerical simulation" is perhaps so general as to be unhelpful. After all, semi-analytic models use numerical methods to solve mathematical relations and explore what might become of galaxies under certain assumptions. They may even depend on N-body cosmological simulations for their merger trees. Yet for galaxy research, the term "numerical simulation" often refers to some combination of N-body and/or fluid methods to model the behavior of dark matter and baryons respectively. First, I will introduce the *kinds* of numerical simulations used by the astrophysical community in Section 1.3.2.1. Then, similar to Section 1.1, I will go through the essential ingredients in a numerical simulation of galaxies: gravity, stars, fluids, and active galactic nuclei (AGN). The ordering of these sections parallels that in Section 1.1 though the divisions are not always as clean; for example, dark matter may be the dominant contributor to the gravitational potential but stars and gas also play an important role. Similarly, the choice for how to solve for the gravitational potential may depend on implementation choices made for the fluids.

1.3.2.1 Three Scales for Numerical Simulations

The simulations used to study galaxy evolution can be broadly divided into two classes: "cosmological" and "idealized." The difference between these two types comes down to three primary factors: the physical scales considered, treatment of the expansion of the universe, and treatment of the simulation's initial conditions. Almost all simulation codes in astrophysics use "explicit" numerical methods; that is, methods where the simulation state at time t_{n+1} depends solely on the state at time t_n. These methods are extremely dependent on the boundary conditions in both space (e.g. at the edges of the simulation domain) and time (e.g. at $t = 0$, a.k.a. the "initial conditions").

Cosmological simulations usually seek to model a large volume of space—on the scale of ∼10–100 cMpc per side[18]—from very early times until the present day. They therefore benefit greatly from detailed characterizations of the dark matter perturbation power spectrum that was imprinted on temperature fluctuations in the CMB. Rigorous studies of the CMB, such as those conducted by the WMAP and Planck collaborations (e.g. Hinshaw et al. 2013; Planck Collaboration et al. 2020), have allowed simulators to generate well-defined initial distributions for both dark matter and baryons. Examples of software dedicated to this task include MUSIC (Hahn and Abel 2011) and NGenIC (Springel et al. 2005; Angulo et al. 2012). Starting from such primordial conditions allows cosmological structure, such as dark matter filaments and galaxies, to form and grow "organically" according to the implemented physics. Complicated and chaotic scenarios, such as the interaction between galaxy-scale outflows and imminent mergers, are emergent phenomena and do not need to be understood *a priori*. Since cosmological simulations model the universe from one of its earliest stages, they must account for the expansion of the space itself. This is done by incorporating the scale factor $a = 1/(1 + z)$ into the equations for, e.g., gravity and fluid dynamics (see Sections 1.3.2.2 and 1.3.2.3).

Typically, cosmological simulations are concerned with simulating a statistically meaningful

[18]The prefix "c" on a unit such as "cMpc" means it is a "comoving" unit. Comoving units adjust for the expansion of space, so that a 1 cMpc^3 volume will always represent the same physical space even as the universe expands. The alternative are "proper" units. A proper 1 Mpc^3 volume will encompass *more* space in the early universe than it does now.

sample of galaxies. This is why they model such a large volume of physical space. Typically their simulation domains are cubic and have "periodic" boundary conditions; that is, gas that flows out one face will wrap around and flow in the opposite face. The reason for this is simply that the actual universe is much, much larger than a $(\sim 100\ \mathrm{cMpc})^3$ box.[19] The choice of periodic boundary conditions allows the simulation domain to be replicated and tiled in all dimensions to assemble a "mock" universe of arbitrary size. In practice, periodic boundaries help avoid making difficult decisions about what to do with the domain edges. Galaxies, for instance, need not be arbitrarily truncated at the edge of the domain because they can simply wrap around and continue on the other side.

Cosmological simulations also have a subtype: the "zoom" cosmological simulation. Because computational resources are finite and a standard "big box" cosmological simulation seeks to model whole populations of galaxies, these simulations cannot resolve any one galaxy particularly well. There is thus an inherent trade-off between the size of the computational domain and the level of detail with which any one galaxy can be resolved. But as we discussed in Sections 1.1.1 and 1.1.2, galaxies are influenced by physical processes beyond their boundaries, so modeling some degree of larger structure is desirable for capturing these effects. Enter the zoomed cosmological simulations[20] to bridge the gap between preserving the cosmological context while also resolving an individual galaxy well. This technique typically involves running a large-scale dark matter-only cosmological simulation first. Halos of interest are then selected according to some scientifically-motivated criteria, such as the requirement that $M_{\mathrm{vir}} \sim 10^{12}\ \mathrm{M}_\odot$ at $z = 0$ or that the galaxy under some number of major mergers. The dark matter particles in the desired halo are then traced back to the initial conditions, before they have collapsed and formed structure, to define a new, smaller simulation domain. This smaller domain is then re-simulated with all of the desired baryonic physics included. Typically the dark matter and gas resolutions are both improved, and this process of simulation, selection, and re-simulation with improved resolution may be done recursively.

While large-scale cosmological simulations all use very similar boundary conditions—what

[19] It may even be infinite!

[20] These may also be referred to as cosmological "zoom" or "zoom-in" simulations.

with well-constrained initial conditions and periodic box edges—significant differences arise from their approach to the hydrodynamics (Section 1.3.2.3) and their handling of sub-resolution models; that is, methods that try to capture the physical impact of processes that happen on scales too small to be resolved. This includes star formation and feedback (Section 1.3.2.4) and AGN feedback (Section 1.3.2.5). Even when simulation codes use the same hydrodynamical treatment, comparison efforts like the AGORA Project reveal just how much of an impact these sub-resolution models have (Kim et al. 2014, 2016; Roca-Fàbrega et al. 2021). Examples of "big box" cosmological simulations include EAGLE (Schaye et al. 2015), IllustrisTNG (Pillepich et al. 2018b), and SIMBA (Davé et al. 2019). Example suites of zoomed cosmological simulations include FOGGIE (Peeples et al. 2019), FIRE-2 (Hopkins et al. 2018a), and Auriga (Grand et al. 2017). These simulations represent a tremendous amount of both human effort and computational resources and are therefore often the result of broad collaborations. Such efforts produce simulations that contain a wealth of information relevant to a wide range of research questions.

At the other end of the simulation spectrum sit the "idealized" simulations. These models are far less uniform in structure than cosmological simulations, but the common thread is the use of idealized circumstances and simplifying assumptions, including ignoring cosmological expansion. Common examples of idealized simulation setups include a cloud in a wind tunnel to study the effects of galactic winds on dense gas blobs (e.g. McCourt et al. 2012; Wiener, Zweibel, and Ruszkowski 2019); a narrow "tall box" simulation to study the potential phenomena that drive outflows from a patch of idealized ISM (e.g. Girichidis et al. 2016; Kim and Ostriker 2017); or an "isolated galaxy" simulation to study some aspect of secular galaxy behavior while ignoring confounding cosmological effects (e.g. Benincasa et al. 2016; Butsky and Quinn 2018; Schneider and Robertson 2018, and Chapter 3 of this dissertation). As these examples show, idealized simulations can be used to study problems on a wide range of physical scales. All except the isolated galaxy simulations consider scales far below what a cosmological simulation can achieve. Idealized simulations are generally less computationally intensive. Even though zoomed cosmological and isolated galaxy simulations may overlap in terms of the physical scales of the problem, their differences highlight

one of the strengths of idealized simulations: the ability to investigate targeted, constrained physical processes.

The drawback of this simulation approach is that the initial conditions are often *not* well-defined like they are for cosmological simulations. Typically the goal is to construct initial conditions that are "close enough" such that, after a short period of time, the simulation will settle into its own steady state as a result of the modelled physics. While all simulations are sensitive to initial conditions (see Genel et al. 2019 for an example of chaos in cosmological simulations), idealized simulations are potentially impacted to a greater degree than their cosmological counterparts because their initial conditions are less well-defined. The consequence is that idealized simulations must be constructed carefully in order to address precise scientific questions.

1.3.2.2 Gravity

Dark matter, stars, and gas all contribute to the gravitational potential of a simulation by the sheer virtue of having mass, with the dark matter dominating the potential of the halo. Depending on the physical scale the simulation is focusing on (see Section 1.3.2.1), this potential may be modelled as a static background; that is, the dark matter potential is described through an analytic expression such as Equations 1.5 or 1.6 without regard for the dark matter evolution. This is useful for isolated galaxy studies, some of which may also include static potentials for the stars (e.g. Schneider and Robertson 2018; Li and Tonnesen 2020; Kopenhafer, O'Shea, and Voit 2022), and is much cheaper computationally than tracking an evolving dark matter field. On even smaller scales, the dependence on radius may be approximately replaced by a dependence on vertical height (e.g. Kim and Ostriker 2017; Butsky et al. 2020). Yet on cosmological scales where the evolution of dark matter *does* matter, dark matter must be explicitly modelled and its potential constantly calculated. Whether the dark matter potential is static or dynamic, contributions from stars and gas may then be added on top.

I will be discussing some of the commonly used algorithms in terms of computational or algorithmic scalability. Scalability encapsulates how the number of individual floating point operations (e.g. additions and multiplications) and/or the overall run time scale with the number

computational units such as particles, grid cells, or matrix elements. As a field, we notate this scaling using "big O" notation; for example, performing a fast Fourier transform (FFT) scales as $O(N \log N)$ where N is the number of data points.[21]

Though it has yet to be confirmed whether or not dark matter is physically a particle, *computationally* we model dark matter as point particles; that is, as discrete entities with mass, position, and velocity. If we were only simulating dark matter—performing a pure N-body simulation—the most intuitive approach might be to directly sum the forces between each pair of particles. If number of particles involved is N, this approach scales as $O(N^2)$; e.g., doubling the number of particles quadruples the computational cost.

A more efficient way of summing the forces between particles is to use the Barnes-Hut algorithm (Barnes and Hut 1986) or one of its variants. These methods are also called "tree" methods (see the review of Vogelsberger et al. 2020) because the particles are distributed into a branching hierarchy of cells. When summing all the forces felt by particle i, this approach allows sufficiently distant particles to be treated as one large conglomerate particle. In the original algorithm, a cubic parent cell is divided into eight children whenever that parent contains more than one particle. This ensures that every "leaf" or end-node of the hierarchy contains just one particle. A parent cell can represent all of its child leaves as if it were one large particle located at the leaves' center of mass. This parent cell is used if its partner i is far away, and leaves (i.e. individual particles) are used if i is close.[22] This algorithm drops the complexity of force summation from $O(N^2)$ to $O(N \log N)$.The complexity can be further reduced to $O(N)$ through the use of fast multipole methods (Greengard and Rokhlin 1987; Dehnen 2000; Vogelsberger et al. 2020). In this method, forces are calculated between tree nodes instead of particles and nodes.

When modelled directly, stars are also treated as point particles (see Section 1.3.2.4). It is therefore easy to account for their contribution to the gravitational potential when using a tree algorithm. Adding gas is also easy *if* it is also treated using particles (see Section 1.3.2.3). The

[21] This notation can also be used to describe how the memory requirements scale with problem size.

[22] The threshold θ for "close" and "far" is a free parameter in the algorithm based on the ratio of the cell width s to the distance d between the cell and particle i. If $s/d < \theta$, the cell is sufficiently far away. Generally, $\theta \approx 0.5$.

smoothed particle hydrodynamics (SPH) code Gasoline2 (Wadsley, Keller, and Quinn 2017), for example, uses a purely tree-based approach for its gravity solver, though other SPH codes and the moving mesh code AREPO (Springel 2010a) typically blend the tree approach with the particle mesh algorithm discussed below (Vogelsberger et al. 2020). This combined "TreePM" algorithm (Bagla 2002) uses the tree algorithm for long-range forces and particle mesh for short range.

So far, all of the methods discussed sum over the forces between particles. This is equivalent to integrating Poisson's equation

$$\mathbf{\Phi}(\mathbf{r}) = -G \int \frac{\rho(\mathbf{r}')}{|\mathbf{r} - \mathbf{r}'|} \, \mathrm{d}\mathbf{r}' \tag{1.16}$$

where the potential $\mathbf{\Phi}(\mathbf{r})$ is being sampled by these particles (Vogelsberger et al. 2020). The alternative approach is to use the *differential* form of Poisson's equation

$$\nabla^2 \mathbf{\Phi}(\mathbf{r}) = 4\pi G \rho(\mathbf{r}). \tag{1.17}$$

This is an elliptic second-order partial differential equation, which is a class of equation for which many numerical methods exist. These methods typically involve finding $\nabla^2 \mathbf{\Phi}(\mathbf{r})$ on a three-dimensional mesh.[23] This synergizes well with mesh-based fluid methods just as the integral methods described above couple well with particle-based fluid methods (see Section 1.3.2.3).

Particles (representing both dark matter and stars) must first have their mass deposited onto this mesh, typically with some form of cloud-in-cell (CIC) interpolation to distribute the mass into a density. This gives the method its name, "particle mesh" (Hockney and Eastwood 1981; Vogelsberger et al. 2020). The gas density, which presumably already lives within a similarly-structured mesh, can then be trivially added to obtain the total mass density of dark matter and baryons. In practice, the gas density may instead be added by treating each cell as a "virtual" particle subject to the same CIC deposition as the real particles (as is done in, e.g., Enzo; Bryan et al. 2014; Brummel-Smith et al. 2019). Once the density has been defined on a mesh, the potential can be found. Methods based on FFTs (e.g. Hockney and Eastwood 1981) naturally support both

[23] A "mesh" is the generalization of a "grid." Grids are rectilinear collection of cells, which are themselves typically cubes of uniform width, while a mesh can be an arbitrary configuration that is not necessarily cubic or rectilinear (e.g. Kravtsov, Klypin, and Khokhlov 1997).

periodic and isolated boundary conditions, the former being essential for cosmological simulations (see Section 1.3.2.1). For two-dimensional $N \times N$ grids, these FFT methods scale as $O(N^2 \log N)$ (LeVeque 2007).

For astrophysical problems, grid-based hydrodynamics approaches require some form of adaptive mesh refinement to selectively enhance the simulation resolution in regions of interest (see Section 1.3.2.3). Solutions for Poisson's equation must take this into account. Typically, an FFT method is employed for the coarsest grid while some variant of a multigrid or multilevel[24] method is used on the refined meshes (see the Vogelsberger et al. 2020 review and Kravtsov, Klypin, and Khokhlov 1997; Teyssier 2002; Bryan et al. 2014 for examples). Such methods can handle more general boundary conditions, typically interpolated from the coarsest meshes, and iteratively "relax" an initial guess to an equilibrium solution. The family of techniques for performing this iteration are called "relaxation" methods. Full multigrid, which is one variation of a multigrid method,[25] requires $O(N^2)$ work for a two-dimensional $N \times N$ grid (LeVeque 2007). This is better scaling with problem size than FFT methods, but the latter are generally faster to compute as they are explicit methods rather than iterative. After the potential has been computed, it can be differentiated and the resulting acceleration is then interpolated back to the particles. This acceleration can also be used as a source term for the fluid dynamics solver.

Regardless of whether the gravitational acceleration is obtained by summing the forces between particles or differentiating the potential, the particle positions and velocities must be updated. The best choice for this is the symplectic family of integration schemes. Such integrators exactly solve an approximate Hamiltonian, ensuring that quantities such as the total angular momentum and the volume in position-velocity phase space are conserved (Vogelsberger et al. 2020). The gravitational time integration scheme is usually not the same as that employed for the fluids, even in codes where the fluid is modelled using particles. Most astrophysically interesting hydrodynamic problems

[24]The name depends on whether grids or cells, respectively, are the base unit of refinement. Kravtsov, Klypin, and Khokhlov (1997), who used a cell- or tree-based refinement, coined the term "multilevel" for their technique. Both the multigrid and multilevel approaches are in essence the same with their main difference being the underlying data structure.

[25]See Kravtsov, Klypin, and Khokhlov (ibid.) and LeVeque (2007) for more on the main differences between multigrid variants.

involve shocks and are as such not reversible (Springel 2010b), so a symplectic integrator is not necessary. Instead, only dark matter and stellar particles are integrated symplectically.

1.3.2.3 Fluids

Though made of individual particles, astrophysical scales are such that gas and plasma are often treated as fluids. Specifically, we typically adopt the Euler equations for an inviscid, compressible flow.[26] The state of a fluid can be tracked with either the set of "conserved" variables—density, momentum, and energy—or with the set of "primitive" variables—density, velocity, and pressure. Converting between the two requires knowledge of the equation of state (EOS). Usually, the ideal EOS for a monotonic ideal gas is assumed, since the universe is dominated by atomic hydrogen and helium:

$$P = (\gamma - 1)\rho u \tag{1.18}$$

where P is the pressure, ρ the density, u the internal energy per unit mass (also known as the "specific" internal energy), and γ is the adiabatic index, which is $5/3$ for a monotonic gas. A given hydrodynamics solver will likely switch between primitive and conserved variables depending on which is numerically or conceptually most convenient.

The two main approaches for modeling fluids vary depending on the reference frame one wishes to adopt: is your reference frame that of the fluid as it travels through space, or one of an external observer who watches the space the fluid is traveling through? The former perspective is dubbed "Lagrangian" and the latter "Eulerian." Confusingly, these are both formulations of the same Euler equations for a compressible, inviscid fluid.

The Lagrangian formulation, which can also be considered the "convective" form, can easily build upon the numerical methods for N-body dark matter dynamics discussed in Section 1.3.2.2. This gave rise to a class of methods known as smoothed particle hydrodynamics (SPH). As the name suggests, SPH's unit of discretization is the particle. Conceptually, these particles sample the underlying "true" continuous fluid at discrete points within the fluid. The connection between

[26]The Euler equations can be seen as a specific case of the more general Navier-Stokes equations where internal stress and heat conduction are ignored (Toro 2009).

the true, underlying fluid and the sampling particles can be made thusly (Springel 2010b). For any field $F(\mathbf{r})$, a smoothed version $F_s(\mathbf{r})$ may be defined through convolution with a kernel $W(\mathbf{r}, h)$, where h is the width of the kernel:

$$F_s(\mathbf{r}) = \int F(\mathbf{r}) W(\mathbf{r} - \mathbf{r}', h)\, \mathrm{d}\mathbf{r}' \,. \tag{1.19}$$

Each particle i that samples the underlying field $F(\mathbf{r})$ has position $\mathbf{r}_i$, mass m_i, density ρ_i, and an associated finite volume element $\Delta\mathbf{r}_i = m_i/\rho_i$. If the underlying field is sufficiently sampled, the smoothed field may be approximated as

$$F_s(\mathbf{r}) \approx \sum_i \frac{m_i}{\rho_i} F(\mathbf{r}_i) W(\mathbf{r} - \mathbf{r}_i, h). \tag{1.20}$$

The kernel is required to be at least twice differentiable and is commonly a cubic spline. Kernels with finite support are preferred so that summation can be limited to some number of nearest neighbors. The smoothing length can be variable in space and time to account for the sampling density of the particles.

As relayed by Springel (ibid.), Eckart (1960) showed that the inviscid Euler equations follow from the Lagrangian

$$L = \int \rho \left(\frac{\mathbf{v}^2}{2} - u \right) \mathrm{d}V \tag{1.21}$$

where $\mathbf{v}$ is the velocity vector and $\mathrm{d}V$ is an infinitesimal volume unit. By discretizing the Lagrangian, the equations of motion for an SPH particle can be derived using the variational principles of classical mechanics (Springel 2010b). Neglecting any sink or source terms (such as gravity and radiative cooling), this gives rise to the equations:

$$\frac{\mathrm{d}\rho}{\mathrm{d}t} = -\rho \boldsymbol{\nabla} \cdot \mathbf{v} \tag{1.22}$$

$$\frac{\mathrm{d}\mathbf{v}}{\mathrm{d}t} = -\frac{1}{\rho} \boldsymbol{\nabla} P \tag{1.23}$$

$$\frac{\mathrm{d}e}{\mathrm{d}t} = -\frac{1}{\rho} \boldsymbol{\nabla} \cdot P\mathbf{v} \tag{1.24}$$

where $\mathrm{d}/\mathrm{d}t = \partial/\partial t + \mathbf{v} \cdot \nabla$ is the Lagrangian derivative and $e = u + v^2/2$ is the specific total energy (Vogelsberger et al. 2020). Examples of SPH codes include GADGET (Springel, Yoshida, and

White 2001; Springel 2005), Gasoline2 (Wadsley, Keller, and Quinn 2017), SWIFT (Schaller et al. 2016), and ChaNGa (Jetley et al. 2008, 2010; Menon et al. 2015).

The Lagrangian approach is elegant in that fluid motions can be described with a set of ordinary differential equations. If the gas only undergoes reversible processes such that entropy is conserved, in theory only the momentum evolution must be followed explicitly (Springel 2010b). Unfortunately, shocks are common features within astrophysical problems and are *not* reversible processes. To handle this, SPH codes introduce an artificial viscosity. This addition necessitates the time-integration of either particle entropy[27] or thermal energy. The two are related by some function A such that, as noted in Springel (ibid.), $P_i = A_i \rho_i^\gamma$ and $u_i = A_i \rho_i^{\gamma-1}/(\gamma - 1)$ where i is the particle index. If the flow is isentropic, A_i is constant. With artificial viscosity, either A or u will have a temporal derivative that depends on the interparticle friction. The choice of which quantity to track is a matter of numerical convenience, but according to Springel (ibid.), entropy is usually the computationally advantageous choice.

Artificial viscosity allows SPH codes to handle shocks by skirting the approach's main drawback: because it is formulated using derivatives, Lagrangian fluid dynamics is only valid when the underlying fluid is smooth and free of discontinuities (Toro 2009; Teyssier 2015). Additional viscosity broadens the shock into a resolvable layer and dissipates kinetic energy into heat, which raises the gas entropy. The main difficulty with adding artificial viscosity is ensuring it only affects the fluid when a shock is present. Outside of a shock, viscosity will cause the fluid to deviate from an ideal gas (Springel 2010b).

The Eulerian formulation can also be called the "conservative" form, as it is derived by integrating over a control volume assuming that conservation of mass, momentum, and energy must

[27] Here, "entropy" is the particle's specific thermodynamic entropy and not the adiabatic invariant K that is commonly referred to as "entropy" elsewhere in this dissertation.

hold (see Toro 2009, Section 1.5). In this form, the equations for pure hydrodynamics are

$$\frac{\partial \rho}{\partial t} + \boldsymbol{\nabla} \cdot (\rho \mathbf{v}) = 0 \tag{1.25}$$

$$\frac{\partial \rho \mathbf{v}}{\partial t} + \boldsymbol{\nabla} \cdot (\rho \mathbf{v} \otimes \mathbf{v} + P \mathbb{I}) = 0 \tag{1.26}$$

$$\frac{\partial \rho e}{\partial t} + \boldsymbol{\nabla} \cdot \mathbf{v}(\rho e + P) = 0 \tag{1.27}$$

where $\mathbb{I}$ is the identity matrix. The zeros on the right hand sides of these equations can be replaced with source and sink terms as required by additional physical models.

Colloquially, many astronomers refer to Eulerian hydrodynamics software as "grid codes."[28] This is because the Eulerian perspective is well suited to a class of numerical methods known as "finite volume methods" that discretize the underlying "true" fluid using a grid of cells. Whereas particle methods represent the precise state of the fluid at a given point, each cell in a finite volume method represents the *average* state of the underlying fluid within that cell. The Godunov class of methods are most commonly used for updating these cell averages (Godunov 1959; Toro 2009; Teyssier 2015). Rather than tracking the motion of particles through the simulation domain, Godunov methods track the fluxes through each cell face, thus ensuring conservation both locally and globally. The first step of any Godunov scheme is therefore to "reconstruct" the field values at the face using nearby cell data, since under the finite volume framework the cell values are averages. Examples of Eulerian hydrodynamics codes include Enzo (Bryan et al. 2014; Brummel-Smith et al. 2019), PLUTO (Mignone et al. 2007, 2012), RAMSES (Teyssier 2002), Athena++ (Stone et al. 2020), and CHOLLA (Schneider and Robertson 2015).

The exercise of solving for the fluxes between two cell faces is known as solving the Riemann problem. The Riemann problem is in essence a contact discontinuity, where one cell with state $(\rho_\mathrm{L}, \mathbf{v}_\mathrm{L}, P_\mathrm{L})$ abuts another with state $(\rho_\mathrm{R}, \mathbf{v}_\mathrm{R}, P_\mathrm{R})$. Multiple wave states, such as shocks and rarefaction waves, then combine to provide the total flux through the cell boundary. Though an exact solution does exist, it is computationally intractable to solve the exact Riemann problem six

[28] Note that Lagrangian codes can also use a grid-based discretization instead of a particle one. A prominent example is the MESA one-dimensional stellar evolution software (Paxton et al. 2011, 2013, 2015, 2018, 2019). Purely Lagrangian grid-based codes are not feasible at higher dimensions, however, as fluid motions can warp the grid and lead to a build-up of large numerical errors (Teyssier 2015).

times for each cell in a three-dimensional simulation. Instead, any of a number of approximate Riemann solvers can be used instead. Several popular ones are covered by Toro (2009). It is common for Eulerian codes to have multiple Riemann solvers available, as more accurate solvers are both less stable near a shock front and more computationally expensive. This can lead to unphysical values such as negative densities in the cells near the front. When this occurs, it is often best to fall back on a less accurate, more diffusive Riemann solver.[29]

The simulations used to study galaxy evolution often span a wide dynamic range. Simulations of cosmological structure, for example, require domains of $(\sim 100\ \mathrm{cMpc})^3$ while galaxies internally need resolutions of 0.1–1 ckpc or better (depending on the mass of the galaxy and its halo) to resolve their internal dynamics. This means that simulations must be able to span 5–6 orders of magnitude in resolution(see arguments in, e.g., Kravtsov, Klypin, and Khokhlov 1997; Teyssier 2002 though the galaxy resolution requirements have been updated to match modern standards). For an Eulerian grid code, the number of cells needed to resolve a $(\sim 100\ \mathrm{cMpc})^3$ box with a uniform resolution of even 10 ckpc is computationally intractable at 10^{12} cells.

The solution to the problem of dynamic range is that almost all astrophysical simulations, whether based on particles or grids, use some form of adaptive refinement. These schemes ensure that regions of interest—typically dense regions, though notable exceptions exist (e.g. Peeples et al. 2019; van de Voort et al. 2019)—are better resolved than other parts of the simulation. Lagrangian simulations naturally have more particles in high density regions,[30] to the point where forcing the resolution to increase in *low* density regions like the CGM requires clever algorithms (e.g. Suresh et al. 2019; van de Voort et al. 2019) Grid-based codes, on the other hand, must implement additional algorithms for a technique known as adaptive mesh refinement (AMR; see, e.g., the algorithms used in Peeples et al. 2019; Simons et al. 2020).

AMR approaches come in two forms depending on what data structures are created and destroyed

[29] A "more diffusive" Riemann solver will lead to a less well-resolved shock front. Inherently, the Euler equations assume an ideal fluid with no viscosity (i.e. no diffusion), but approximate Riemann solvers introduce some degree of artificial, "numerical" viscosity. A less accurate Riemann solver will introduce a larger amount of numerical viscosity.

[30] Though length scales were used to demonstrate the need for adaptive resolution, discussing resolution in terms of mass is more natural for particle codes. Comparing their spatial resolution with grid-based codes depends on the smoothing kernel and its (potentially variable) width.

as (de)refinement occurs: grid- and cell-based (also referred to as patch- and tree-based by Teyssier 2002). Grid-based AMR has historically followed the method of Berger and Colella (1989). When cells are flagged as needing refinement (e.g., because their density exceeds some multiple of the background density) this AMR approach seeks to "cover" these cells in an optimal arrangement of new grids with smaller cell sizes. The optimization typically seeks to balance grid size and aspect ratio according to memory and communication constraints, and cells widths on the refined grid typically improve by a factor of two. The resulting hierarchy of grids is tracked and periodically entirely rebuilt. This is the algorithm used by Enzo (Bryan et al. 2014; Brummel-Smith et al. 2019) and in the stellar fluid codes CASTRO (Almgren et al. 2010) and MAESTRO (Nonaka et al. 2010).[31]

Alternatively, the flagged cell may refine *itself* by splitting into eight children (in three dimensions). Successive refinement therefore leads to an (oct)tree of parent and child cells with the most refined cells (i.e. those with the smallest cell width) as the leaves (Khokhlov 1998). This is the approach used by RAMSES (Teyssier 2002) and ART (Kravtsov, Klypin, and Khokhlov 1997). Indeed, in the original method paper for ART, this tree structure is why those authors prefer the name "multilevel" for their Poisson solver (see Section 1.3.2.2): all of the cells at the same refinement level, which may not be spatially contiguous, are used for each phase of the Poisson algorithm.[32] An octree approach may also be applied to *grids* rather than cells (i.e. a grid that has been flagged for refinement will split into eight child grids). This approach has largely replaced the patch-based AMR of Berger and Colella (1989), such as in the successor to Enzo, Enzo-E.[33]

A hydrodynamics code need not be purely Lagrangian or purely Eulerian in its approach. The Arepo code (Springel 2010a; Weinberger, Springel, and Pakmor 2020) uses an arbitrary Eulerian-Lagrangian method. Fluid quantities are tracked via Lagrangian particles that move with the gas, but rather than use a kernel to exchange hydrodynamic quantities like in SPH, a mesh

[31] Neither CASTRO nor MAESTRO can be used for simulating galaxies, but the Eulerian fluid methods described in this Section can be applied to a wide range of astrophysical problems. Similarities in numerical methods are both inevitable and insightful.

[32] Similarly, the possibility for spatial discontinuity is why the arrangement of cells on the same level is a "mesh" and not a "grid."

[33] https://enzo-e.readthedocs.io/

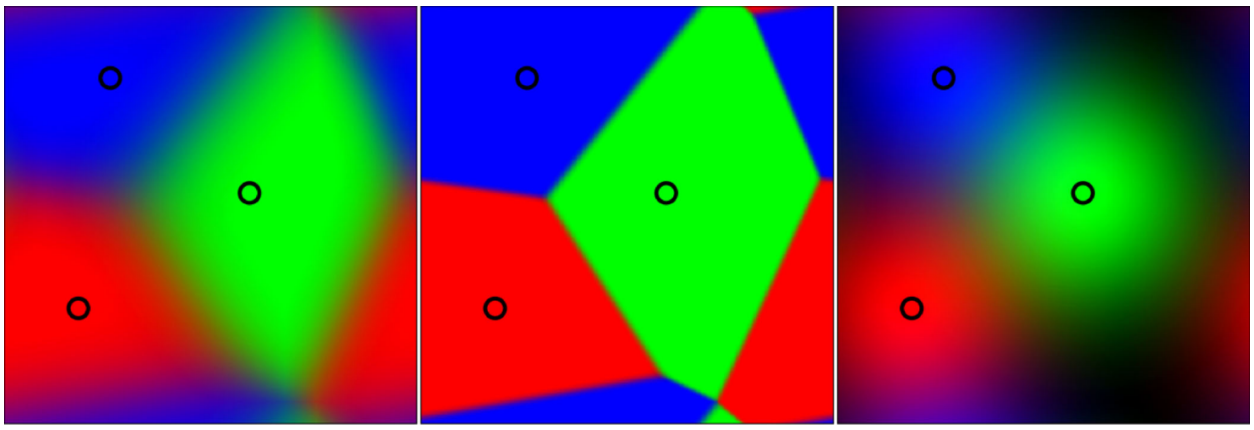

Figure 1.7 Demonstration of particle-based approaches for fluid modeling. Colors represent the weighted area of influence for each particle (black circles). Left is the meshless Eulerian-Lagrangian approach from Hopkins (2015), middle shows the Voronoi tessellations used in the Eulerian-Lagrangian approach of Springel (2010a), and right shows traditional SPH. Modified from Hopkins (2015).

is constructed around the fluid particles across which Eulerian fluxes are calculated. The word "mesh" is used in this case because the resulting cells are not rectilinear. They are instead the result of an (approximate) Voronoi tessellation and can have arbitrary shape. Indeed, sometimes these methods are referred to as having "unstructured meshes." A Voronoi tessellation is defined such that all points within a Voronoi cell are closer to their parent particle than to any other particle.

Another arbitrary Eulerian-Lagrangian approach is utilized by the Gizmo code (Hopkins 2015). Rather than construct a mesh via Voronoi tessellation, Gizmo's fluid algorithm is mesh-free. Again, fluid quantities are tracked with particles that move along with the gas. Yet when integrating the Euler equations, the control volume is not a discrete cell (as in finite volume methods) but is instead partitioned among the nearest neighboring particles using a weighting kernel $W(\mathbf{r}, h)$. As Hopkins (ibid.) notes, "in the limit where W is sufficiently sharply-peaked . . . we should recover exactly a Voronoi tessellation, because 100% of the weight will be associated with the nearest particle." This results in "cells" with fuzzy "faces," as can be seen in Figure 1.7. This figure, borrowed from Hopkins (ibid.), compares the discretization of the meshless method therein with both a Voronoi tessellation and with an SPH smoothing kernel.

With the meshless approach, the "faces" between particles can shift with time. This has

implications for the Riemann problem and therefore the interparticle fluxes. One option is to assume the faces are fixed, since the field at those faces is reconstructed in the reference frame of the most heavily weighted "central" particle. This assumption is the same one made by finite volume methods. Correspondingly, when operating under this assumption Gizmo is in "meshless finite volume" mode. The alternative mode is "meshless finite mass," where the face is assumed to move with the mean motion of the entire cell volume. In practice, this adds a residual velocity to the Riemann problem. This assumption eliminates mass flux between particles (hence the name) and is analogous to the finite element methods commonly used in engineering applications.

Regardless of whether fluids are treated in a Eulerian or Lagrangian manner (or some mixture of the two), the maximum possible timestep is limited by the Courant-Friedrichs-Lewy (CFL) condition. This criterion ensures that, in one timestep, the fastest waves in the simulation cannot travel farther than one resolution element. For a grid code, this means waves cannot travel farther than one cell; for SPH, they cannot travel beyond the width of the smoothing kernel h. If the maximum signal speed is $c_{\rm max}$, the dimensionless "CFL coefficient" or "Courant number" is $C_{\rm CFL} = c_{\rm max}\Delta t/\Delta x$ for grid codes (Toro 2009) or $C_{\rm CFL} = c_{\rm max}\Delta t/h$ for SPH (Springel 2010b). If $0 < C_{\rm CFL} \leq 1$, the method is stable.[34] It then follows that the timestep is $\Delta t = C_{\rm CFL}\Delta x/c_{\rm max}$ (where again, the kernel width h takes the place of Δx for an SPH code). In practice, $C_{\rm CFL}$ is a free parameter; for example, the Enzo documentation[35] recommends $C_{\rm CFL} = 0.4$ while Springel (ibid.) report that $C_{\rm CFL} \sim 0.1$–0.3 is typically used for SPH codes. The maximum signal speed may then be, e.g., $\max_i(c_{s,i} + \mathbf{v}_i)$ where i denotes an individual gas particle or cell and c_s is the gas sound speed. If the simulation is not purely hydrodynamical, other speeds may be faster. In a cosmological simulation that contains dark matter particles (see Sections 1.3.2.1 and 1.3.2.2), the fastest signal speed may be the individual velocity of one of those particles. If the simulation includes magnetic fields, it may be the Alvén speed.

While most of this section has focused on the main approaches for fluid modeling and their

[34] Technically, this requirement is only true for explicit methods. Implicit (i.e. iterative) methods may have $C_{\rm CFL} > 1$, but in practice, all astrophysical fluid codes use explicit methods.

[35] https://enzo.readthedocs.io/en/latest/

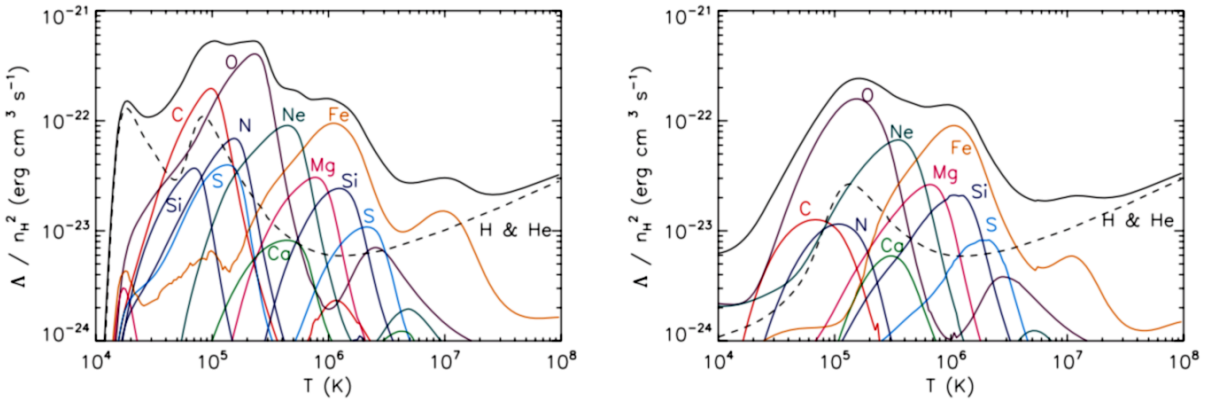

Figure 1.8 Normalized cooling rate as a function of temperature assuming solar abundances. Left panel assumes only CIE; right panel assumes PIE for optically thin gas at $n_{\rm H} = 10^{-4}$ cm^{-3} exposed to the Haardt and Madau (2001) UV and X-ray metagalactic background. Black solid curves show the total cooling function. Black dashed curves show contribution from H and He, while colored curves show contribution from individual metal elements. Adapted from Wiersma, Schaye, and Smith (2009).

respective considerations, there remains one final component crucial for modeling gas: cooling. Gas can dissipate its internal energy through a variety of collisional and radiative processes. The dominant atomic or molecular coolant varies with temperature; for example, various metal lines dominate from $10^5 \lesssim T \lesssim 10^7$ K while the CO molecule dominates around number densities of $n \sim 100$ cm^{-3} and $T \lesssim 50$ K (Vogelsberger et al. 2020). The complex interaction of processes that result in cooling are encapsulated in the cooling function $\Lambda(T, Z, n, z)$ which depends on temperature, metallicity, density, and redshift respectively. The redshift dependence arises from the time variance of the metagalactic UV and X-ray radiation field after cosmic reionization is complete. In Section 1.1.2 we introduced the cooling function as $\Lambda(T, Z, n)$. Technically, the physics that govern gas cooling are independent of any background radiation; yet from a practical standpoint, it is easier to integrate the metagalactic radiation background into the cooling function. This is because the background can result in a negative cooling rate in some regimes; that is, net heating. Models for this background include Faucher-Giguère et al. (2009), Haardt and Madau (2012), and Khaire and Srianand (2019).

The cooling function assumes both collisional and photoionization equilibrium (CIE and PIE,

respectively). It can be incorporated into simulations in a variety of ways, from fits to the complex functional form (as done by Hopkins et al. 2018a for $T \lesssim 10^4$ K and/or $n \gtrsim 1$ cm^{-3} and by Schneider, Robertson, and Thompson 2018 for all densities and temperatures) to using pre-computed tables (e.g. those generated by Sutherland and Dopita 1993; Kravtsov 2003; Wiersma, Schaye, and Smith 2009; Smith et al. 2017). The most common code for calculating such tables is CLOUDY (see Ferland et al. 2017 for the latest release). These tables can then be coupled to chemistry networks such as that provided by the Grackle cooling and chemistry library (Smith et al. 2017). As an example, Figure 1.8 shows the normalized cooling rates (i.e. the cooling function Λ divided by the hydrogen number density $n_{\rm H}^2$, which for charge neutral H II gas is exactly the rate of energy loss) as a function of temperature as calculated by Wiersma, Schaye, and Smith (2009). These rates assume the metals match Solar abundances. The left panel assumes only CIE (which is independent of density), while the right assumes PIE for optically thin $n_{\rm H} = 10^{-4}$ cm^{-3} gas exposed to the Haardt and Madau (2001) model for the metagalactic radiation background. The solid black curve shows the total cooling rate, the colored curves show the contributions from individual elements, and the dashed line shows the contribution from hydrogen and helium.

1.3.2.4 Star Formation & Feedback

The earliest galaxy formation simulations to include hydrodynamics and cooling produced galaxies that had too much cold gas and too much gas overall. Critically, these simulations did not account for star formation and feedback (see Naab and Ostriker 2017 and references therein). As discussed in Section 1.1.3, "feedback" is the injection of mass, momentum, and/or energy that inhibits or (more rarely) promotes further star formation.[36] In this way, stars act as both sinks (for cold, dense gas) and sources of feedback.

Addressing the "sink" portion is more straightforward than feedback. Especially in cosmological simulations (see Section 1.3.2.1), stars are often modelled as particles. At minimum, when the density exceeds a certain threshold, an amount of gas is removed and a particle of equivalent mass is inserted at that same location. This is most often done in a Schmidt-type manner (Schmidt

[36]This same definition also applies to AGN feedback; see Sections 1.1.4 and 1.3.2.5.

1959; Naab and Ostriker 2017) with the star formation rate related to the gas density divided by a timescale. This timescale is often either the cooling time or the dynamical time (Cen and Ostriker 1992; Katz 1992 as reviewed by Naab and Ostriker 2017). Star formation prescriptions include free parameters such as the star formation efficiency that controls the conversion from gas mass to stellar mass. Such parameters are often tuned so that simulations reproduce e.g. the Kennicutt-Schmidt relation (Schmidt 1959; Kennicutt 1989, see Section 1.1.3). It is important to note that in all but simulations of individual dwarf galaxies or pieces of the ISM, these particles represent *populations* of stars whose constituents are described by an initial mass function (IMF). Otherwise, modeling individual stars would overwhelm computational capabilities. Moreover, the spatial resolution is often insufficient to track individual star-forming regions; in cosmological simulations, the ISM is typically only resolved on the scale of hundreds of parsecs.

The Illustris and IllustrisTNG simulations (Vogelsberger et al. 2013, 2014; Pillepich et al. 2018b) use a comoving number density threshold of $n < 0.13$ cm^{-3} for star formation. These simulations also require that the gas temperature does not exceed the temperature dictated by their effective ISM equation of state (EOS). This effective EOS defines temperature as a function of density in an attempt to capture small-scale effects like supersonic turbulence, thermal instabilities, thermal conduction, and molecular cloud formation and evaporation (Springel and Hernquist 2003; Vogelsberger et al. 2013). The EAGLE simulations (Schaye et al. 2015) also use an effective EOS to dictate the temperature threshold and have a metallicity-dependent comoving density threshold (Schaye 2004), though their density criteria are of a similar order of magnitude to those used in IllustrisTNG.

Both Illustris(TNG) and EAGLE are focused on simulating large cosmological volumes with statistically-meaningful numbers of galaxies. The FIRE-2 simulations (Hopkins et al. 2018a) are cosmological zoom-in simulations (see Section 1.3.2.1) with a specific focus on high resolution in the ISM. As such, their number density threshold for star formation is much higher ($n = 1{,}000\,\mathrm{cm}^{-3}$) since more ISM structure can be resolved. Instead of a temperature requirement, these simulations also check that gas is locally gravitationaly self-bound and that there is enough molecular hydrogen

to self-shield from the local radiation field. The FOGGIE zoom-in simulations (Peeples et al. 2019) focus their resolution on the CGM, and so adopt a comoving number density threshold of $n \approx 0.1$ cm^{-3} that is more in line with IllustrisTNG and EAGLE. Their additional requirements come from Cen and Ostriker (1992): the gas must be contracting ($\boldsymbol{\nabla} \cdot \mathbf{v} < 0$), the gas must be sufficiently cold ($T < 1.1 \times 10^4$ K) or cooling quickly ($t_{\rm cool} < t_{\rm dyn}$ where $t_{\rm dyn}$ is the local gas dynamical time), and the cell must have enough mass to warrant forming a particle.[37]

After a star particle is created, it can then act as a source of feedback. The feedback mechanism that has received the most focus is Type II supernovae, which are both powerful (yielding approximated 10^{51} erg per star with zero-age main sequence mass $\gtrsim 8$ M$_\odot$) and relatively prompt (occurring within ~ 5 Myr after formation for the most massive stars in the several tens of solar masses and within ~ 50 Myr for those closer to 8 M$_\odot$). As discussed in Section 1.1.3, Type Ia supernovae release similar amounts of energy but after a considerable time delay, and stellar winds are not as powerful as supernovae. Type II supernovae can also inject $\sim$ 1–10 M$_\odot$ of gas (Kim and Ostriker 2015). Therefore, Type II supernovae have been long suspected as playing a critical role in galaxy formation (e.g. Larson 1974; Dekel and Silk 1986; Navarro and White 1993 as reviewed in Naab and Ostriker 2017).

Supernovae drive shocks, both a forward shock or "blastwave" and a resulting reverse shock. The material interior to the leading blastwave is called the supernova remnant (SNR). This system evolves through a number of phases that are reviewed by e.g. Draine (2011), Kim and Ostriker (2015), and Naab and Ostriker (2017). The first is the free-expansion phase, but the momentum injected during this phase is insufficient to accelerate the surrounding gas to high velocities. When the SNR has swept up additional mass that is roughly equivalent to its original ejecta mass, the reverse shock becomes important for heating the SNR. Once this shock has reached the interior of the SNR the free-expansion phase has ended and the Sedov-Taylor phase begins. In this phase, energy is conserved and the expanding SNR can be described by the blast solution of Sedov

[37] Both the FIRE-2 (Hopkins et al. 2018a) and Cen and Ostriker (1992) star formation algorithms include a criterion based on the Jeans mass. In practice, with today's simulation resolution such a criterion is always fulfilled if all other criteria are met.

(1959) and Taylor (1950). The Sedov-Taylor phase is responsible for the bulk of the energy and momentum generation, so it is important to resolve in simulations. It ends once radiative cooling is able to dominate, reducing the blastwave to a thin shell. What follows are two "snowplow" phases, so named because the still-expanding shell "sweeps-up" surrounding material. For a time, the pressure of the SNR is able to drive this shell forward in what is appropriately called the "pressure-driven snowplow" phase. As the thermal energy of the SNR radiates away, the shell enters the momentum-conserving snowplow phase before dissipating.

One of the oldest approaches for modeling Type II supernova energy injection can be called the "thermal dump" method as in Rosdahl et al. (2017). This method emulates the heating that occurs during the Sedov-Taylor phase by injecting the entire supernovae energy budget as thermal energy. This energy could be distributed over several resolution elements (cells or particles) or contained to the star particle's most immediate surroundings. Yet unless the Sedov-Taylor phase is adequately resolved in both space and time, energy injected by this method is likely to quickly radiate away (e.g. Katz 1992 as noted in Rosdahl et al. 2017). This is because the resulting temperature is often near the peak of radiative cooling efficiency at $T \sim 10^5$ K (see Figure 1.8) for cells with resolution typical for galaxies in cosmological simulations.

The comparisons from Rosdahl et al. (2017) and Smith, Sijacki, and Shen (2018) discuss a number of alternative algorithms designed to overcome this flaw with the thermal dump model. One such approach is to artificially disable cooling for a short time, as used in Stinson et al. (2006) and Teyssier et al. (2013). Naab and Ostriker (2017) note that, although this method is often criticized for being unphysical, its intent is to allow for the growth of superbubbles (see e.g. Mac Low and McCray 1988). Another is to perform feedback stochastically, where feedback is "held in reserve" until enough time has passed such that the energy increase will ensure a temperature threshold can be exceeded (e.g. Dalla Vecchia and Schaye 2012). This is the algorithm used by the prominent EAGLE cosmological simulations (Schaye et al. 2015).

Yet another alternative is to skip the potentially unresolved Sedov-Taylor phase and directly inject kinetic energy that emulates the momentum-conserving snowplow phase (Rosdahl et al.

2017). Both Rosdahl et al. (2017) and Smith, Sijacki, and Shen (2018) call this "kinetic feedback." Like thermal feedback, the kinetic energy can be injected into only one resolution element (as in Smith, Sijacki, and Shen 2018, where it is injected into the particle's host cell) or distributed (e.g. Dubois and Teyssier 2008).

The final kind of feedback injection investigated by Rosdahl et al. (2017) and Smith, Sijacki, and Shen (2018) can be dubbed "mechanical feedback" because these schemes focus on the momentum generated during the various supernova phases. These methods, which include Hopkins et al. (2014), Kimm and Cen (2014), Kim and Ostriker (2015), and Hopkins et al. (2018b), adjust the amount of momentum and energy deposited based on e.g. whether or not the Sedov-Taylor phase is resolved. These algorithms are perhaps some of the most sophisticated feedback treatments because of this adaptability.

Particle-based simulation codes (see Section 1.3.2.3) can use feedback prescriptions that decouple particle evolution from the hydrodynamics (Naab and Ostriker 2017). Hot and cold gas may be evolved separately, with supernova energy stored in the cold gas particles (i.e. decoupled from the hydrodynamics) that is only released when said particle joins the hot phase (Marri and White 2003; Scannapieco et al. 2006). The superbubble-based feedback model of Keller et al. (2014) uses a similar idea, following two phases that interact with each other. Feedback may also launch "wind" particles that travel decoupled from the hydrodynamics for a time. This method was first introduced by Springel and Hernquist (2003) and used in both Illustris and IllustrisTNG (Vogelsberger et al. 2014; Pillepich et al. 2018b).

The sheer variety of implementations for supernova feedback and their accompanying multitudes of parameters constitute perhaps the single largest source of uncertainty in simulations of galaxy evolution (e.g. Kim et al. 2016; Roca-Fàbrega et al. 2021). Supposedly, this vast array of methods are all supposed to model the same underlying physical process. The discrepancies between methods therefore makes it difficult to interpret whether simulation results are physically informative or merely a result of tuning a given feedback model to a set of e.g. scaling relations (Section 1.2.2; Naab and Ostriker 2017). Figure 1.9 shows the density-temperature phase diagrams from the

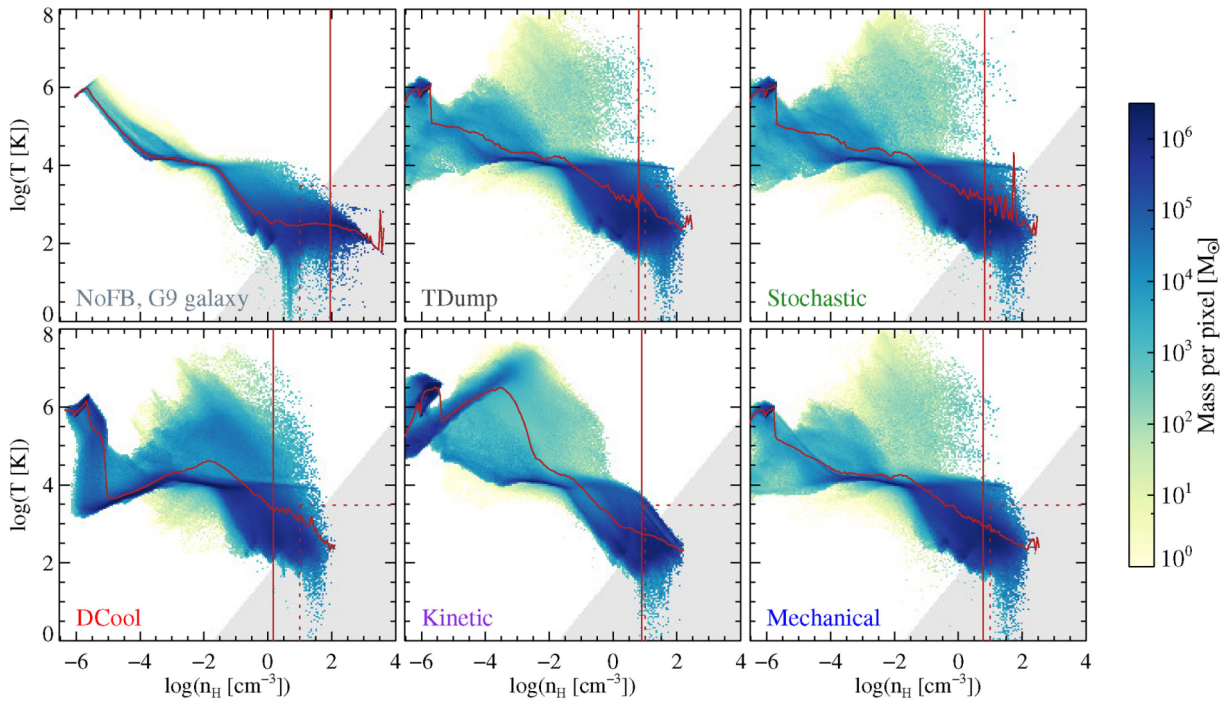

Figure 1.9 Density-temperature phase diagrams for a cosmological zoom-in galaxy simulation with varying supernova feedback implementations and halo mass $M_{200} = 10^{11}$ $M_\odot$. The color shows the total amount of mass in each bin. The solid red curve shows the mass-weighted mean temperature as a function of density, while the solid red vertical line is the overall mass-weighted mean density for the galaxy. The dashed red lines make the parameter region where star formation is allowed. The gray region shows where gas receives additional artificial pressure support. NoFB: no feedback; TDump: thermal dump; DCool: delayed cooling. Reproduced from Rosdahl et al. (2017).

supernova feedback comparison of Roberts-Borsani (2020). This work used the RAMSES code (Teyssier 2002) to perform zoomed simulations of galaxies with halo masses of 10^{11} and 10^{12} $M_\odot$. Smith, Sijacki, and Shen (2018) used the AREPO code (Springel 2010a) to perform a similar study for idealized Milky Way-like galaxies. The phase diagrams from Rosdahl et al. (2017) compare the gas distributions for a simulation of the 10^{11} $M_\odot$ halo with no feedback to simulations using the thermal dump, stochastic, delayed cooling, kinetic, and mechanical feedback methods described above. The dashed red lines delineate the density and temperature thresholds for star formation, while the shaded triangle shows the region of phase space where the equation of state is modified to include additional ISM pressure support. The vertical red line makes the mass-weighted mean

density of each simulation, and the red curve follows the mass-weighted mean temperature as a function of density. Rosdahl et al. (2017) highlight that the delayed cooling simulation has an excess of gas with $T \sim 10^5$ K. This gas should be able to cool very efficiently (see Figure 1.8) but instead accumulates unphysically because of the delayed cooling. In both this comparison and a similar one shown in Figure 2 of Smith, Sijacki, and Shen (2018), the thermal dump, kinetic, and mechanical feedback prescriptions provide similar results; however, in their larger galaxy ($M_{200} = 10^{12}$ $M_\odot$), Rosdahl et al. (2017) find that the thermal dump feedback becomes significantly weaker at driving outflows. They argue that this is because the larger galaxy is relatively less well resolved for its mass. Smith, Sijacki, and Shen (2018) also find that the ability of mechanical feedback to drive outflows is very resolution dependent, with outflows being virtually non-existent at their lowest resolution (which matches that of Rosdahl et al. (2017) who find similar results).

Outside of the context of phase diagrams, these different feedback approaches may well differentiate even when the resolution is high enough for thermal dump feedback to avoid excessive cooling.

Instead of using particles, idealized simulations may take alternative approaches to modeling stars. The CGM simulations from Fielding et al. (2017) and Li and Tonnesen (2020) track the mass inflow through an inner boundary and inject stellar winds scaled to that inflow mass, skipping over the star formation step. Other idealized simulations, such as the CGOLS isolated galaxy simulations (Schneider and Robertson 2018; Schneider, Robertson, and Thompson 2018; Schneider et al. 2020), may opt to model only feedback and ignore star formation all together. Still others, such as Butsky et al. (2020) or Buie II, Fumagalli, and Scannapieco (2020), Buie II et al. (2020), and Buie II, Scannapieco, and Mark Voit (2022), may make no effort to model feedback processes such as winds or supernovae at all (though the latter three works include explicit turbulent energy injection, which is one byproduct of stellar feedback).

Type Ia feedback can be implemented with the same numerical prescriptions as Type II supernovae but with a suitable time delay representing white dwarf formation. Options for this time delay include using analytic formulas (e.g. EAGLE; Schaye et al. 2015) or using tabulated rates

obtained from stellar population synthesis (e.g. Hopkins et al. 2018a; see Section 1.1.3).

As mentioned in Section 1.1.3, secondary sources of feedback include winds from massive stars, heating from photoionization, and radiation pressure (e.g. Hopkins et al. 2018a; Keller, Kruijssen, and Chevance 2022). Mass return from massive AGB stars is a common but not ubiquitous feature of cosmological simulations (see Schaye et al. 2015; Pillepich et al. 2018b, and the Gadget-3 and CHaNGa variants in Roca-Fàbrega et al. 2021 for example uses) as it is easily added to the masses returned by Type II and Ia supernovae. AGB stars also contribute a set of metal yields unique from both types of supernovae. These winds may also contribute energetically (as implemented in Hopkins et al. 2018a and the Gadget-3 and ART-1 variants in Roca-Fàbrega et al. 2021).

Less common are implementations of radiation pressure and photoheating. In the AGORA Project's comparison of CGM simulations, for example, only two of the seven participating codes include the effects of radiation pressure (compared to three codes with some form of AGB contribution; ibid.) Neither the EAGLE or IllustrisTNG simulations—two widely studied cosmological simulations—include either pressure or heating from radiation (Schaye et al. 2015; Pillepich et al. 2018b). Hopkins, Quataert, and Murray (2012a) found that including these two radiative processes alongside winds from both AGB and OB stars and both Type II and Ia supernovae led to the creation of multiphase outflows that no one feedback mechanism could reproduce. In Hopkins, Quataert, and Murray (2012b) it was also found that radiation pressure and heating from photoionization could prevent an excess of star formation in GMCs. In both of these works (which laid the groundwork for the feedback mechanisms deployed in the FIRE-2 simulations; see Hopkins et al. 2018a) radiation pressure and heating are implemented with unique numerical prescriptions. An alternative approach was formulated by Keller, Kruijssen, and Chevance (2022), whose model for "pre-supernova" feedback is agnostic to whether the feedback disrupting a star-forming GMC comes from massive stars, radiation pressure, or photoionization. It instead relies on observationally-inferable parameters for a simple analytic model. Like Hopkins, Quataert, and Murray (2012b), this feedback approach is able to prevent excessive star formation by disrupting star-forming clouds.

1.3.2.5 AGN

As with stars, black holes may be modelled with particles or the energy injection of AGN may be tied to a geometric region, with particles prevailing in cosmological simulations. I'll use the EAGLE (Schaye et al. 2015) and IllustrisTNG simulations (Weinberger et al. 2017; Pillepich et al. 2018b) as examples throughout this section. Both of these sets of simulations have been widely studied by the community.

While the origin of today's supermassive black holes is still uncertain (see Section 1.1.4), SMBH particles in cosmological simulations are usually seeded in dark matter halos with mass $M_{\rm vir} \gtrsim 10^{10}$–$10^{11}$ $M_\odot$ (Somerville and Davé 2015). This includes our two example simulation sets. Since cosmological simulations have limited resolution at the center of halos, dynamical friction is usually unable to keep black holes within the deepest part of the potential well. Instead, simulations like EAGLE and IllustrisTNG periodically adjust the SMBH's position to coincide with the local potential minimum.

Black holes grow in mass over time and this is usually computed using the Bondi-Hoyle-Lyttleton formula (usually shortened to "Bondi accretion"; (Hoyle and Lyttleton 1939; Bondi and Hoyle 1944; Bondi 1952 as reviewed by Somerville and Davé 2015; Naab and Ostriker 2017):

$$\dot{M}_{\rm Bondi} = \alpha \frac{4\pi G^2 M_{\rm BH}^2 \rho}{(c_s^2 + v_{\rm rel}^2)^{3/2}} \tag{1.28}$$

where $M_{\rm BH}$ is the mass of the black hole, c_s and ρ are the sound speed and density of the gas respectively, $v_{\rm rel}$ is the velocity of the black hole relative to the gas, and α is a boost parameter that adjusts for the unresolved multiphase gas near the black hole. Historically, models have used a constant $\alpha \sim 100$ (as noted in Somerville and Davé 2015) while others have made it density dependent (e.g. Booth and Schaye 2009). Recent simulations (like EAGLE and IllustrisTNG) find that they have sufficient resolution to set $\alpha = 1$ (Somerville and Davé 2015).

The accretion rate is typically limited by the Eddington limit

$$\dot{M}_{\rm Edd} = \frac{4\pi G M_{\rm BH} m_{\rm p}}{\epsilon_r \sigma_{\rm T} c} \tag{1.29}$$

where m_p is the mass of the proton, σ_T is the cross-section for Thomson scattering, c the speed of light, and ϵ_r is the radiative efficiency of the accretion disk (usually 10%; see e.g. Schaye et al. 2015). This limit is set by the balance between inwardly falling material and outward radiation pressure. Both Bondi accretion and the classical Eddington limit assume spherical accretion, though because of angular momentum conservation, accretion is more likely to occur through a disk. Rosas-Guevara et al. (2015) include a modification factor for the accretion rate to account for this morphology, reducing the overall accretion rate:

$$\dot{M}_\mathrm{BH} = \dot{M}_\mathrm{Bondi} \times \min\left(\frac{(c_s/V_\phi)^3}{C_\mathrm{visc}},\ 1\right). \tag{1.30}$$

Here, V_ϕ is the rotation speed of gas around the black hole (Equation 16 in ibid.) and C_visc is a free parameter for the viscosity of the (unresolved) accretion disk. This correction is used in, e.g., the EAGLE simulations.

Black holes modelled with Bondi accretion tend to have their growth regulated by the black hole's own feedback, but there is no precedent for this in nature (Alexander and Hickox 2012; Anglés-Alcázar, Özel, and Davé 2013). Naab and Ostriker (2017) include in their review an alternative model for black hole accretion, where gas is driven to the center of galaxies by gravitational torques. A sub-resolution model for this accretion mode was put forth by Hopkins and Quataert (2011). Simulations by Anglés-Alcázar, Özel, and Davé (2013) and Anglés-Alcázar et al. (2017) used this model and were able to recover scaling relations such as the M_BH–M_bulge and M_BH–σ relations (see Section 1.1.4) without the black hole mass becoming self-regulated by feedback. The SIMBA cosmological simulations (Davé et al. 2019) have since incorporated this torque-limited accretion model.

The energy injected by AGN feedback is tied to the black hole accretion rate. The most basic approach is to assume that some fraction of the radiation from the accretion disk heats the surrounding gas (Somerville and Davé 2015; Naab and Ostriker 2017 and references therein). The bolometric luminosity of the disk is assumed to be proportional to the accretion rate such that $L_\mathrm{bol} = \epsilon_r \dot{M}_\mathrm{BH} c^2$ with a radiative efficiency of $\epsilon_r = 0.1$ (Shakura and Sunyaev 1973; Soltan 1982). The amount of energy injected due to heating is then $\dot{E} = \epsilon_\mathrm{therm} \epsilon_r \dot{M}_\mathrm{BH} c^2$, where ϵ_therm describes

the efficiency with which radiation heats the gas. Early idealized disk simulations showed that $\epsilon_{\rm therm} \sim 5\%$ was enough to halt further black hole accretion and remove enough cold gas to quench star formation (Springel, Di Matteo, and Hernquist 2005 as recounted by Somerville and Davé 2015). Practically, this energy is usually injected as thermal energy similar to the earliest methods for supernova feedback (Section 1.3.2.4). As with supernova feedback, AGN energy may be deposited stochastically by waiting until the resulting temperature increase exceeds some threshold (e.g. Schaye et al. 2015).

In Section 1.1.4, we introduced the two modes for AGN feedback—quasar/bright mode and jet/radio mode. This thermal dump approach most closely mimics quasar mode feedback, but in this mode, it is uncertain whether AGN winds are primarily driven by energy input or by the injection of momentum (see Somerville and Davé 2015). When winds shock the surrounding gas they will generate thermal energy and the distinction between the two driving mechanisms depends on how quickly that thermal energy is radiated away. If these losses are negligible, the momentum flux is boosted by work done on the surrounding gas, similar to the Sedov-Taylor phase of a supernova explosion discussed in Section 1.3.2.4. Real winds are likely a mixture of these two driving mechanisms, however, and purely thermal AGN feedback models neglect any momentum deposition. Both Somerville and Davé (2015) and Naab and Ostriker (2017) cover simulations that model momentum-driven winds. DeBuhr et al. (2010) and DeBuhr, Quataert, and Ma (2011, 2012) include the effects of radiation pressure on dust surrounding the AGN. The simulations of Choi et al. (2012, 2014) and Hopkins et al. (2016) include winds driven by broad absorption line features as well as heating from radiation. Recent examples of simulation using the latter models include Choi et al. (2017) and Hopkins et al. (2022).

Sijacki et al. (2007) proposed an approach for incorporating both quasar and jet feedback modes that depends on the accretion rate of the black hole. A version of this approach was incorporated into both the original Illustris cosmological simulation (Vogelsberger et al. 2014) and its successor IllustrisTNG (Weinberger et al. 2017; Pillepich et al. 2018b). In this two-mode approach, the feedback prescription changes based on the ratio of $\dot{M}_{\rm BH}/\dot{M}_{\rm Edd}$. When this ratio is low, the AGN is

assumed to be radiatively inefficient and in jet mode. A high ratio puts the AGN into quasar mode. The ratio at which these modes switch varies with simulation but it is typically 0.1–0.2 (Weinberger et al. 2017). For IllustrisTNG, AGN in quasar mode will inject thermal energy as previously discussed. Both the original Illustris simulations and Sijacki et al. (2007) adopt a "bubble" model for the low-accretion jet mode which attempts to mimic the hot X-ray bubbles associated with radio jets (see Section 1.1.4). The Illustris approach was highly criticized by the community, so the jet model was switched to kinetic energy injection in IllustrisTNG (see Weinberger et al. 2017 for implementation details). Unlike the thermal energy, the kinetic energy injection scales directly with the black hole accretion rate $\dot{E}_{\rm kin} = \epsilon_{\rm kin}\dot{M}_{\rm BH}c^2$, ignoring the bolometric luminosity since the AGN is assumed to be radiatively inefficient. This energy is then injected as a momentum kick in a randomly oriented direction that varies with injection event. This approach was chosen to avoid resolution effects. In practice, kinetic energy is accumulated until it exceeds a minimum threshold (analogous to stochastic thermal feedback) so that the occurrence of injection events is not influenced by the simulation's timesteps.

At the other end of the simulation spectrum, methods for AGN feedback have been explored in idealized simulations. These simulations have primarily focused on galaxy clusters, such as Meece, O'Shea, and Voit (2015), Prasad, Sharma, and Babul (2015), Li, Ruszkowski, and Bryan (2017), and Glines, O'Shea, and Voit (2020). Because of their idealized nature, these works are better able to investigate the impacts that different feedback models have on the surrounding gas (see Section 1.3.2 for more on the advantages of idealized simulations). Meece, O'Shea, and Voit (2015) gloss over the exact details of how feedback couples to the surrounding gas and instead enforce a heating rate that exactly matches the average cooling rate as a function of height or radius (depending on the geometry). This setup allows them to explore the conditions necessary for the onset of cold gas condensation. Building on this, Glines, O'Shea, and Voit (2020) test a variety of different heating kernels that deposit thermal energy in a spherically symmetric way such that the total amount of cooling and heating balance over 10 Myr. They find that purely thermal energy injection leaves the system prone to runaway cooling. Li, Ruszkowski, and Bryan (2017) adopt a momentum-driven

AGN model jet and find that hot bubbles formed via shocks are able to convectively heat the cluster core. Prasad, Sharma, and Babul (2015) adopt a similar approach. Both works find that AGN can undergo cycles of outburst followed by enhanced cold gas condensation (a.k.a "precipitation") that then fuels future outbursts. These and other simulations (e.g. Prasad et al. 2020; Prasad, Voit, and O'Shea 2022) lend strong support to theories of precipitation-regulated AGN activity, the principles of which extend to star formation in galaxy clusters and possibly also star formation in lower mass halos (Voit et al. 2015, 2017, 2020, see Chapter 3 for more).

1.4 Outlining the Following Chapters

The chapters that follow contain works for which I am the primary intellectual contributor, signified in astronomy by lead authorship. In these chapters, it will also be instructive to keep in mind the three simulation types described in Section 1.3.2.1, as each chapter acts as a representation for how each simulation type can contribute to the study of galaxy evolution.

Chapter 2 uses the cosmological simulation IllustrisTNG (Pillepich et al. 2018b) in an attempt to understand an unusual population of galaxies, called the breakBRDs (Tuttle and Tonnesen 2020). These galaxies fall within the "green valley" and so are interesting for the study of galaxy quenching (see Section 1.2.1). This chapter was originally published as Kopenhafer et al. (2020). For this dissertation, some bibliography entries have been updated from preprints to the final published version.

Chapter 3 uses idealized simulations to explore how galaxies self-regulate their star formation. Over long periods of time, this self-regulation is believed to be a result of interactions between the galaxy and its CGM (see Section 1.1.2). The contents of this chapter are currently under review with The Astrophysical Journal. A preprint representing the submitted version of this article is available as Kopenhafer, O'Shea, and Voit (2022). The version within this dissertation has been edited slightly since submission for style and grammar.

Chapter 4 uses the FOGGIE zoom simulations (Peeples et al. 2019) to understand the uncertainties that arise when connecting simulations to observations or interpreting observed spectra. In

particular, we examine the uncertainties introduced by commonly made assumptions. Quantifying these uncertainties—in essence, adding error bars to measurements—makes for more robust scientific comparisons. This chapter contains work that is currently ongoing and is as yet unpublished.

Chapter 5 summarizes the results of the preceding three scientific chapters. I also briefly discuss extensions to the above works.

CHAPTER 2

THE BREAKBRD BREAKDOWN: USING ILLUSTRISTNG TO TRACK THE QUENCHING OF AN OBSERVATIONALLY-MOTIVATED SAMPLE OF CENTRALLY STAR-FORMING GALAXIES

The following chapter was originally published as Kopenhafer et al. (2020). Some of the citations have been updated to reflect journal publication of previously referenced pre-prints.

2.1 Chapter Abstract

The observed breakBRD ("break bulges in red disks") galaxies are a nearby sample of face-on disk galaxies with particularly centrally concentrated star formation: they have red disks but recent star formation in their centers as measured by the D_n4000 spectral index (Tuttle and Tonnesen 2020). In this paper, we search for breakBRD analogues in the IllustrisTNG simulation and describe their history and future. We find that a small fraction (~4% at $z = 0$; ~1% at $z = 0.5$) of galaxies fulfill the breakBRD criteria, in agreement with observations. In comparison with the mass-weighted parent IllustrisTNG sample, these galaxies tend to consist of a higher fraction of satellite and splashback galaxies. However, the central, non-splashback breakBRD galaxies show similar environments, black hole masses, and merger rates, indicating that there is not a single formation trigger for inner star formation and outer quenching. We determine that breakBRD analogue galaxies as a whole are in the process of quenching. The breakBRD state—with its highly centrally concentrated star formation—is uncommon in the history of either currently quiescent or star-forming galaxies; however, approximately 10% of $10^{10} < M_*/M_\odot < 10^{11}$ quiescent galaxies at $z = 0$ have experienced SFR concentrations comparable to those of the breakBRDs in their past. Additionally, the breakBRD state is short-lived, lasting a few hundred Myr up to ~2 Gyr. The observed breakBRD galaxies may therefore be a unique sample of outside-in quenching galaxies.

2.2 Introduction

In the standard picture of galaxy formation, galaxies form in an "inside-out" sense: high densities and rapid gas cooling cause an early formation of the inner regions, while the outer parts form

later due to lower densities and slower gas accretion and cooling (e.g. Larson 1976; Matteucci and Francois 1989; Burkert, Truran, and Hensler 1992; Chiappini and Gratton 1997; van den Bosch 1998; Kepner 1999).

By far, most galaxies in the Local Universe seem to follow this general picture for their formation and growth, which can be traced through metallicity gradients and/or stellar age gradients and trends of scale radii with stellar age (e.g. Pagel and Edmunds 1981; Shaver et al. 1983; Vila-Costas and Edmunds 1992; Williams et al. 2009; Dale et al. 2016; see Maiolino and Mannucci 2019 for a review), even when taking into account processes such as stellar radial orbit migration (Magrini et al. 2016; Frankel et al. 2019). High resolution and spatially resolved observations largely corroborate the general "inside-out" picture (e.g. Sánchez et al. 2014; Belfiore et al. 2017; López Fernández et al. 2018; Poetrodjojo et al. 2018; Sánchez-Menguiano et al. 2018; reviewed by Sánchez 2020), but also reinforce a number of caveats. For example, outside-in growth has been observed in dwarf galaxies (Gallart et al. 2008; Zhang et al. 2012; Pérez et al. 2013; Pan et al. 2015; Ibarra-Medel et al. 2016; Wang et al. 2019), and galaxy interactions may affect metallicity gradients through dry mergers as well as through triggering gas flows (Mehlert et al. 2003; Sánchez-Blázquez et al. 2007; Queyrel et al. 2012).

In more detail, the distribution of star formation within galaxies may be related to the global star formation rate. For example, Morselli et al. (2019) found that star formation is centrally enhanced in galaxies near the star-forming sequence and centrally suppressed below it. In agreement with this work, several authors have found that galaxies not only form inside-out but also quench from the inside-out (Li et al. 2015; Nelson et al. 2016; Ellison et al. 2018; Rowlands et al. 2018; Spilker et al. 2019). Using the MaNGA survey (Bundy et al. 2014; Yan et al. 2016), Lin et al. (2019) find that the fraction of galaxies quenching inside-out grows with mass (see also Belfiore et al. 2018). Similar central sSFR suppression in galaxies below the star forming main sequence was found for both the CALIFA (Sánchez et al. 2012) and SAMI (Croom et al. 2012; Bryant et al. 2015) surveys (González Delgado et al. 2016; Medling et al. 2018). On the other hand, post-starburst galaxies, and galaxies with post-starburst or recently quenching regions, show large diversity and irregularity

in the distribution of their star-forming and quiescent regions (Rowlands et al. 2018; Chen et al. 2019; Quai et al. 2019).

The presence of a bulge may also affect the global star formation rate and the distribution of star formation within a galaxy (Martig et al. 2009; Genzel et al. 2014; Méndez-Abreu, Sánchez, and de Lorenzo-Cáceres 2019; Gensior, Kruijssen, and Keller 2020, although see also Martig et al. 2013; Su et al. 2019; Kretschmer and Teyssier 2020). Observations indicate that a large bulge component is often correlated with galaxy quenching, but that it is unlikely to cause quenching on its own. Lang et al. (2014) and McPartland et al. (2019) argue that the growth of the bulge precedes the global shutdown of star formation. However, when we focus on the disk, Abramson et al. (2014) have argued that excluding the bulge leads to a constant sSFR for the star forming disk component of galaxies. In agreement, Medling et al. (2018) find that bulges have little effect on the star formation in the disks of even early-type galaxies.

There are, of course, many factors that can affect star formation and its distribution within a galaxy. Feedback from Active Galactic Nuclei (AGN) may decrease or even quench the SFR from the center outwards. It could play a critical role in the regulation of star formation (Prasad et al. 2020; Voit et al. 2020) and is often argued to be required to keep galaxies quenched (e.g. Su et al. 2019). AGN feedback is also related to bulge mass, illustrated in the M_{BH}-M_{bulge} relation (e.g. Kormendy and Ho 2013; Heckman and Best 2014 and references therein; but see also Martin et al. 2018; Ding et al. 2020). In large-scale cosmological simulations, the tuning of AGN feedback makes it the dominant feedback mechanism at low redshift: it decreases the SFR of highly star-forming objects (e.g. Katsianis et al. 2017; Davé et al. 2019) and is associated with quenching galaxies (e.g. Weinberger et al. 2018).

Major as well as minor mergers can bring in additional gas and increase star formation (Mihos and Hernquist 1994; Cox et al. 2008; Kaviraj 2014; Willett et al. 2015; Hani et al. 2020) and interactions can redistribute angular momentum and funnel gas toward the central regions (e.g. Mihos and Hernquist 1994; Hernquist and Mihos 1995; Naab et al. 2014; Blumenthal and Barnes 2018; Lagos et al. 2018). These processes may also be related to the possible correlation between

mergers and AGN activity (Ellison et al. 2011; Goulding et al. 2018; Ellison et al. 2019; McAlpine et al. 2020).

Smaller star-forming galaxies in dense regions tend to be influenced strongly by their environment. Satellite galaxy evolution can be driven by processes such as tidal gas stripping, ram pressure stripping, starvation, or strangulation (Boselli and Gavazzi 2006). Indeed, some work has argued that ram pressure stripping can quench galaxy outskirts while enhancing central star formation (Fujita and Nagashima 1999; Koopmann and Kenney 2004; Tonnesen and Bryan 2012). Byrd and Valtonen (1990) use simulations to argue that the tidal field of clusters could drive cloud collisions and subsequent star formation.

Recently, a population of observed galaxies was introduced by Tuttle and Tonnesen (2020, hereafter TT20), called the “Breaking Bulges in Red Disk" galaxies, or breakBRDs. These galaxies were selected to have had recent central star formation (using D_n4000) and red disks (using $g - r$ color). The parent sample consisted of a bulge/disk decomposed sample (Lackner and Gunn 2012) based on the galaxy sample and spectral information from the NYU Value Added Galaxy Catalog (VAGC, Blanton et al. 2005) from the the Sloan Digital Sky Survey (SDSS) DR7 (Abazajian et al. 2009), while using images with improved sky subtraction from SDSS DR8 (Aihara et al. 2011).

BreakBRDs appear transitional in the optical bands, while presenting as star-forming in the UV and IR bands. Most of this sample has stellar masses above 10^{10} $M_\odot$, so on the basis of mass they should present "inside-out" star formation. In addition, TT20 found that *both* the sSFR and the bulge-to-total (B/T) mass ratio in breakBRD galaxies tended to be larger than that in the star-forming parent sample galaxies (sSFR $> 10^{-10.9}$ yr^{-1}), indicating that the large B/T ratio is not driving a decrease in sSFR. Finally, breakBRD galaxies are well-distributed across environmental density in a similar fashion to their parent sample, indicating that environmental processes are not driving their unusual star formation distribution.

In this paper we use the large-scale cosmological hydrodynamic simulation IllustrisTNG100 (Marinacci et al. 2018; Naiman et al. 2018; Nelson et al. 2018; Pillepich et al. 2018a; Springel et al. 2018) to gain insight into this unusual galaxy sample. We note that it is well-known that

simulations cannot recreate the observed universe with perfect accuracy or completeness. For example, the quenched fraction of low-mass satellites is poorly reproduced in simulations (Davé, Rafieferantsoa, and Thompson 2017; Donnari et al. 2021), there are too few low-mass black holes at $z = 0$ in simulations (Habouzit et al. 2020), and the green valley galaxies in many simulations have too-centrally concentrated star formation (Starkenburg, Tonnesen, and Kopenhafer 2019). However, we can account for this by comparing galaxies within the simulation to each other, rather than directly to observations. This way, we can find breakBRD analogue galaxies within the simulation and determine what makes them unique. This investigation draws upon the strengths of cosmological simulations: for all galaxies, we know the stellar, gas, and black hole masses, the star formation rates, and the environment with complete accuracy. Moreover, and particularly interesting for studying galaxy evolution, we can trace galaxies through time to determine their evolutionary histories and futures.

The IllustrisTNG100 simulation agrees well compared to observations for a number of galaxy characteristics, among them the $z = 0$ galaxy color distribution (Nelson et al. 2018; Pillepich et al. 2018b). Moreover, while Starkenburg, Tonnesen, and Kopenhafer (2019) show that simulated green valley galaxies can be too centrally concentrated compared to observations, green valley galaxies in IllustrisTNG100 show more diversity in radial star formation rate profiles.

In this paper, we begin by describing our selection of parent and breakBRD analogue samples in Section 2.3. In Section 2.4 we compare the breakBRD analogues identified at $z = 0$ with the $z = 0$ parent sample. We consider evolutionary pathways that may encourage breakBRD galaxy formation (Section 2.4.2) as well as the breakBRD growth history (Section 2.4.3). We then introduce the breakBRD analogues at $z = 0.5$ (Section 2.5), comparing them to the concurrent parent sample in Section 2.5.1, and focusing on the future evolution of these galaxies in Section 2.5.2. In Section 2.6 we discuss our findings and compare our breakBRD analogues directly to the observed breakBRD population. Finally, we summarize our conclusions in Section 2.7.

Table 2.1 Number of galaxies in our TNG100 parent sample and its subsamples

Name	Selection Criteria	$z = 0.0$	$z = 0.03$	$z = 0.1$	$z = 0.5$
Parent	$10 < \log(M_*/\mathrm{M}_\odot) < 12$ and $R_{1/2} > 2$ kpc	6092 (63%)	6029 (63%)	5857 (63%)	5057 (67%)
D_n4000	*Parent* $\cap$ $\mathrm{D}_n4000 < 1.4$ for $r < 2$ kpc	2650 (70%)	3008 (68%)	2918 (68%)	3196 (69%)
g-r	*Parent* $\cap$ $g - r > 0.655$ for $r > 2$ kpc	2816 (50%)	2579 (49%)	2383 (49%)	890 (49%)
bBRDa	*D_n4000* $\cap$ *g-r*	235 (37%)	288 (28%)	247 (29%)	72 (19%)

NOTE. - Selection criteria described in Sections 2.3.1 and 2.3.2. The "*bBRDa*" designation is short for "breakBRD analogues". Numbers in parentheses are the percentage of that subsample that are central galaxies.

2.3 Methods

The IllustrisTNG100 (public data release: Nelson et al. 2019b)[1] is part of a suite of simulations run using the AREPO moving mesh code (Springel 2010a) with upgraded subgrid models compared to the Illustris simulation (Genel et al. 2014; Vogelsberger et al. 2014); in particular, the upgrades modified the black hole accretion and feedback model (Weinberger et al. 2017), galactic winds (Pillepich et al. 2018b), and added magnetohydrodynamics (Pakmor, Bauer, and Springel 2011). TNG100 has a volume of 110.7 Mpc^3 and a mass resolution of 7.5×10^6 $\mathrm{M}_\odot$ and 1.4×10^6 $\mathrm{M}_\odot$ for dark matter and baryonic elements, respectively. The gravitational softening is 0.74 kpc at $z = 0$ for the collisionless particles and adaptive with a minimum of 0.18 kpc at $z = 0$ for the gas cells. The gas cells have a minimum (median) radius of 14 pc (15.8 kpc), and star-forming gas cells have a mean radius of 355 pc.

We select our sample of breakBRD analogues (also referred to as the bBRDa sample) and their parent sample from the TNG100 snapshots at redshifts 0, 0.03, 0.1, and 0.5, which were chosen for their lookback times of 0.48, 1.3, and 5.2 Gyr respectively. These times allow us to assess how long the breakBRD state lasts and determine their future evolution. In this paper we primarily focus on redshifts 0 and 0.5, looking at the bBRDa properties and their histories and futures. The

[1] www.tng-project.org

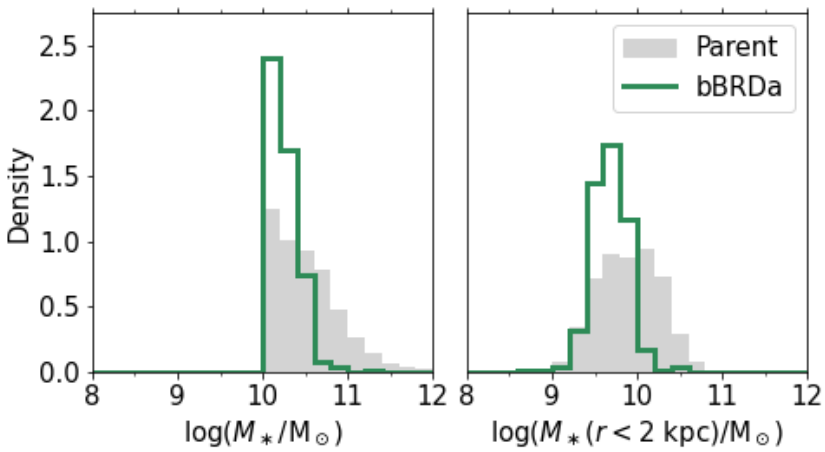

Figure 2.1 Normalized histograms of stellar mass of the whole galaxy (left) and the inner 2 kpc (right) for our parent (solid grey) and breakBRD analogues (green) selection at $z = 0.0$ (see Table 2.1). The break at $\log(M_*/\mathrm{M}_\odot) = 10$ is due to our selection criteria.

other redshifts are included to help better understand how long the breakBRD analogue state might last. The analogue selections were made with a combination of photometric and spectral criteria, as described in Section 2.3.2.

2.3.1 Parent Sample

We define the "parent" sample of our analogues with two different criteria. We first require that galaxy stellar mass must lie within $10^{10} < M_* < 10^{12}$ $\mathrm{M}_\odot$. The lower mass limit was chosen out of concern for mass resolution: since our analysis requires that we directly measure properties in the central 2 kpc of our galaxies, we must be sure there is significant mass both in the entire galaxies and in the central regions. Histograms of the total and central mass distributions of the parent sample at $z = 0.0$ are shown in Figure 2.1, and we see that even the lowest-mass central regions have more than several hundred particles. We ignore galaxies with $M_* > 10^{12}$ $\mathrm{M}_\odot$, as these have low numbers in TNG100, and can be assumed to be giant ellipticals. Moreover, most (~80%) of the galaxies in the *observed* breakBRD sample have $M_* > 10^{10}$ $\mathrm{M}_\odot$, and all have $M_* < 10^{12}\mathrm{M}_\odot$ (TT20).

We also require galaxies in our parent sample to have $R_{1/2} > 2$ kpc, where $R_{1/2}$ is the stellar

half mass radius. This removes galaxies which do not have a well-defined central region. The first row in Table 2.1 lists the size of our parent samples at $z = 0.0$, $z = 0.03$, $z = 0.1$, and $z = 0.5$. The percentage of galaxies that are central galaxies is quoted in parentheses.

2.3.2 BreakBRD Analogue Sample

Our breakBRD analogues are selected from the parent sample using two additional criteria. These criteria are designed to mimic the selection criteria of the observational breakBRD sample, and select for galaxies with red disks and outskirts (and therefore little-to-no total star formation) but recent star formation in their centers. We accomplish this through an SDSS color cut of $g - r > 0.655$ for $r > 2$ kpc and a cut on the D_n4000 spectral measure of < 1.4 for $r < 2$ kpc. The 4000 Å break is sensitive to the luminosity-weighted stellar age and is seen as an indirect measure of recent ($\lesssim$1 Gyr) star formation (Hamilton 1985; Brinchmann et al. 2004; Moustakas, Kennicutt, and Tremonti 2006).

The galactocentric radius r is defined relative to the particle with the lowest gravitational potential in the galaxy. We use this instead of the galaxy center of mass, which may not reflect the galaxy's rotation center due to its sensitivity to structure at large radii (Genel et al. 2015). We use 2 kpc as the boundary between our inner and outer regions both to exceed the minimum spatial resolution of IllustrisTNG and to approximate the size of the SDSS spectral fiber at $0.003 < z < 0.05$, which is the redshift range of the breakBRD observational sample. These considerations are again why we restrict the parent to have $R_{1/2} > 2$ kpc.

In order to apply our selection criteria, we generate mock spectra of two radial bins for each parent galaxy, as well as for the whole galaxy. This requires star formation histories for both $r < 2$ kpc and $r > 2$ kpc. We combine the star formation history information of the star particles (in bins of 10 Myr) with the instantaneous SFR from the gas (added to the most recent bin), creating a full star formation history for both radial bins and for the entire galaxy.

These star formation histories are then fed to the Flexible Stellar Population Synthesis (FSPS) code of Conroy, Gunn, and White (2009) (updated in Conroy and Gunn 2010), through the Python interface from Foreman-Mackey, Sick, and Johnson (2014), to generate mock spectra. For this

generation we use the MIST isochrones (Paxton et al. 2011, 2013, 2015; Choi et al. 2016; Dotter 2016) and the Miles spectral library (Sánchez-Blázquez et al. 2006; Falcón-Barroso et al. 2011). We use a Chabrier (2003) IMF and the Charlot and Fall (2000) dust model with an effective absorption of $\tau = 1.0(\lambda/0.55\ \mu\mathrm{m})^{-0.7}$, which is reduced by a factor of 3 for stars older than 3×10^7 yr. This is the same dust model employed by Torrey et al. (2015) for stellar mocks of the original Illustris simulation. We emphasize that we only use the photometric colors and D_n4000 spectral index to select our breakBRD analogue (bBRDa) sample; omitting or changing the dust model in computing the spectra has only a small effect on our selection.

We generate separate spectra for the inner ($r < 2$ kpc) and outer ($r > 2$ kpc) regions, as well as for the whole galaxy for comparisons to observations (Section 2.6.4). We convolve the spectra with the SDSS bandpass functions to generate broadband magnitudes such as g and r. We also calculated the D_n4000 measure for the spectra of the inner 2 kpc region following the narrow definition from Balogh et al. (1999). Galaxies with $D_n4000 < 1.4$ in the inner region have had star formation within the last $\sim$ 1 Gyr, and comprise the D_n4000 selection. This selection is composed of 2650 galaxies at $z = 0.0$ and 3196 at $z = 0.5$ (second row in Table 2.1). Galaxies with $g - r > 0.655$ outside 2 kpc comprise our $g - r$ selection (third row in Table 2.1). There are 2816 such galaxies at $z = 0.0$, and 890 at $z = 0.5$.

The intersection of the D_n4000 and $g - r$ selections yields our breakBRD analogue galaxies, also referred to as the bBRDa galaxies. We refer to them as "analogues" because the observational sample in TT20 are the "true" breakBRDs. There are 235 such galaxies at $z = 0.0$, 269 at $z = 0.03$, 247 at $z = 0.1$, and 72 at $z = 0.5$ (final row in Table 2.1).

We will also occasionally reference the "breakBRD state," which is the state in which a galaxy meets our D_n4000 and $g - r$ criteria. Since galaxies evolve over time, galaxies that were breakBRD analogues at one redshift may not qualify at another; we discuss this, and what we can infer from this about the length of the breakBRD state, in Section 2.5.2.

In Figure 2.2 we plot the D_n4000 values measured in the inner 2 kpc of parent galaxies at $z = 0.0$ against their $g - r$ color in the outer region ($r > 2$kpc). The breakBRD analogue subsample

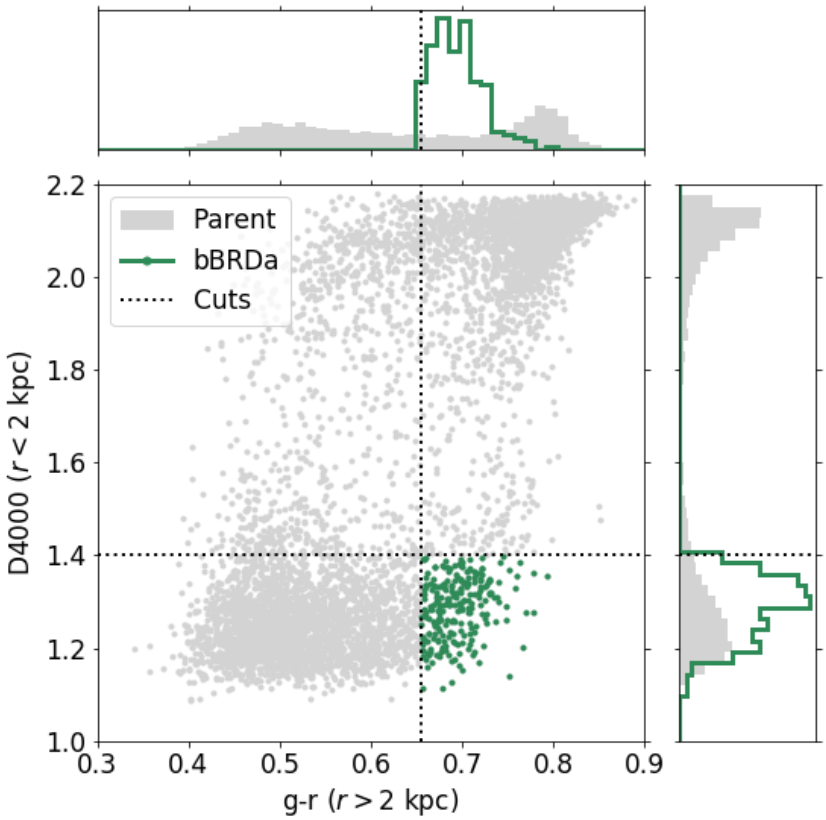

Figure 2.2 D_n4000 in the inner 2 kpc vs $g-r$ color in the $r > 2$ kpc disk for our selection at $z = 0.0$. The parent sample is shown in grey, while the breakBRD analogues are green. Dashed black lines show the $D_n4000 < 1.4$ and $g - r > 0.655$ selection cuts. Note that the histogram bins used for plotting straddle these cuts.

is separated out in green. Each 1-dimensional distribution is shown in the histograms along the sides. Clearly the breakBRD analogue sample is composed of an unusual subset of galaxies: most of the galaxies with central star formation have blue disks, and most of those with red disks have had little recent central star formation, but the bBRDa galaxies have star forming central regions with red disks.

The stellar mass distribution of our analogue sample is shown in Figure 2.1, along with the stellar mass within 2 kpc. The total (and central) stellar mass of the bBRDa galaxies tends to be lower than that of the parent sample. Many of the quantities explored in our analysis are correlated with stellar mass; to that end, we weight the parent sample so that its mass distribution matches that

Table 2.2 Percentage of centrals that are splashbacks

Definition	bRRDa	Parent	$\|z\|$
After $z = 0.1$	8%	4%	1.14
After $z = 0.5$	23%	10%	2.26

NOTE. - Reported for the $z = 0$ bBRDa and *weighted* parent samples. Splashbacks are centrals that "recently" transitioned from being satellites, defined as either after $z = 0.1$, or $z = 0.5$ (see text). The fourth column gives the two-proportion z-test statistic comparing the two proportions. Proportions are significantly different at the $\alpha = 0.05$ level if $|z| > 1.96$, and at $\alpha = 0.01$ if $|z| > 2.58$.

of the bBRDa galaxies, as we discuss below. This weighting is applied from Figure 2.3 onward. We note that for all figures, the breakBRD galaxies are included in the parent samples. This does not affect our results.

2.3.3 Sample Comparison

Many of the properties we examine in Sections 2.4 and 2.5 are dependent on both galaxy mass and galaxy classification as a central or satellite. We therefore separate centrals and satellites in our analysis for both the parent and breakBRD analogue samples. The fraction of central galaxies for each sample is given in parentheses in Table 2.1.

To minimize the influence of stellar mass when examining differences between the parent and bBRDa galaxies (see Figure 2.1), we apply a weighting to the parent central and satellites so that their stellar mass distributions match their respective analogue sample.

As we are treating centrals and satellites separately, we also make a point to identify those galaxies that are splashbacks: galaxies that were considered to be satellites of more massive hosts at earlier times but have since escaped that halo. Splashback galaxies (also called backsplash galaxies or ejected satellites) are approximately related to a known caustic in the phase space structure of dark matter halos beyond the virial radius: the splashback radius (see e.g. Adhikari, Dalal, and Chamberlain 2014; Diemer et al. 2017; Haggar et al. 2020; Diemer 2021),[2] but we

[2]In IllustrisTNG the central/satellite definition depends on halos identified through the Friends-Of-Friends (FOF, Davis et al. 1985) and SUBFIND (Springel et al. 2001) algorithms, and are therefore not identical to central/satellite definitions based on halo radii determined through spherical overdensity criteria or phase space structure-motivated

note that our definition can also include galaxies that interacted with the more massive host in a flyby encounter and were never gravitationally captured. Because, according to our definition, a splashback galaxy "recently" made the transition from satellite to central, it may exhibit properties similar to satellites (Diemand, Kuhlen, and Madau 2007; Knebe et al. 2011b; Wetzel et al. 2014; Buck et al. 2019). For $z = 0.0$, we use both $z = 0.1$ and $z = 0.5$ as our cutoffs: if a galaxy has transitioned since the chosen redshift, it is counted as a splashback. We found that splashbacks only had an impact on the properties discussed in Sections 2.4.2.2 and 2.4.2.3, as we discuss in those sections. Table 2.2 contains the fractions of splashbacks in both the bBRDa and *weighted* parent samples.

Throughout the following sections we make use of three statistical tools to help quantify the differences and similarities between our various subsamples. First, in most figures, we have annotated the medians and median absolute deviations (MADs)[3]—robust statistical measures that are resilient to outliers—for relevant distributions. As a reference, the MAD $\approx 0.67\sigma$ for a Gaussian distribution; however, there is no strong indication that our data follow Gaussian distributions and so we keep our statistical evaluations distribution-free.

Second, we perform two-sample Kolmogorov-Smirnov (KS) tests to measure the "distance" between distributions and determine if it is statistically significant. Our tests take into account the weighting that we apply to the parent distributions to remove any dependencies on stellar mass. More sensitive tests, such as Anderson-Darling, exist; but, since we are trying to establish statistically meaningful differences rather than similarities, and the KS test functions best when differences are global, we consider the KS test to be the more conservative choice.

Finally, there are a few instances in which we compare proportions instead of distributions. To determine if two proportions are statistically different from each other, we use a two-proportion z-test. This test functions by comparing the difference in proportions to zero.

size definitions. More et al. (2011) show that corresponding spherical overdensities for FOF halos with linking length $b = 0.2$ are correlated with on halo concentration and thus halo mass but are likely larger than the virial (Bryan and Norman 1998) overdensity. The resulting halo radii are therefore smaller than the virial radius, and also smaller than the splashback radius (see e.g. Diemer 2020, 2021). We conclude that there may be true splashback galaxies among our centrals.

[3]Defined as med($|X_i - \tilde{X}|$) where $\tilde{X}$ is the median of $\{X_i\}$

Both the KS test and the z-test have critical values for when to accept or reject the null hypothesis. For the two-sample KS test, the null hypothesis is that both empirical distributions are drawn from the same underlying distribution. For the two-proportion z-test, the null hypothesis is that the two proportions are equal. We use two common significance levels, $\alpha = 0.05$ and 0.01. A KS test result of $p < \alpha$ indicates the null hypothesis can be rejected. For the two-proportion z-test, these significance levels correspond to critical values of $|z| > 1.96$ and 2.58, respectively.

2.4 breakBRD Analogue Galaxies in the Local Universe

In this section we focus on the breakBRD analogues identified at $z = 0$. We first compare them to the $z = 0$ parent sample, and then attempt to identify a formation mechanism for the breakBRD galaxies.

2.4.1 Star Formation and Gas Properties

Here we explore the properties of the $z = 0$ breakBRD analogue sample with respect to its parent population (see Sections 2.3.1 and 2.3.2 for their selection).

2.4.1.1 Global Star Formation

We first consider where breakBRD analogues lie in the stellar mass-sSFR plane. Figure 2.3 compares galaxy total stellar mass to total specific SFR (sSFR). Galaxies with no current star formation (SFR = 0) and those with $\log(\mathrm{sSFR/yr}) < -13$ were set to $\log(\mathrm{sSFR/yr}) = -13$. The top row shows central galaxies, and the bottom shows satellites.[4] We remind the reader that in each case, as discussed in Section 2.3.3, the (central or satellite) parent sample has been weighted to match the total stellar mass distribution of the bBRDa centrals and satellites, respectively.

To consider this quantitatively, we calculate the median and median absolute deviations (MAD) of these distributions, taking into account the weighting, which are annotated on Figure 2.3. When calculating these values we ignore galaxies that were set to $\log(\mathrm{sSFR/yr}) = -13$. All of the bBRDa galaxies have $\log(\mathrm{sSFR/yr}) > -13$ and so have not been modified.

[4]For all figures with contours, the background (white) contour level contains, on average, 5% of parent galaxies. The percentage is at most 11%.

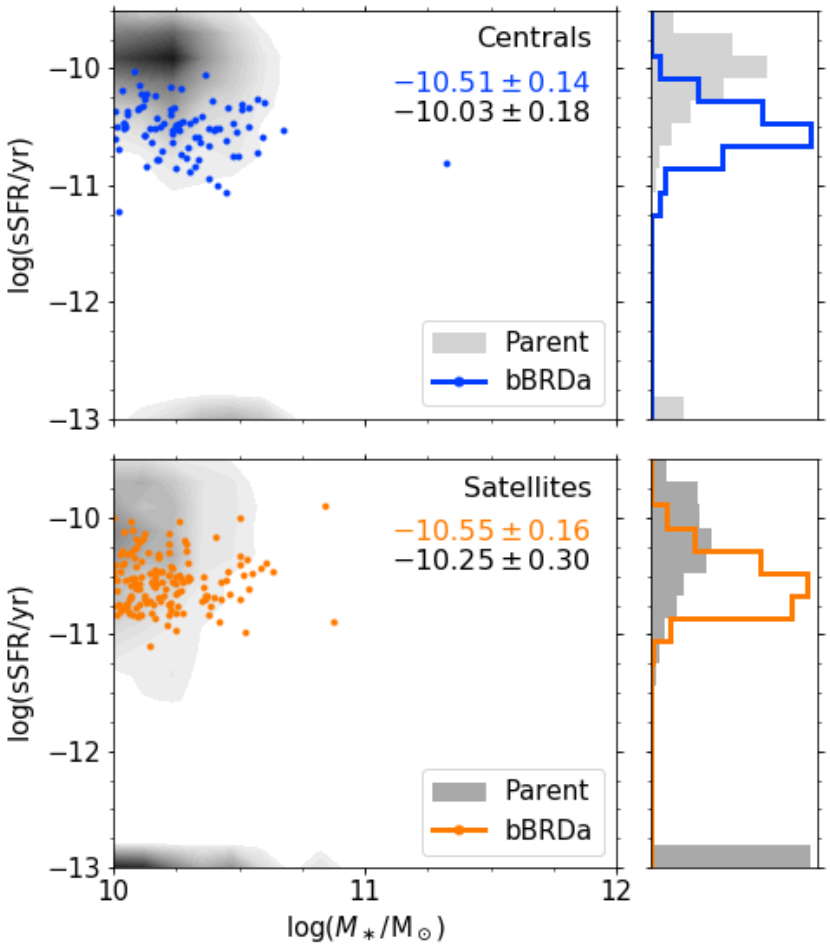

Figure 2.3 Total specific star formation rate vs total stellar mass for central galaxies (top) and satellites (bottom) in our $z = 0.0$ selection. The weighted parent sample is represented by the grey contours. The weighting is described in Section 2.4.1. There is a floor imposed at $\log(\mathrm{sSFR/yr}) = -13$, to which galaxies with no star formation were also set. The numbers in the upper right give the median and MAD when ignoring these galaxies.

The two subsets of bBRDa galaxies cover roughly the same sSFR range, and tend to be lower in sSFR than each of their respective parents. Though the centrals' distributions overlap slightly, the median + MAD of the parent and breakBRD centrals do not, indicating each subsample is well clustered around their respective medians. The two bBRDa medians lie almost on top of each other and their MADs are of similar magnitude, in contrast to the two parent subsamples. The low sSFR of both breakBRD samples may be a signature of our selection criteria.

This shows that the two bBRDa populations are more similar to each other in sSFR than they are to their respective parent populations, highlighting that in particular central breakBRD analogues are different from the general central star-forming galaxy population.

2.4.1.2 The Concentration of Stars and Gas

In Figure 2.4 we examine the concentration of star formation and gas using the ratio of the inner 2 kpc of galaxies to their whole. From top to bottom, the three concentration ratios we examine are in star formation rate, "dense" gas mass, and total gas mass. Dense gas is that which is above 0.1 cm^{-3}, the threshold for star formation in IllustrisTNG (Pillepich et al. 2018b). Each ratio is plotted against both total stellar mass and total instantaneous sSFR, the two quantities from Figure 2.3. Once again, the parent and breakBRD analogues are broken into central and satellite galaxies. For some parent galaxies, these ratios are undefined: 1439 parent galaxies (563 centrals) have no SFR at all, 1385 (517 centrals) have no dense gas, and 620 (9 centrals) have no total gas. None of these galaxies belong to the breakBRD analogue subsample. These galaxies are naturally excluded from Figure 2.4 and are ignored in the ensuing discussion. We apply the same weighting to the parent sample as used in Figure 2.3, and even though some galaxies are excluded, the mass distributions of the weighted parents remains similar to those of the bBRDa galaxies for all ratios plotted (the lowest p-value from two-sample KS tests is 0.80).

The combination of the $g - r$ photometric selection and D_n4000 spectral selection detailed in Section 2.3.2 is expected to select galaxies with centrally concentrated star formation. The top row of Figure 2.4 shows that we have indeed selected galaxies with this property. For both central and satellite galaxies, the concentration of SFR in the breakBRD analogue galaxies is clustered

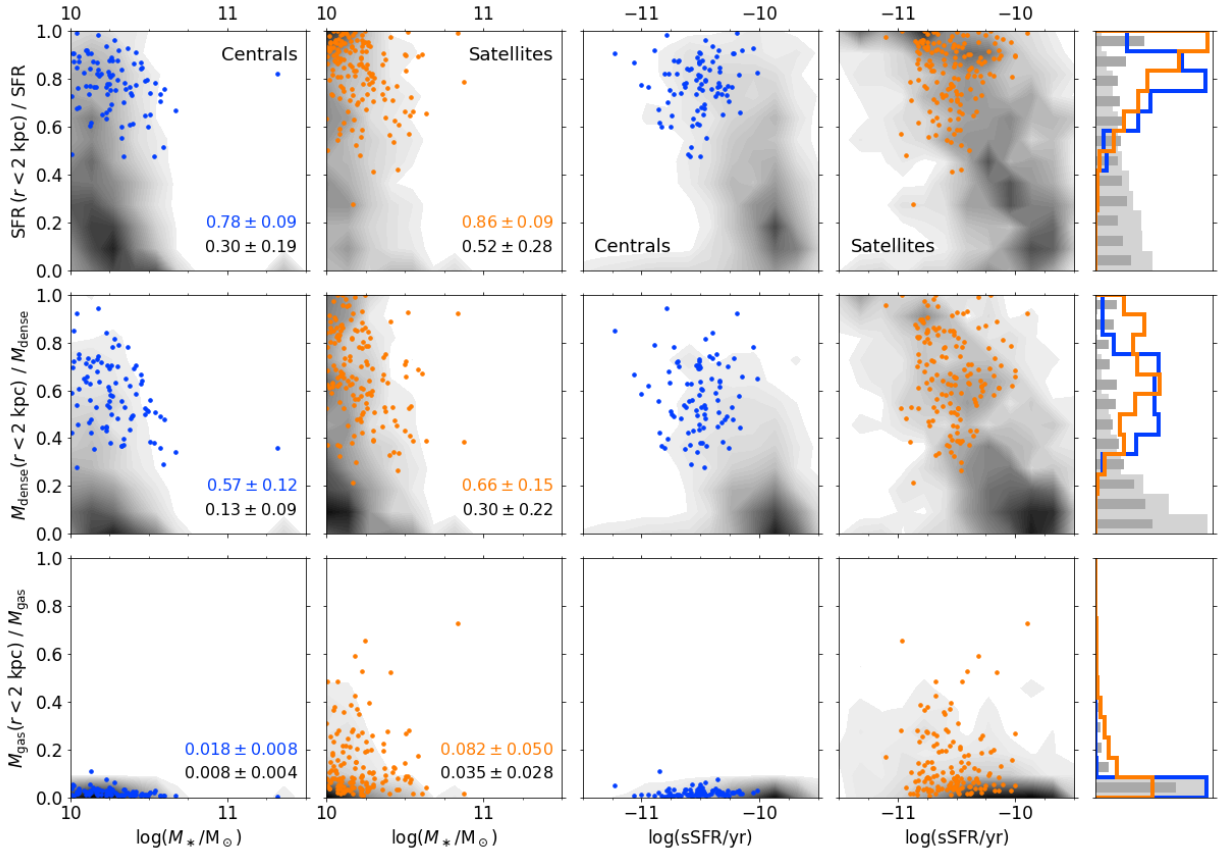

Figure 2.4 Concentration of star formation rate (top), mass of "dense" gas (middle), and total gas mass (bottom) within the inner 2 kpc of galaxies with nonzero SFR in our $z = 0.0$ selection. "Dense" gas is gas above the density threshold for star formation in IllustrisTNG (Pillepich et al. 2018b). These concentrations are plotted against total stellar mass (left two columns) and total specific star formation rate (next two columns) with normalized histograms (far right column). Both the weighted parent (contours) and breakBRD analogue samples (points) are split into central galaxies (blue) and satellites (orange). Median and MAD concentrations are labeled. The histogram colors follow Figure 2.3: filled for parent centrals (light grey) and satellites (dark grey bars), and lines for breakBRD analogue centrals (blue) and satellites (orange).

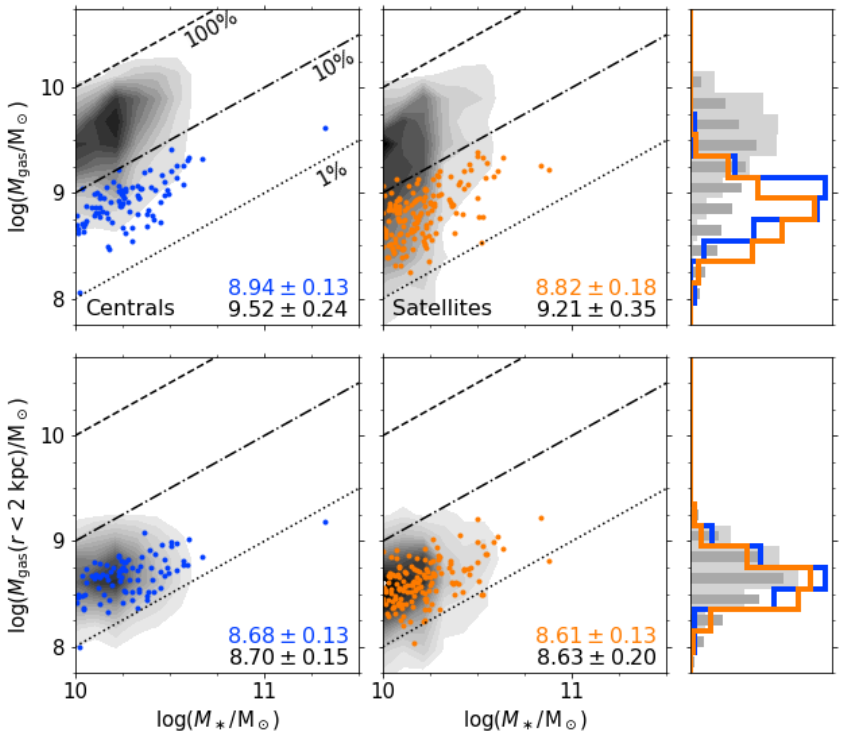

Figure 2.5 Total mass of dense gas (top) and mass of dense gas within the inner 2 kpc (bottom) vs total stellar mass for our selection at $z = 0.0$. "Dense" gas is defined by the SF threshold in IllustrisTNG (Pillepich et al. 2018b). Both the weighted parent (contours) and breakBRD analogue samples (points) are split into central galaxies (left) and satellites (right). Guides show where the gas mass is 100% (dashed), 10% (dot-dashed) and 1% (dotted) of the stellar mass. Medians and MAD gas masses are labeled; they change by less than 0.2% when splashbacks are removed. See Figure 2.4 for a description of the normalized histograms to the far right.

above 50%. While some parent galaxies, especially satellites (dark bars), also have high SFR concentrations, their overall distribution is much flatter. Among the bBRDa galaxies, the satellites tend to be slightly more concentrated than the centrals, but their MADs are roughly the same and both distributions skew towards high concentrations. The parent satellites also have a higher median than the parent centrals, but again, both distributions are quite broad. We note that classification as a parent or a breakBRD has a stronger impact on SFR concentration than being a satellite or central, with the bBRDa galaxies consistently more concentrated. The two breakBRD subpopulations are also more similar to each other than the parent populations.

Given that star formation requires cold, dense gas, it's not surprising that in the middle row

of Figure 2.4 we see that dense gas is also more centrally concentrated in the bBRDa galaxies than in the parent sample. The dense gas concentration in the breakBRD analogues never falls below 20%. The bBRDa populations have overlapping median + MAD ranges, though as with the SFR, satellites exhibit slightly higher concentrations. The difference in concentration between the parent and bBRDa galaxies is once again more pronounced than the differences between centrals and satellites in either sample. We also highlight that the dense gas concentrations of breakBRD satellites and centrals are more alike than those of the parent satellites and centrals.

Finally, the bottom row of Figure 2.4 shows the degree to which *all* gas in the galaxies is centrally concentrated. Both classifications of parent and breakBRD galaxies tend to have concentrations near 0. This trend is stronger for the centrals: 99.5% of parent centrals have 5% or less of their total gas in their inner 2 kpc, compared to 74.4% of parent satellites. As satellites are expected to experience ram pressure stripping, this difference is not surprising. For both satellites and centrals, the breakBRD analogues tend to have slightly higher concentrations than their corresponding parents, but these differences are not as strong as for the other quantities in Figure 2.4. Because all of the populations skew towards zero concentration, we use a two-sample Kolmogorov-Smirnov (KS) test to further distinguish the parent and bBRDa galaxies. This KS test accounts for the weighting in the parent (see Section 2.3.3). Testing centrals against centrals and satellites against satellites yields p-values of order 10^{-13} or less, indicating the breakBRD analogues and parent samples are *not* drawn from the same underlying distribution.

For all of the quantities shown in Figure 2.4, the breakBRD analogues always have much higher concentrations than the parent sample. We clearly see that for the concentrations of dense gas and SFR, the two breakBRD subpopulations are more similar than the two parent subsamples. These trends are unchanged when splashbacks are removed from the central subsamples.

With Figure 2.5, we re-examine the spatial distribution of dense gas in our galaxies in order to determine whether this gas is more concentrated in the center of galaxies because the central regions have additional gas, or because dense gas is missing from galaxy outskirts. As a function of stellar mass, we plot the galaxy's total dense gas mass in the top row, and the mass of dense gas within

2 kpc in the bottom. Central galaxies are on the left and satellite galaxies are on the right. Lines are included to guide the eye: they show where the gas mass is equivalent to 1%, 10%, and 100% of the stellar mass. As with Figure 2.4, we exclude parent galaxies that do not have any dense gas (1385 total, 517 centrals), or lack dense gas in their inner 2 kpc (1610 total, 1199 centrals). Figure 2.5 again uses the same weighting as Figure 2.3. The exclusion of the aforementioned galaxies does alter the mass distribution of the weighted parent sample, but KS test p-values remain acceptable ($p \sim 0.8$ for the total mass distributions and $p \sim 0.2 - 0.3$ for the inner gas).

The top row of Figure 2.5 shows that both bBRDa subsamples are systematically lower than their respective parents in total dense gas mass, and are more similar to each other in terms of median and MAD than the two parent samples. Specifically, the central bBRDa galaxies are significantly different from the parent central distribution. This result also holds when splashbacks are removed from the central samples (the medians and MADs change by less than 0.2%).

In contrast to the total mass of dense gas, all of our galaxy subpopulations have very similar distributions for the mass of dense gas in their inner 2 kpc (bottom row of Figure 2.5). We clearly see that their medians and MADs all lie on top of each other, and unlike Figure 2.4 and the total dense gas mass, the difference in central gas mass is more pronounced between satellites and centrals than between parents and breakBRDs. This is born out when using a two-sample KS test: comparing satellites to satellites and centrals to centrals results in p values above a threshold of 0.05, while comparing the two bBRDa (and parent) samples to each other yield p below 0.01. Removing splashbacks from the central samples only strengthens the similarity between those two distributions. These results suggest that breakBRD galaxies exhibit an outer deficit of gas and not an central enhancement.

We note that Figure 2.5 is qualitatively the same when we use *all* of the bound gas instead of only the dense gas in the galaxies. The total gas masses are low in the bBRDa galaxies while the central gas masses are similar in all subpopulations.

In summary, we find that the breakBRD analogues have more centrally-concentrated SFRs than the weighted parent samples. Dense, SF-eligible gas is also more centrally concentrated

in the bBRDa galaxies. Being a breakBRD is a stronger predictor of concentration for these two quantities than being a central or satellite. When considering all of the dense gas, the two breakBRD subsamples are both lower than their respective parents, but all subpopulations have roughly the same mass of dense gas in their central 2 kpc. The breakBRD analogues therefore seem to be missing gas in their outer regions with respect to the parent galaxy sample.

2.4.2 Possible Evolutionary Drivers

Thus far we have shown that the galaxies in the breakBRD analogue sample at z=0 lie somewhat below the star-forming main sequence (Figure 2.3), and their central concentration of star formation seems correlated with a lack of gas and star formation in their outer regions (Figures 2.4 and 2.5). Here we focus on three mechanisms that may drive galaxy evolution; namely, black hole feedback, mergers, and environment. For each we determine whether breakBRD analogues differ from the parent population.

2.4.2.1 Black Hole Mass

It has often been argued that there is a correlation and co-evolution of galaxies, or the central regions of galaxies, and their central supermassive black holes (see e.g. Heckman and Best 2014). Thus, the centrally-concentrated gas and star formation in breakBRD galaxies could also be reflected in their black hole mass. We might expect high black hole mass because high central gas density may enhance black hole accretion and possibly also AGN activity. The causal link may be reversed, however, and strong AGN feedback from massive black holes may remove gas from a galaxy's outskirts. Indeed, in IllustrisTNG AGN feedback is an important mechanism quenching star formation in galaxies (Weinberger et al. 2018).

Therefore, we now look at the mass of the central black hole in breakBRD analogues as compared to the mass-weighted parent sample in Figure 2.6. This is plotted against total stellar mass. A line is included where the black hole mass is 5% of the total stellar mass only to guide the eye. Some parent galaxies do not have black holes (their masses are stored as negative infinity). There are 121 such satellites, 10 of which are also breakBRD analogues. There is also one parent

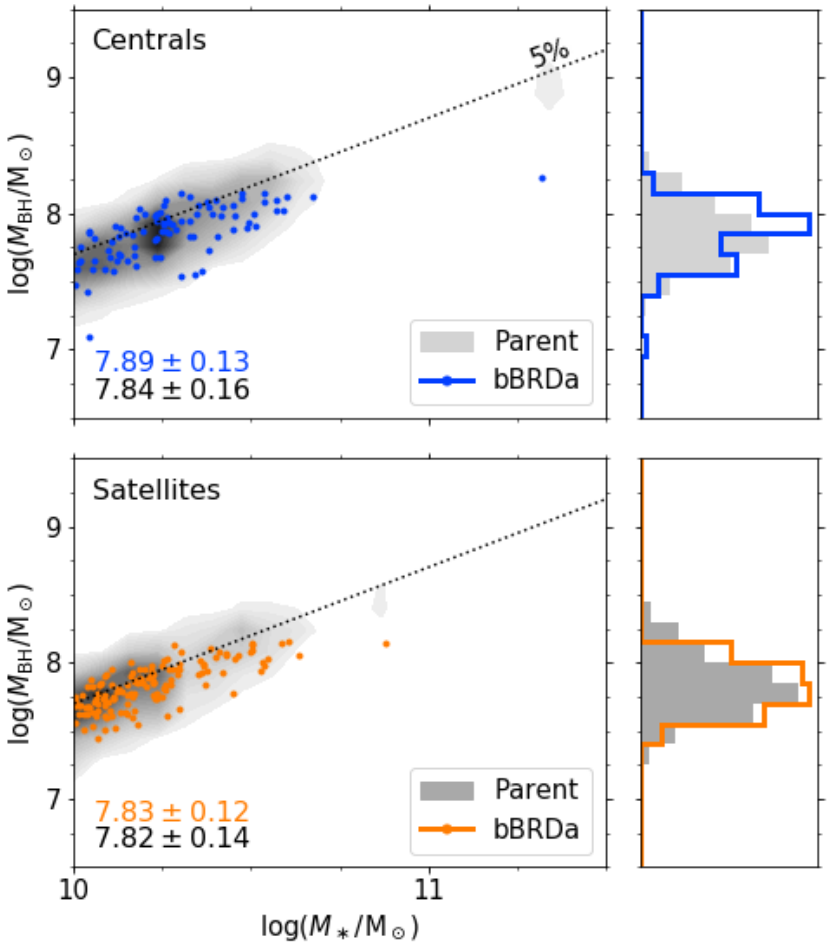

Figure 2.6 Black hole mass vs total stellar mass for central galaxies (top) and satellites (bottom) in our $z = 0.0$ selection. The weighted parent sample is represented by the grey contours. A line where the black hole mass is 5% of the total stellar mass is included to guide the eye. Medians and MADs for the black hole mass are labeled.

central without a black hole. These have been omitted from Figure 2.6 and our analysis, and do not significantly impact the weighting of the parent sample.

The black hole mass distributions of the central and satellite breakBRD galaxies match well with their parent distributions. As seen in Figure 2.6, their medians and MADs are all very similar. This result remains when we instead calculate these statistics for $\log(M_{\rm BH})/\log(M_*)$, where the statistics are all $\sim 0.77 \pm 0.01$.

Additionally, we have performed a similar comparison of the black hole accretion rates, both the present-day accretion rates as well as the maximum black hole accretion rates for each galaxy

since $z < 0.03$ and since $z < 0.5$. Because AGN feedback is related to black hole accretion rates (Weinberger et al. 2018), if breakBRD galaxies had experienced strong AGN feedback, the maximum black hole accretion rate within their recent history would likely be high as well. Yet the median + MAD accretion rate ranges heavily overlap between the breakBRD analogues and their parents, whether using the rates at $z = 0$ or finding the maximum recent accretion rate since $z = 0.5$. There is no evidence that the growth of the BHs in breakBRDs differs from that of the parent sample.

Using weighted two-sample KS tests to statistically assess the similarity of the distribution shape (Section 2.3.3), we cannot reject the null hypothesis that the parent and analogue satellites or centrals are drawn from the same underlying distributions ($p > 0.1$ for both). Both of these test results support what is seen by eye in Figure 2.6, that the black hole mass distribution is very similar in the bBRDa and parent galaxy populations. This result is unaffected by the removal of splashbacks. We thus find that breakBRDs sit on the same black hole mass – stellar mass relation as the parent sample and do not have unusual black hole masses.

2.4.2.2 Environment

As we have discussed in the introduction, satellite galaxies are more likely to experience environmental effects that may quench their outskirts by removing gas while enhancing star formation in the inner regions. We might expect breakBRD galaxies to only reside in dense environments; although, as we discuss in Section 2.6.4, the observed sample shows no environmental influence. Thus, in this section we consider several indicators for the environment of breakBRD analogues and the parent sample.

First, we can simply compare the satellite fractions in the bBRDa and parent samples using Table 2.1. The parent sample has a ~37% satellite fraction while the breakBRD analogue sample has a ~63% satellite fraction. This difference is statistically significant according to a two-proportion z-test ($|z| = 4.49$; $|z| > 2.58$ is significant at $\alpha = 0.01$). Given that there are multiple potential pathways for satellites to become centrally concentrated, the enhanced satellite fraction among breakBRDs is not a surprise; however, there remains a large fraction of central bBRDa galaxies.

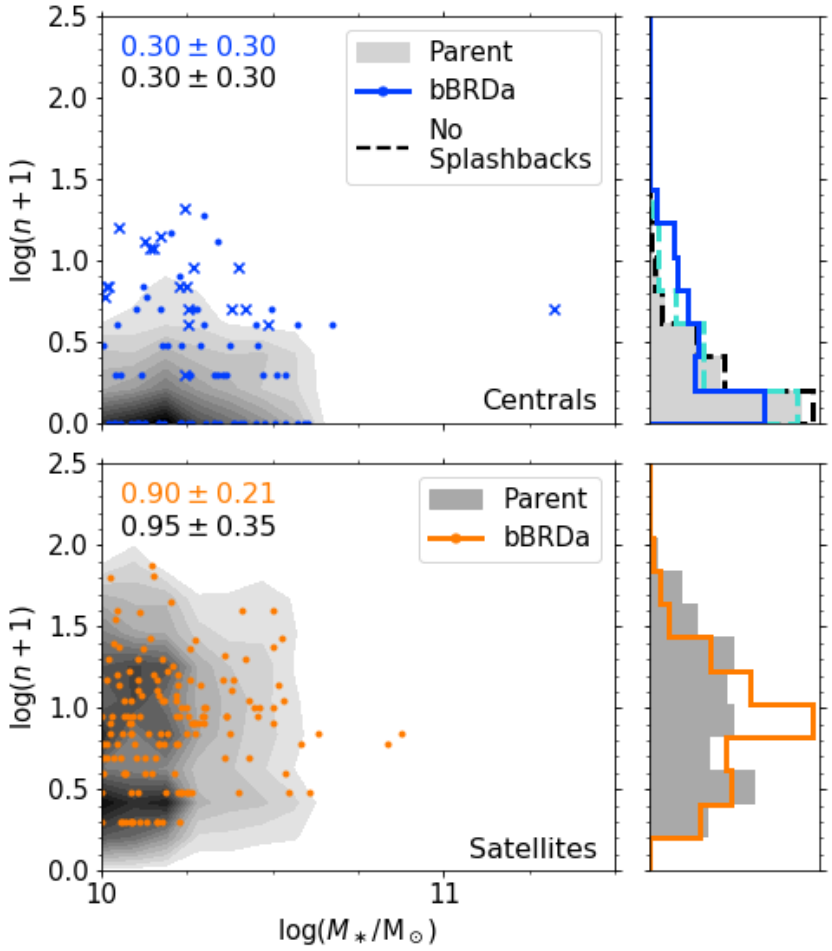

Figure 2.7 Number of galaxies with $M_* > 10^{10}$ $M_\odot$ within 2 Mpc vs total stellar mass, broken into centrals (left) and satellites (right), for our $z = 0.0$ selection. The number n of neighboring galaxies is plotted as $\log(n+1)$. The weighted parent sample is represented by the grey contours and the histograms are normalized. Dashed lines on the centrals' histogram are the distributions if galaxies that have been splashbacks since $z = 0.5$ are removed. BreakBRD splashbacks are marked (crosses); these galaxies tend to live in the densest environments. Medians and MADs for $\log(n+1)$ are labeled for the full sample, including splashbacks. We note that the host galaxies of the satellites are not excluded from our environment measurement for either the parent or breakBRD samples.

In Section 2.3.3 we introduced Table 2.2 and the fraction of splashback galaxies in the analogue and weighted parent samples. In both cases, the proportion of splashbacks in the bBRDa sample is double that in the parent sample; however, the statistical significance of this difference depends on the redshift used. The table includes the two-proportion z-test statistic, which tells us whether to reject the null hypothesis that the two proportions are statistically the same. At the $\alpha = 0.05$ level, the breakBRD analogues have a significantly higher proportion of splashbacks since $z = 0.5$. The proportions of splashbacks since redshift $z = 0.1$ are generally low, which likely leads to the lack of significance under this definition. Thus only 77% of central breakBRD analogues have not previously been satellites (since $z = 0.5$) compared to 90% of the parent.

Within our central and satellite galaxy selections we can also measure the environmental density. In Figure 2.7, we look at the number of $M_* > 10^{10}\mathrm{M}_\odot$ galaxies within 2 Mpc as a measure of the density of surrounding galaxies. The number of neighboring galaxies that meet this criteria are plotted as $\log(n + 1)$.

First we note that the median and MAD values for the parent and bBRDa distributions are quite similar. They are quoted in $\log(n + 1)$ space in the figure, so are equivalent to 1 galaxy for both central samples and 7 and 8 galaxies for the bBRDa and parent satellite samples, respectively. There is significant overlap in the MADs.

When we remove either kind of splashback (from $z = 0.1$ or 0.5; see Table 2.2), the parent's median density drops from 1 galaxy with $M_* > 10^{10}\mathrm{M}_\odot$ within 2 Mpc to 0 galaxies, while the bBRDa median density remains at 1 galaxy. We see that removing splashbacks decreases the width of the tail in the centrals' histogram at higher densities; this is shown with the dashed lines in the upper right of Figure 2.7. This is to be expected: since splashbacks are galaxies that were recently satellites, we should find them in denser environments. However, even with splashbacks removed, the MADs overlap for the parent and breakBRD central samples.

For a closer look at the environmental density distributions we also performed two-sample KS tests. The breakBRDs' density distributions are significantly different from those of the parents ($p = 0.011$ for the satellites, and the centrals have $p = 7 \times 10^{-5}$). The p-value for the centrals

increases as we remove galaxies that have been splashbacks since earlier times, reaching $p = 0.29$ when removing those since $z = 0.5$. The non-splashback central breakBRD galaxies thus live is similar environments to the non-splashback central parent sample.

While the two satellite distributions have an insignificant p-value, they cover roughly the same density range. Because the median values are close and the MADs overlap, even though the shapes of their distributions are different, we do not consider the satellite breakBRDs to be in meaningfully different environments than the parent sample satellites.

Additionally, we check whether these results change if we look at the distance and mass of the nearest more massive galaxy, or at the distance and mass of the nearest cluster (where we define cluster as a halo with $M_{DM} > 10^{14}$ $M_{\odot}$). We find that the environment of breakBRD analogues are similar using both of these measures. This similarity exists in both the shape of the distribution measured using the KS test, and in the close overlap of the medians and MADs.

Therefore, while the fraction of current or recent satellite galaxies is higher in the breakBRD than in the parent sample, the environment of galaxies within either the satellite or central samples is quite similar to the corresponding parent sample. This may indicate that a more subtle environmental effect is responsible for the evolution of breakBRDs and that this avenue is worthy of further investigation.

2.4.2.3 Merger History

We counted the number of central and satellite galaxies that experienced at least one merger with mass ratio $M_{*,2}/M_{*,1} \geq 0.01$ since $z = 0.5$. Mergers were classified by the stellar mass ratio of the galaxies involved: $M_{*,2}/M_{*,1} \geq 1/3$ are defined as as "major" mergers while those from 1/10–1/3 are minor (Crain et al. 2015; Lagos et al. 2018; Katsianis et al. 2019). We also include the 1/100–1/10 range, which is composed of very minor mergers that could be considered cosmological accretion. We compare the fraction of galaxies that experience at least one of our defined events and determine statistical significance using two-proportion z-tests (see Section 2.3.3); note that the parent fractions include the mass weighting that has been applied throughout this paper.

The frequency of major and minor mergers is not significantly different between the breakBRDs

and their weighted parent samples. This is true even though *none* of the breakBRD galaxies have experienced a major merger, because only ∼2% of galaxies in the weighted central and satellite parent samples have. This lack of significance holds when we remove centrals that have been splashbacks since redshift 0.1 and 0.5.

According to our z-tests, the only significant difference is in the frequency of *very* minor mergers (mass ratios of 1/100–1/10) experienced by the centrals: 26% of the parent centrals experience at least one accretion event, versus 10% of breakBRD centrals. This is significant at $\alpha = 0.01$, even when removing splashbacks since redshift 0.1, and is significant at $\alpha = 0.05$ when removing splashbacks since redshift 0.5.

The decreased frequency of low mass accretion events can be interpreted as a sign of less cosmic accretion overall (including smooth, which this method poorly accounts for), as small satellites are often accreted onto more massive halos together with general accretion along a filament. This makes it unlikely that breakBRD analogue galaxies are generally formed by gas being brought in from outside the halo or funneled from the outskirts to the central region through tidal effects. Both central funneling and the addition of new gas are mechanisms that would increase the central concentration of gas and star formation rate as seen in Section 2.4.1.2. However, the dearth of recently experienced minor accretion events could point to indirect and subtle starvation-like environmental effects on the evolution of the central breakBRD galaxies.

2.4.3 The History of breakBRDs

In an effort to understand why and how breakBRD analogue galaxies have their unique star-forming and color characteristics, we now trace the history of the $z = 0.0$ sample. While the current properties of breakBRD galaxies give us some insight into how they differ from the parent sample, tracking their evolution allows us to understand these differences in more detail. Moreover, as Table 2.3 shows that none of the $z = 0.0$ breakBRDs qualify as breakBRD galaxies at $z = 0.5$, the $z = 0.0$ breakBRDs must have evolved into the breakBRD state somewhere in this window, and we may identify the physical drivers of this evolution by studying their history since $z = 0.5$.

Figure 2.8 shows the relative growth (the differences in log, or ratio, of the amounts at $z = 0.5$

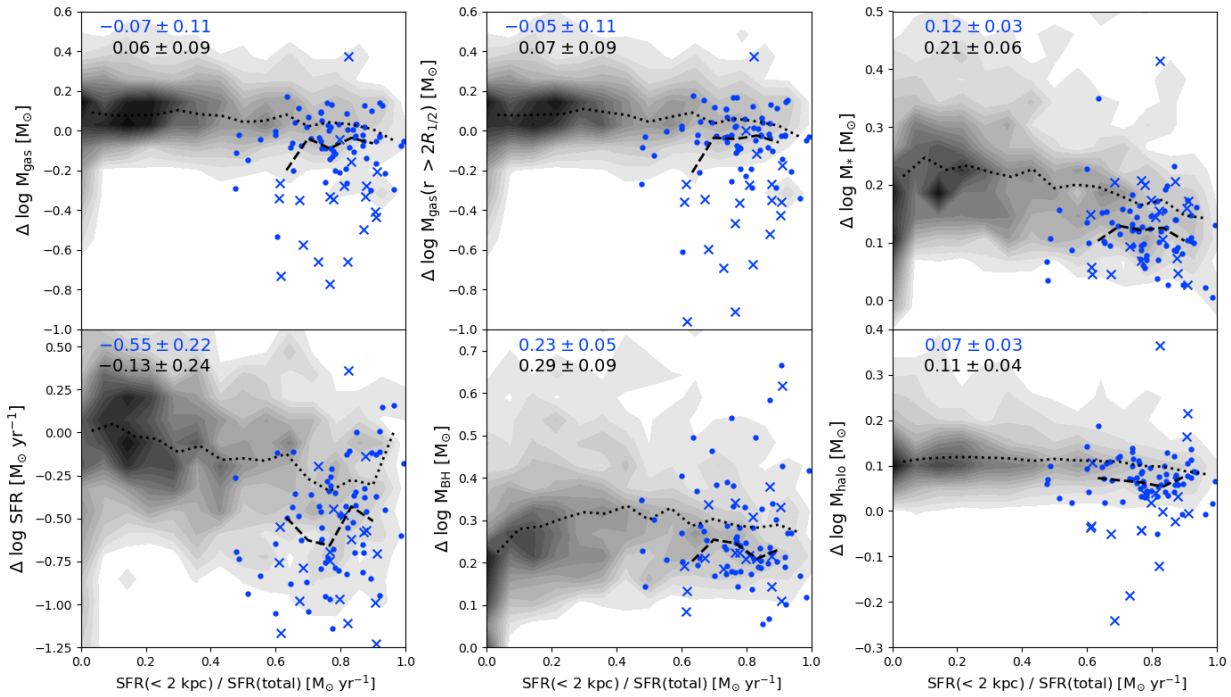

Figure 2.8 Present day star formation rate concentration against relative growth ($\log X(z = 0.0) - \log X(z = 0.5)$) of total gas mass (top left), star formation rate (bottom left), outer gas mass (top middle), supermassive black hole mass (bottom middle), total stellar mass (top right), and total halo mass (bottom right), since $z = 0.5$ for the parent central galaxies sample (grey contours) and our breakBRD-analogues central galaxies sample (blue scatter points). Running median trends are highlighted in black for both the parent sample (dotted) and our breakBRD-analogues (dashed), with the overall medians and MADs in the top left corner. The parent central sample is mass-weighted to its respective bBRDa central sample. Splashback breakBRD centrals are indicated (crosses).

and at $z = 0$) of a number of galaxy properties since redshift $z = 0.5$ for the redshift $z = 0$ bBRDa and parent *central* galaxies: the total gas mass, the gas mass outside the disk, the total stellar mass, the total star formation rate, the total black hole mass, and the total halo mass. This is compared against the SFR concentration at the present day. The parent sample is mass-weighted with respect to the mass distribution of the breakBRD galaxies at $z = 0$. Overplotted lines indicate the rolling median trends for the parent (dotted) and breakBRD analogues (dashed) samples. We choose to show the relative growth with time against the $z = 0$ SFR concentration because that is one of the most distinguishable features of the breakBRD analogue galaxies (as we have shown in Section 2.4.1). We have found that the bBRD satellites experience similar evolution as the parent satellite

sample and therefore show the central galaxies only.

While the total gas mass for the central parent sample has predominantly grown for non-concentrated galaxies, and is stable for galaxies with high star formation rate concentration, the central breakBRD analogues have almost all lost significant amounts of gas (up to 0.77 dex, or 68%; see the upper left panel of Figure 2.8). The most dramatic gas loss in breakBRD analogue galaxies is for splashback galaxies, without which the breakBRD analogues lie closer to the parent sample with a median and MAD of -0.04 ± 0.07.

We note that, in contrast to central galaxies, the majority of satellite galaxies have lost gas since $z = 0.5$. This trend is stronger for more centrally concentrated satellites. This is to be expected if these satellites lose their gas through, for example, ram-pressure stripping.

When we check the growth of the gas mass in the outer regions of the galaxies, we find that the mass in total gas that is lost is predominantly lost from the outskirts ($r > 2R_{1/2}$, see the upper middle panel of Figure 2.8). While not shown, we have checked that the gas evolution in the inner parts is similar to that of the parent sample (akin to the differences between the upper and lower panels of Figure 2.5).

Additionally, we check whether the amount of gas that is lost is converted into stars, as opposed to being removed from or never accreted by the galaxy. About half of the central bBRDa galaxies (including most of the splashbacks and about a third of the non-splashbacks) have lost more gas mass than they have gained in stars that formed over the same time interval. The other half of the central breakBRDs have retained more gas than they have converted into stars, or even gained a small amount of gas since $z = 0.5$. So, for the bBRDa galaxies that have lost significant amounts of gas, some of that gas may have been converted into stars, but even more gas is still lost. Overall, the upper right panel of Figure 2.8 shows that the bBRDas have formed fewer stars since $z = 0.5$ than galaxies in the parent sample, although the difference is smaller when comparing to parent galaxies with similar high SFR concentration.

The star formation rate evolution for the central breakBRDs (lower left of Figure 2.8) follows a trend similar to that of the total gas mass: the central breakBRD analogues experience a higher

reduction of SFR compared to the parent sample. This remains high even compared to the highly-SF-concentrated parent sample. However, the amount of reduction is larger for the breakBRDs: the median value of SFR loss is 0.55 dex, which amounts to a reduction in star formation of 72%, with losses up to 1.25 dex (94% SFR reduction). It is noteworthy that excluding splashback galaxies has less of an impact on the evolution of the SFR than on the gas content: when removing splashbacks, the median + MAD is -0.48 ± 0.22 for the breakBRDs.

Studying the evolution of the central black hole is particularly interesting as AGN related feedback can strongly influence both the central regions as well as the more extended gas distributions of galaxies. In Figure 2.6 we show that the breakBRD analogue galaxies fall on the black hole mass – stellar mass relation of the parent; in Figure 2.8, we study their black hole growth since $z = 0.5$ (lower middle). While the breakBRD analogues have no unusual black hole masses, their growth history from before they were breakBRD analogue galaxies could point to whether their central black hole properties are correlated with their centrally concentrated gas and SFR distributions. The black hole growth in Figure 2.8 shows similar trends to the gas mass and star formation rate growth when comparing the breakBRD analogues to their parent sample in that the growth is less; however, the difference for black hole growth is much less than for the other quantities. This is reflected in the parent and analogue medians (0.23 ± 0.05 vs. 0.29 ± 0.09, and removal of splashbacks only brings the bBRDas to 0.24 ± 0.06). We note that we reach similar conclusions when comparing the maximum black hole accretion rates in each galaxy's recent history (see Section 2.4.2.1). Black holes are therefore unlikely to be the main driver of the breakBRD state.

Lastly, we measure the growth of the dark matter halos between $z = 0.5$ and $z = 0$ (lower right panel of Figure 2.8). While central galaxies in the parent sample grow in halo mass, as significant fraction (predominantly splashbacks) of breakBRD centrals have lost halo mass, while the rest of the sample has only grown slightly. For the latter, we find that the halo mass growth is approximately proportional to the stellar mass growth over this time interval. In particular, the decrease in halo mass that a subset of the central breakBRDs experience, but also the relatively small growth in halo mass, suggest that environmental effects could have played a part in forming

the current state of these galaxies. For the splashback breakBRD galaxies this is very likely the case. For the non-splashback central breakBRD analogues, the environment may have played a more subtle role in their formation. However, as the current environment of the breakBRDs is very similar to that of the parent sample, this may indicate that the past environment of breakBRDs may have been different.

By following the change in galaxy properties, we see that for the central galaxy samples, both the gas mass and SFR has decreased more in the breakBRD sample than in the parent sample, and the black holes masses, stellar masses, and halo masses have grown less. We see that these differences are partially ameliorated when restricting the parent to high SFR concentration, but that even when the breakBRD centrals are compared only to this subsample of parent centrals, differences remain (see e.g. the running medians in Figure 2.8). The largest difference is in the change in the SFR over time, likely because breakBRDs are selected to not only have centralized SF, but also to have red disks.

Our results indicate that before reaching the breakBRD state, the $z = 0$ breakBRD sample experience a process (or processes) that removes gas and reduces or even stops star formation outside the central regions between at least $z = 0.5$ and the present day. When we reproduce Figure 2.8 using the growth since $z = 0.1$, we find that while the trends are similar, the differences between the bBRDa and the parent samples are much smaller. Moreover, while the breakBRD galaxies have lost gas and SFR since $z = 0.1$ (1.3 Gyr ago), this is much less than what they have lost since $z = 0.5$ (5.2 Gyr ago). We reiterate that there is little-to-no overlap in the galaxies of the breakBRD samples at these different redshifts (see Table 2.3). We therefore conclude that the process involved must have affected breakBRD galaxies over a significant time range and is likely to have gradually changed the galaxies to the breakBRD state.

We now look more closely at the intrinsic breakBRD sample at $z = 0.5$ and use that sample to study the future evolution of breakBRD galaxies.

2.5 breakBRD Analogues at Higher Redshifts

In the previous section, we focused on the breakBRD analogue population at $z = 0.0$ and looked at what these galaxies were like in the past. We have also applied the selection criteria laid out in Section 2.3 to IllustrisTNG galaxies at $z = 0.5$ ($\sim$ 5.2 Gyr ago) and $z = 0.1$ ($\sim$ 1.3 Gyr ago) and $z = 0.03$ ($\sim$0.48 Myr ago), giving us new parent and breakBRD analogue samples. The number of galaxies in these samples is given in the righthand columns of Table 2.1. The existence of analogues across more than 5 Gyrs indicates that breakBRDs galaxies exist at a range of redshifts. Though not necessarily common, they may therefore be a part of a regular evolutionary path.

Two possibilities for this existence at multiple snapshots, gigayears apart, immediately spring to mind: either the same galaxies exhibit breakBRD properties for a long period of time, or the breakBRD state is a (short) phase in galaxy evolution that happens for some or even most galaxies. We discuss both these possibilities when studying the future of breakBRD galaxies in Section 2.5.2.

In the following sections, we briefly show the similarity of $z = 0.5$ breakBRDs' properties to those at $z = 0$, and then look at the future of the $z = 0.5$ galaxies. We also consider the future of the $z = 0.1$ sample. For brevity, we do not show the properties of the $z = 0.1$ or 0.03 bBRDa galaxies, but they follow the same patterns as the redshift 0 and 0.5 samples.

2.5.1 Properties

Both Table 2.1 and Figure 2.9 show that there are more galaxies at $z = 0.5$ that have central $D_n4000 < 1.4$, and therefore recent star formation, which is consistent with our expectations for increased star formation rates at this redshift compared to $z = 0$. There are fewer galaxies at $z = 0.5$ with red disks, making the breakBRD analogues at $z = 0.5$ an even more unusual sample than at $z = 0.0$. This is not unexpected, as the increased star formation will make disks tend to bluer. While we compute g-r color magnitudes in the local frame, our selection cut ($g - r > 0.655$) is not adjusted for changes in galaxy population composition. These slight differences, however, do not affect the overall behavior of the selection cuts, as we also select galaxies at extreme ends of the distributions at $z = 0$. The fraction of analogues that are centrals is also lower, being 19% instead of

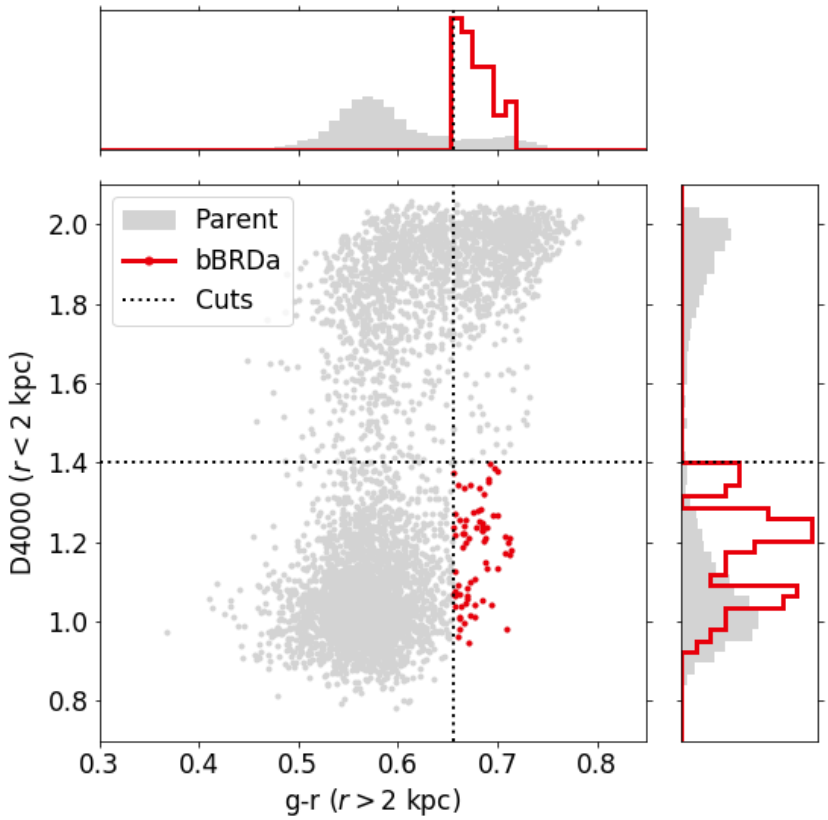

Figure 2.9 D_n4000 in the inner 2 kpc vs $g-r$ color in the $r > 2$ kpc disk for our selection at $z = 0.5$. The histograms at the top and right are normalized. The parent sample is shown in grey, while the $z = 0.5$ breakBRD analogues are red. Dashed black lines show the $D_n4000 < 1.4$ and $g - r > 0.655$ selection cuts. Note that the histogram bins used for plotting straddle these cut, and the axis limits are different from Figure 2.2.

the 37% at $z = 0.0$. This is despite a relatively consistent fraction of centrals in the parent samples at both redshifts.

In order to compensate for correlations with stellar mass, we again weight the $z = 0.5$ parent satellite and central subsamples to match the mass distribution of the corresponding breakBRD analogues, just as we did with our $z = 0.0$ samples. The stellar mass distributions of both the parent and bBRDa galaxies are similar to those at $z = 0.0$. Figure 2.10 shows the $z = 0.5$ stellar mass-specific star formation rate relationship, which can be compared to Figure 2.3. Once again, galaxies with no (or particularly low) star formation were set to $\log(\mathrm{sSFR/yr}) = -13$. We see the same trend here as we did in Figure 2.3, where the breakBRD analogues tend to be at lower sSFR

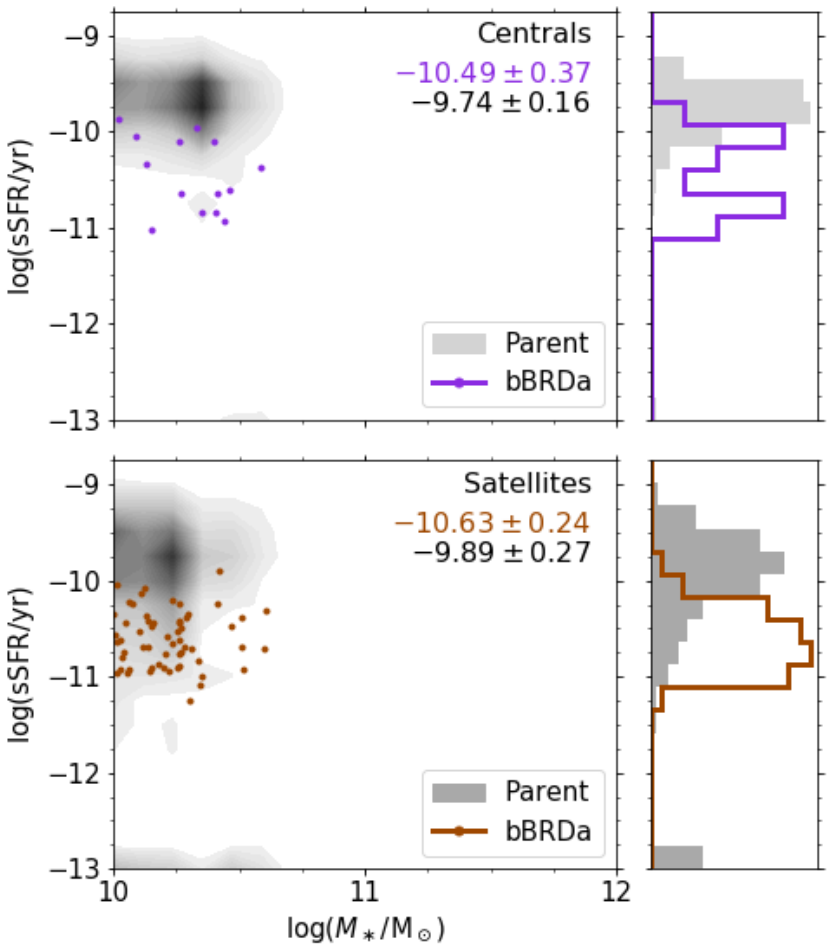

Figure 2.10 Total instantaneous specific star formation rate vs total stellar mass for central galaxies (top) and satellites (bottom) in our $z = 0.5$ selection. The parent sample is represented by the grey contours and the side histograms are normalized. Galaxies with no star formation were set to $\log(\mathrm{sSFR/yr}) = -13$.

than their weighted parent samples. For the satellites, this difference is even more pronounced at $z = 0.5$—where the parent is more clustered—than at $z = 0.0$.

Briefly, we find the redshift 0.5 analogues generally follow the same trends with respect to their weighted parent as the $z = 0.0$ galaxies in Figures 2.3–2.7. There is no significant difference between the black hole mass distributions, just like at $z = 0.0$. Despite the samples being smaller, the breakBRD analogues at $z = 0.5$ have dense gas masses consistent with the trends seen in Figure 2.5: the breakBRD analogues tend to have lower total gas masses than their parents, but an

Table 2.3 Overlap in breakBRD analogue samples

Redshifts	Δt (Gyr)	Number	Percentage
0.0 & 0.03	0.48	135	46.9
0.03 & 0.1	0.86	126	51.0
0.0 & 0.1	1.3	63	25.5
0.1 & 0.5	3.9	2	2.8
0.03 & 0.5	4.7	1	1.4
0.0 & 0.5	5.2	0	0.0

NOTE. - Table is ordererd by the time elapsed between the two redshifts. Percentages are calculated relative to the higher redshift, using the bBRDa numbers in Table 2.1.

equivalent amount of dense gas in their central regions.

In some cases the trends seen at $z = 0.0$ are more pronounced at $z = 0.5$. Using the concentration measures introduced in Figure 2.4, the $z = 0.5$ breakBRDs have dense gas and SFR concentration distributions that are even more clustered at the high end. The satellite fraction remains roughly constant for the parent sample but increases by 20% for the breakBRDs. Central breakBRDs at $z = 0.5$ have a stronger tendency to live in high density environments than at $z = 0$, where there was only a slight enhancement over the parent sample (see Figure 2.7). The primary goal of the $z = 0.5$ sample is to see what happens to breakBRD analogues as they continue to evolve, and while it is meaningful that the two bBRDa populations have similar properties (see Section 2.6.3), a detailed characterization of the redshift 0.5 sample is not relevant to this goal.

2.5.2 The Future of breakBRDs

In Table 2.3 we provide the overlap in bBRDa samples, i.e. the number of galaxies that are breakBRDs at two epochs, at our four redshifts: 0, 0.03, 0.1, and 0.5. It is out of the scope of this paper to find breakBRD analogues at every TNG snapshot in order to quantify the length of the breakBRD state in detail, but we can draw some conclusions based on our limited redshift sampling. The overlap between the $z = 0.0$ and $z = 0.03$ samples shows that ~50% of the breakBRDs at $z = 0.03$ are still in that state 0.48 Gyr later, at redshift 0. This percentage drops to ~25% over the 1.3 Gyr span between $z = 0.1$ and 0.0. This strongly suggests a relatively short-lived breakBRD

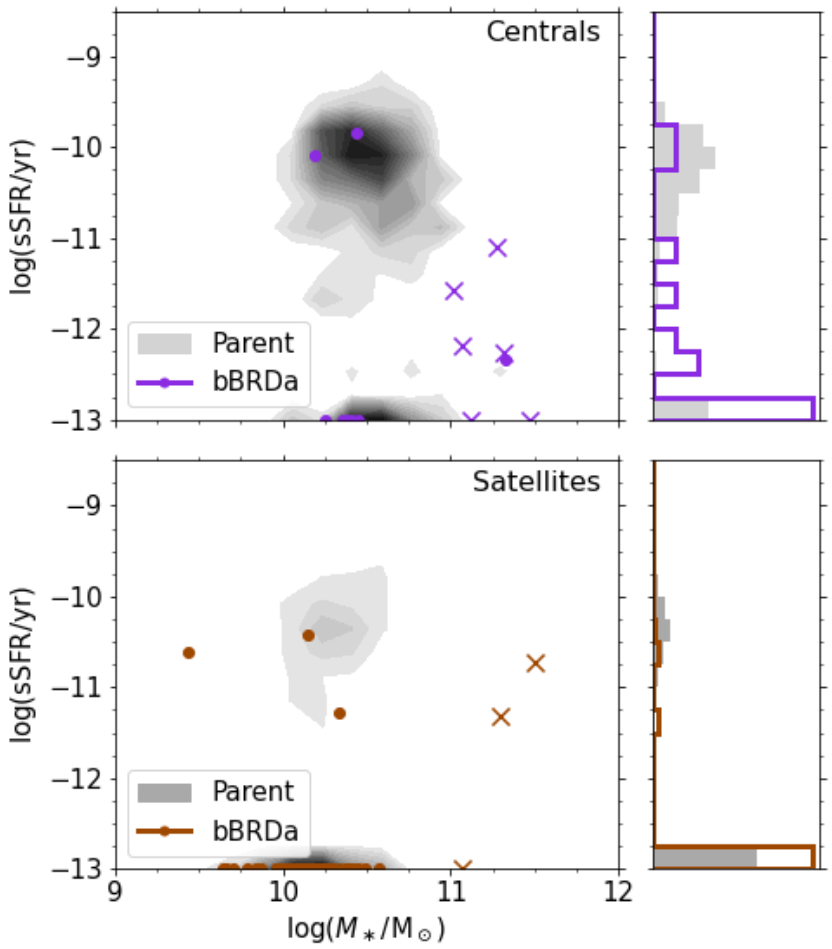

Figure 2.11 Same as Figure 2.10 but the parent and breakBRD samples selected at $z = 0.5$ have been tracked forward to $z = 0.0$. Parent galaxies maintain the weighting applied in Figure 2.10; see text for more details. X's mark breakBRD galaxies that have merged with one of the parent sample by $z = 0.0$.

state of a few hundred Myr up to ~2 Gyr. Moreover, the galaxies that are in the breakBRD state for two of our sampled redshifts include both centrals and satellites. This suggests that there may be similar physical processes at work that facilitate the formation of a breakBRD state for both central and satellite galaxies.

We tracked our $z = 0.5$ samples forward to $z = 0.0$ to study the galaxies' evolution after the breakBRD state. In Figure 2.11 we again plot total stellar mass and specific SFR, but for this tracked set of galaxies. Galaxies with no or very low star formation were once again set to

$\log(\mathrm{sSFR/yr}) = -13$. Parent galaxies have the same weights applied to them as assigned in Figure 2.10. About 20% of the parent galaxies have merged with another parent between $z = 0.0$–0.5; descendent parents are only counted once, and are weighted according to the most massive of their progenitors in the $z = 0.5$ parent sample. Some of the breakBRD analogues have also merged with galaxies from the parent sample; these are indicated with crosses in Figure 2.11. The bBRDa that have merged with a parent galaxy are always the less massive of the progenitor pairs. No breakBRD galaxies have merged with another breakBRD.

In Figure 2.10, all but four, or 1.7%, of the breakBRD analogues have $\log(\mathrm{sSFR/yr}) \gtrsim -11$, which we use as our delineation between the star-forming and quiescent galaxy populations (see e.g. Cassata et al. 2010; Tamburri et al. 2014; Katsianis et al. 2019; Matthee and Schaye 2019). Three of these are centrals. When tracked to redshift 0 (Figure 2.11), 85.7% of central breakBRD analogues (12 out of 14), and 94.8% of satellites (55 out of 58) have $\log(\mathrm{sSFR/yr}) < -11$; therefore, most of the galaxies that were breakBRDs at $z = 0.5$ end up quenched.

Determining the fraction of parent galaxies that transition from star forming to quiescence is more complicated, because of mergers. To determine if a tracked galaxy was star forming at $z = 0.5$, we use the sSFR of the most massive progenitor in the sample, akin to how we handled the weighting. Again, some bBRDa galaxies have merged with redshift $z = 0.5$ parent galaxies, but are always the less massive of the pair and so have no impact on whether a descendent galaxy was considered star-forming at $z = 0.5$. With weighting applied, the fraction of parent centrals and satellites that quench by redshift $z = 0$ is 25.3% and 51.3%, respectively. Unsurprisingly, two proportion z-tests indicate that the quenched fraction is significantly higher for the bBRDa galaxies at the $\alpha = 0.01$ level.

Though not shown, we also track forward the redshift $z = 0.1$ breakBRD analogue and perform the same analysis. At $z = 0.1$, these galaxies display the same sSFR pattern as seen in Figures 2.3 and 2.10; yet when tracked to $z = 0.0$, these galaxies have quenched to a lesser extent. Of the satellites, 51.1% of the bBRDa galaxies have $\log(\mathrm{sSFR/yr}) <= -11$, compared to 10.7% of the weighted parent. For the centrals, 26.0% of the bBRDa have $\log(\mathrm{sSFR/yr}) <= -11$ versus

4.5% of the parent. Both fractions are significantly different at $\alpha = 0.01$. Preferential quenching in satellites is not unexpected, because in satellites, the breakBRD state may indicate strong ram pressure stripping or tidal effects which could rapidly quench the satellite. Such a straightforward explanation would not apply to the centrals, however.

We see a similar set of properties for the breakBRDs at redshifts 0, 0.1, and 0.5, which suggests that the breakBRD selection criteria chooses a consistent set of galaxies. We therefore feel confident that the quenching experienced by the $z = 0.5$ breakBRDs implies that all low redshift galaxies in the breakBRD state will eventually quench.

2.6 Discussion

The following discussion will use the results put forth in Sections 2.4 and 2.5 to answer a series of questions about the formation and evolution of breakBRD analogues. Finally, we will briefly compare the simulated analogues to the observational sample.

2.6.1 Central Enhancement vs Outer Deficit

In Figure 2.4 and the accompanying discussion, we find that the breakBRD analogues have SFR and gas distributions that are centrally concentrated. In the case of SFR and dense, star formation-eligible gas, these concentrations can be quite high, with at least 40% of each contained within the central 2 kpc-radius. Our selection criteria were designed to choose galaxies with highly concentrated star formation, and these stars must be forming out of dense gas, so high concentrations are expected. Note, however, that the parent sample also includes non-breakBRD galaxies with highly concentrated SFR and dense gas: the bBRDa galaxies differ from these because these non-breakBRD SFR-concentrated galaxies also have some star formation in their outer regions. We now ask: did a process cause breakBRD galaxies to have higher central concentrations? Or do they appear this way because gas was removed from their outskirts?

Figure 2.5 is useful for distinguishing central gas enhancement from outer gas deficit, as the dense gas ratio from Figure 2.4 is separated into its components. Here we find that the breakBRD analogues have roughly the same gas mass in their interiors as parent galaxies weighted for the

same stellar mass, despite being lower in dense gas mass overall. We interpret this as a strong indication that gas has been removed from the outskirts ($r > 2$ kpc) of the breakBRD galaxies.

It could also be the case that gas has been funneled from the outskirts into the centers of the breakBRD analogues, rather than stripped from the galaxies completely. Though not shown here, we examined the mass of total gas in a manner similar to Figure 2.5 and found a similar trend: bBRDa galaxies have a lower total gas mass, but inner gas mass equivalent to the parent. This structure, as well as the patterns in Figure 2.4 could also be explained by gas redistribution. However, Figure 2.8 shows that breakBRD analogues tend to have lost more gas than is accounted for by their growth in stellar mass. It is therefore extremely likely that the breakBRD galaxies have lost significant amounts of gas from their outskirts; gas which therefore does not get converted into stars or accreted onto the central black hole. Because of the reduced amount of gas in the outskirts and normal central gas mass, breakBRD analogues appear centrally concentrated.

2.6.2 The Formation of breakBRDs

The selection criteria laid out in Section 2.3.2 certainly select a unique sample of galaxies, and it is instructive to investigate how these galaxies form. Indeed, the stripping suggested by Figure 2.5 (and discussed in Section 2.6.1) motivated Section 2.4.2, as black holes, environment, and merger history could all possibly explain a deficiency of outer gas (see Section 2.2). While we discuss these processes separately, here we endeavor to synthesize what the results of 2.4.2 tell us about the formation of breakBRD analogues.

First, we consider black holes. With Figure 2.6, we find no difference between the black hole mass of $z = 0$ bBRDa and parent galaxies. Their strong agreement persists when we remove the power law dependency on stellar mass, and also holds for breakBRD analogues at higher redshift. We also looked at black hole growth over the past 5 Gyr with Figure 2.8. We do not see a strong difference between parent and bBRDa galaxies in terms of their black hole growth: though the bBRDa centrals tend to have black holes that grow more slowly, the apparent difference is not significant.

Second, we examined the fraction of galaxies that experienced at least one merger of a given

size, including very small mergers that could be instead defined as clumpy cosmological accretion. We only find a statistically significant difference for the fraction of centrals that have had at least one minor accretion event (mass ratio of $1/100$–$1/10$): bBRDa centrals are less likely to have had such an accretion event than parent centrals. This leads us to conclude that the highly centrally concentrated SFR exhibited by breakBRD galaxies is unlikely to be caused by mergers and other growth history. On the other hand, this low frequency could be related to a general decrease in cosmic gas accretion (including smooth accretion) which may then have induced the low total gas mass discussed above, and the low halo and stellar mass growth for breakBRD galaxies in Figure 2.8. This effect would still not fully explain the breakBRD state, however, given that most breakBRD galaxies have lost significant amounts of gas.

Finally, satellite galaxies may have outlying gas stripped by environmental processes (either gravitational or hydrodynamical). We do see a much higher satellite fraction and splashback fraction in the breakBRD analogue sample than the parent sample, indicating that environmental processes could be an important process forming breakBRD galaxies. Also, when we examined the change in gas mass of central $z = 0$ breakBRD galaxies before they reached the breakBRD state (Figure 2.8), we found that the outer gas mass had generally decreased from $z = 0.5$. They have also experienced a commensurate change in dark matter mass, possibly hinting at subtle environmental effects forming even the central breakBRD population.

However, when measuring the density of their present day environment (Figure 2.7), the median + MAD values overlap for the non-splashback breakBRD analogues and the non-splashback parent sample. Though not shown, we also quantified their environment through the distance to the nearest more massive neighbor and to the nearest cluster. Here we also found significant overlap between the median + MAD of the central breakBRD and parent samples. Therefore, while environmental processes can explain the properties of the satellites and splashback galaxies in the breakBRD sample, if the environment has an important role in the formation of central breakBRD analogues, this may indicate that the environment of breakBRD central galaxies has changed.

The strongest difference between breakBRD analogues and their TNG parent sample seems to be

environment; however, the difference is not a "smoking gun." Importantly, we stress that throughout our findings, breakBRD analogues are more like each other (across the satellite-central divide) than galaxies in the parent sample. For example, the median dense gas mass and concentration of breakBRD satellites and centrals are similar, and both are significantly larger than the concentrations of the parent subsamples. While environment may be an influencial factor in the formation of breakBRDs, the exact way in which it exerts this influence appears to be subtle and worthy of further, more detailed investigation beyond the gross statistics explored herein.

2.6.3 Quenching vs Stochastic Star Formation

One benefit of cosmological simulations is that we can answer the question "what will happen to this galaxy in the future?". This is exactly the question we asked of the $z = 0.5$ breakBRD analogues in Figure 2.11, where we concluded that breakBRDs largely became quenched by $z = 0.0$. Though we conclude that the $z = 0.5$ breakBRDs quench, we have not determined whether the breakBRD state is common to galaxies in TNG100.

We now consider whether or not the breakBRD state is a common state in the lives of galaxies, either generally, only within the mass range typical to the bBRDa sample (see Figure 2.1), or specifically for galaxies that will quench. Because the breakBRD state is phenomenologically characterized by high SFR concentration (Figure 2.4), we can asses whether or not a galaxy *could* have ever been in the breakBRD state by looking at maximum SFR concentration each galaxy has reached during its history. We first split our $z = 0.0$ parent sample into star-forming and quiescent subsamples using $\log(\mathrm{sSFR/yr}) = -11$ as the boundary. For the star-forming sample, the maximum SFR concentration of the parent sample is determined across *all* IllustrisTNG outputs between $z = 0.5$ and $z = 0$. Redshift 0.5 is chosen as the endpoint because there is no overlap in the breakBRD population between $z = 0.5$ and $z = 0.0$. For the quiescent sample, we find the maximum SFR concentration since the galaxy was on the star-forming main sequence (at $\log(\mathrm{sSFR/yr}) > -10$), which can occur more recently than $z = 0.5$ or at higher redshift. We reiterate that this search is performed at all outputs, not just those redshifts at which we found breakBRD analogues. We note that high SFR concentration does not necessarily mean a galaxy

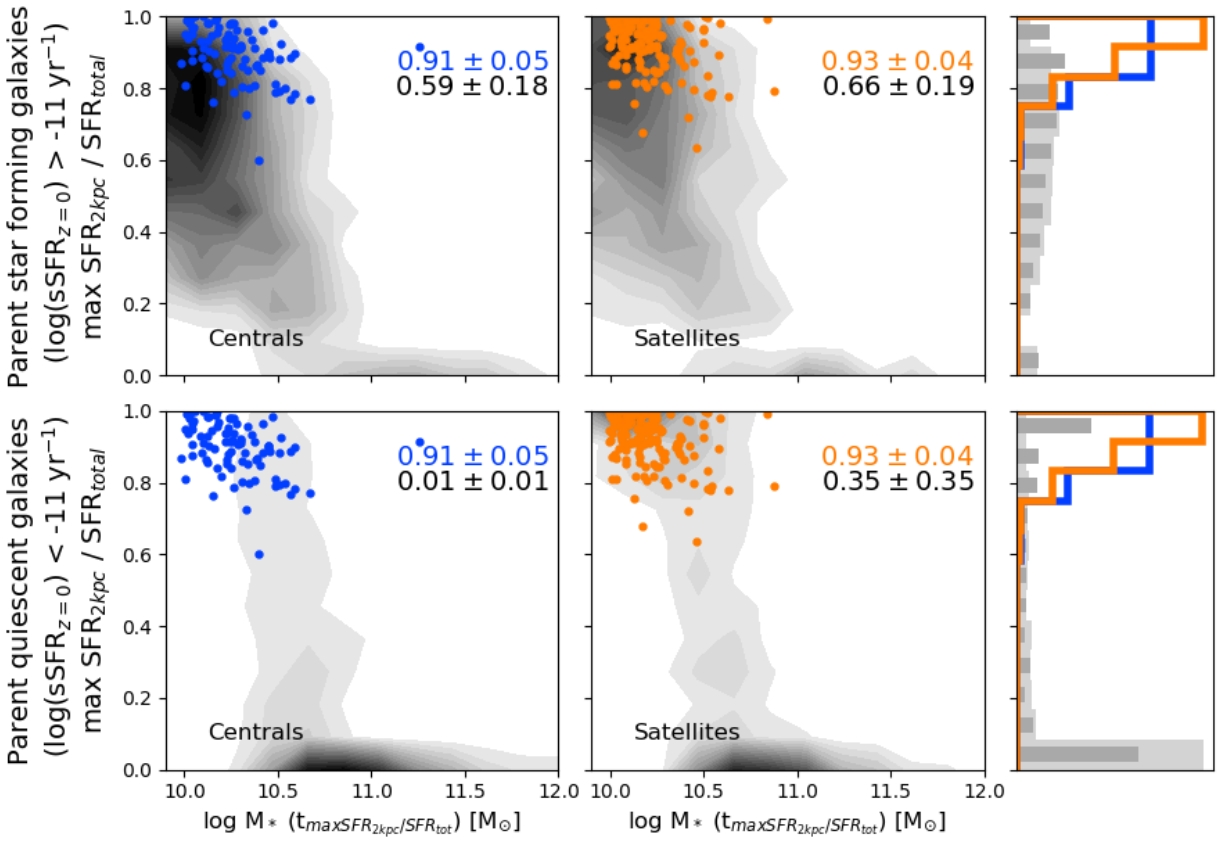

Figure 2.12 Maximum star formation rate concentration, $\max(\mathrm{SFR}_{2\mathrm{kpc}}/\mathrm{SFR}_{\mathrm{total}})$, of each galaxy, either since $z = 0.5$ for star-forming parent galaxies (top), or since having $\log(\mathrm{sSFR/yr}) \geq -10$ for quenched parent galaxies (bottom) against the stellar mass they had at the time of peak SFR concentration. The plot is broken into centrals (left) and satellites (right). Overplotted is the $z = 0$ breakBRD analogue sample, also shown with their historically highest SFR concentration and corresponding stellar mass since $z = 0.5$. In contrast to other figures, the breakBRD sample is not included in either the star-forming or quiescent parent sample. Note that in contrast to most other figures, here we show *all parent galaxies without weighting*.

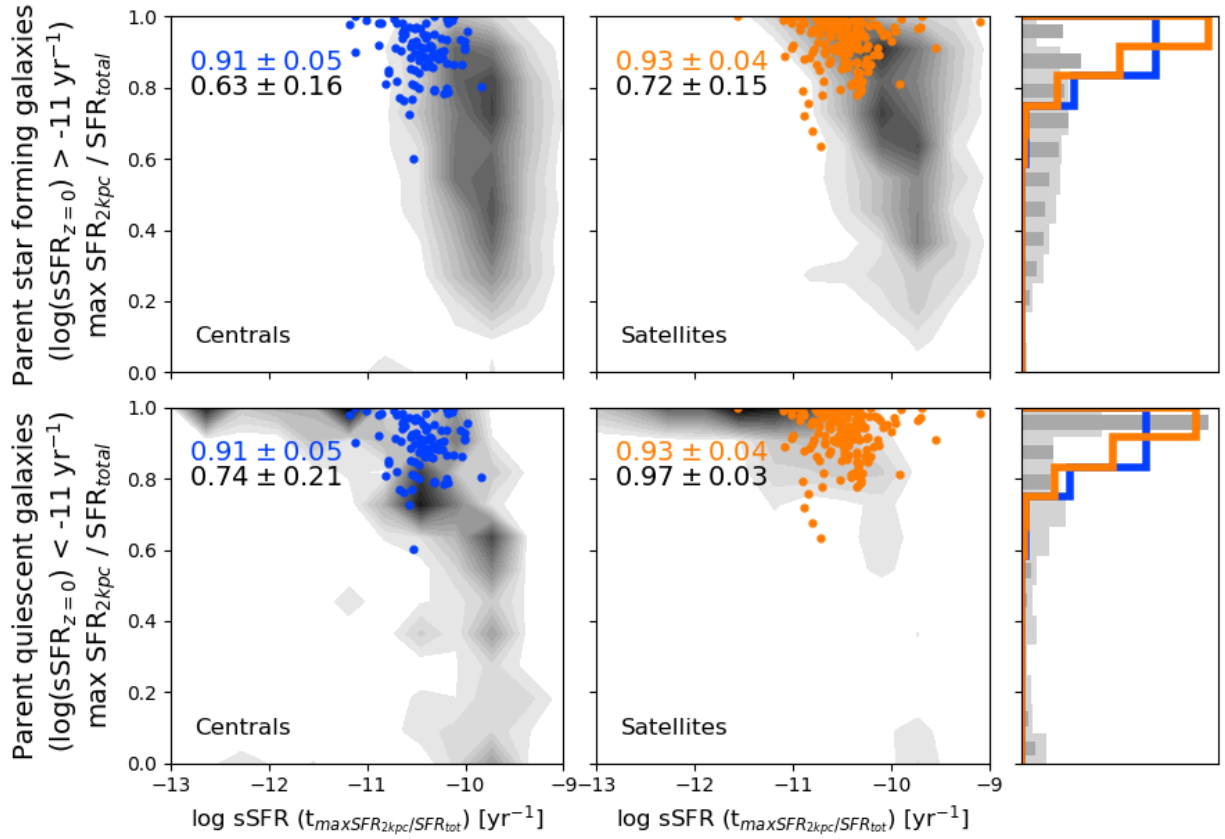

Figure 2.13 Similar to Figure 2.12 but with peak SFR concentration plotted against the sSFR at the time of peak SFR. Moreover, here we show the parent galaxy sample distribution *weighted* to have the same present-day stellar mass distribution as the $z = 0.0$ breakBRD analogue sample. Star-forming/quenched satellites/centrals are all weighted separately. As in Figure 2.12 the breakBRD sample is not included in either the star-forming or quiescent parent sample.

would meet the breakBRD selection criteria, as this additionally requires red disk color (see Section 2.3.2).

Figure 2.12 shows the maximum SFR concentration for the *unweighted* parent sample in grey, while Figure 2.13 shows maximum SFR concentration for the *weighted* parent sample. Note that the star-forming/quenched satellites/centrals have their weights calculated separately, making their weightings slightly different than those used in Section 2.4. Additionally, the parent sample excludes the breakBRD subsample in both of these figures, in contrast to the rest of this work. The central (blue; left) and satellite (orange; right) $z = 0.0$ breakBRD analogues are repeated in both

Figures 2.12 and 2.13 as a reference, with their peak SFR since $z = 0.5$.

In Figure 2.12 we show, for the unweighted parent and bBRDa samples, the maximum SFR concentration against the total stellar mass at the time of maximum SFR concentration. Removing the mass weighting allows us to explicitly see the distribution of SFR concentration over our full stellar mass range, for both star-forming and quiescent galaxies, and compare these to our breakBRD samples.

For the weighted parent sample shown in Figure 2.13 we plot the maximum SFR concentration against the *total sSFR* at that time. This is because in addition to SFR concentration, breakBRD galaxies tend to cluster in total sSFR space (Figures 2.3 & 2.10). The combination of star-forming center and red disks tends to make breakBRDs sit somewhat below the star-forming main sequence while still well above the sSFR of quenched galaxies, so this may give us more discriminating power in our comparison with the parent sample.

We first focus on the star-forming galaxies in the top panels of Figures 2.12 and 2.13. Whether we consider the weighted (Figure 2.12) or unweighted (Figures 2.13) samples, we see that the maximum concentration of star-forming galaxies extends to much lower values than the breakBRD sample. This is also reflected in their median + MAD values. The central and satellite breakBRD MAD ranges overlap with each other, but generally not with their respective parent populations. The breakBRDs only have overlapping median+MADs with the weighted quenched parent population. We note that at the time of maximum concentration, the sSFR of star-forming parent galaxies extends to higher values than the breakBRD analogue sample. This is very dramatic in the central parent sample, but can be seen even in the star-forming satellite parent galaxies. We therefore conclude that the breakBRD state is unlikely to be a result of stochastically-distributed star formation in galaxies on the star-forming main sequence. This comes as no surprise since we found that breakBRD galaxies (identified at $z = 0.5$) are likely to quench.

We next focus on the quenched galaxies in the bottom panels of Figures 2.12 and 2.13. When we examine the unweighted sample, we clearly see that most quenched galaxies have not passed through a breakBRD state: there is a the large number of galaxies with low concentrations, especially at

higher masses. Focusing on the unweighted parent sample in Figure 2.12 allows us to highlight the unusual mass distribution of breakBRD galaxies with respect to quenched galaxies—they tend to be lower mass. At the mass range typical for breakBRD galaxies, there seems to be a high fraction of quenched galaxies that have experienced centrally concentrated star formation in their past.

When looking at the weighted sample in Figure 2.13, which emphasises the breakBRD mass range, we see that nearly all quenched satellites and about half of the quenched centrals have had high SFR concentrations, indicative of a breakBRD-like state. Looking at central galaxies in detail, we see that the median is below most of the range of the breakBRD sample, but because the distribution is so extended there is significant overlap in the concentrations. This state is therefore more common among quenching galaxies with lower stellar masses, but even among low-mass quenching galaxies the breakBRD state is far from ubiquitous.

Because both central star formation (measured using D_n4000) and a red disk is required for the breakBRD state, by only looking at SFR concentration, we are being conservative in our estimate of the historic overlap in the breakBRD and parent populations. BreakBRD galaxies are likely more unique than the median + MAD values in Figure 2.13 indicate. We can begin to see this when we examine the range of sSFR values in the parent sample in Figure 2.13. We see that for galaxies quenched at $z = 0$, the sSFR at maximum SFR concentration can be much lower than that found in the breakBRD sample, indicating that these galaxies might not meet the the star-formation threshold for $D_n4000 < 1.4$.

This brings us to an important caveat in our comparison. It is outside of the scope of this work to search for every breakBRD galaxy at all of the IllustrisTNG outputs. All we are finding for the parent sample is the simulation snapshot with the maximum SFR concentration. There may be other times when the SFR concentration is still quite high and the total sSFR is more in line with that found for breakBRDs. We can only draw conclusions about the fraction of galaxies that *could* reach the breakBRD state criteria based on this simple proxy.

By searching for the maximum SFR concentration of quenched parent galaxies, we conclude that the majority of these galaxies do *not* experience a breakBRD state. Moreover, when we look

at quenched parent galaxies at similar stellar masses as the breakBRDs, at least half of central galaxies never reach high SFR concentrations.This difference in SFR concentrations between high- and low-mass quiescent galaxies does suggest that these galaxies can experience different quenching pathways in IllustrisTNG. Nevertheless, we conclude that breakBRD galaxies remain an unusual sample of quenching galaxies, even when attempting to align our samples to the same point in their evolution.

2.6.4 Comparison with the Observational Sample

In this paper we have specifically chosen to compare galaxies within the TNG100 simulation, rather than compare simulated galaxies directly to observed galaxies. This way, we mitigate any "systematic" errors in the simulation, which we know does not exactly reproduce the observed universe. For instance, for the stellar mass range of the breakBRDs, the TNG black hole mass-stellar mass relation tends towards the higher end of what is observed (Habouzit et al. 2020), and the satellite quenched fraction is higher than seen in SDSS (Donnari et al. 2021). That said, because we are using this work to draw conclusions about the evolution of breakBRD galaxies, it is worthwhile to make some comparisons between the simulated and observed breakBRD galaxy samples.

Looking at the stellar mass distribution of the breakBRD observed and analogue samples, we find that they are quite similar. Although we require that IllustrisTNG galaxies have $M_* > 10^{10}$ $M_\odot$, about 80% of observed breakBRDs are above this mass. The majority of observed breakBRDs are between 10^{10} - $10^{10.5}$ $M_\odot$ (see Figure 3 in TT20), roughly agreeing with the tendency of breakBRD analogues to have lower masses within our selected range of 10^{10} - 10^{12} $M_\odot$ (Figure 2.1).

Figure 2.14 compares the sSFR and color distributions of the observed and simulated breakBRD samples, as well as the weighted TNG parent sample. Note that a mass cut of $\log(M_*) > 10$ $M_\odot$ has been applied the observed breakBRD sample, in agreement with the mass cut used to select the TNG parent sample (Section 2.3.1).

We first focus on the top panel, which compares the sSFR of the aforementioned samples. The TNG data combines satellites and centrals from Figure 2.3. The observed parent is omitted, but its star-forming component ($\log(\text{sSFR/yr}) > -10$) has an sSFR distribution that is very similar to

the weighted TNG parent's. With this in mind, we can see that the sSFR distribution of observed breakBRDs (green points) is similar to that of its star-forming parent sample, while the simulated breakBRDs (blue points) have sSFRs lower than the median of their parent samples. This may indicate that the breakBRDs in the simulation have already begun quenching while the observed galaxies are still on the star-forming sequence. However, the global sSFR from Brinchmann et al. (2004) is used in TT20. This uses the emission lines in the SDSS spectra from the central region (the region covered by the spectral fiber) as well as the optical colors from the SDSS photometry inside and outside the fiber regions to place galaxies on a global sSFR relation. Brinchmann et al. (ibid.) note however, that the likelyhoods of SFR/L_i for redder colors are broader and sometimes multipeaked, and the SFR/L_i is therefore less well constrained. Because the breakBRD galaxies have unusual central star formation rates for their red disk colors, the global sSFRs from Brinchmann et al. (ibid.) may be more uncertain for these galaxies.

In the lower panels of Figure 2.14, we compare the global $(g - r)$ and $(u - r)$ colors of the simulated and observed galaxies. We see that particularly in the $(g - r)$ galaxy color, the observed (green points) and simulated (blue points) breakBRD galaxies are quite similar, although more of the observed breakBRDs extend to bluer colors. In addition we have shown the observed "green valley" with black dashed lines, as fit using color-stellar mass diagrams (Mendel et al. 2013; Schawinski et al. 2014). We also have found the minimum of the color distributions in the TNG100 parent sample as a function of stellar mass. It is nearly constant with mass, and we denote the ±0.5 dex region with red dashed lines to show a rough "green valley" for the simulated parent sample. We see that the simulated valley is at redder colors than the observed valley for most of the galaxies in the sample. Thus the $(g - r)$ colors for the simulated sample are bluer with respect to the parent than the observed sample. The $(u - r)$ colors are similar with respect to the valley in both the simulated and observed samples.

Finally, we compare the environmental measures of the observed and simulated breakBRD galaxies. The satellite fraction of observed breakBRD galaxies seems to be quite similar to the observed parent sample (40% and 39%, respectively), while the satellite fraction of breakBRD

analogues is much larger than that of the parent sample (see Table 2.1). However, for both the observed and analogue breakBRD samples, the environmental density is similar to that of their parent samples, even when including splashback galaxies (which cannot be removed from the observed sample).

In summary, we find that there is generally good agreement between the observed and simulated samples. However, when compared to the parent samples, the sSFRs of the simulated breakBRDs tend to be lower than the sSFRs of the observed breakBRDs, and the satellite fraction of breakBRD galaxies is comparatively higher in the simulations than in the observations.

2.7 Conclusion

Tuttle and Tonnesen (2020) discovered an unusual sample of galaxies in observations, called breakBRDs, with red disks and recent star formation in their centers. By generating synthetic observations, we applied similar cuts to galaxies within IllustrisTNG to find galaxies in a state analogous to the observed breakBRDs. These cuts were applied at multiple redshifts: 0.0, 0.03, 0.1, and 0.5.

- IllustrisTNG contains galaxies that are analogous to the observational sample of TT20 in terms of their disk colors and D_n4000 measures (Figure 2.2).

- Our color- and D_n4000-based selection criteria find TNG galaxies with centrally-concentrated star formation (Figure 2.4), as expected from TT20. Simulated breakBRD galaxies tend to have lower stellar masses than the parent TNG sample (Figure 2.1). When we weight the parent sample by its stellar mass distribution, we find that the dense (> 0.1 cm^{-3}) gas mass is low and centrally concentrated in bBRDa galaxies (Figure 2.5)

- The bBRDa populations have a higher satellite fraction than in the parent sample (Section 2.4.2.2; Table 2.1). This aligns with our idea that environmental effects could drive centrally-concentrated star formation. We also find a somewhat higher splashback fraction in the central galaxies of the bBRDa sample compared to the central parent sample (Section 2.4.2.2; Table

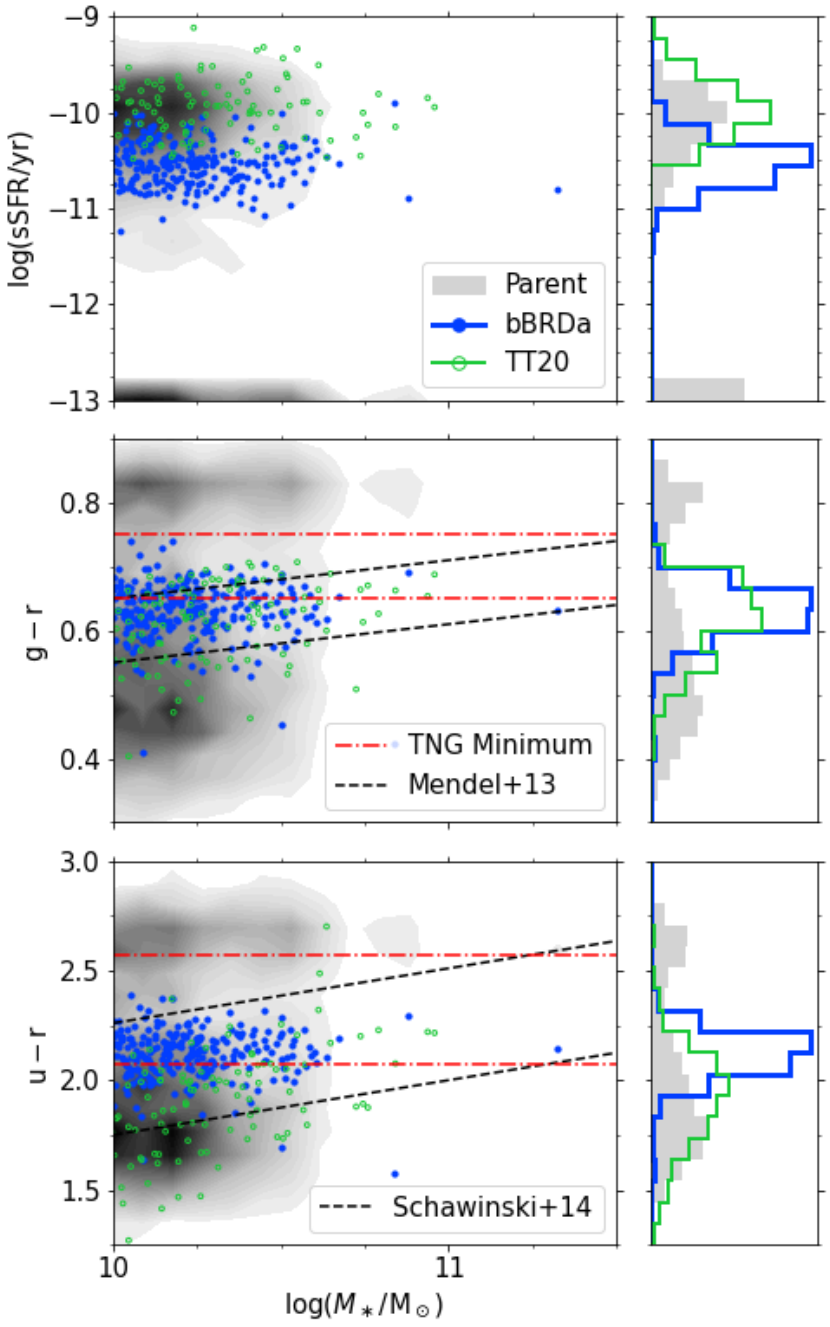

Figure 2.14 Whole-galaxy sSFR (top), $g - r$ (middle) and $u - r$ (bottom) for the full breakBRD analogue sample (blue solid) and its weighted parent (greyscale). The sSFRs and colors of the observed breakBRD sample (Tuttle and Tonnesen 2020) with $\log(M/\mathrm{M}_\odot) > 10$ are shown as green open circles and thin lines. In the lower two plots, black dashed lines show the "green valley" (Mendel et al. 2013; Schawinski et al. 2014), and red dot-dashed lines bracket the "valley" present in the colors of the un-weighted TNG parent; see text for more details.

2.2). Together this suggests that environment may have been a driver in forming a significant fraction of our breakBRD sample.

- Central breakBRD galaxies at $z = 0$ have lost significant amounts of gas, mainly from their outskirts, and an even higher fraction of star formation since $z = 0.5$ (Figure 2.8). They also generally have grown less in dark matter mass, stellar mass, and black hole mass, compared to the parent sample, although the differences between the samples are not significant.

- When we only consider central galaxies that have not been splashbacks since $z = 0.5$, we find no clear cause for the breakBRD state. The black hole mass distribution and local environment are similar between the bBRDa and parent samples (Figures 2.6 & 2.7). Mergers are similarly prevalent in both samples, with the exception that central breakBRD galaxies have experienced less very minor mergers or clumpy cosmological accretion (Section 2.4.2.3). We infer that any environmental driver must therefore be subtle, and possibly act over long timescales.

- Within IllustrisTNG, the breakBRD-analogue state is a transient one, lasting between a few hundred Myr to ~ 2 Gyr (Table 2.3 and Section 2.5.2).

- We find that breakBRD analogues at $z = 0.5$ largely quench by $z = 0$ (Figure 2.11). Because breakBRD galaxies at multiple redshifts have similar properties, this suggests that the majority of breakBRD galaxies are in the process of quenching, and that the observed breakBRD galaxies may also be quenching.

- We argue that breakBRD galaxies are a unique population of quenching galaxies. They are of lower stellar mass than most quenching or quiescent galaxies. By-and-large, both star-forming and quiescent galaxies do not reach the same high SFR and dense-gas concentrations exhibited by the breakBRD samples (Figures 2.12 and 2.13) and therefore never experience a breakBRD state. However, present-day low-mass quiescent galaxies are more likely to have experienced a centrally-concentrated phase in their past.

This paper was motivated by the observational breakBRD sample from TT20, in the hopes that IllustrisTNG could provide an explanation for the appearance of the observed sample. Our findings place breakBRDs in a unique space outside of the general picture of galaxy inside-out formation and quenching. Most observations, as discussed in the introduction, find that as the global star formation rate decreases, central star formation is suppressed. We have found here that, as in observations, the fraction of these highly-concentrated breakBRD galaxies is small at any given time in TNG. We briefly note that in Illustris and EAGLE the quenching populations are mainly composed of galaxies that have centrally concentrated star formation (Starkenburg, Tonnesen, and Kopenhafer 2019), unlike TNG. Importantly, upon closer inspection, we found that*a significant fraction of quenching, low stellar mass central galaxies* undergo a phase of centrally-concentrated star formation (Figure 2.12 and 2.13). Therefore, understanding the breakBRD state in more detail may be an important step in understanding the process by which low mass central galaxies quench.

It is worth noting that breakBRD galaxies are not alone in indicating that galaxies may follow several paths to red, quenched, early-type galaxies. For example, Suh et al. (2010) identify early-type galaxies in the Sloan Digital Sky Survey DR6, and find that about 30% of their sample are "blue-cored". They find that these early-type galaxies tend to be lower mass and posit that they may be formed via mergers with gas-rich galaxies, while the majority of early-type galaxies are formed via equal-mass "dry" mergers. Evans, Parker, and Roberts (2018) find a population of "red misfits" characterised by red optical colors and high sSFRs, and conclude that they are likely to be gradually quenching via internal processes.

Another interesting class of galaxies are passive spirals, first found in clusters (van den Bergh 1976; Poggianti et al. 1999). More recent studies have found passive spirals across environments (Bamford et al. 2009; Masters et al. 2010). Bundy et al. (2010) argue that up to 60% of spirals may pass through this phase on the way to the red sequence. Interestingly, the authors find that passive spirals are bulge-dominated at all masses, indicating that the simple fading of disks is not a viable formation mechanism. Given that we find that nearly half of quenching central galaxies (and most quenching satellite galaxies) in IllustrisTNG pass through a breakBRD-like state (Figure

2.13), more study of a possible connection between these galaxy classes may be warranted.

Through our analysis of breakBRD galaxies we have made testable predictions that require more detailed observations of the gas distribution of observed breakBRD galaxies. Specifically, we argue that the observed breakBRD population will show normal central gas masses and apparent outer deficits (see Section 2.6.1). Given that breakBRD analogues within IllustrisTNG appear to quench, it will also be useful to search the observed sample for additional signs of quenching. Both of our predictions can be evaluated by searching for the gas supply of breakBRD galaxies, which should be low overall but normal in the galaxy center.

CHAPTER 3

SEEKING SELF-REGULATING SIMULATIONS OF IDEALIZED MILKY WAY-LIKE GALAXIES

The following chapter is work that is currently under review at The Astrophysical Journal. A preprint of the submitted version can be found as Kopenhafer, O'Shea, and Voit (2022). The following has been slightly modified from this submitted version for grammar and style.

3.1 Chapter Abstract

Precipitation is potentially a mechanism through which the circumgalactic medium (CGM) can regulate a galaxy's star formation. Here we present idealized simulations of isolated Milky Way-like galaxies intended to examine the ability of galaxies to self-regulate their star formation, particularly via precipitation. Our simulations are the first CGM-focused idealized models to include stellar feedback due to the explicit formation of stars. We also examine the impact of rotation in the CGM. Using six simulations, we explore variations in the initial CGM $t_{\rm cool}/t_{\rm ff}$ ratio and rotation profile. Those variations affect the amount of star formation and gas accretion within the galactic disk. Our simulations are sensitive to their initial conditions, requiring us to gradually increase the efficiency of stellar feedback to avoid destroying the CGM before its gas can be accreted. Despite this gradual increase, the resulting outflows still evacuate large, hot cavities within the CGM and even beyond r_{200}. Some of the CGM gas avoids interacting with the cavities and is able to feed the disk along its midplane, but the cooling of feedback-heated gas far from the midplane is too slow to supply the disk with additional gas. Our simulations illustrate the importance of physical mechanisms in the outer CGM and IGM for star formation regulation in Milky Way-scale halos.

3.2 Introduction

Galaxies obey a number of scaling relations that suggest they have a mechanism for regulating their star formation rates (SFRs). These scaling relations include the star-forming main sequence (e.g. Renzini and Peng 2015; Sherman et al. 2021; Popesso et al. 2022) and the stellar mass–halo mass (SMHM) relation (Somerville and Davé 2015; Behroozi et al. 2019). Gas must be continually

supplied to a star-forming galaxy as its own interstellar medium (ISM) only contains enough gas to fuel star formation for a few gigayears. The circumgalactic medium (CGM) has gained much attention as a possible locale for self-regulation as it mediates both inflowing and outflowing gas in addition to functioning as a substantial baryonic reservoir in its own right (Tumlinson, Peeples, and Werk 2017).

One potential self-regulation mechanism is known as "precipitation" (Voit et al. 2015). Under this framework, feedback (either stellar or from an AGN) works to maintain the median $t_{\rm cool}/t_{\rm ff}$ ratio around 10. Throughout this paper we'll refer to the median value τ of $t_{\rm cool}/t_{\rm ff}$ in the CGM as the "precipitation limit parameter." Importantly, τ is the median of a $t_{\rm cool}/t_{\rm ff}$ *distribution* for the CGM gas that may have a broad dispersion (Voit 2021). When $\tau \sim 10$, the $t_{\rm cool}/t_{\rm ff}$ distribution allows for the formation of a multiphase medium. If τ declines, additional cold dense gas is able to accrete onto the galaxy, driving a burst of star formation and feedback. This feedback in turn heats and inflates the CGM, lowering its density and reducing its ability to cool. Conversely, a CGM driven above $\tau \sim 10$ should feed less cold, dense gas into the galaxy. This reduction of the cold gas supply then stalls feedback until the CGM is again able cool and contract, thereby lowering τ.

Precipitation as a regulation mechanism was originally proposed for galaxy cluster cores heated by active galactic nuclei (AGN). It was motivated by observations suggesting that that the black hole fueling rate depends on the development of a multiphase medium (Pizzolato and Soker 2005; Cavagnolo et al. 2008; Voit et al. 2008), which happens in simulations when a CGM in approximate thermal balance becomes thermally unstable (Pizzolato and Soker 2010; McCourt et al. 2012; Sharma et al. 2012). In simulated multiphase media, cold clouds are able to precipitate out of the hot, ambient medium when $t_{\rm cool} \lesssim 10\, t_{\rm ff}$ (Gaspari, Ruszkowski, and Sharma 2012; Gaspari, Ruszkowski, and Oh 2013; Li and Bryan 2014a,b; Gaspari, Brighenti, and Temi 2015; Prasad, Sharma, and Babul 2015). If the medium is sufficiently turbulent, these cold clouds are then able to accrete chaotically toward the center, and in the systems originally considered, they trigger a strong AGN feedback response. This feedback then heats and expands the CGM, raising $t_{\rm cool}$ and diminishing accretion. See Donahue and Voit (2022) for an in-depth review of this process.

Regulation via precipitation is observationally supported in both clusters (Voit and Donahue 2015) and elliptical galaxies (Frisbie et al. 2020). The physical principles that underpin precipitation regulation are agnostic to the source of feedback in a galaxy, and so could extend to smaller galaxies not dominated by AGN feedback. This possibility is supported by recent theoretical (Voit et al. 2019) and observational (Babyk et al. 2018) developments.

In this work, we explore the viability of precipitation as a regulatory mechanism for star formation in Milky Way-like galaxies lacking AGN activity. Self-regulation is broadly defined as a balance between gas accretion on the one hand and stellar feedback on the other (Bouché et al. 2010; Schaye et al. 2010; Davé, Finlator, and Oppenheimer 2012; Zaragoza-Cardiel et al. 2019). This balance might ultimately be what places galaxies on the stellar mass-halo mass relation (Voit et al. 2015; Mitchell and Schaye 2022).

Spiral galaxies like the Milky Way tend to live in complex environments where they are continuously interacting with companion galaxies and cosmological filaments. Such environments make it difficult to isolate the interactions of the CGM and its host galaxy and to understand the long-term behavior of an undisturbed Milky Way-like halo. We therefore use idealized simulations of an isolated galaxy for our investigation, seeking to understand what a Milky Way-like galaxy would look like without external interference. Idealized simulations also allow us to maintain a constant dark matter halo mass, as changing the dark matter mass should eventually change the stellar mass of the galaxy according to the SMHM relation. With idealized simulations, we are also able to achieve higher spatial resolution in the CGM for reasonable computational cost. High CGM resolution broadens the distributions of gas densities and temperatures (Corlies et al. 2020) and increases the overall amount of neutral hydrogen (van de Voort et al. 2019). Both of these effects should have an impact on precipitation (Voit 2021).

Historically, idealized simulations of isolated Milky Way-like galaxies have fallen into two types: simulations of a star-forming gaseous disk with no CGM, and simulations of a CGM with no explicit star formation. The former include the AGORA simulations of Kim et al. (2016), works using the AGORA initial conditions such as Butsky and Quinn (2018) and Shin, Kim, and Oh

(2021), and others (Benincasa et al. 2016). Instead of a CGM, the gas disk of these simulations is surrounded by a very low density medium with very long cooling times and low total mass. In the latter category are the simulations from Fielding et al. (2017) and Li and Tonnesen (2020). These CGM-focused works include stellar feedback, but this feedback is tied to the gas flow rate through an inner boundary rather than the explicit formation of stars in a gas disk. This work is the first to combine both approaches, modeling star formation and the resulting feedback in the context of both a gas disk and its surrounding non-uniform CGM to create a fully self-consistent picture of how the galaxy and its CGM interact. This is particularly important for modeling the inner CGM and the disk-halo interface.

We detail our simulation setup in Section 3.3. Then, in Section 3.4, we examine how the galactic disk is affected by our simulation setup and its variations. In Section 3.5, we follow the movement of gas between the disk and the CGM by tracing inflows, outflows, and the CGM's gas supply. Section 3.6 looks at the structure of the CGM in our simulations. We discuss various aspects of our simulations in Section 3.7. Finally, we summarize and conclude our work in Section 3.8.

3.3 Simulation Setup

We perform idealized simulations of isolated, Milky Way-like galaxies and their circumgalactic media. Our simulations are performed with the Eulerian astrophysical hydrodynamics code Enzo (Bryan et al. 2014; Brummel-Smith et al. 2019). Enzo models stellar populations with particles and we include feedback from Type II supernova, as will be discussed more in Section 3.3.2.

We employ a 9-species, non-equilibrium primordial chemistry network through the Grackle cooling and chemistry library (Smith et al. 2017). This network includes all ionization states of H, He, and H_2, including H^-, as well as the density of free electrons. Grackle provides cooling rates for H, He, and metals through precomputed Cloudy[1] tables (Ferland et al. 2013). These tables include the extragalactic UV background of Haardt and Madau (2012), which is fixed at $z = 0$ for the purposes of our simulations.

We adopt a static NFW dark matter potential (Navarro, Frenk, and White 1996) with M_{200} =

[1] A slightly modified version of Cloudy 10 is used which saves outputs with more precision.

10^{12} $M_\odot$ and a concentration of 10. We define the edge of the dark matter halo using $r_{200} \approx 206$ kpc, which is the radius enclosing a density that is 200 times the critical density.

On top of this we also impose a static stellar disk potential from Miyamoto and Nagai (1975). For this potential we adopt $M_* = 5.8 \times 10^{10}$ $M_\odot$, which is the uncertainty-weighted average of observations compiled in Table 6 of Côté et al. (2016). We also set the radial and vertical scale heights of the stellar potential to match those of the gas for simplicity (see Table 3.1). This potential is included because, though the simulation is not initialized with any star particles, we want to model the gravitational effects that the pre-existing stellar population of a $z \sim 0$ Milky Way-like galaxy would provide. In particular, this potential influences the circular velocity of the disk gas. Star particles are allowed to form as the simulation evolves, effectively allowing the stellar component of the disk to grow from $M_* = 5.8 \times 10^{10}$ $M_\odot$.

Our galaxy and its background potentials are fixed to the center of a (1,638.4 kpc)^3 box with periodic boundary conditions. While periodic boundary conditions are not physically motivated, they are an easy way to ensure the total mass of the box is conserved. Additionally, the width of the box is about 8 times $r_{200} \approx 206$ kpc, ensuring that the periodic conditions will not lead to any unexpected consequences.

The initial construction of the disk and CGM are covered in Sections 3.3.1.1 and 3.3.1.2, respectively. Section 3.3.2 covers the details of our star formation and feedback models. In Section 3.3.3 we discuss our simulations' approach to AMR. Finally, Section 3.3.4 covers the multiple simulation variants we run.

3.3.1 Initial Conditions

The bulk values used to initialize our simulation can be found in Table 3.1. Initial mass-averaged profiles are shown in Figure 3.1. The profiles are split into disk and CGM components at small radii.

Our stellar mass is taken as the uncertainty-weighted average of the observations in Table 6 of Côté et al. (ibid.). We then use the findings of Peeples et al. (2014) to derive the ISM mass and metallicity based on this stellar mass. The disk metallicity is $Z_{\rm ISM} = 2.3\,Z_\odot$, assuming

Table 3.1 Important simulation parameters

Quantity	Name	Value
M_{200}	virial mass	1.0×10^{12} $M_\odot$
$C_{\rm NFW}$	dark matter concetration	10
r_{200}	virial radius	206 kpc
M_*	background stellar mass	5.8×10^{10} $M_\odot$
$M'_{\rm ISM}$	effective initial disk gas mass	7.0×10^9 $M_\odot$
$Z_{\rm ISM}$	initial disk metallicity	2.3 $Z_\odot$
$R_{\rm s}$	disk radial scale height	3.5 kpc
$z_{\rm s}$	disk vertical scale height	0.325 kpc
$M_{\rm CGM}$	initial CGM mass (fiducial)	2.3×10^{10} $M_\odot$
$Z_{\rm CGM}$	initial CGM metallicity	0.3 $Z_\odot$

NOTE. - See text for references and derivations. The actual initial disk mass $M'_{\rm ISM}$ ends up being slightly higher than the value of the parameter used in Equation 3.1, which is $M_{\rm ISM} = 5.0 \times 10^9$. The actual disk mass that results is determined from a temperature cut, as the initial disk is isothermal and distinctly cooler than the surrounding CGM.

$M_{\rm dust} = M_{\rm Z,dust}$. Peeples et al. (2014) suggests $M_{\rm ISM} = 9.8 \times 10^9$ $M_\odot$, but we lower this to 7×10^9 $M_\odot$ to help minimize the initial burst of star formation experienced by the simulation; see Section 3.3.2.1 for more discussion.

The CGM is initialized to a constant uniform metallicity of 0.3 $Z_\odot$. This is the median value from Prochaska et al. (2017). The metallicity of the CGM changes, however, as stellar populations inject supernova feedback and drive outflows (see Section 3.3.2).

3.3.1.1 Gaseous Disk

The gas of the disk follows the softened profile of Tonnesen and Bryan (2009):

$$\rho(R, z) = \frac{M_{\rm ISM}}{8\pi R_{\rm s}^2 z_{\rm s}} \,\mathrm{sech}\left(\frac{R}{R_{\rm s}}\right) \mathrm{sech}\left(\frac{z}{z_{\rm s}}\right), \tag{3.1}$$

where R is the cylindrical radius, and $R_{\rm s} = 3.5$ kpc and $z_{\rm s} = 0.325$ kpc are the scale heights of the gas. For $R > 24$ kpc, Equation 3.1 is multiplied by a smoothing factor of

$$0.5 \left[1 + \cos\left(\pi \frac{R - 24 \text{ kpc}}{7.2 \text{ kpc}}\right)\right] \tag{3.2}$$

that tapers the radial edges of the disk. The disk gas is given a circular velocity prescribed by the combination of our NFW and stellar potentials, with $v_\phi = \sqrt{R \cdot g(r, R, z)}$.

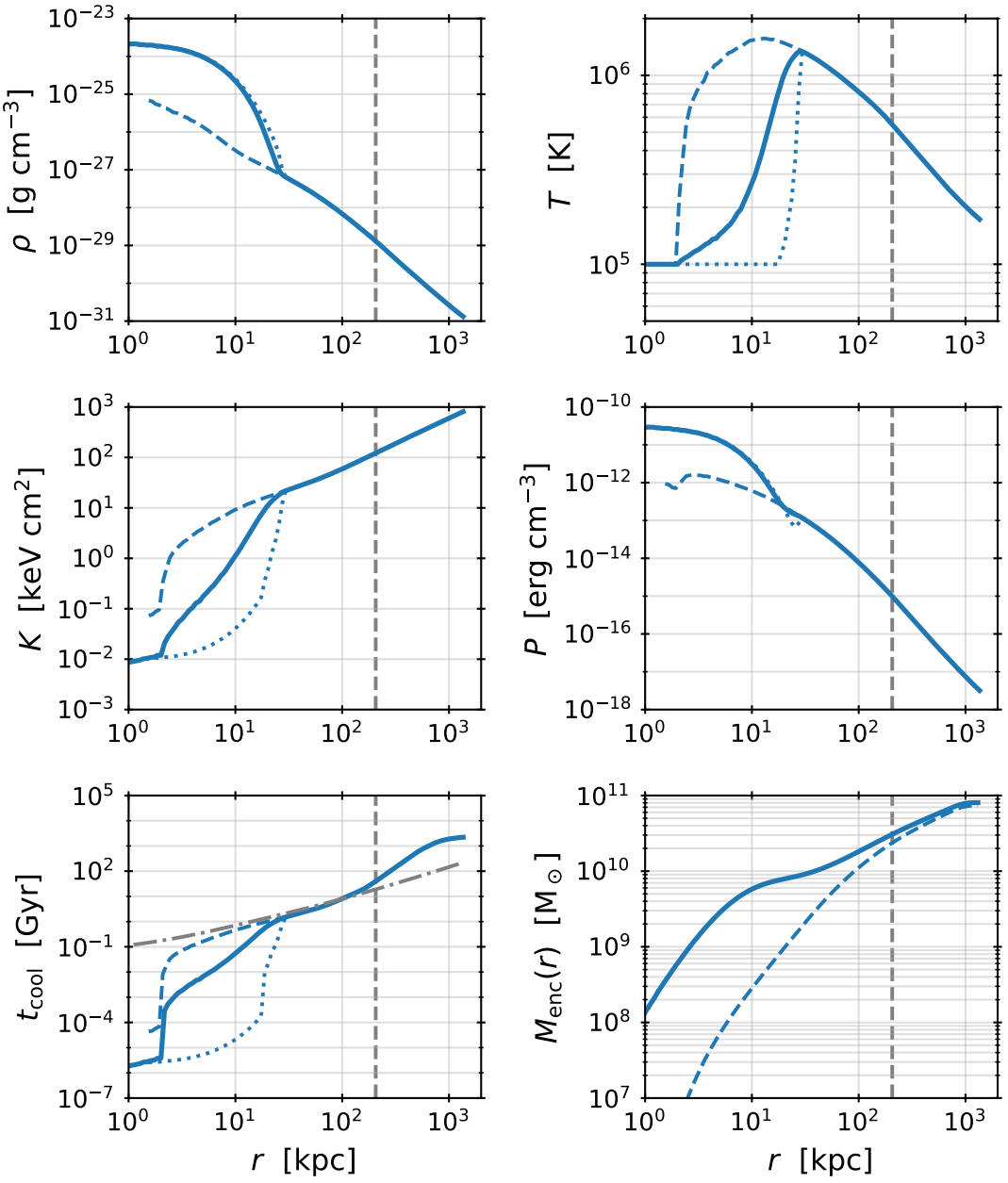

Figure 3.1 In rows from top left, as a function of radius: initial mass-weighted average density, temperature, entropy, pressure, and cooling time, and total enclosed mass. The independent contributions of the disk (dotted) and inner CGM (dashed) are shown for small radii, except for the enclosed mass. For the enclosed mass, the entire CGM is shown as a dashed line. Though the smallest cell size in the simulation is 100 pc, the x-axis does not extend this far because of the low number of cells. The vertical dashed line marks $r_{200} \approx 206$ kpc. The gray dot-dashed line shows where $t_{\rm cool}/t_{\rm ff} = 10$.

The disk is set to an initial uniform temperature of 10^5 K. In reality, galaxy disks are usually at 10^4 K or below, but gas cools very efficiently around 10^5 K. Our disk is initialized at this higher temperature so that gas would be well above our temperature threshold for star formation (3×10^3 K; see Section 3.3.2) but also rapidly cool. The variation in disk density means that the temperature does not uniformly, which helps spread out the initial burst of star formation across time.

The initial conditions for the disk and CGM are blended together based on density; if $\rho_{\rm disk}(r) > \rho_{\rm CGM}(r)$ in a cell, that cell is considered part of the disk. Otherwise, it is initialized to be part of the CGM.

3.3.1.2 Circumgalactic Medium

The density and temperature structure of the CGM is set following Voit (2019), who describes an entropy profile that precipitation-regulated galaxies in NFW halos would follow under the assumption of hydrostatic equilibrium. This assumption is reasonable for a $M_{200} = 10^{12}$ $M_\odot$ halo (Oppenheimer 2018; Lochhaas et al. 2020). The profile therein assumes the median $t_{\rm c}/t_{\rm ff} = 10$, but we make $\tau \equiv t_{\rm c}/t_{\rm ff}$ a free parameter in our model of the entropy profile, so that

$$K(r) = (39\ \text{keV cm}^2)v_{200}^2\left(\frac{r}{r_{200}}\right)^{1.1} + (2\mu m_p)^{1/3}\left[\frac{2n_i\tau}{3n}r\Lambda\left(2T_\phi(r), Z_{\rm CGM}\right)\right]^{2/3}, \tag{3.3}$$

for entropy quantified in terms of $K \equiv kTn_e^{-2/3}$. This way we can test halos that deviate from the apparent precipitation limit of $\tau \approx 10$. We assume $n_e = n_i$ such that $2n_i/n = 1$. The initial metallicity is $Z_{\rm CGM} = 0.3$. The term Λ is the cooling rate as a function of of temperature and metallicity, which we calculate with the Grackle chemistry and cooling library (Smith et al. 2017). The term $T_\phi(r)$ is the gravitational temperature $kT_\phi(r) = \mu m_p v_{\rm c}^2(r)/2$.

To calculate the initial density and temperature profiles of the CGM, we combine Equation 3.3 with $\mathrm{d}P/\mathrm{d}r$ from hydrostatic equilibrium. We adopt the boundary condition $kT(r_{200}) = 0.25\mu m_p v_{c,\rm max}^2$ suggested by Voit (2019). Beyond r_{200}, the temperature begins to plummet dramatically. To mitigate this, we abandon a functional form for the entropy and instead fix $\mathrm{d}\log_{10}P/\mathrm{d}\log_{10}r$ to its value just inside r_{200}. We then set the temperature with a sigmoid function

that smoothly blends $T(r_{200})$ with a floor of 4×10^4 K. The resulting mass-weighted profiles for the initial density, temperature, entropy, pressure, cooling time, and enclosed mass are shown in Figure 3.1. For $\tau = 10$, the actual cooling time deviates slightly from the target value, falling between 7–10$t_{\rm ff}$ within $\sim 0.5 r_{200}$ and rises to $\sim 20 t_{\rm ff}$ at the virial radius.

For simplicity, we use a modified NFW profile to calculate the circular velocity $v_{\rm c}$ used in Equation 3.3. This modification approximates the presence of a galactic disk at the center of the potential well: $v_{\rm c}^2(r) = v_{\rm c,max}^2$ for $r \leq 2.163 r_s$, where r_s is the scale radius of the NFW profile, and

$$v_{\rm c}^2(r) = v_{\rm c,max}^2 \cdot 4.625 \left[\frac{\ln(1 + r/r_s)}{r/r_s} - \frac{1}{1 + r/r_s} \right] \tag{3.4}$$

otherwise. Using this modified NFW profile to represent the inner contents of the halo is slightly incongruous with the construction of our gas disk and static stellar potential; however, the modified NFW profile is spherically symmetric, making it easier to calculate the CGM's density and temperature profiles. This modified NFW profile is only used to set up the initial CGM conditions, while the unmodified NFW potential, the Miyamoto and Nagai (1975) stellar potential, and the gaseous disk's own gravity are what are actually applied to the simulation during execution. Any incongruities introduced into the initial hydrostatic equilibrium through our use of two slightly differing potentials will quickly fade as the simulation evolves.

We give the CGM an initial azimuthal velocity, the strength of which is determined by

$$v_\phi(r, \theta) = v_0 \sin^2 \theta \left(\frac{r}{r_0} \right)^\beta . \tag{3.5}$$

Here, r is the spherical radius and θ is the polar angle. This function replaces the disk's Keplerian velocity profile wherever the CGM density dominates, as described above. We do not consider Equation 3.5 when placing the CGM in hydrostatic equilibrium, meaning the CGM may be slightly oversupported against gravity in the cylindrically radial direction. We use Hodges-Kluck, Miller, and Bregman (2016) to choose $v_0 = 180$ km/s and $r_0 = 10$ kpc, which is roughly the radius where their halo model's specific angular momentum matches that of the disk (see their Figure 5). It should be noted that Hodges-Kluck, Miller, and Bregman (ibid.) adopt a constant v_ϕ with their

model, which they assume is reasonable within $\sim$ 50 kpc. We leave β as a free parameter; for our fiducial simulation, $\beta = -1/2$ (see Table 3.2).

3.3.2 Star Formation & Feedback

Our star formation and feedback algorithms are modified from the implementation of Cen and Ostriker (1992) as described in Section 2.1 of Oh et al. (2020). We require that gas in a grid cell have

1. $\boldsymbol{\nabla} \cdot v < 0$
2. either $t_{\rm cool} \leq t_{\rm dyn}$ or $T < 3 \times 10^3$ K
3. $n \geq 10$ particles/cm^{-3}
4. $m_* \equiv f_* m_{\rm cell} \frac{\Delta t}{t_{\rm dyn}} > 10^4$ M$_\odot$

where the local gas dynamical time is $t_{\rm dyn} = \sqrt{3\pi/(32G\rho)}$. If all these criteria are met, a "star particle" is created representing a population of individual stars with total mass m_*. An equivalent amount of gas is also removed from the host cell, and the particle is given a velocity such that momentum is conserved. The minimum stellar mass of 10^4 M$_\odot$ is chosen as a balance between resolving the star formation with more particles and the computational expense of tracking and managing these particles. As in Smith et al. (2011), we ignore the Jeans instability criterion as it is always met by the star forming gas in our simulations. We set $f_* = 0.2$ and impose a minimum dynamical time of one million years.

Stellar feedback proceeds as described in Section 2.2 of Oh et al. (2020) and is the same algorithm as used in Peeples et al. (2019). Though a star particle is formed immediately, for the sake of stellar feedback, the accumulation of stellar mass is assumed to be a drawn-out process that peaks in efficiency after one dynamical time (Oh et al. 2020, Equation 3). The amount of mass, momentum, and energy that are returned in timestep Δt is then tied to this extended star formation model through the mass of stars $\delta M_{\rm SF}$ that would form in that timestep; e.g.

$$\Delta E = \epsilon_{\rm FB} \cdot c^2 \delta M_{\rm SF} \tag{3.6}$$

We adopt the same efficiencies as Oh et al. (2020) for the returned fraction of total and metal masses. Energy, momentum, mass, and metals are then deposited into the cube of 27 cells centered on the star particle's host cell.

It should be noted that there are no star particles present in the simulation initial conditions. This means that there are no pre-existing stellar populations affecting the gas in the earliest moments of the simulation. This artificiality has interesting consequences that are discussed in the following subsection.

3.3.2.1 Ramping Stellar Feedback Efficiency

One of the consequences of idealized, isolated galaxy simulations like ours is the behavior of the cold gas disk at early times. The dense gas of the idealized disk is rotationally supported in the radial direction, but does not have sufficient support against gravity in the vertical direction. It therefore immediately starts to compress as the simulation begins to evolve, allowing stars to form in a large volume of the disk as the density rises. This leads to a large burst of star formation and feedback at very early times, which disrupts the CGM before it can cool significantly. This means the CGM has no time in which to influence the disk through accretion. Moreoever, feedback raises cooling times and evacuates the gas above and below the disk by successive supernova-driven shocks, preventing the CGM from interacting with the disk on a reasonable timescale. The previous isolated galaxy simulations listed in Section 3.2 did not have this problem because they either lacked a significant CGM or did not explicitly model the star-forming disk.

Galaxies in the real universe, as well as in cosmological simulations, are slowly built up over time. They do not "begin" as a $\sim 7 \times 10^9$ $M_\odot$ disk of cold, dense gas. This assembly history means there have been successive generations of both stars and stellar feedback. Real galaxies will have effects such as stellar velocity dispersions and ISM turbulence that support against vertical collapse. Additionally, the CGM's dynamical and thermodynamic structure will be impacted by the accretion of matter over time and by historical outflows.

In spite of its artificiality, the value of an idealized galaxy system is that it provides a controlled environment in which to explore the interactions of the CGM and star formation. Ideally the

modelled system can quickly "relax" into a state where the oversimplification of the initial conditions has been erased. We could minimize the collapse of the disk by adding, for instance, an initial stellar distribution (so that feedback is active at the very start of the simulation to limit the burst of star formation) or a 3D velocity dispersion; however, both of these require multiple further parameter choices to specify their distributions.

Instead, we choose to modulate the *efficiency* of stellar feedback, $\epsilon_{\rm FB}$ (Equation 3.6). This dimensionless parameter is linearly increased between $t = 1$ Gyr and $t = 2$ Gyr from $\epsilon_{\rm FB} = 5 \times 10^{-8}$ to 5×10^{-6}. Our final $\epsilon_{\rm FB}$ is 0.5 dex lower than both the cosmological simulations of (Oh et al. 2020) and FOGGIE (Peeples et al. 2019). The efficiency ramp begins at 1 Gyr of simulation time in order to give CGM gas with $t_{\rm cool} \lesssim 1$ Gyr time to interact with the disk before being disrupted by feedback.

3.3.3 Resolution

Enzo uses block-structured Cartesian Adaptive Mesh Refinement (AMR; Berger and Colella 1989) to control the resolution of its grid cells. The base grid of our simulation is 128^3 cells (12.8 kpc per cell side) and the resolution of a region is refined by a factor of two if the cell exceeds a mass threshold of 2.67×10^5 $M_\odot \times 2^{(-0.5l)}$, where l is the zero-based level index. The mass threshold for refinement therefore decreases with level in a super-Lagrangian way, preventing excessive refinement on the lowest levels which would increase computational cost. The highest levels are concentrated in the galactic disk, which, while not the focus of this study, is important to resolve for the purposes of star formation.

Given the low density of the CGM, a mass-based refinement criterion is not enough for the CGM gas to become well-resolved. The importance of good CGM resolution has been demonstrated by Hummels et al. (2019), Peeples et al. (2019), Suresh et al. (2019), and van de Voort et al. (2019). Smaller clouds are allowed to develop with higher CGM resolution, and turbulent structures are resolved to smaller scales. We therefore also define six nested rectangular regions of fixed minimum resolution (the first four of which are cubic). Cells within these regions are allowed to refine further based on mass. An example of this is shown in Figure 3.2. We allow up to seven levels of refinement

Table 3.2 Our set of simulations and their varied parameters

Name	FB	t_c/t_{ff}	β
Fiducial	Y	10	-1/2
CoolFlow	**N**	10	-1/2
LowRatio	Y	**5**	-1/2
HighRatio	Y	**20**	-1/2
LinRot	Y	10	**-1**
NoRot	Y	10	**N/A**

NOTE. - Variations from the fiducial model are highlighted in bold. The parameter β refers to the power law index of the initial azimuthal rotation profile.

(a minimum spatial resolution of 100 pc).

3.3.4 Simulation Variants

The goal of our simulations is not only to test if we can create a (precipitating) self-regulating system, but also to explore the robustness of self-regulation. To that end, we explore five variations on our fiducial simulation, as laid out in Table 3.2. The first variation, CoolFlow, is identical to the fiducial run in its initial conditions but has stellar feedback completely disabled (star formation is still allowed in order to remove cold gas and preserve numerical stability). In this way, it functions as a control to demonstrate the importance of feedback.

The next two variants, LowRatio and HighRatio, modify the precipitation limit parameter τ in Equation 3.3. Their values of τ are chosen to be the approximate lower and upper bounds experienced, on average, by a precipitating system (Voit et al. 2017; Voit 2018, 2021). We note that, because the CGM's radial density profile is defined by the initial τ through Equation 3.3, these variants start with CGM masses different by about a factor of 2. Compared to the fiducial CGM mass given in Table 3.1, the HighRatio variant starts with 1.3×10^{10} $M_\odot$ of CGM gas and the LowRatio with 3.9×10^{10} $M_\odot$.

Though the CGM of galaxies likely rotates (Hodges-Kluck, Miller, and Bregman 2016; DeFelippis et al. 2020), the shape of its rotation profile is not well-constrained. The LinRot variation modifies the initial rotation profile of the CGM, changing the index β in Equation 3.5, while NoRot

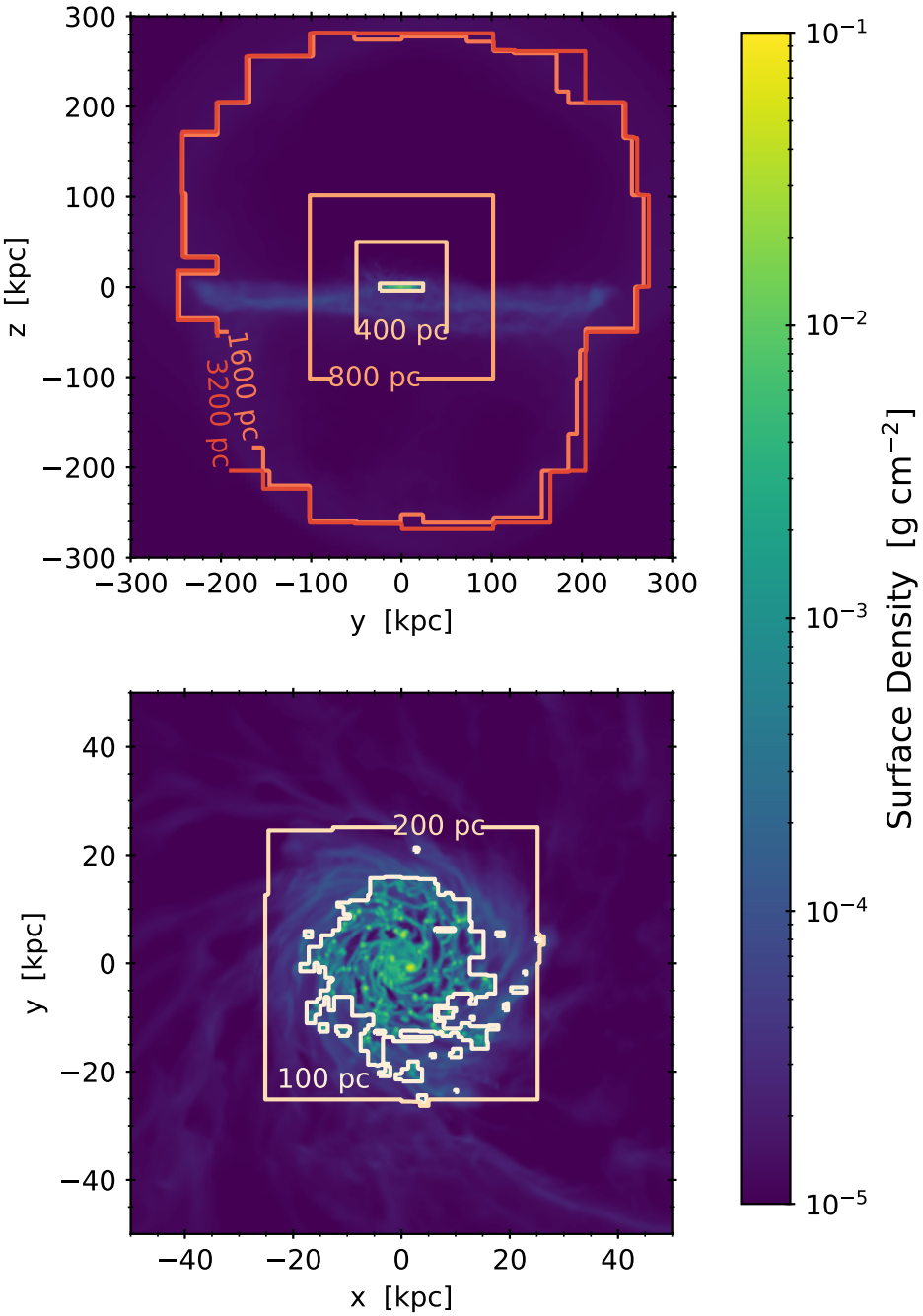

Figure 3.2 Demonstration of our AMR scheme with edge-on (top) and zoomed face-on (bottom) density projections at t = 3 Gyr. Orange contours enclose regions of uniform resolution at the center of the projection. Our refinement scheme defines nested boxes that must be at a fixed minimum resolution, but cells are allowed to refine beyond this minimum if they exceed a mass threshold. This behavior can be seen with the 3,200, 1,600, and 200 pc contours. The 100 pc contour is based exclusively on mass refinement and is the highest resolution allowed.

Table 3.3 Mean and standard deviation of the maximum star formation radius

Variant	Mean (kpc)	Std Dev (kpc)
CoolFlow	15.4	2.1
LowRatio	11.7	4.2
LinRot	10.4	3.7
NoRot	10.4	5.1
Fid	9.0	3.9
HighRatio	8.1	3.7

NOTE. - Statistics cover 2–4 Gyr of simulation time, in kpc. The maximum SF radius is defined as the largest cylindrical radius at which a star formed in the last 50 Myr (which is the time between simulation outputs).

is a control for the impact of CGM rotation on the evolution of the system. This latter variant has no initial rotation in the CGM, but still maintains Keplerian rotation in the disk.

3.4 The Galactic Disk

We start by looking at the gas content of the galactic disk and its star formation. In later sections, we will look in detail at the exchange of gas between the disk and CGM, but the effects of CGM accretion are readily apparent within the disk.

3.4.1 Appearance

Figure 3.3 compares the disks of our simulation variants at a simulation time of 3 Gyr. We show the density, temperature, and radial velocity within a slice through the disk midplane. The solid white circles represent the average radius within which stars form, which is determined as follows: for each simulation snapshot (Δt = 50 Myr), we determine the maximum cylindrical radius of star particles formed since the last snapshot. The average of these maxima over t = 2–4 Gyr give the white circles in Figure 3.3. The numerical values of these radii, as well as their standard deviations over time, are reported in Table 3.3. The dotted circles show the edge of each variant's initial gas disk. Due to differences in initial CGM structure and the way the disk and CGM are blended together (see Section 3.3.1.2), the LowRatio and HighRatio simulations have slightly different initial radii than the other variants, but all are around 28 kpc.

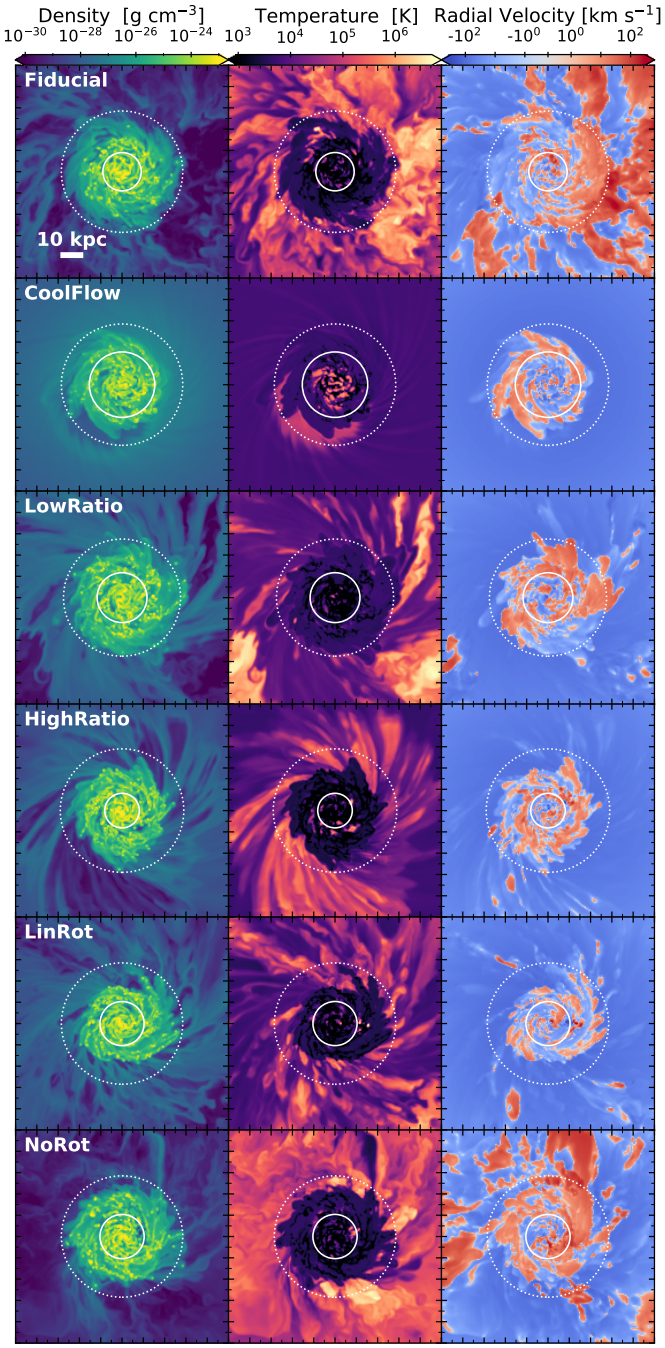

Figure 3.3 Slices of density, temperature, and radial velocity through the disk midplane in each simulation variant at 3 Gyr. Cells are 100 pc thick in the center of the galaxy, 200 pc thick out to ±25 kpc, and 400 pc thick out to the edge of the field of view at ±50 kpc from the center. Solid white circles show the average radius within which stars form over 2–4 Gyr. Dotted white circles mark the extent of the initial gas disk (∼ 28 kpc). Note that the colormap for radial velocity covers $\pm 3 \times 10^3$ km/s.

From these slices we see that the gas in the disk is around 10^4 K on average, reaching 10^3 K and lower in the densest spiral arms and near the center. Star formation is most prevalent in the very center of the disk. There are hotspots of $\sim 10^5$ K gas within the star-forming center of each variant's disk that are the result of feedback. The exception is the CoolFlow simulation, which has more prominent hotspots but no feedback. For this variant, the gas heating is due to a "pile-up" of accreting gas. This pile-up will be discussed further in Section 3.5.1.

The radial velocity slices show us that the hottest gas at $T \sim 10^6$ K is not strictly outflowing. Clear examples of this can be seen in the right side of the fiducial slices, in the bottom corner of the LowRatio images, and throughout the NoRot slices. The fiducial simulation, in particular, shows evidence of a radial velocity gradiant across a hot, low density cloud. This, along with the highly variable gas temperature outside the galactic disk, suggests that hot gas is mixing with cooler gas in the disk midplane. The prevalence of radial inflow in hot gas also suggests that gas is cooling as it moves towards the disk. Though highlighted in Figure 3.3 by LowRatio and NoRot, cooling inflow is present for $t > 2$ Gyr in all variations.

The size of the disk's star forming region appears impacted by the CGM's $t_{\rm cool}/t_{\rm ff}$ properties, as seen from the solid white circles in Figure 3.3 and the values in Table 3.3. For both of these, we use the average maximum radius within which stars form as a measure of the star forming region. The LowRatio variant has an SF region that is statistically larger than the fiducial and the HighRatio variants (adopting $\alpha = 0.05$ or a 95% confidence interval), though we note that the fiducial's region is not signficantly larger than HighRatio's. This suggests a small dependence on the simulation's initial $t_{\rm cool}/t_{\rm ff}$ ratio. Moreover, the fiducial, LinRot, and NoRot simulations are statistically indistinguishable when tested against each other.[2] These simulations all have the same initial $t_{\rm cool}/t_{\rm ff}$ ratio. The CoolFlow simulation has a star forming region that is statistically significantly larger than all the other simulation variants, but this follows from its lack of feedback and aggressive star formation rather than a difference in its CGM.

[2]A slight difference between the fiducial, LinRot, and NoRot simulations appears when testing each of these simulations against other variants. While the LowRatio simulation has a statistically larger star forming region than the fiducial, it fails to test as significantly larger than the LinRot and NoRot simulations. Additionally, while the fiducial simulation does not test as significantly larger than the HighRatio simulation, the LinRot and NoRot variants do.

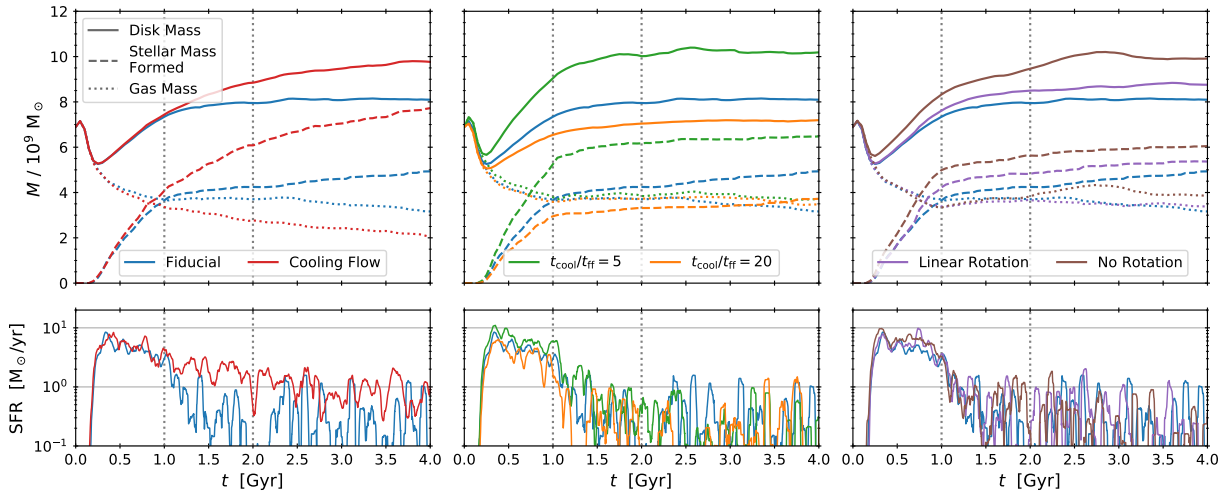

Figure 3.4 Disk mass (top) and SFR (bottom) as a function of simulation time. Disk mass (solid) is broken into gas (dotted) and stellar (dashed) components. The stellar mass reflects the cumulative mass of stars formed and neglects stellar mass loss. To improve clarity, the SFR is shown as the rolling mean with a 60 Myr rectangular window. The region between the two dotted grey lines is when the stellar feedback efficiency is ramped (Section 3.3.2.1). From left to right, the Fiducial model (blue) is compared with CoolFlow, LowRatio and HighRatio, and LinRot and NoRot. Compared to the CoolFlow variant, the mass growth in each component remains fairly stable after the onset of feedback at 1 Gyr. The final stellar mass varies for each variant, along with the early-time ($t < 1$ Gyr) SFR and gas consumption.

3.4.2 Mass Growth

Figure 3.4 shows the disk mass and star formation rate over the full simulation time (4 Gyr) for each variant. The disk mass is split into gaseous and stellar components. The disk gas is defined by a cylindrical region with $R \approx 5.7R_s = 20$ kpc and thickness $8z_s = 2.6$ kpc. This cutoff in cylindrical radius is somewhat arbitrary, but corresponds roughly to a transition point in the profiles of density and temperature that is visible from 2–4 Gyr. The disk's stellar mass is defined as the total mass of all stars formed, and neglects stellar mass loss. Including stellar mass loss lowers the stellar masses at $t > 1$ Gyr by $\sim 1.5 \times 10^9$ $M_\odot$. The accompanying SFR has been smoothed using a trailing moving average over a $\sigma = 60$ Myr rectangular window. Vertical dotted lines denote the beginning and end of the feedback efficiency ramp laid out in Section 3.3.2.1. The fiducial simulation is recreated in all three panels.

In the leftmost panel, the fiducial simulation is compared to the CoolFlow run. For the fiducial

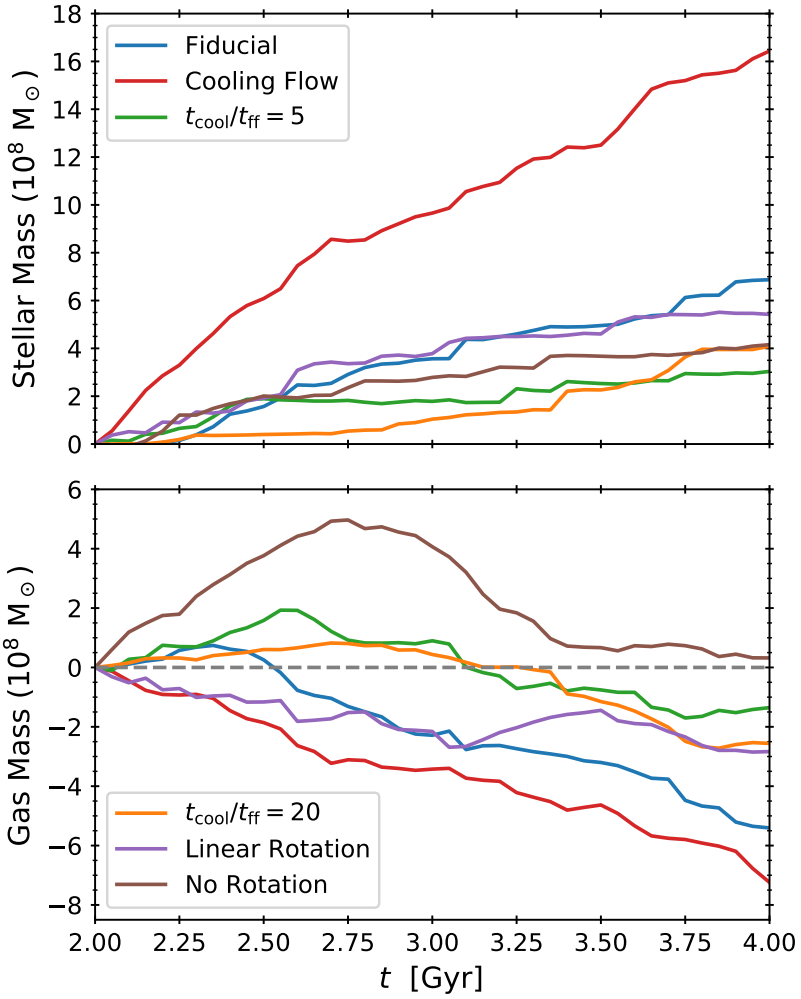

Figure 3.5 Mass of the stellar (top) and gaseous (bottom) disk components relative to t = 2 Gyr. The legend is split between both panels. The stellar mass grows similarly among the non-CoolFlow runs, but the gas mass varies widely.

model, the growth in stellar mass slows past 1 Gyr, when the stellar feedback efficiency begins to ramp. In the CoolFlow model, however, the stellar mass continues to grow significantly as the simulation progresses, depleting the disk's gas mass more appreciably than in the fiducial variant. The SFR is also generally higher in the CoolFlow simulation. This behavior is expected as the CoolFlow model has stellar feedback disabled. This also indicates the flattening of the fiducial model's stellar growth is due to feedback, which is confirmation of an expected result.

In the middle panel, variations in the initial $t_{\rm cool}/t_{\rm ff}$ ratio are explored by comparing the fiducial simulation to the LowRatio and HighRatio runs. The rightmost panel explores the rotation variants LinRot and NoRot. All of the variants with stellar feedback demonstrate remarkably similar gas mass curves. Stellar growth and gas mass loss flatten out around 1 Gyr, when the feedback efficiency begins to increase. The variants are primarily distinguished by the total amount of stellar mass they form, with the largest difference observed between the $t_{\rm cool}/t_{\rm ff}$ variants.

For the first $\sim$ 0.7 Gyr, the fiducial and LinRot simulations have the same stellar mass curves. This is also true for the fiducial and CoolFlow simulations before $\sim$ 0.5 Gyr. Since these simulations all start with an identical initial disk, deviations in stellar mass can be attributed to gas accretion from the CGM. The NoRot variant has little apparent overlap in stellar mass growth with the fiducial simulation, indicating an earlier deviation in the amount of CGM accretion. We attribute NoRot's early differentiation to the lack of CGM angular momentum, which should make it easier for gas to settle onto the disk and form stars. The LowRatio and HighRatio simulations start with slightly smaller/larger initial disk radii, respectively, due to how the disk and CGM are blended (Section 3.3.1.1). This has a negligible effect on their disk mass, while their CGM masses deviate from the fiducial by about a factor of two with LowRatio being the most massive. Given that the LowRatio simulation goes on to form the most stars (of the variants with feedback), this is further evidence that CGM accretion is a major contributor to stellar growth.

The fiducial model and all other variants with $\tau = 10$ start with about 8×10^8 $M_\odot$ of CGM gas with $t_{\rm cool} \leq 1$ Gyr, which is the timescale on which stellar feedback is kept inefficient. The LowRatio variant has $\sim 4 \times 10^9$ $M_\odot$ of this short-cooling time gas ($\sim$ 5 times greater than the

fiducial), and forms the most stars before 1 Gyr. On the other hand, the HighRatio variant forms the fewest stars by 1 Gyr, and its CGM only has $\sim 1 \times 10^8$ $M_\odot$ of gas with $t_{\rm cool} \leq 1$ Gyr (a factor of 8 lower than the fiducial). These differences support the interpretation that star formation within the first gigayear is fueled not only by disk mass, but also by the accretion of gas from the CGM. Additionally, there is evidence for continued CGM inflow as the gas mass continues to increase past 1 Gyr. The inflow of gas will be discussed more in Section 3.5.2.

Though each variant experiences a different amount of star formation, particularly at early times, their gas masses remain both relatively constant and similar across variants. Additionally, the smoothed star formation rates are also quite consistent once stellar feedback reaches its full strength at $t = 2$ Gyr. We attribute the constancy of the disk mass among simulation variants to the Toomre criterion (Toomre 1964). A mass of $\sim 4 \times 10^9$ $M_\odot$ appears to be the value at which the disk is marginally stable against gravitational instability. As gas is added to an isothermal disk, the disk gas is able to fragment and form stars until the surface density falls back below the threshold for instability. This effect can also explain why the LowRatio variant experiences more star formation from 1–2 Gyr while maintaining a fairy stable gas mass in the disk. The role of the Toomre instability will be discussed more in Section 3.7.3.

In Figure 3.5 we focus on the late time ($t \geq 2$ Gyr) stellar and gas masses. These quantities are shown relative to each simulation's gas and stellar masses at $t = 2$ Gyr. Once again, stellar mass loss is ignored in order to show the integrated star formation. Including stellar mass loss drops the final stellar mass increase by $\sim 1 \times 10^8$ $M_\odot$ for the simulations with feedback and $\sim 4 \times 10^8$ $M_\odot$ for the CoolFlow variant.

The most dramatic stellar mass increase can again be seen in the CoolFlow simulation, while the variants with feedback experience more gradual increases in their stellar masses. The fiducial and LinRot simulations grow at a similar rate, while the LowRatio and NoRot variants "taper off" in their stellar mass increase after 2.5 Gyr. The HighRatio variant appears to be a "late bloomer," with stellar mass increases smaller than the other variants with feedback until around 3.6 Gyr. All of the variants with feedback form between 3–7 $\times 10^8$ $M_\odot$ more stars after $t = 2$ Gyr.

These final increases in stellar mass are partially compensated by overall decreases in gas mass, which, ignoring the NoRot and CoolFlow variants, are between 1.5 and 5.5×10^8 $M_\odot$ at $t = 4$ Gyr. Each simulation variant, however, took a very different path to reach this point. Except for the LinRot and CoolFlow simulations, most variants see an increase in their disk's gas mass at some point before ~ 2.3 Gyr. The NoRot simulation sees the largest increase in disk gas mass, and is the only simulation to end with more gas at $t = 4$ Gyr than it had at $t = 2$ Gyr. Despite this, it is not the variant with the largest increase in stellar mass. The differences in disk gas mass between the variants highlight that the story of accretion is complex. We will explore it more in Section 3.5.2.

3.5 Outflows and Inflows

Feedback processes in the disk are able to drive large-scale galactic outflows. In our simulations, these "feedback processes" are limited to Type II supernovae. Indeed, self-regulation requires that inflowing gas must balance gas loss through outflows and star formation. Given that our idealized models ignore galaxy mergers, gas filaments, and other cosmological processes, their evolution is a story of inflowing and outflowing CGM gas. Therefore, in this section we examine the exchange of gas between the CGM and the disk as our simulations evolve.

3.5.1 System Dynamics

Figure 3.6 shows the evolution of the fiducial simulation in four thermodynamic quantities—density, temperature, entropy, and pressure—and radial velocity. Average values along the line of sight are shown at four times (in gigayear intervals) using an edge-on thin slab. These slabs are two radial scale heights ($2R_s = 7$ kpc) thick and 600 kpc square on their sides, centered on the disk. By averaging through a thin subdomain, we can show a more representative visualization of the domain (as compared to a slice) while not oversmoothing turbulent gas structures. The white circle denotes r_{200}. The ramp in stellar feedback efficiency, as described in Section 3.3.2.1, occurs from 1–2 Gyr.

At 1 Gyr, the initial burst of star formation begins to subside as the feedback efficiency starts to increase. The initial disk has collapsed as described in Section 3.3.2.1, pushing out gas in the

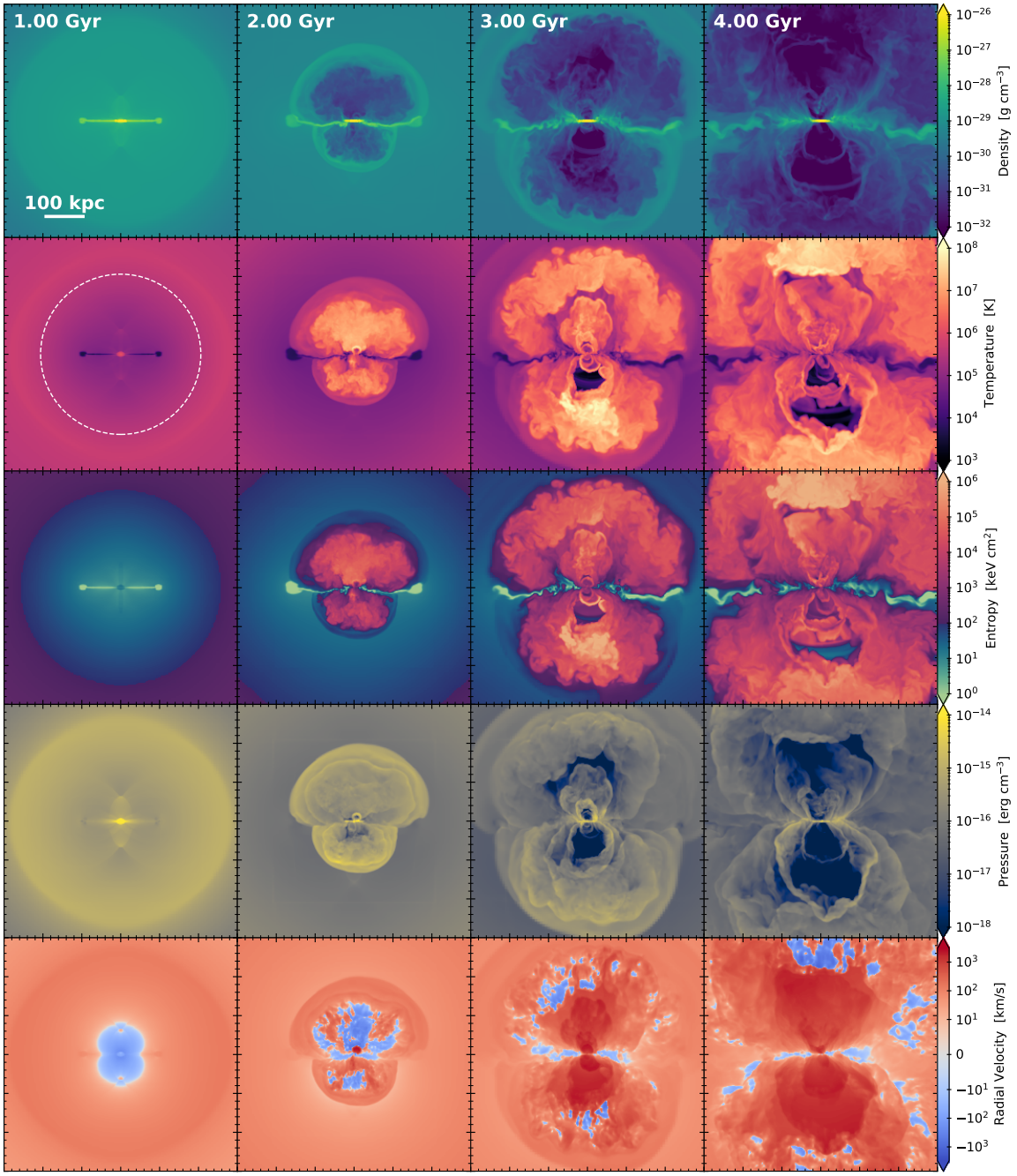

Figure 3.6 Average line-of-sight density, temperature, entropy, pressure, and radial velocity of the fiducial run at four different times. Averages are taken from a thin slab two radial scale heights $2R_s = 7$ kpc thick and 600 kpc square centered on the disk, which is shown edge-on. The white circle shows $r_{200} \approx 206$ kpc. The entropy color bar separates gas with $K > 10^2$ keV cm^2 in pink, which should not cool within a few Gyr. The efficiency of stellar feedback is ramped between 1 and 2 Gyr (Section 3.3.2.1).

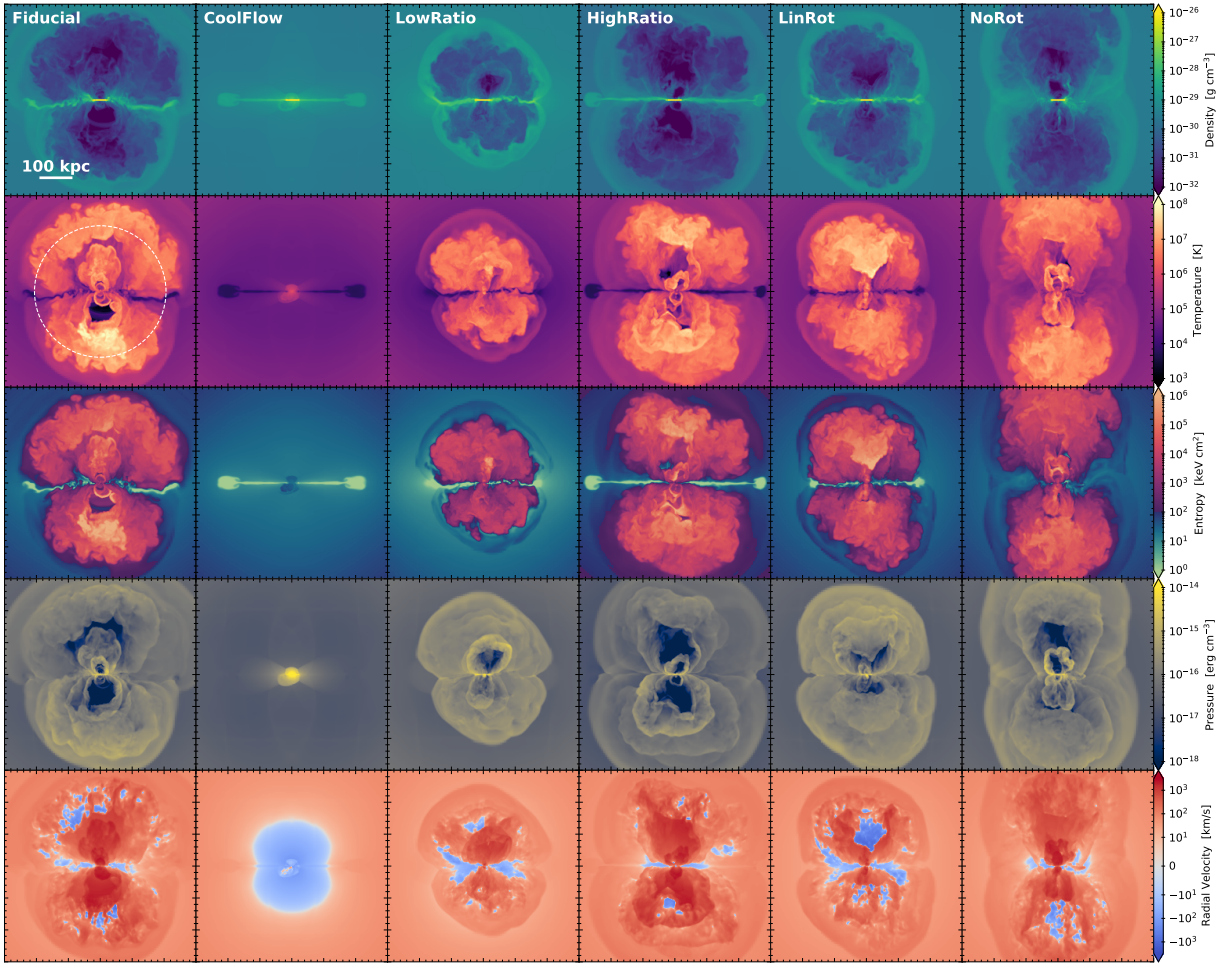

Figure 3.7 Same as Figure 3.6 but for each simulation variant at 3 Gyr. The leftmost column is reproduced from Figure 3.6.

radial direction. Sound waves were driven by the disk's initial collapse, including a spherical wave that has propagated beyond the virial radius at 1 Gyr. Its propagation has resulted in a positive radial velocity throughout the domain. Gas behind this wave has cooled from its initial temperature profile and started falling inward. Net inward flow can be seen in blue in the bottom row of Figure 3.6 and is approximately 50 kpc in radius at $t = 1$ Gyr. Further evidence of sound waves can be seen faintly in the pressure above and below the disk. These intersecting wave patterns will eventually be wiped away by stellar feedback, which we can see starting to happen at 2 Gyr.

At $t = 2$ Gyr we see outflows have disrupted the inflowing gas above and below the disk. Some gas inside these outflows has started falling back towards the galaxy. By 3 Gyr, these outflows have expanded past the virial radius. Gas near the edge of older outflows still exhibits some inward radial motion, but is disrupted by younger outflows. The interior of these recent outflows has very low densities and pressures; lower than at 2 Gyr. At both $t = 2$ and 3 Gyr, cold dense gas is feeding the disk along its midplane.

By 4 Gyr, we can see that the history of successive feedback-driven outflows has created a complex shock structure within 100–200 kpc directly above and below the disk. Visible at the very top of the projection is an inflowing front with high temperature and entropy, but very low density ($< 10^{-32}$ g/cm^3). Indeed, there is very little gas above and below the disk. Meanwhile, accreting material continues to flow inward along the midplane. There is gas infall at large radii that is outside the disk midplane, but this is prevented from reaching the disk by younger outflows.

In Figure 3.7, we compare the fiducial simulation at 3 Gyr to each of the variants, still using the line-of-sight average through a thin slab. With no feedback to disrupt its CGM, the CoolFlow variant has a rough sphere of inflowing gas around its disk. The high pressure region at the disk's center steadily grows in radius from the continually infalling gas. This increase in pressure also drives an increase in temperature.

All other variants have outflow "plumes" that vary in size and shape. The NoRot variant has a taller, narrower outflow envelope than the fiducial and LinRot models, indicating that rotation in the CGM may be important for distributing outflowing material such as metals evenly through

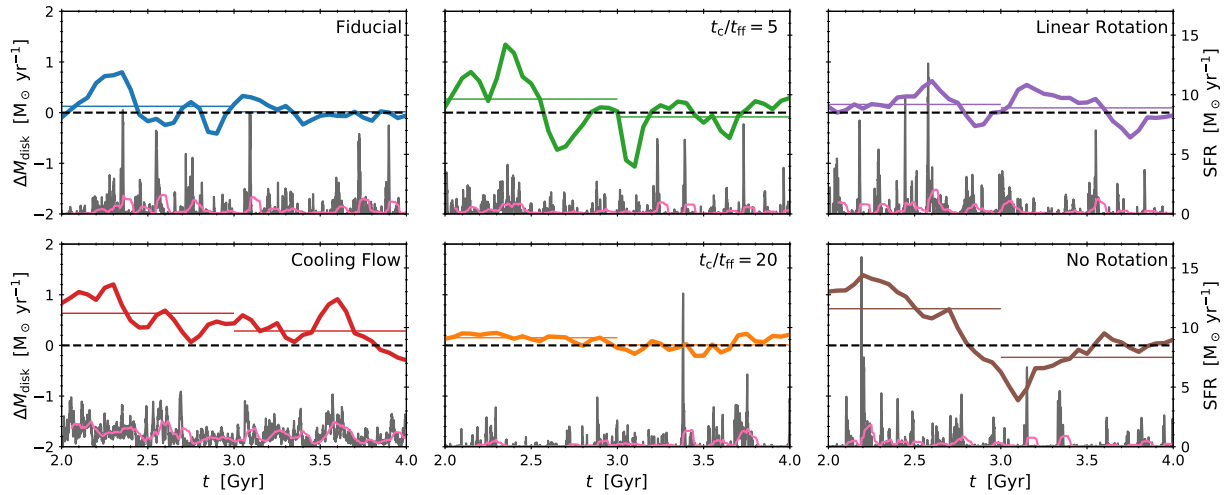

Figure 3.8 Net rate of change in disk mass $\dot{M}_{\rm disk}$ (left axis; thick lines) compared to the star formation rate (right axis; gray and pink). The rate of disk mass change is calculated as $\dot{M}_{\rm disk} = \dot{M}_* + \dot{M}_{\rm gas}$. The dashed horizontal line marks the zero-point for this quantity. Note that all displayed quantities are sampled at different cadences: $\Delta t = 50$ Myr for the $\dot{M}_{\rm disk}$ and $\Delta t = 0.6$ Myr for the gray SFR. The 60 Myr moving-averaged SFR from Figure 3.4 is shown in pink for comparison, and the horizontal lines indicate average net $\dot{M}_{\rm disk}$ over 1 Gyr.

the CGM. Visible in the LinRot model is another high-entropy, low-density front of gas falling back towards the disk. These features develop in many of the simulations, but are prevented from reaching the disk by futher feedback.

Clearly visible in the CoolFlow variant, but present in all simulations except NoRot, is the remnant of the initial disk's radial spread due to vertical collapse (Section 3.3.2.1). This gas is very low entropy, and though not shown, has metallicity associated with the initial disk. This initial disk spreads out the least for the NoRot simulation (reaching about half as far as the fiducial simulation at $t = 2$ Gyr), indicating the initial expansion of the disk is encouraged by the CGM's own angular momentum. For NoRot, this smaller spreading feature is easily disrupted by feedback, which is why this feature is not as prominent in Figure 3.7 and why hot gas appears much closer to the spiral disk in Figure 3.3.

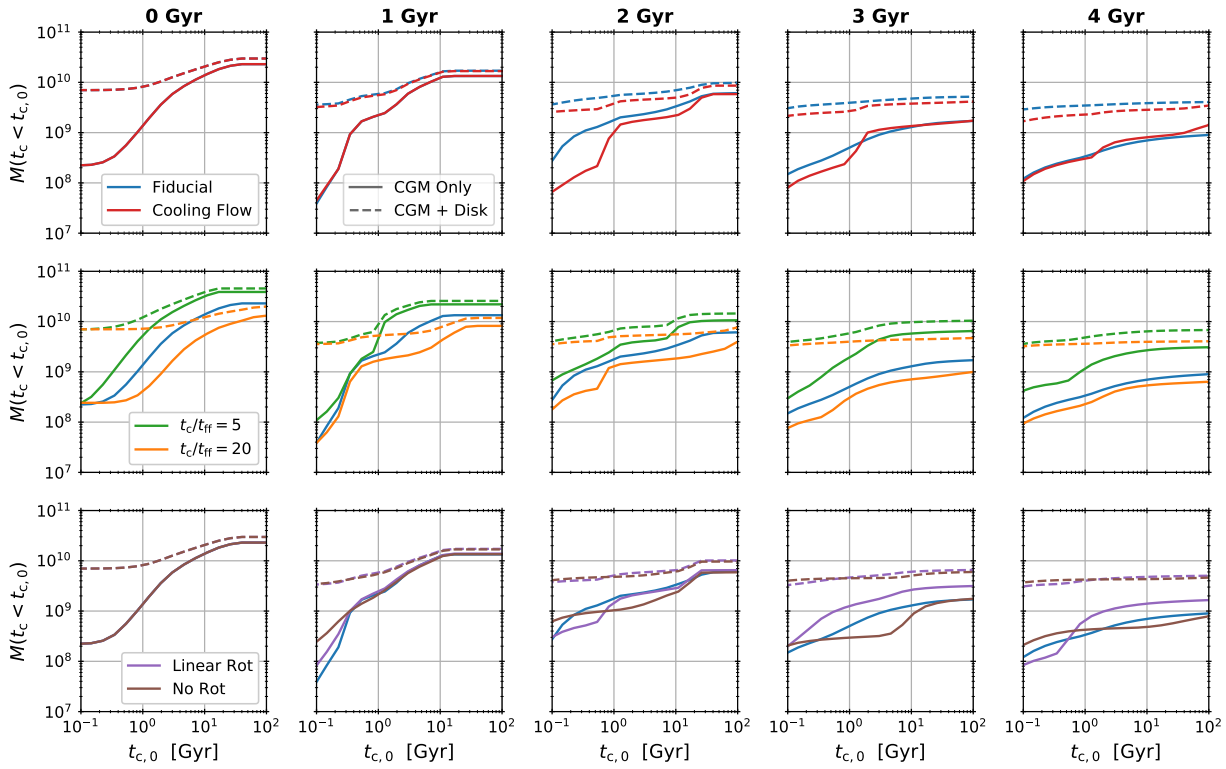

Figure 3.9 Cumulative mass distribution of CGM gas as a function of cooling time at five simulation times: 0, 1, 2, 3, and 4 Gyr. The CGM is defined by $r < r_{200} = 206$ kpc, with a cylinder 40 kpc in diameter and $8z_s = 2.6$ kpc thick excised to remove the disk. The top row compares the Fiducial model (blue) with the CoolFlow variant, the middle row with LowRatio (green) and HighRatio (orange), and the bottom row with LinRot (purple) and NoRot (brown). The initial distribution (leftmost column) is identical for all but the t_{cool}/t_{ff} variants.

3.5.2 Gas Availability & Accretion

In our simulations, there are two major sources of gas for star formation: cold gas that was present in the disk from the initial conditions, and CGM gas that accretes onto the galaxy. Dying stars also return gas to the disk, but their contribution over a $\lesssim 1$ Gyr timescale is negligible in comparison to these other two sources (unlike in ellipticals; see Voit and Donahue 2011). The story of gas accretion can also be thought of as the story of gas availability: what gas can cool and fall inward toward the disk? How much is gas in a rotating CGM able to shed angular momentum? In Figure 3.4, the differences in stellar mass formed by 1 Gyr are a clear indicator that our simulation variants experience different rates of gas accretion and star formation. In Section 3.4.2 we noted

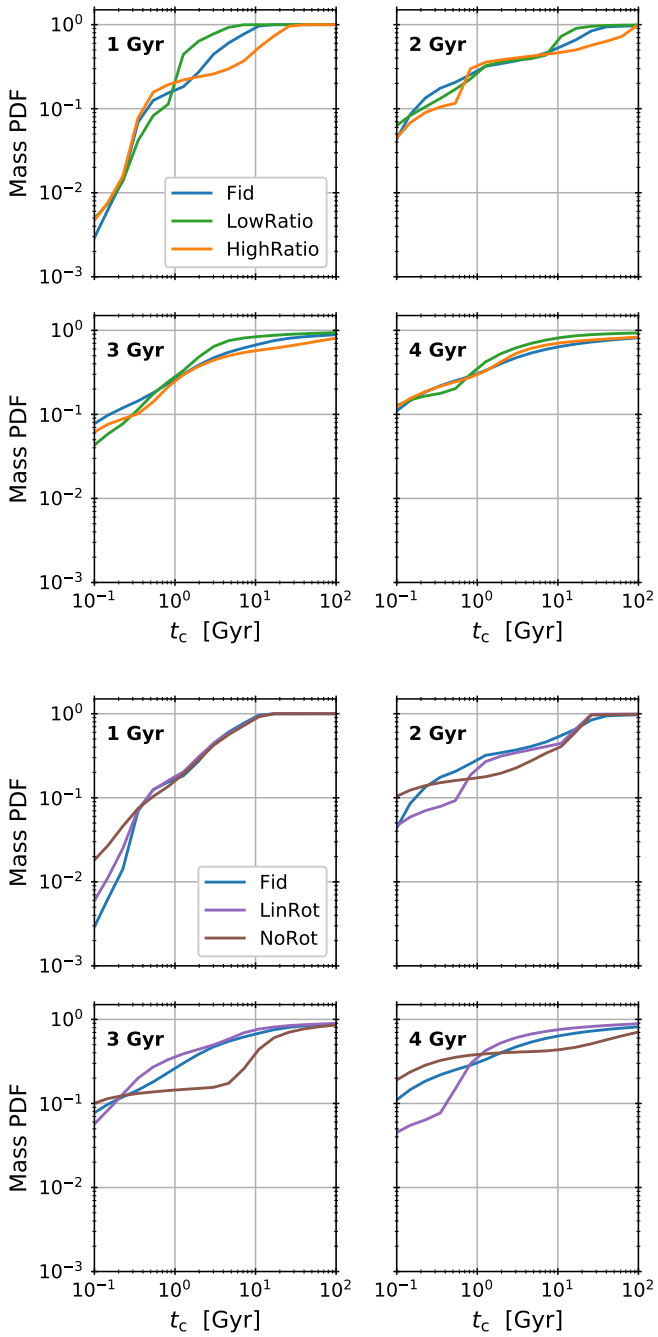

Figure 3.10 The same as the middle (left) and bottom (right) rows of Figure 3.9, but the mass distributions have been normalized in order to highlight differences in shape at each timestamp. The simulations with varying initial $t_{\rm cool}/t_{\rm ff}$ maintain cooling time distributions with similar shapes. On the other hand, the variants with different CGM rotation profiles vary considerably from each other across time.

that these differences depend primarily on the mass of CGM gas with $t_{\rm cool} < 1$ Gyr and on the presence of rotation. Figure 3.5 suggests that the simulation variants have unique and variable patterns of gas inflow over time. In this section, we delve more deeply into the ability of the CGM to contribute gas to the disk.

Figure 3.8 shows the net rate of change in disk mass for $t > 2$ Gyr, which is when stellar feedback is at its full efficiency. The disk is restricted to a cylinder with $R = 20$ kpc and thickness $8z_{\rm s} = 2.6$ kpc at the center of the simulation domain. Net $\dot{M}_{\rm disk}$ is calculated as the sum of the star formation rate $\dot{M}_*$ and the rate of gas change $\dot{M}_{\rm gas}$. If $\dot{M}_{\rm disk} = 0$, gas consumption by star formation precisely accounts for all the gas lost from the disk. If $\dot{M}_{\rm disk} < 0$, star formation accounts for only part of the gas loss, meaning that outflows have removed some of the disk gas. And if $\dot{M}_{\rm disk} > 0$, then consumption of gas by star formation is more than compensated by CGM accretion and the gas shed by stars, although the latter process contributes on the order of 0.1 $\rm M_\odot\ yr^{-1}$ or less over $t = 2$–4 Gyr.

We compare $\dot{M}_{\rm disk}$ to the star formation rate on the right axis, but the SFR has been binned at a higher rate than was used for the net $\dot{M}_{\rm disk}$ calculation ($\Delta t = 0.6$ Myr for the SFR instead of $\Delta t = 50$ Myr for $\dot{M}_{\rm disk}$). A pink line shows the smoothed SFR that was used in Figure 3.4. Horizontal bars show the average $\dot{M}_{\rm disk}$ over 1 Gyr.

This figure makes it clear that the CoolFlow variant's persistent star formation (as seen in Figure 3.4) is accompanied by a persistent inflow of gas. This is the expected behavior for a simulation without feedback. Intriguingly, the NoRot simulation also sees a net growth in its disk gas from 2–3 Gyr. This corresponds to the large growth (and then steady decline) in gas mass seen in Figure 3.5.

The HighRatio variant has the most stable disk mass of the variants, being the simulation with $\dot{M}_{\rm disk}$ that is consistently closest to zero. The other variants exhibit much larger fluctuations (even CoolFlow, though its net $\dot{M}_{\rm disk}$ is almost always positive). Yet for the variants with feedback, averaging the net $\dot{M}_{\rm disk}$ over Gyr timescales brings the net rate of change in disk mass closer to zero.

Visually, there is no clear time correlation between net $\dot{M}_{\rm disk}$ and SFR. Sometimes $\dot{M}_{\rm disk}$ decreases following a burst of star formation, such as the fiducial simulation at $t \approx 2.4$ and 3.1 Gyr, LinRot at 2.6 Gyr, NoRot at 2.2 Gyr, and HighRatio at 3.4 Gyr. Other times, a dip in $\dot{M}_{\rm disk}$ *precedes* a burst of star formation, as in NoRot at $t \approx 3.1$ Gyr and LinRot at 3.8 Gyr. Bursts of high instantaneous SFR and more prolonged periods of steady star formation both tend to be close in time to large changes in $\dot{M}_{\rm disk}$, but the sign of this change is not consistent, nor is the magnitude or whether the star formation precedes or follows a $\dot{M}_{\rm disk}$ change. This lack of a clear correlation will be discussed more in Section 3.7.4.

In Figure 3.9 we look at the cooling time distribution of CGM gas. We define the CGM as a sphere with radius $r_{200} = 206$ kpc, with a cylinder 40 kpc in diameter and $8z_{\rm s} = 2.6$ kpc thick excised to remove the disk. This is consistent with the region used for the disk in Figures 3.4, 3.5, and 3.8. The cumulative mass distributions are presented in intervals of 1 Gyr, starting from the initial conditions. The stellar feedback efficiency is ramped from 1–2 Gyr as explained in Section 3.3.2.1. The second column therefore represents the cooling time structure of the CGM after it has had a chance to evolve and interact with the disk, but before the impact of feedback. Dashed lines show the cooling time mass distribution when the disk is *not* removed (but we still restrict to gas with $r < r_{200}$).

The LowRatio and HighRatio variants have higher and lower CGM masses than the fiducial simulation, respectively, as noted in Section 3.3.4. Indeed, the initial $t_{\rm cool}/t_{\rm ff}$ ratio is the only thing that affects the initial cooling time distribution.

The overall mass of the CGM drops over time in all variants, irrespective of feedback. The majority of the mass loss (all but $\sim 2 \times 10^5$ M$_\odot$) is an artifact of the initial conditions: as explained in Section 3.5.1, the collapse of the initial disk pushes back on the CGM, inflating it and pushing gas beyond r_{200}. Indeed, by 4 Gyr, the CGM mass within r_{200} has dropped by over an order of magnitude, with the fiducial CGM mass dropping to $\sim 1.8 \times 10^9$ M$_\odot$.

At 1 Gyr, we can see that each variant has increased its amount of CGM gas with $t_{\rm cool} \sim 0.4$ Gyr. Given the difference between the solid and dashed lines at $t_{\rm cool} \lesssim 0.4$ Gyr and the flatness of the

disk-included profile in this region, most of the very low cooling time gas has been accreted onto the disk. The NoRot simulation is the one variant with notably more gas with $t_{\rm cool} \lesssim 0.4$ Gyr left in its CGM at 1 Gyr. This is intriguing given its rapid growth in stellar mass seen in Figure 3.4.

From 2–3 Gyr, the CoolFlow simulation has less CGM gas at short cooling times ($t_{\rm cool} < 1$ Gyr) than in the fiducial, but a roughly equivalent amount of gas at longer cooling times. This is the imprint of the CoolFlow simulation's constant inflow of gas (Figure 3.8), which depletes gas with short cooling times. The fiducial simulation experiences gas inflow as well of course, but in a reduced capacity thanks to stellar feedback: at the 0 and 1 Gyr snapshots—before the feedback efficiency is increased—the fiducial and CoolFlow variants have essentially identical cooling time-mass distributions. The distributions (both with and without the disk) deviate at 2 Gyr after feedback has become effective. This also means that any variations in cooling time distribution before 2 Gyr are due to CGM differences. Interestingly, the fiducial and CoolFlow CGM distributions come roughly back into agreement at 4 Gyr (though the fiducial simulation has a more massive disk).

Figure 3.10 highlights the differences in shape between the CGM cooling time-mass distributions of our variants by normalizing them. On the left we show the $t_{\rm cool}/t_{\rm ff}$ variants: the fiducial, LowRatio, and HighRatio simulations. On the right are our rotation variants: the fiducial, LinRot, and NoRot runs.

We first focus on the $t_{\rm cool}/t_{\rm ff}$ variants. At 1 Gyr, the LowRatio variant has more of its mass in gas with $1 < t_{\rm cool} < 10$ Gyr than the other two, and slightly less in gas with $t_{\rm cool} < 1$ Gyr. The excess of gas with $t_{\rm cool} \sim 1$ Gyr seems consistent with the large, positive $\dot{M}_{\rm disk}$ exhibited by the LowRatio simulations from $t = 2$–2.5 Gyr in Figure 3.8. The fiducial simulation also has positive $\dot{M}_{\rm disk}$ during this time, though of less magnitude than LowRatio. Furthermore, the fiducial simulation has an intermediate amount of CGM gas with $1 < t_{\rm cool} < 10$ Gyr. These differences in shape are accompanied by differences in absolute mass of gas with $1 < t_{\rm cool} < 10$ Gyr. It nevertheless seems an intuitive result that the (relative and absolute) amount of gas with $t_{\rm cool}$ of a few gigayears affects the amount of gas accreted by a disk a few gigayears in the future.

By 3 Gyr, we see that the three simulations have evolved cooling time-mass distributions with

the same general shape. These similarities are for the most part retained by 4 Gyr. This suggests that, despite initial differences in the CGM's structure, feedback has impacted their cooling-time mass distributions in a similar manner. This is despite the morphological differences in their feedback (Figure 3.7).

The similarity between the fiducial and CoolFlow simulations in Figure 3.9 tells us that the LowRatio, HighRatio, and fiducial cooling time distributions have the same shape because *feedback does not affect the cooling time mass distribution much at all.* This seems strange given the dramatic outflows in Figure 3.7, but most of that outflowing gas has $t_{\rm cool}$ longer than a Hubble time and therefore should not be expected to return to the disk. The gas that is visible in Figure 3.9, particularly that with $t_{\rm cool} \lesssim 10$ Gyr, is gas that has necessarily not been heated by outflows. This is likely gas near the disk midplane which avoids being heated.

What *does* have an impact on the CGM's cooling-time structure is rotation, as seen in the right side of Figure 3.10. Not only is there a difference between NoRot and the other variants with rotating CGMs, but there are also variations due to the different rotation profiles. We adopt a very straightforward prescription for the CGM's rotation (Equation 3.5), but these differences highlight the importance of understanding the angular momentum of the CGM.

3.6 The Circumgalactic Medium

The CGM has a complex, multiphase structure that can be difficult to encapsulate. The digestability of information must be balanced against the loss of detail. We can see in Figures 3.6 and 3.7 that our simulations do not have a spherically symmetric CGM and are instead closer to having cylindrical symmetry. Trying to encapsulate the structure of the CGM with e.g. mass-weighted spherical profiles therefore constitutes a loss of information. Furthermore, averages are biased towards the highest values, even when mass-weighted.

Therefore, in an attempt to encapsulate the radial structure of the CGM, we subdivide the gas within the virial radius based on its polar angle θ. This creates a set of cones (at the poles) and circular wedges. We choose to have seven regions subtending $\Delta\theta = 30°$; for example, the region

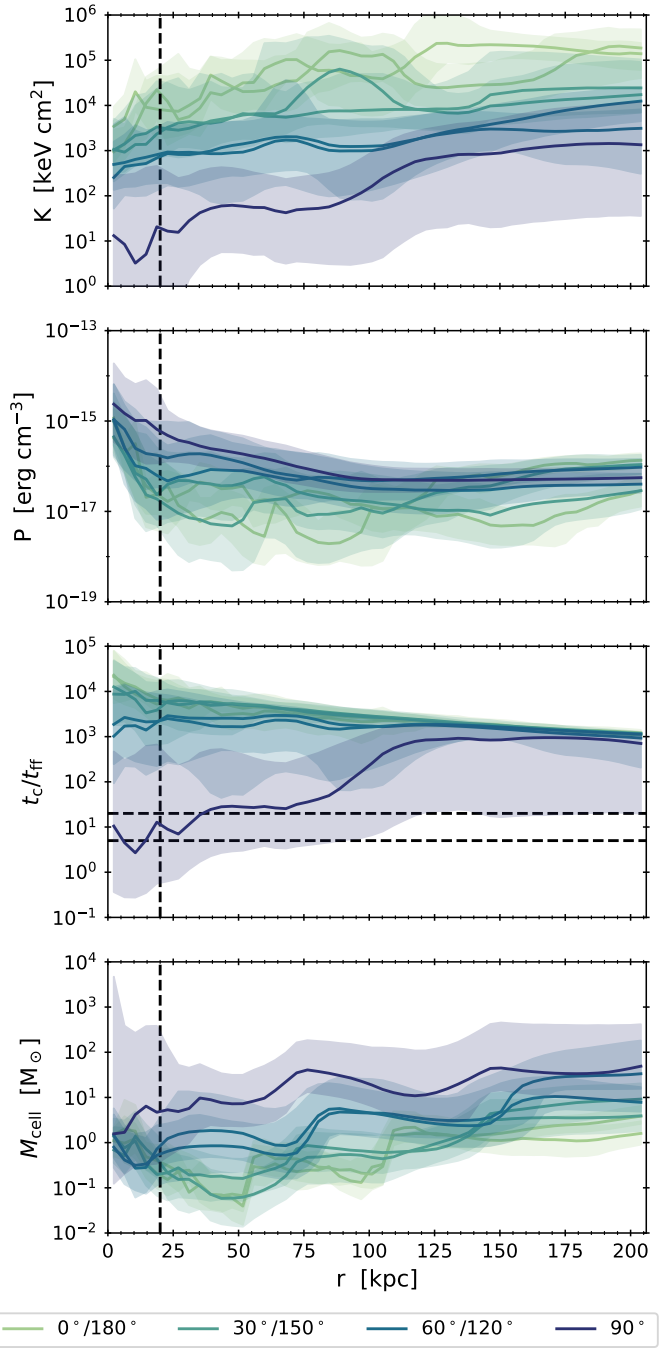

Figure 3.11 Entropy, pressure, t_{cool}/t_{ff}, and gas mass radial profiles of the fiducial CGM as a function of polar angle θ_{cen} at late times (t = 3–4 Gyr). The disk midplane corresponds to $\theta = 90°$. Solid lines are the time average of the 50th percentiles (medians), and shaded regions are of the 16th and 80th percentiles; see text for more details on our analysis. The vertical dashed line at 20 kpc represents the approximate extent of the disk adopted throughout this text, while the horizontal dashed lines show the t_{cool}/t_{ff} range of 5–20 predicted by precipitation theory.

with $\theta \in (0°, 15°)$ covers the top pole of the simulation domain, and $\theta \in (75°, 105°)$ encompasses the disk midplane. To keep our notation concise, we will refer to these regions based on their central polar angle, $\theta_{\rm cen}$. For the previous examples, these would be $\theta_{\rm cen} = 0°$ and $\theta_{\rm cen} = 90°$.

Within each region, we radially bin quantities of interest from $r = 2$ to $r = 206$ kpc $\approx r_{200}$ using 51 bins. This gives a bin width of $\Delta r \approx 4$ kpc. For each radial bin, we find the 16th, 50th, and 84th percentiles. This analysis is done for each simulation output (whose cadence is $\Delta t = 50$ Myr). Figures 3.11 and 3.12 show the time-average of these percentiles from $t = 3$ to $t = 4$ Gyr. We restrict the average to the last gigayear as the feedback ramp is at its full strength and the profiles are visually the most stable over time.

Figure 3.11 shows the radial profiles of entropy, pressure, $t_{\rm cool}/t_{\rm ff}$, and gas mass for the fiducial simulation. A vertical dashed line at $r = 20$ kpc marks the rough edge of the disk used throughout our analysis. The horizontal dashed lines in the $t_{\rm cool}/t_{\rm ff}$ panel indicate the 5–20 range predicted by precipitation (Voit et al. 2017; Voit 2018, 2021). For $\theta_{\rm cen} = 90°$ (the disk midplane), the 16th percentile of entropy is cut off at $r \sim 30$ kpc, reaching values of $\sim 10^{-4}$ keV cm^{-2} at the smallest radii. This is the influence of the galactic disk, which, unlike in much of our analysis, we do *not* excise. The disk is also evident in the 84th percentile of the mass profile.

It is clearly visible that all four quantities vary with polar angle: entropy and $t_{\rm cool}/t_{\rm ff}$ decrease towards the disk midplane at 90° while cell mass and pressure rise. The simulation is roughly symmetric about the disk plane. The higher entropy, lower pressure, and lower mass near the poles are consistent with the bipolar outflows seen in Figure 3.7, while the opposite trends at the disk midplane are consistent with the inflow seen along the midplane. All simulation variants demonstrate these trends. Near the poles (far from the disk midplane), the time-averaged $t_{\rm cool}/t_{\rm ff}$ ratio tends toward a smoothly declining profile. At these high angles, the time-averaged cooling time is approximately constant at $t_{\rm c} \sim 2 \times 10^3$ Gyr. The shape of $t_{\rm cool}/t_{\rm ff}$ is set primarily by the freefall time and, by extension, the NFW halo profile. On the other hand, only the $t_{\rm cool}/t_{\rm ff}$ profile centered on 90° (the plane of the disk) is remotely consistent with the $t_{\rm cool}/t_{\rm ff}$ range of 5–20 predicted by precipitation. This is also the polar angle with the highest cell mass, and is the angle

at which most of the cold gas inflow is located.

The mass dominance of the $\theta_{\rm cen} = 90°$ profiles, as well as their association with the inflowing gas along the disk midplane in Figure 3.7, motivates isolating these profiles for comparison across the simulation variants. This is done in Figure 3.12, where the time-averaged profiles of entropy, $t_{\rm cool}/t_{\rm ff}$, and radial velocity for the $\theta \in (75°, 105°)$ wedge are shown for all of the simulation variants with stellar feedback. The time averaging is again restricted to the last 1 Gyr of simulation evolution. A vertical line at 20 kpc again marks the nominal edge of the disk, and horizontal dashed lines mark $t_{\rm cool}/t_{\rm ff} = 5$–$20$ and $v_r = 0$ km/s. The initial entropy profiles are shown as dotted gray curves. Colored dotted lines are used to highlight the 16th percentile of the radial velocity, which is predominantly negative. The entropy profile within the disk is once again cut off to better demonstrate the CGM.

For all simulations, the spread in entropy and $t_{\rm cool}/t_{\rm ff}$ between the time-averaged 16th and 84th percentiles crosses several orders of magnitude. Though this spread is still less than the overall dependence on polar angle (Figure 3.11), we can see from the radial velocity that our wedges encompass both inflowing and outflowing gas. Figures 3.6 and 3.7 show that the inflow region is very thin. We chose a large $\Delta\theta$ in order to capture potential warping of this region (most evident in the fiducial simulation; see the 3rd and 4th columns of Figure 3.6) and so inevitably we capture a mix of gas phases.

Focusing on the $t_{\rm cool}/t_{\rm ff}$ ratio, we see that the *median* of gas near the midplane is predominantly higher than predicted from precipitation theory, though the 16th percentile does extend into the 5–20 range for all but the NoRot simulation. Precipitation requires a local $t_{\rm cool}/t_{\rm ff} \sim 1$ for gas to actually condense, which may not be captured by the 16th percentile. Yet this Figure is strong evidence that our simulated galaxies are *not* being regulated by precipitation, even if we search for precipitation *only* in the disk midplane.

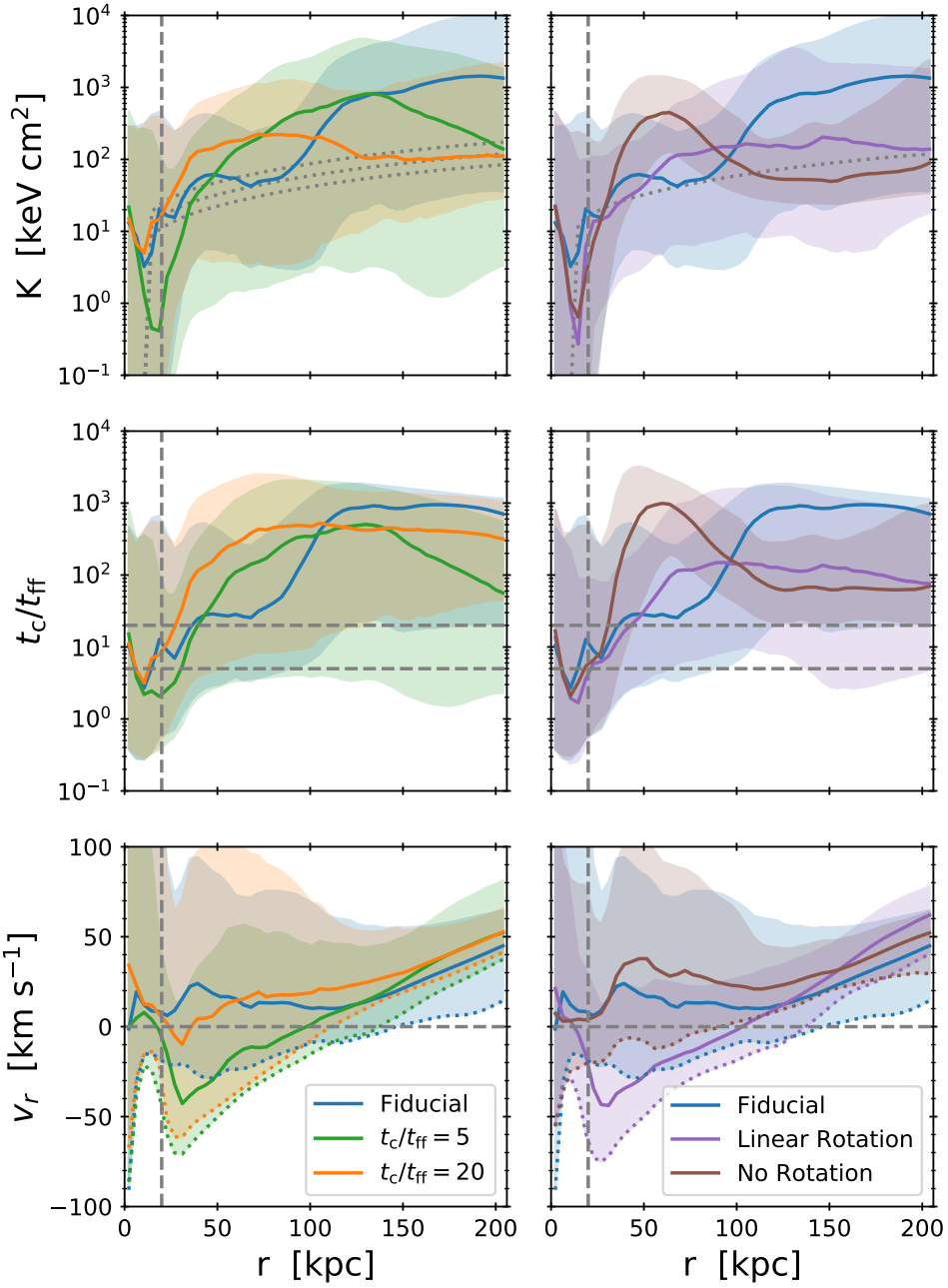

Figure 3.12 Entropy, $t_{\rm cool}/t_{\rm ff}$, and radial velocity profiles for the cones at $\theta_{\rm cen} = 90°$ (i.e., covering the disk midplane), averaged over t = 3–4 Gyr, for the simulation variants with stellar feedback. Solid and shaded lines are the same as in Figure 3.11. The vertical dashed line at 20 kpc marks the approximate edge of the disk, and the horizontal dashed lines mark $t_{\rm cool}/t_{\rm ff}$ = 5–20 and v_r = 0 km/s. The initial entropy profiles are shown as dotted gray lines, and dotted colored lines highlight the time-averaged 16th percentiles in radial velocity.

3.7 Discussion

We simulated a suite of idealized galaxies that are similar to the Milky Way in order to explore the conditions under which self-regulating feedback might arise. Our hypothesis was that these galaxies would naturally regulate their star formation rates according to the predictions of precipitation theory if initialized with a CGM having $t_{\rm cool}/t_{\rm ff} \sim 10$ (Voit 2019). This work therefore complements that of Prasad et al. (2020), who studied the precipitation-regulation of larger AGN-dominated systems with Type Ia supernova feedback (i.e., massive central ellipitcal galaxies in groups and clusters), in that it explores the ability of less massive galaxies to regulate themselves through stellar feedback alone.

In light of the results from Prasad et al. (ibid.), the question motivating our work is: can we also create a self-regulating galaxy-CGM system but with feedback coupled to star formation instead of AGN and older stellar populations? We broadly take self-regulation to mean that feedback tunes the net inflow of CGM gas to match the disk's time-averaged star formation rate. Since our only feedback mechanism is Type II supernovae, this also implies that the star formation rate of self-regulated systems would be tuned to the inflow of cold gas.

Ultimately, we do not consider the galaxies we have simulated to be self-regulating. Instead, the CGM in our simulations experiences large-scale disruption due to outflows. Only gas along the disk midplane is of low enough entropy to be able to cool and accrete onto the disk. Even this limited accretion mode does not appear to be precipitation-regulated based on the most general measure, the median ratio of cooling and freefall times. Our star formation rates drop to very low values of order 0.1 $M_\odot$/yr after the onset of our feedback efficiency ramp. This limited gas accretion and star formation keep the average disk growth, $\dot{M}_{\rm disk}$, near zero. Rather than creating a system that maintains a moderate SFR, we have created a system in which feedback essentially shuts off star formation.

We start our discussion with Section 3.7.1, where we examine the impacts of variations in the simulation parameters. Then, in Section 3.7.2, we compare the structural features of our simulations to other works, both observational and theoretical. Section 3.7.3 highlights the role the Toomre

instability plays in the evolution of our galaxies. Our simulations do *not* have self-regulated star formation, but their failure to self-regulate is illuminating. In Section 3.7.4 we interrogate the definition of self-regulation and highlight the ambiguity as to the expected timescales involved. Finally, in Section 3.7.5 we discuss the physical effects missing in our simulations that could better couple gas accretion and stellar feedback.

3.7.1 Impact of CGM Variations

The overall behavior of our simulations is unaffected by variations in the CGM: once stellar feedback is at its full strength the CGM becomes disrupted by wind-driven bubbles and the SFR drops by an order of magnitude. The exception is, of course, the CoolFlow variant which completely lacks stellar feedback. Yet despite observing no impact on the overall behavior, we do see important differences manifest in our simulation variations. The variations in initial conditions exert their biggest influence at $t < 1$ Gyr, when feedback is made artificially weak. In the following subsections we will discuss the differences resulting from changes to the initial $t_{\rm cool}/t_{\rm ff}$ ratio (Section 3.7.1.1) and from alterations to the CGM's initial rotation profile (Section 3.7.1.2).

3.7.1.1 Variation in Initial $t_{\rm cool}/t_{\rm ff}$

The LowRatio and HighRatio variants are distinguished by modifying the condensation criterion τ in Equation 3.1. This parameter is essentially the initial $t_{\rm cool}/t_{\rm ff}$ ratio of the CGM, though as discussed in Section 3.3.1.2 the actual $t_{\rm cool}/t_{\rm ff}$ ratio deviates slightly. Including the fiducial simulation, we sample $\tau \in [5, 10, 20]$.

Because the CGM's density structure is set by τ, these variants have different starting CGM masses. The LowRatio variant has the most mass at 3.9×10^{10} $M_\odot$, followed by the fiducial with 2.3×10^{10} $M_\odot$ and the HighRatio with 1.3×10^{10} $M_\odot$.[3] Therefore, a higher τ results in an overall less massive CGM.

Moreover, a higher τ lowers the relative amount of gas with initial $t_{\rm cool} < 1$ Gyr. This is seen in

[3]The CGM is defined as a sphere with $r = r_{200} \approx 206$ kpc with a cylinder excised for the disk. This disk has height $z = 4z_{\rm s} = 1.3$ kpc from the midplane and radius $R = [27.5, 28.5, 29]$ kpc for the LowRatio, fiducial, and HighRatio variants respectively.

Figure 3.9. For a real multiphase CGM, this can be understood via the framework of Voit (2021): the median $t_{\rm cool}/t_{\rm ff}$ of the CGM defines the center of a *distribution* in $t_{\rm cool}/t_{\rm ff}$. Moving the median to higher values means that less of the distribution covers low cooling times, and therefore less gas is able to efficiently cool, condense, and reach the galaxy. Our simulations, however, do *not* start with a multiphase CGM; rather, the temperature and density are smooth, spherically symmetric functions of radius. In fact, the initial temperature profile is very similar between the fiducial, LowRatio, and HighRatio simulations. The differing masses of gas with $t_{\rm cool} < 1$ Gyr are then a result of both variations in the initial density profiles and the different initial $t_{\rm cool}/t_{\rm ff}$.

The initial stellar mass growth of the HighRatio and LowRatio simulations is easily described by the different masses of gas with $t_{\rm cool} < 1$ Gyr. This is seen in Figure 3.4, where at $t < 1$ Gyr the LowRatio simulation has the highest disk gas mass, greatest growth in stellar mass, and highest SFR. Conversely, the HighRatio variant has the least growth in stellar mass and lowest SFR, although its gas mass is not as distinct from the fiducial simulation as the LowRatio simulation is.

The difference in low cooling time gas also seems to have a slight impact on the physical size of the disks, as seen in Figure 3.3 and Table 3.3. The LowRatio simulation has the most gas with $t_{\rm cool} < 1$ Gyr and correspondingly has the largest radius within which star formation occurs. The converse is not quite true for the HighRatio simulation, whose average radius of star formation is not statistically significantly different from the fiducial simulation's. The average star formation radii in Table 3.3 are determined over $t = 2$–4 Gyr, after the feedback ramp has ended and the bulk of star formation has occurred. This therefore suggests that the initial differences in CGM gas accretion between the LowRatio, HighRatio, and fiducial simulations have lingering effects on the structure of the galactic disk. This effect would appear to be on the same scale as natural variation in the maximum radius of star formation. These differences are likely not a result of the difference in initial disk radius, as the initial LowRatio disk is about 1 kpc *smaller* than the fiducial's gas disk.

Feedback does not generally seem to have much impact on the $t_{\rm cool}$ distribution function for CGM gas. This is seen between the $t_{\rm cool}/t_{\rm ff}$ variants in Figure 3.10. Though the $t_{\rm cool}/t_{\rm ff}$ variants have different star formation histories and stellar masses, feedback neither amplifies nor diminishes

any pre-existing differences in the $t_{\rm cool}$ distribution function. The similarity between the fiducial and CoolFlow distributions at $t = 4$ Gyr further indicates that feedback has minimal impact on the CGM's overall availability of low cooling time gas.

Even though the cooling time distribution is largely unaffected by feedback, the $t_{\rm cool}/t_{\rm ff}$ variants do not evolve identically. In Figure 3.7 we can see that outflows in the LowRatio simulation have traveled less far than in either the fiducial or HighRatio simulations. For $t < 1$ Gyr, the LowRatio simulation has the highest CGM pressure of the $t_{\rm cool}/t_{\rm ff}$ variants, and HighRatio the lowest. This generally tends to remain true for the outer CGM ($r \approx 150$–200 kpc) even as outflows drop the overall CGM pressure.

The $\dot{M}_{\rm disk}$ in Figure 3.8 also shows interesting differences. The HighRatio variant experiences the smallest $\dot{M}_{\rm disk}$ fluctuations of the simulations considered here, suggesting that relatively little mass is involved in the cycle of accretion and star formation. The fluctuations of $\dot{M}_{\rm disk}$ in the LowRatio simulation are on par with and occasionally larger than those experienced by the fiducial simulation. Generally, the fluctuations in $\dot{M}_{\rm disk}$ get smaller as the simulations go on, as seen by the average from $t = 3$–4 Gyr.

It may be that the LowRatio simulation, being able to accrete more cool gas initially, was set onto a cycle of large amounts of gas accretion followed by productive periods of star formation, rather like an oscillator with a large initial perturbation. Also like most oscillators found in nature, the LowRatio simulation experiences damping in its cycle of accretion and star formation. Though it is the simulation with the highest stellar mass, Figure 3.5 shows that it had only moderate gains in stellar mass after 2 Gyr. This figure also shows that the LowRatio simulation continued to accrete gas from $t = 2$–3 Gyr, despite the stronger feedback. This may be the LowRatio simulation "refueling" in order to maintain a more moderate SFR at the end of the simulation. On the other hand, the fiducial simulation gains the most stellar mass over $t = 2$–4 Gyr in Figure 3.5, while the HighRatio simulation is with LowRatio near the bottom of the pack, although it is something of a "late bloomer." It may be that the fiducial simulation has the most ideal conditions of these variants for sustained star formation growth. Whether or not we consider it "self regulating" is a question

we defer to Section 3.7.4.

To summarize, the LowRatio, HighRatio, and fiducial simulations all exhibit a number of differences that are a consequence of how the condensation criterion τ determines both the initial $t_{\rm cool}/t_{\rm ff}$ ratio and density structure of the CGM. These density differences result in differences in total mass. The LowRatio simulation not only starts with more gas, but a larger fraction of it is able to cool efficiently. The converse is true for the HighRatio simulation. These differences are persistent even in the face of feedback. The structure of the disk and its star formation therefore retain their early differences throughout the simulation runtime.

3.7.1.2 Variation in CGM Rotation

We now consider variations that arise from the CGM's rotation. Apparent from Figure 3.4 is that both the presence of rotation, as well as its variation with radius, has an impact on the ability of the CGM to supply gas to the disk.

We have indicated throughout this work that the NoRot simulation should be able to accrete gas more efficiently because its CGM gas does not have to shed angular momentum to reach the disk. This is evident in the stellar growth of Figure 3.4 at $t < 1$ Gyr. It may also explain the large growth in gas mass seen over $t \sim 2$–3 Gyr in Figures 3.5 and 3.8. In Section 3.5.1, we noted a remnant of the initial disk conditions that is present in the CGM: due to insufficient vertical support against gravity, the initial disk collapses and spreads outwards into the CGM. The NoRot variant's initial disk has the smallest amount of radial spread due to the lack of rotation in its CGM.

The mere inclusion of rotation in the CGM has a large effect on gas accretion and simulation evolution, but the radial profile of that rotation also has an impact. The LinRot simulation forms more stars than the fiducial model within the first 1 Gyr, before stellar feedback has much effect. The LinRot simulation also has lower angular momentum at all CGM radii, making it easier for gas to accrete than in the fiducial simulation. Rotation is also able to change the shape of the cooling time-mass distribution in Figure 3.10, affecting the availability of gas that can be accreted in addition to the ease of accretion.

Su et al. (2020) also performed isolated galaxy simulations that included a rotating CGM. These

simulations targeted cool-core clusters with halo masses between 10^{12} and 10^{14} $M_{\odot}$. Rotation followed a β-profile with $\beta = 1/2$, set to be twice the net dark matter spin. Rotation therefore comprised 10-15% of the CGM's support against gravity, with the rest being supplied by thermal energy. This is in contrast to our simulations, where rotation was not considered in the calculation of hydrostatic balance. The simulations of Su et al. (2020) were included in the Fielding et al. (2020) meta analysis, where it is noted that these simulations had an enhanced cold phase at $r < 0.2r_{200}$ compared to the other isolated galaxy simulations in the analysis. This enhancement is attributed to CGM rotation—which was not included in Fielding et al. (2017) and Li and Tonnesen (2020)—in agreement with our results.

DeFelippis et al. (2020) studied the CGM angular momentum of Milky Way-mass galaxies in IllustrisTNG. They split these galaxies into samples based on the stellar specific angular momentum, resulting in high- and low-momentum populations. Both populations have inflowing cold CGM gas near the disk plane. In the sample with high specific angular momentum, this inflow is well aligned with the disk; however, the radial inflow disappears for $r < 0.2r_{200}$. Much like with our simulations, it is suggested that this is due to the presence of strong rotation. We note that our rotation speeds (derived from Hodges-Kluck, Miller, and Bregman 2016) are higher than the rotational speeds measured by DeFelippis et al. (2020).

3.7.2 Comparison of Structural Features to Other Works

It is worth comparing some of the structures seen in our simulations with those seen or predicted in other works. These works include observations, analytic predictions, and cosmological simulations. We'll begin with the gas disk, expand outward to the accretion flows seen along the disk midplane, and finally consider the structure of our feedback-driven outflows.

3.7.2.1 Extended Gas Disk

Starting with the disk, we can see in Figure 3.3 that there is cold, dense, rotating gas that extends beyond the average radius of star formation in all of our variants. This is consistent with observations of spiral galaxies in the THINGS survey (Leroy et al. 2008). These observations show

that spiral galaxies have high star formation efficiency in their H_2-dominated cores. This efficiency declines with radius in the extended neutral hydrogen disk.

The structure of our galactic disk is also consistent with the findings of Lopez et al. (2020) and Tejos et al. (2021). These papers present two instances of extended Mg II disks ($r \sim$ 20–40 kpc) that are co-rotating with the interstellar medium. Our extended cool disks are of order $r \sim$ 20-30 kpc. We note that, while an extended cool disk is an emergent feature of our simulations, we purposely aligned the angular momentum vectors of the CGM and the disk. It is unclear what impact misaligned angular momentum vectors might have on our extended gas disk.

3.7.2.2 Accretion Along the Midplane

Figures 3.6 and 3.7 make it clear that, while inflowing gas can be found throughout the CGM, only inflowing gas near the disk midplane is able to reach the disk. Inflowing gas *not* along the midplane is disrupted by outflows. The exception to this is of course the CoolFlow variant, which lacks stellar feedback.

Inflow within the disk plane is not unprecedented in cosmological simulations. Trapp et al. (2022) find this inflow mode in the FIRE-2 simulations and note that it is the dominant source of accretion there just as it is in our simulations. Gas accretion in the EAGLE simulations is also anisotropic, favoring low heights relative to the disk and inflow speeds of 20–60 km/s (Ho, Martin, and Turner 2019). This inflow is predominantly cold gas found near the disk or in low-angular momentum streams, and estimates of the mass rate are enough to meet or exceed the SFR.

Within IllustrisTNG, DeFelippis et al. (2020) also see this inflow structure in $10^{11.75}$–$10^{12.25}$M$_\odot$ halos. Truong et al. (2021) see a global anisotropy in the CGM, with density enhanced parallel to the disk plane, and temperature and metallicity enhanced along the orthogonal minor axis. Their anisotropies are more subtle than what we see in our own simulations, being of only 0.1–0.3 dex. These anisotropies peak in Milky Way-like galaxies with $M_* \sim 6 \times 10^{10}$ M$_\odot$, which is the mass at which super massive black hole feedback turns on in TNG. Generally, the anisotropies are larger in galaxies with SMBH feedback, except for metallicity: the metallicity anisotropy is more pronounced in star-forming and disky galaxies.

The inflowing gas spans a temperature range from $\sim 5 \times 10^3$–5×10^5 K, with the coldest gas living in denser filaments. Gas condenses and cools while being part of a rotating inflow. This is reminiscent of the accretion mode observed in Hafen et al. (2022) and described in detail in Stern et al. (2021). Gas inflow is hot until it reaches $\sim$ 20 kpc scales, at which point angular momentum slows its inward motion. Radiative cooling then exceeds heating due to compression, and the gas temperature drops to $\sim 10^4$ K or below. Importantly, Hafen et al. (2022) note that the angular momentum of inflowing gas aligns itself with the galaxy before cooling, but because the angular momentum of our CGM and disk are constructed to be aligned, we cannot make any comparison on this point.

3.7.2.3 Outflow Structure

Our simulations are dominated by outflows to an unrealistic degree. Very low density cavities extend out to the virial radius by $t = 4$ Gyr. Outflows have a very wide opening angle of essentially 180°, covering the face of the disk. The CGM essentially becomes obliterated above and below the disk.

That said, the structure of our outflows matches well to analytic models from Lochhaas et al. (2018). These models describe how relatively slow-moving gas bubbles can be inflated by fast galactic winds. In their model, winds drive a forward shock through the CGM. Their interaction leads to the development of a reverse shock, and between these two fronts lies a contact discontinuity. This discontinuity separates material driven out by the winds from the swept-up CGM gas. Lochhaas et al. (ibid.) refer to the region between the reverse shock and the contact discontinuity as the "shocked wind." It is this shocked wind that is responsible for the growth of the gas bubble. Immediately behind this shocked wind (inside the reverse shock) lies cool, unshocked gas, followed by hot unshocked gas immediately next to the galaxy.

We can clearly see the shocked wind in the density projections of Figure 3.6, often with winds inside winds. The models of Lochhaas et al. (ibid.) use a continuous wind, while our simulations have multiple discrete winds driven by episodic Type II supernova feedback. At 2 Gyr, a band of shocked winds is visible both above and below the disk. Subsequent winds are able to travel faster

due to the evacuated region that follows behind the first (Lochhaas et al. 2018). The thickness of the outermost shocked wind grows as its reverse shock propagates. It travels with speeds on the order of $\sim$ 100 km/s, which is an order of magnitude lower than the feedback-driven winds, corroborating the major result of Lochhaas et al. (ibid.). The density of the shocked wind is also relatively constant across its width as assumed by the analytic models, though that density drops as the shocked wind expands.

Instead of a layer of cold unshocked gas, the gas behind the shocked wind is very hot ($\gtrsim 5{\times}10^6$ K) and chaotic thanks to successive feedback events. Additionally, these continued outflows prevent the outermost shocked wind from stalling and falling back onto the galaxy, as seen in the additional tests run for Section 5.3 of Lochhaas et al. (ibid.). They also appear to disrupt any dense, cooling material that may fall inward towards the galaxy. Lochhaas et al. (ibid.) note that such gas could be seeded by a Rayleigh-Taylor or Vishniac (Vishniac 1983; Vishniac and Ryu 1989) thin-shell instability. While we see plenty of turbulence, we see no evidence of infalling material reaching the galactic disk outside of the disk midplane.

3.7.3 The Role of the Toomre Criterion

One of the most striking features of Figure 3.4 is that the disk gas mass is almost identical between our variants with feedback. This is true at all times, both during the $t < 1$ Gyr star formation burst and late into the simulations, despite vast differences in stellar mass. This feature is consistent with the Toomre criterion Q for disk fragmentation

$$Q = \frac{c_s \kappa}{\pi G \Sigma_{\rm g}} \tag{3.7}$$

where c_s is the sound speed, κ is the epicyclic frequency of the rotating disk, and Σ_g is the gas surface density of the disk's face (Toomre 1964). If $Q > 1$ at a given disk radius, the gas is stable against fragmentation. If Q locally drops below 1, then at that radius, the disk is able to fragment into clumps that lead to star formation.

Important for our discussion is the dependence of Q on the gas surface density, $\Sigma_{\rm g}$. As gas accretes, the surface density rises and thus Q drops. Star formation lowers $\Sigma_{\rm g}$, bringing Q back

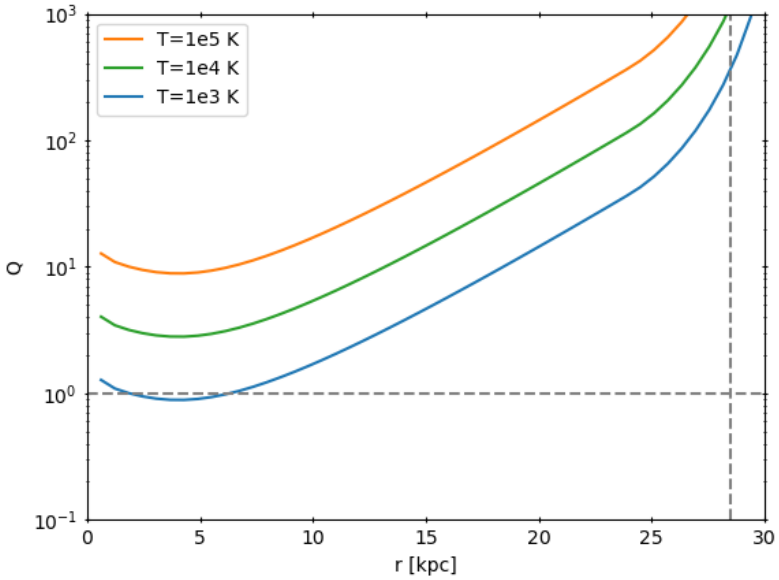

Figure 3.13 Toomre parameter Q as a function of radius for our simulation initial conditions. We calculate Q analytically based on the static background gravitational potentials and the initial disk density profile (Section 3.3.1.1). The disk is initially isothermal with $T = 10^5$ K (orange), but other profiles are shown assuming the disk cools uniformly to 10^4 K (green) and 10^3 K (blue). The latter is just below the minimum temperature for star particles to form (3×10^3 K). The vertical dashed line marks the edge of the fiducial disk, based on how it blends with the CGM.

towards 1 and the disk back towards stability. Gas accretion and fragmentation therefore conspire to keep $Q \sim 1$, which results in a fairly stable gas surface density and, by extension, overall mass. All disks are constructed to have the same initial Σ_g profile through Equations 3.1 and 3.2 (though the HighRatio and LowRatio disks extend to larger or smaller radii, respectively). They also all evolve within the same static gravitational potential, which sets κ, and remain roughly isothermal with $T \sim 4 \times 10^3$ K (although $T \sim 10^2$ K in the densest clumps), setting c_s. The similarity in disk temperature and sound speed between all of the variants indicates that the Toomre criterion is involved in keeping all variants near the same disk mass. The exception to this is the CoolFlow variant, whose disk mass notably deviates from the other variants despite having only a slightly warmer disk overall ($T \sim 5 \times 10^3$ K). The lower disk gas mass in the CoolFlow variant may occur because there is no supernova feedback to generate turbulence, which would raise the *effective* value of c_s in Equation 3.7.

Figure 3.13 shows the Q parameter calculated as a function of radius for the simulation initial conditions (Section 3.3.1.1). We perform this calculation analytically (i.e., we do not estimate Q from the simulation itself) using the background stellar and dark matter potentials and the initial disk density profile (Equations 3.1 and 3.2) to calculate the epicyclic frequency κ and surface density Σ_g, respectively. Since the initial disk is isothermal at 10^5 K, the sound speed c_s is constant. We also include Q calculated for lower temperatures, assuming the disk cools uniformly: 10^4 and 10^3 K. The latter is close to the minimum temperature required for stars to form (3×10^3 K) and is therefore an approximate representation of $Q(r)$ when stars begin to form. We only have $Q \sim 1$ within the inner $\sim$ 10 kpc, which is commensurate with the average star formation radii in Table 3.3 (with exception of the CoolFlow variant).

3.7.4 The Timescale of Self-Regulation

Broadly speaking, self-regulation is a balance between gas inflow and feedback. This definition is used in e.g. Mitchell and Schaye (2022) and Prasad et al. (2020). Self-regulation can be understood through analogy to a thermostat, which works to keep the temperature of a room at a specified "set point." Self-regulation in a galaxy should work to keep the star formation rate near a particular set point. What this set point is, exactly, is not set externally (as with a thermostat), but would be set by the conditions of the galaxy and its environment. Thermostats turn off and on a furnace, which in our analogy, is the star formation. The product of a furnace is heat, and the product of our galactic "furnace" is stellar feedback.

Real thermostats do not keep a room at the set point all the time. When the temperature drops, the furnace is turned on. When the room gets sufficiently warm (either reaching the set point exactly or maybe slightly above to compensate for cooling), the furnace is shut off. We expect the same thing of galaxies: gas accretion should lead to star formation. The feedback from this star formation will influence the galaxy's ability to accrete gas, modulating future star formation.

The connection between gas accretion and star formation is not temporally or spatially immediate, however. As we discussed in Section 3.7.2.2, gas is often seen to accrete along the plane of the disk, but star formation is often concentrated at the center of the disk where densities are highest.

Recent estimates put the inward radial mass flow rate at less than 1 $M_\odot$/yr (Di Teodoro and Peek 2021). During a feedback burst (when the furnace is on), it is therefore probably not the case that inflow is perfectly balanced by star formation. Rather, the two balance each other *on average over some timescale*.

With Figure 3.8, we attempted to identify by eye correlations between the SFR and the net rate of change in disk mass, $\dot{M}_{\rm disk}$, but ultimately found no consistent relation. While there are certainly rigorous statistical tools for addressing time correlations, this analysis is sufficient to raise questions about what precisely one should be looking for in order to decide if a galaxy is self-regulating its star formation.

The ambiguity over timescale is exacerbated when examining self-regulation with simulations. Because we are limited in resolution and computational power, simulations of Milky Way-mass galaxies must use particles to represent entire stellar populations rather than individual stars. This modeling limitation introduces shot noise into the SFR. It is therefore also worth considering the timescales over which we are concerned with changes in the SFR.

The timescale uncertainties are in large part due to the temporal and spatial separation between gas accretion and feedback. Within our simulations, CGM gas that accretes onto the galaxy is more likely to contribute to a star particle if it reaches the denser disk center. The formation of a star particle obfuscates the physical and temporal scales involved in the actual formation of molecular clouds and protostars, but these are assumed to be below the temporal resolution of the simulation. Connections between inflow and star formation in simulations seem clearer when made on smaller physical scales, such as gas inflow along dust lanes at the very nucleus of a barred spiral galaxy (Moon et al. 2022).

Our efforts to directly explore the self-regulation of galaxy star formation has highlighted the need to refine our questions. Specifically, if we as a community are to define self-regulation as a balance between gas accretion and star formation, we should consider on what timescale we expect this balance to be achieved. This way, we may better identify which physical processes contribute to the self-regulation of galaxies.

3.7.5 Missing Model Components

One of the key takeaways from Prasad et al. (2020) and Voit et al. (2020) is that feedback from Type Ia supernovae assists an AGN in self-regulating its own feedback. Similarly, it seems that our simulations are missing one or more important features that work in concert with Type II supernova feedback to regulate a Milky Way-like galaxy. While there may be evidence for weak coupling between gas inflow and star formation, as discussed in Section 3.7.4, we believe that our simulations are likely not capturing physical features or effects that would make this coupling more obvious and/or tighter.

The biggest evidence for this is the large feedback-driven bubbles that are present in all of our simulation variants with stellar feedback (i.e., excluding the CoolFlow variant). Though the ramp in feedback efficiency, described in Section 3.3.2.1, delays the onset of these bubbles, we don't expect further tweaks to the ramp (such as modifications to its start and end points in both time and efficiency values) to significantly affect the presence of these large bubbles. This is because the dramatic cavities seen in at late times in Figures 3.6 and 3.7 are due to successive bubbles being blown into the same volume. Earlier feedback winds clear away material, making it easier for later winds to travel faster and farther, and to further remove material from the bubble's cavity.

These bubbles travel well beyond the virial radius by the end of the simulations at $t = 4$ Gyr, leaving cavities of high entropy gas that will not cool within a Hubble time. The density of the ambient medium continues to decrease beyond the virial radius (Figure 3.1), providing nothing for the feedback-driven bubbles to meaningfully collide with and halt against. Additionally, the cooling time at large radii is high enough that material cannot "backfill" the bubble cavities. The behavior of these outflows suggest that we are missing either material that the winds would stall against, a mechanism which would fill the cavities in with low entropy gas, or both.

The idealized nature of our simulations may be working against us in this regard. Fielding et al. (2020) compared idealized and cosmological simulations of Milky Way-like galaxies and found that the outer CGM structure of the latter ($\gtrsim 0.5 r_{200}$) was highly impacted by cosmological effects such as nonspherical gas accretion and the presence of satellites. No attempt to model cosmological

accretion was included in our simulations, but these could address the large wind-driven bubbles in our simulations. This is especially true considering that the FOGGIE simulations (Peeples et al. 2019) use the same feedback algorithm and a slightly *higher* feedback efficiency but do not see the same long-term disruption due to outflows. Appropriately modeling inflow in an idealized simulation is a challenge, however. Typically, cosmological accretion in idealized simulations is treated as being spherically symmetric, as in Fielding et al. (2017) (albeit with added density fluctuations), but as stated above, Fielding et al. (2020) emphasized that this spherical treatment is not sufficient. That work highlighted the strength of idealized simulations for studying the inner CGM ($\lesssim 0.5 r_{200}$), but our work indicates that for self-regulation the outer CGM and perhaps the nearby IGM exert an important influence.

Our initial CGM is also smooth and spherically symmetric. A more realistic CGM would be properly multiphase, with fluctuations in density, temperature, and velocity (both radial and tangentially). We initially expected to see such fluctuations develop over the course of the simulation as a result of outflows, but including these from the start would likely have a profound effect. A nonuniform CGM will have a distribution of cooling times at a given radius, better mixing, and may be better able to disrupt early outflows. In the simulations presented in this work, the earliest outflows are able to expand through the CGM nearly uniformly.

Initial density perturbations are the easiest way to disrupt this spherical symmetry, but require a choice of power spectrum. A more natural way of introducing perturbations at large radii may occur from adjusting our CGM beyond r_{200}. Our current treatment for this "outer" gas was motivated by practical considerations rather than observations. Notably, our entropy initial profile increases monotonically with radius. More realistic halos are likely to have low-entropy gas beyond r_{200}: gas that has either not yet passed through a cosmological accretion shock, or has passed through the shock with enough density for its current entropy to be less than the mean at r_{200}. The relaxation of the simulation's initial state could push this gas to become Rayleigh-Taylor unstable, and either over time or with the assistance of instabilities seeded in the initial conditions, could grow dense clumps of gas that may affect the outflows and overall precipitation within our simulations.

Cosmological inflow would further assist in seeding and/or maintaining CGM fluctuations, naturally creating them as infalling material combines with the galaxy. This is true both for filamentary inflow as well as the presence of and mergers with small satellites and dwarf galaxies.

The failure of our simulations to "close the feedback loop" is not entirely novel. Prasad et al. (2020) simulated an elliptical galaxy of similar mass (2×10^{12} $M_{\odot}$), dominated by AGN feedback, and also saw a highly disrupted CGM emerge. Generally, lower mass galaxies have a weaker gravitational potential and lower CGM pressure. Outflows can more easily escape the halo. This reinforces our earlier observation that some physical mechanism at the edge of the halo—cosmological inflows or simply more generic density perturbations, to name two candidates—appears necessary for lower mass halos to maintain their CGM structure.

Though we suspect the lack of cosmological effects is the biggest missing piece from our simulations, there are other physical processes to consider. Our current simulations use Type II supernovae as their only feedback source. Though our simulations do not currently suffer from a lack of outflows, efforts to counteract their current behavior may highlight the need to include other forms of feedback, such as Type Ia supernovae and AGN. We adopt a fairly straightforward prescription for rotation in the CGM and assume its angular momentum is aligned with that of the disk, but the angular momentum of the CGM is likely quite complicated (Cadiou, Dubois, and Pichon 2022). This could facilitate better mixing between outflows and the ambient medium, disrupting the structures that develop in our simulations.

Finally, our simulations omit two important plasma components: magnetic fields and cosmic rays. These two influences would significantly alter the behavior of outflows. Magnetic fields can slow outflows and raise the density of the inner CGM, though they also hinder metal mixing (van de Voort et al. 2021). Cosmic rays provide a form of non-thermal pressure support, allowing cold gas to occupy more CGM volume (Ji et al. 2020). Cosmic rays also lead to larger, lower density cold clouds, and keep cold gas in the CGM for longer (Butsky et al. 2020). All of these changes have implications for the galaxy's accretion of CGM gas.

Disruption is not a universal feature of CGM-focused idealized simulations. Fielding et al.

(2017) and Li and Tonnesen (2020) do not include a cold gas disk nor explicitly model star formation. Instead, they tie outflows to the amount of inflow through an inner boundary. In both cases, outflows do not cause a large-scale disruption of the CGM. Li and Tonnesen (ibid.) see a clear net balance between gas inflow and outflow in the latter half of their simulation, and both works observe clear cold gas condensation near the galaxy ($r \lesssim 100$ kpc). Yet tying outflows directly to inflows, rather than depending on the intermediary process of star formation, may under-predict the strength of stellar feedback because it neglects star formation due to gas already present in the disk. It also inputs feedback energy into a region that is spatially removed from star formation, where gas is more likely to be lower density.

3.8 Conclusions

We have run a suite of isolated, idealized Milky Way-like galaxy simulations in order to examine the ability of galaxies to self-regulate their star formation. They were specifically designed to explore the precipitation theory of self-regulation (Voit et al. 2015). The circumgalactic medium (CGM) in our galaxies was initialized in hydrostatic equilibrium with entropy profiles set by expectations from precipitation (Voit 2019). The CGM was also given an initial azimuthal rotation scaled off the estimates of Hodges-Kluck, Miller, and Bregman (2016). We explored variations in the entropy profile through the precipitation limit parameter τ in Equation 3.3 as well as variations in the rotation profile of the CGM (Equation 3.5).

Ours are the first idealized simulations to include both the CGM and explicit star formation in a rotating disk. Previous idealized CGM simulations (Fielding et al. 2017; Li and Tonnesen 2020) tied outflow directly to inflow through an inner boundary. Explicitly modeling star formation brings additional challenges, as the cold gas disk typically used as an initial condition in isolated galaxy models leads to large initial burst of star formation. Outflows from the resulting feedback quickly disrupt the CGM. This has historically not been a challenge for isolated galaxy simulations (e.g. Benincasa et al. 2016; Kim et al. 2016) because they have had an essentially non-existent CGM. To prevent the initial star formation burst from disrupting our CGM before its gas can accrete onto the

disk, we implement a ramp in the stellar feedback's efficiency parameter (Section 3.3.2.1). This ramp minimizes the impact of feedback for the first 1 Gyr. As a result, the impacts of our CGM variations become apparent.

Our work highlights that including explicit star formation in idealized simulations is crucial to understanding the galaxy-CGM connection. Alternative solutions, such as tying outflow rates directly to gas accretion rates, obfuscate important steps connecting accretion and feedback. We ultimately fail to produce isolated galaxies that are able to self-regulate their star formation, but this failure is illuminating in several ways. The primary results of our simulations are as follows:

- Idealized galaxy simulations are highly sensitive to their initial conditions. Our simulation setup is not unusual among isolated disk galaxy simulations, but complications arise when including the CGM. Chief among these is a large initial burst of star formation that can disrupt the CGM.

- Even after mitigating the initial star formation burst, our simulations contain outflows that are very disruptive to the CGM. Disruptive feedback seems to be a common feature of isolated galaxy simulations at this halo mass (Prasad et al. 2020). This indicates that current idealized simulations are missing important features that would constrain, disrupt, or backfill these outflows, such as cosmological inflow.

- Our galaxies continue to accrete gas along the midplane of the disk, despite the disruption of the CGM by outflows. Though this accretion channel contains gas with the lowest $t_{\rm cool}/t_{\rm ff}$ ratio, it is still higher than expected for a precipitation-regulated system. This accretion is able to maintain low SFRs of ~ 0.1 $M_\odot$/yr.

- Rotation in the CGM impacts the ability of gas to accrete onto the disk. This accretion also varies with the rotation profile. Rotation is therefore an important component of idealized CGM studies, and better understanding angular momentum in the CGM is an important prerequisite to informative modeling.

Understanding the balance between accretion rate and star formation first requires an understanding of the time scales over which we expect these processes to balance. While our work is not able to answer this question, we find it important for the community to consider as studies of the CGM's impact on star formation continue.

Future work will incorporate some of the physical features we have identified as potentially important for mitigating the dominance of outflows in our idealized simulations. We also wish to investigate the importance of magnetic fields and cosmic rays, particularly since the latter can dramatically affect the CGM's cold gas fraction (Butsky and Quinn 2018; Ji et al. 2020).

CHAPTER 4

QUANTIFYING THE UNCERTAINTIES IN DERIVING COLUMN DENSITIES FOR THE SIMULATED CGM

The following chapter represents work that is currently in progress. When published, the author list will likely be as follows: C. Kopenhafer, E. Taira, A. Rollins, E. Fuhrman, and B. W. O'Shea. The second, third, and fourth authors are all undergraduate students I had the pleasure of mentoring.

4.1 Chapter Abstract

Simulations of the circumgalactic medium (CGM) often compare to observations by deriving column densities for individual metal ions. This is often done by post-processing simulations and therefore involves a number of assumptions. We investigate the uncertainties introduced by two of these: the use of Solar abundances for individual elements (this work), and the choice of metagalactic UV background model for photoionization equilibrium (future work). We use chemical evolution modelling to create plausible alternatives to the Solar abundance pattern and present preliminary results for the impact of these non-Solar abundances on the column density of absorbers in the CGM. Adopting such an abundance pattern results in differences of at most ±1 dex from Solar abundance. This is larger than the differences between the multiple non-Solar abundance patterns—10^{-2}–10^{-1} dex—which were generated by assuming different set of AGB and Type II SNe yields. These differences may be used to estimate uncertainties when obtaining ionic column densities via simulation post-processing.

4.2 Introduction

The circumgalactic medium (CGM) is most commonly observed with absorption spectra. Typically, the background source for these spectra is a quasar, which is a super-luminous active galactic nucleus (AGN). Such quasar absorption spectra have been used to study the CGM in a number of surveys, including COS-Halos (Tumlinson et al. 2013), COS-Burst (Heckman et al. 2017), the COS CGM Compendium (Lehner et al. 2018), KODIAQ and KODIAQ-Z (Lehner et al. 2014; Lehner et al. 2016, 2022), Red Dead Redemption (Berg et al. 2019), CASBaH (Burchett et al. 2019; Prochaska

et al. 2019), CUBS (Chen et al. 2020), and CGM^2 (Wilde et al. 2021). Tumlinson, Peeples, and Werk (2017) provide a review of results from surveys such as these, which together paint a picture of the CGM as a chemically enriched multiphase medium traced by a wide range of metal ions.

With such a prevalence of absorption line data, more attention has been paid to the uncertainties that arise when extracting physical information from quasar spectra. Generally, absorption features are fitted to extract information such as the column density, velocity centroid, and velocity dispersion. Multiple ions, including metal ions, may then be used in conjunction to estimate gas properties such as density, temperature, and metallicity. A key assumption of this analysis is that absorption features map to distinct "clouds" with singular values for each of the gas properties. Features at the same line of sight (LOS) velocity are typically assumed to be part of a coherent flow but Haislmaier et al. (2020) show that multiple gas components may be necessary to describe all observed ionization states. Using a single component is only able to reproduce the average metallicity of a multiphase structure (Marra et al. 2021). By analyzing synthetic spectra made from simulations, Marra et al. (2022) found that spatially distinct cloud structures could contribute to the same absorption feature by virtue of overlapping in LOS velocity. Moreover, estimating gas properties from absorption lines requires assuming both collisional and photoionization equilibrium. Establishing photoionization equilibrium requires a choice for modelling the metagalactic UV background (UVB). Acharya and Khaire (2022) and Gibson et al. (2022) have both estimated uncertainties for how variations in the extreme-UV (EUV) portion of the background at $\sim$ 1–1000 Ryd (where 1 Ryd = 13.6 eV) affect estimations of metallicity and density. Acharya and Khaire (2022) find that in low-density gas ($\sim 10^{-5}\mathrm{cm}^{-3}$), the (number) density and metallicity can be uncertain by factors of 6.3 and 3.7, respectively. This is lowered for high-density gas ($\sim 10^{-3}\mathrm{cm}^{-3}$) with factors of 3.3 and 2.2 respectively. Gibson et al. (2022) found that altering the EUV slope induced changes of ~ 3 dex in metallicity.

Simulations of the CGM often compared to observations by deriving ionic column densities and then possibly full quasar spectra. Examples of such comparisons include Hummels et al. (2013), Fielding et al. (2017), Peeples et al. (2019), DeFelippis et al. (2021), and Butsky et al. (2022).

To obtain these column densities, simulators must make assumptions of their own. Typically simulations do no track individual metal elements, much less individual metal ions. Instead, ionic column densities are almost always obtained via post processing. For metal elements that are amalgamated into a single metallicity field, an elemental abundance pattern must first be assumed in order to break the metallicity into individual elements. Then to obtain ionization states, an equilibrium model and ionizing background must be assumed, just as with observations. Therefore, while simulations always have the "ground truth" about gas density, temperature, and metallicity readily available, their comparison to observations via ionic column densities may also be subject so some uncertainty from both the choice of abundance pattern and ionizing background.

A common assumption for the elemental abundances is to use the Solar abundance pattern. This is the assumption used by the Trident package[1] (Hummels, Smith, and Silvia 2017, and references therein for the Solar abundances) which is able to generate synthetic quasar absorption spectra from simulations compatible with the yt analysis framework (Turk et al. 2011). Trident is used by Peeples et al. (2019), DeFelippis et al. (2021), and Butsky et al. (2022), which were given as examples above, and a similar approach (including the use of Solar abundances) was used in Hummels et al. (2013). While the Solar abundance pattern presents its self as a straightforward choice given the effort expended to measure it, there is mounting evidence that the CGM of other galaxies does not follow the abundance pattern of our sun (Berg et al. 2019; Chen et al. 2020; Das et al. 2021; Gupta et al. 2021; Zahedy et al. 2021). Indeed, even within our own galaxies, astronomers have found a wide range of metal-poor stars such as those in the JINAbase (Abohalima and Frebel 2018). Our current understanding is that the CGM is enriched by outflows from multiple generations of dying stars (Tumlinson, Peeples, and Werk 2017), making the choice of Solar abundances convenient but poorly justified from a physical perspective.

The other piece of the inference puzzle lies in the ionization equilibrium model. Like observers, simulators also depend on the Cloudy software package (Ferland et al. 1998, 2013, 2017) to calculate ionization fractions. While accounting for non-equilibrium ionization could impact ionic column

[1] http://trident-project.org/

densities (e.g. Sarkar, Sternberg, and Gnat 2022), it is not possible to assume non-equilibrium ionization during post-processing and most simulations are not set up to handle the computational complexity and expense *in situ*. We therefore focus our attention on the main uncertainty incurred by equilibrium ionization models for both simulations and observations: the metagalactic UVB. As mentioned above, the impact of alternative UVB models has been characterized for observations (Acharya and Khaire 2022; Gibson et al. 2022) but this same exercise has not yet been completed for simulations.

Additionally, a key assumption of metagalactic UVB models is that they represent the radiation field far from any one individual source. Galaxies are themselves a source of UV radiation due to both their young and post-main sequence stellar populations, so it is feasible that this radiation could affect the ionization of the CGM. Both Werk et al. (2014) and Upton Sanderbeck et al. (2018) have estimated the impact of galaxy UV emission on quantities inferred from quasar spectra. Upton Sanderbeck et al. (ibid.) estimated the impacts of non-stellar galaxy emission and found it could be comparable to the UVB within 100 kpc of Milky Way-like galaxies. In their Appendices, Werk et al. (2014) found that stellar emission may dominate over the background depending on distance, star formation rate (SFR), and escape fraction ($\sim$ 5%), dominating at $r \lesssim 50$ kpc for even modest SFR < 1 $M_\odot$ yr^{-1} but only affecting absorbers with column densities below $\log_{10}\ N/(\mathrm{g\ cm^{-2}}) \sim 16.5$. We believe the effects of stellar UV emission on the CGM are worth revisiting from the simulation perspective, especially since simulations have more complex star formation histories (SFHs) easily available. Additionally, dust models incorporated into stellar population synthesis codes such as FSPS (Conroy, Gunn, and White 2009; Conroy and Gunn 2010; Foreman-Mackey, Sick, and Johnson 2014) allow for a more nuanced frequency-dependent attenuation of UV radiation than a constant escape fraction.

In this work, we estimate the uncertainty introduced into post-processed CGM ionic column densities by both the assumption of elemental abundance pattern and incident ionizing radiation. The latter is further broken down into two parts: the metagalactic UVB and contributions from host galaxy stellar populations. What is presented here are preliminary results from this investigation that

cover modifications to the abundance pattern. In Section 4.3 we discuss the multiple components used for this investigation including the simulations we are analysing, the algorithms for identifying absorbers and their column densities and our methods for modelling non-Solar abundance patterns. Section 4.4 contains preliminary results, and in Section 4.5 we discuss these results and present our initial conclusions. Expansions to the pilot studies present herein, as well as planned modifications to the ionizing UV spectrum, are discussed in the next chapter in Section 5.3.

4.3 Methods

We have used five of six the FOGGIE cosmological simulations[2] for our preliminary investigation (Peeples et al. 2019; Simons et al. 2020).[3] This is a suite of zoom-in simulations of galaxies chosen to resemble the Milky Way at $z = 0$. These simulations are structured to have high spatial resolution in the CGM. This high resolution broadens the metallicity distribution of the gas without affecting its median (Corlies et al. 2020). It has also been shown by many groups that improved CGM resolution naturally leads to the development of small clouds (Mandelker et al. 2019; Peeples et al. 2019; Rhodin et al. 2019; Suresh et al. 2019; van de Voort et al. 2019). Lehner et al. (2022) find that there is remarkably good agreement between the gas metallicity of HI-absorbing clouds in FOGGIE and the inferred metallicity of HI absorbers from the KODIAQ-Z survey at $z \sim 2$–3. These traits make the FOGGIE simulations an ideal testbed for our uncertainty quantification. The properties of the six FOGGIE halos are summarized at both $z = 0$ and $z = 2$ in (Simons et al. 2020). The halos we use are named Hurricane, Blizzard, Squall, Maelstrom, and Tempest.

Our analysis focuses on redshifts $z = 1.5$, 2.0, and 2.5 (though only results for $z = 2.0$ and 2.5 are presented herein). At these epochs, the FOGGIE halos have properties resembling typical star-forming galaxies (i.e., Milky Way progenitors) and do not experience major mergers at $z < 2$. The reason for this is twofold. The cosmic star formation rate density peaks at $z \sim 2$ ("cosmic noon"), driving up the amount of enriched material being blown into the CGM. Though explorations of the impact of galaxy UV emission on CGM ions is not discussed in our preliminary results, the

[2]Full list of papers and collaborators at https://foggie.science.

[3]Data from the sixth FOGGIE halo—named Cyclone—was presenting technical challenges that were not resolved in time for the writing of this dissertation. Issues with this halo should not affect preliminary results for any other halo.

cosmically high rate of star formation should also translate to a high rate of UV emission from young stars in any individual galaxy. Additionally, this is also a redshift range targeted by several quasar absorption studies of extragalactic CGMs because absorption features from this restframe are accessible to ground-based telescopes (Lehner et al. 2014; Fumagalli, O'Meara, and Prochaska 2016; Lehner et al. 2016; Nielsen et al. 2020; Lehner et al. 2022).

For quantifying the uncertainty in abundance pattern, we do not vary the UVB and instead assume the Haardt and Madau (2012) model.

4.3.1 Identifying Absorbers

The Trident software package (Hummels, Smith, and Silvia 2017) was created to generate mock quasar spectra from simulations along arbitrary lines of sight. As one of its intermediate steps, Trident calculates number densities for any combination of desired ionization states. It is this latter capability for which we use Trident.

Even if a simulation tracks the individual density of certain metal elements (e.g. EAGLE, which tracks C, N, O, Ne, Mg, Si, and Fe; Schaye et al. 2015), most metals are agglomerated into a single metallicity field. This is the case for the FOGGIE simulations, where no metal elements are tracked individually. The number density n_X of an individual element X must then be inferred assuming an abundance pattern A following

$$n_X = n_{\rm H} Z \left(\frac{n_X}{n_{\rm H}}\right)_A \tag{4.1}$$

where n_H is the total hydrogen number density, Z is the metallicity, and $(n_X/n_{\rm H})_A$ is the abundance of X relative to hydrogen. By default, Trident assumes Solar abundances $(n_X/n_{\rm H})_\odot$. The number density n_{X_i} of an individual ion i of element X is then given by

$$n_{X_i} = n_X f_{X_i} \tag{4.2}$$

where f_{X_i} is the ionization fraction of the ith ionization state. These ionization fractions are interpolated from pre-computed CLOUDY tables (Ferland et al. 2013). Trident offers several such tables, as well as the ability for the user to supply their own. One of the primary differences between the tables Trident offers is the assumed metagalactic UVB.

Once the desired ionic number densities n_{X_i} have been calculated, we are able to extract absorbers using the SALSA code (Boyd et al. 2020). For observations, absorbers are identified through their absorption line features within quasar spectra. Underlying gas properties such as density and temperature may then be inferred from the line properties. While SALSA offers a similar method for identifying absorbers (fitting Voigt profiles to mock quasar spectra produced by Trident) it has an additional algorithm that identifies absorbers directly from simulation cell (or particle) data. This method, called SPICE, retains the underlying gas information for each absorber.

SPICE identifies absorbers based on their number density.[4] First, a threshold number density is set such that a significant fraction—typically 80%—of the total column density along the LOS lies above the threshold. Intervals are then defined to encompass all regions that have number density above this threshold. A new number density threshold is calculated to repeat the process ignoring those regions already identified as having sufficient column density. These two generations of intervals are combined if they overlap physically along the LOS and their average line-of-sight velocities are within 10 km/s of each other. This value is below the velocity resolution of most moderate resolution spectrographs. This process is repeated until the total column density of the remaining, unmasked cells falls below a column density cutoff. By default this cutoff $\log_{10} N_{X_i} = 13$ but in future alternative thresholds may be tested. The result is a set of intervals—pairs of start and end indices for cells along the LOS—defining absorption features.

In addition to identifying absorbers, SALSA also offers tool for identifying lines of sight. The impact parameter for each LOS is randomly chosen such that $b < 15$ kpc. The center of the LOS is then randomly placed at this radius in a spherical shell around the galaxy, defining a vector between the galaxy center and the LOS center. Perpendicular to this vector, the LOS extends 300 kpc to either side in a random orientation. For this pilot study, we restrict our analysis to four lines of sight around each halo at each redshift.

The general procedure for our investigation is then as follows:

1. Select a redshift ($z = \{2.0, 2.5\}$) and one of the five FOGGIE halos.

[4] A detailed example of the algorithm can be found at https://salsa.readthedocs.io/en/latest/absorber_extraction.html

2. Select four lines of sight through the CGM.

3. Calculate number densities for desired ions using Trident.

4. Identify absorbers using SALSA and the SPICE algorithm.

5. Adjust the assumed abundance pattern (Section 4.3.3) or UVB (future work).

6. Repeat steps 3–5 until all alternative models are exhausted.

7. Repeat steps 1–6 for all 10 combinations of halo and redshift.

4.3.2 The Superclump Indexing System

Anything that impacts the ionic number density n_{X_i} will also impact the column density N_{X_i} of an absorber. This includes the alternative abundance patterns and UVBs explored in this work. Since SALSA's SPICE algorithm maintains the connection between an absorber and the physical space it occupies, adjusting the number density will also affect the extent of the absorber along the LOS. Lowering n_{X_i} by, e.g., adopting a non-Solar abundance pattern may result in an absorber that is shorter along the LOS than that identified in the same region of space when assuming Solar abundances. Alternatively, an absorber composed of two peaks in n_{X_i} may split into two independent absorbers when n_{X_i} is lowered. The potential for splitting in particularly a concern because it changes the total number of absorbers along the LOS.

To ensure we are comparing the same physical regions of gas between model alterations, we have developed the "superclump" indexing system. SALSA returns the starting and ending cell index of all absorbers it finds along the LOS.[5] A superclump is defined as the largest contiguous span of cells covered by an absorber. An example of this system is shown in Figure 4.1 using N IV for a single LOS. The top panel shows the span in cell index of a few superclumps and their associated absorbers. The black bars indicate some of the superclumps in this LOS, which are labeled with their (zero-indexed) ID. The thinner colored bars correspond to three different CGM abundance patterns. These patterns will be discussed more in Section 4.3.3. The bottom

[5]The absorber's span of cell is a half-open interval such that the ending cell is excluded from the interval.

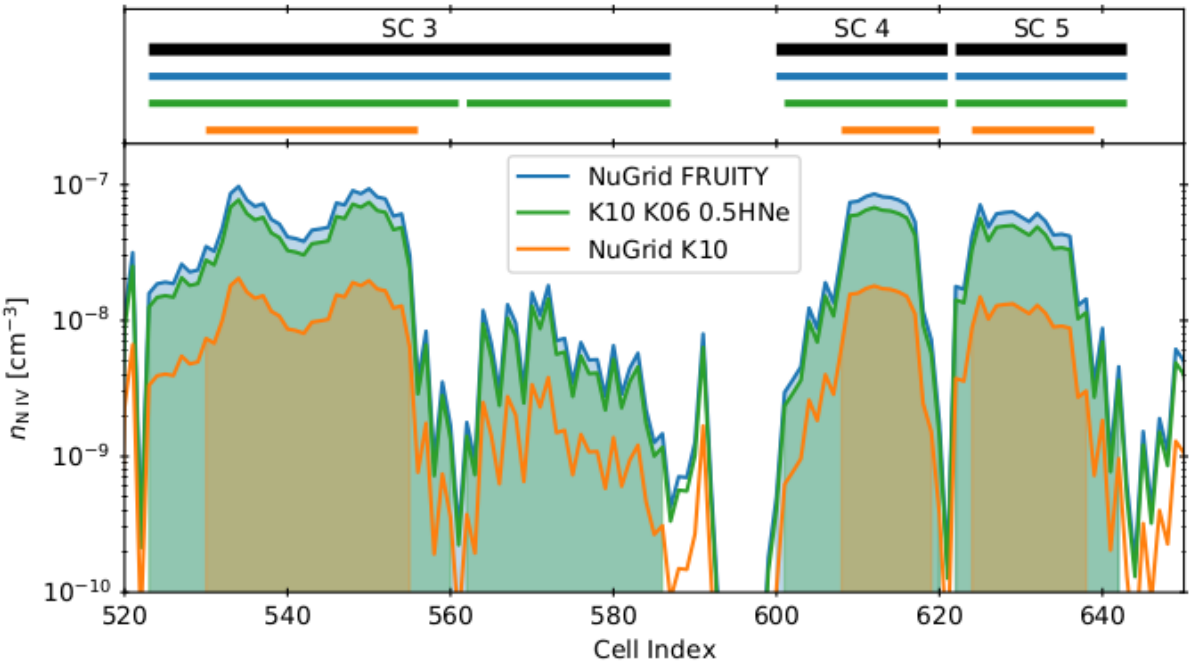

Figure 4.1 Demonstration of the superclump indexing system using the N IV number density along one LOS for three different model abundances (see Section 4.3.3). Top panel shows the span in cells of superclumps 3, 4, and 5 (black) and its constituent absorbers (colors) for this LOS. Each color represents a CGM abundance pattern based on a different set of AGB and Type II SNe yields (see Section 4.3.3). The bottom panel shows the number density for each of these models with the absorbers shaded. Adjusting the abundance pattern affects the overall normalization of the number density, affecting what absorbers are identified. Data taken from the FOGGIE Tempest halo at $z = 2.0$.

panel shows the N IV number density $n_{\mathrm{N\,IV}}$ corresponding to these three abundance patterns. The absorbers are shaded.

From Figure 4.1 we can see how adjusting the abundance pattern can alter the $n_{\mathrm{N\,IV}}$ normalization. For superclump SC 3 in this LOS, lowering the normalization first causes SALSA to find two separate absorbers instead of one (which we call absorber "splitting"). Continuing to lower the normalization causes SALSA to only identify a much shorter span as an absorber (dubbed absorber "shortening"). SC 4 and 5 also demonstrate absorber shortening. The NuGrid FRUITY model has absorbers that "match" the span of each of the three superclumps presented here. Altogether these are examples of three of the four ways that absorbers may associate with a superclump depending on their abundance pattern: they may match its extent along the LOS, the span may split into two or

more absorbers, or the absorbers may be short compared to the superclump. The fourth possibility is that a superclump may not have an associated absorber for every abundance pattern modelled. This absorbers are simply "missing." The NuGrid K10 model in Figure 4.1 illustrates how this might happen. Even though its SC 3 absorber is technically classified as shortened, we can see from comparison with the K10 K06 0.5-HNe model that there is a second region that is no longer identified as containing an absorber when the normalization is lowered. This same phenomenon leads to missing absorbers.

There is one major caveat to defining superclumps as contiguous spans of cells. Sometimes, SPICE may find two absorbers that abut each other along the LOS; that is, the ending index of one absorber may be the starting index of another. SPICE recognizes these absorbers as separate on the basis of their LOS velocities. SPICE's threshold for merging absorbing regions is that they be within 10 km/s of each other (Section 4.3.1). To prevent the superclump system from inadvertently merging distinct absorbers, abutting "split" absorbers may only belong to the same superclump if their velocities are within 1.5σ of each other, where σ is the LOS velocity dispersion of the absorber. The value 1.5σ was chosen from individually-inspected subsets of split absorbers that were determined to belong to the same superclump and truly independent absorbers that should not be assigned the same superclump. Since 1.5σ can be a more lenient definition than the strict 10 km/s used by SPICE, this sometimes means that absorbers not merged by SPICE will be merged into the same superclump. We deem this acceptable for the sake of uniformly indexing absorbers across models.

4.3.3 Modelling Alternative Abundance Patterns

As previously noted, the FOGGIE simulations track all metal elements as a single metal density field. We turn to chemical evolution modelling to develop plausible alternatives to the Solar abundance pattern that is assumed by default by Trident. In particular, we use the OMEGA+ two-zone semi-analytic model (Côté et al. 2018), which builds on the NuGrid chemical evolution pipeline for galactic chemical evolution (Côté et al. 2017b).[6] OMEGA+ follows the evolution of

[6]https://github.com/becot85/JINAPyCEE

two reservoirs: one representing the cold gas and stellar content of the ISM and another filled with the hot gas of the CGM. Gas can be exchanged between the two reservoirs, or enter and exit the system via the CGM component. Gas within the ISM reservoir may also be converted into stars. The elemental yields of these stars throughout their evolution are traced using precomputed tables. These individual elements may flow then through the two-zone system alongside the gas assuming instantaneous mixing.

OMEGA+ supports a number of tabulated and analytic models for the evolution of key masses: the stellar mass M_*, the ISM gas mass $M_{\rm ISM}$, the CGM gas mass $M_{\rm CGM}$, and the mass of the dark matter halo $M_{\rm vir}$. The halo mass $M_{\rm vir}$ and SFR $\dot{M}_*$ as functions of time are extracted from the FOGGIE simulations (with M_{200} used for $M_{\rm vir}$). Because of its high temporal variability and frequent snapshot cadence of 5.38 Myr, the FOGGIE SFH is first smoothed using a Gaussian filter with σ = 53.8 Myr (or 10 outputs). Star formation in OMEGA+ uses as Chabrier (2003) IMF, consistent with star formation in FOGGIE. The lower and upper bounds for the IMF are 0.1 and 100 $M_\odot$ respectively, while elemental yields are restricted to 1–30 $M_\odot$. Gas flow between the CGM and ISM, characterized as $\dot{M}_{\rm ISM,in}$ and $\dot{M}_{\rm ISM,out}$, as well as gas flow into and out of the CGM ($\dot{M}_{\rm CGM,in}$ and $\dot{M}_{\rm CGM,out}$), are characterized analytically. Out of the many analytical forms offered by OMEGA+, we select models that minimize the number of free parameters while also maintaining an evolution in behavior across cosmic time.

Gas accretion onto the ISM is directly proportional to the free-fall time $t_{\rm ff} = 0.1 H_0^{-1}(1+z)^{-3/2}$ as first defined by White and Frenk (1991) (see Côté et al. 2018). For consistency with the FOGGIE simulations, we adopt H_0 = 69.5 km s−1 Mpc^{-1} from Planck Collaboration et al. (2014). The rate of infall is then $\dot{M}_{\rm ISM,in} = M_{\rm CGM}/(C_\tau t_{\rm ff})$, where the free parameter C_τ is an overall normalization. The rate of ISM outflow $\dot{M}_{\rm ISM,out} = \eta \dot{M}_*$ is selected to be both mass- and redshift-dependent (Côté et al. 2017a), with the mass loading factor $\eta = C_\eta M_{\rm vir}^{-\gamma_\eta/3}(1+z)^{-\gamma_\eta/3}$ with $\gamma_\eta = 2$. Similar to C_τ, C_η is a free parameter specifying the normalization while γ_η affects the mass and redshift dependencies.

The CGM may also accrete mass from the intergalactic medium even though the IGM is

not explicitly tracked by OMEGA+. This accretion is given by $\dot{M}_{\rm CGM,in} = \dot{M}_{\rm vir}(\Omega_{\rm M,0}/\Omega_{\rm b,0} - 1)^{-1}$. Again, we take our cosmological parameters from Planck Collaboration et al. (2014) for consistency with FOGGIE: $\Omega_{\rm M,0} = 0.285$ and $\Omega_{\rm b,0} = 0.0461$. OMEGA+ optionally allows outflow from the CGM using a fixed fraction of the galaxy mass loading factor to represent outflows that are powerful enough to escape the halo: $\dot{M}_{\rm CGM,out} = f_\eta \eta \dot{M}_*$; however, we elect to not enable CGM outflow. Our reasoning for this, as well as our choices for γ_η, C_η, and C_τ, is as follows.

The abundance pattern has a slight dependence on the CGM mass because its enriched gas is accreted by the ISM. This impacts the metallicity of future star formation, which can in theory affect elemental yields. In practice, though the parameters γ_η, C_τ, and C_η have a noticeable affect on $M_{\rm CGM}$, they have a negligible effect on the abundance pattern (0.1% at the most). By this same reasoning, we do no enable CGM outflow. We retain CGM inflow in order to fuel the star formation required by the smoothed FOGGIE SFHs, and by the same token allow the CGM to replenish itself from the IGM. ISM outflows are of course necessary to populate the CGM with metals.

Since we define $\dot{M}_{\rm vir}(t)$ and $\dot{M}_*(t)$ from the FOGGIE simulations, it should theoretically be possible to define $\dot{M}_{\rm ISM,in}(t)$, $\dot{M}_{\rm ISM,out}(t)$, $\dot{M}_{\rm CGM,in}(t)$, and $\dot{M}_{\rm CGM,out}(t)$ from these simulations as well; however, this is definitionally much more challenging. It is uncertain if the CGM—in the sense of a reservoir of multiphase gas that is in dynamical conversation with the ISM rather than a necessarily bound state of gas—extends beyond the virial radius, much less its estimate r_{200} (Lehner et al. 2020; Ho, Martin, and Schaye 2021). Moreover, the boundary between the ISM and CGM is poorly defined. Therefore, we rely on a mixture of extracted and analytic quantities as our goal is to create plausible alternative to the Solar abundance pattern rather than to recreate element-by-element the metallicity evolution of the FOGGIE simulations.

For each of the five FOGGIE halos at our two target redshifts, we create a variety of abundance patterns by swapping which tables are used for the stellar population synthesis yields. Specifically, we adjust the yield tables that combine both AGB and massive stars (i.e., core-collapse or Type II supernovae; SNe). These yield tables have the largest effect on the abundances of elements commonly observed in the CGM; in particular, carbon through sulfur. Abundance patterns made

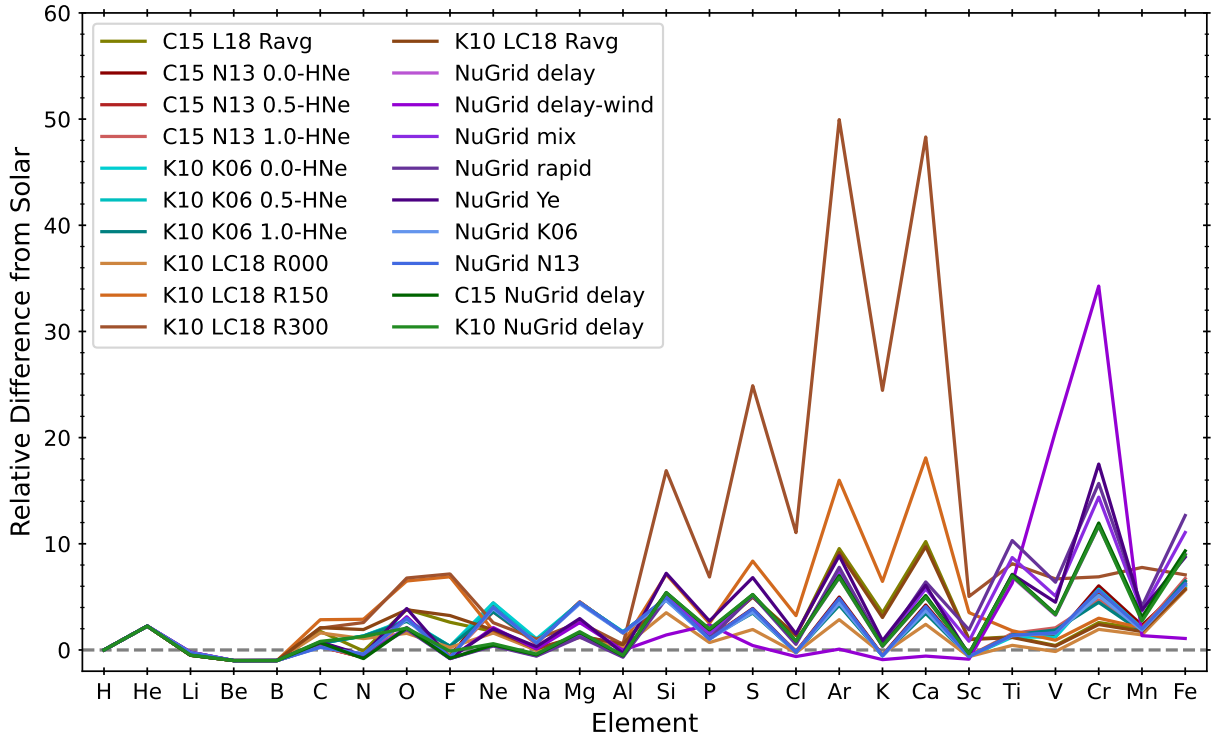

Figure 4.2 Abundance patterns (relative to Solar) generated using the AGB and Type II SNe yields in OMEGA+ and the stellar and dark matter growth of the Tempest halo up to $z = 2.0$. Colors roughly group the patterns into families. The first part of each model name references the AGB model, the second part the Type II SNe model, and any third part references variations in the Type II SNe model. The prescriptions for Type II SNe cause large variations as the elements approach iron.

for Tempest at $z = 2.0$ using all of the combined AGB and Type II SNe yield tables available in OMEGA+ are shown relative to Solar in Figure 4.2. The patterns are roughly grouped by color to show model families.

The first part of each model name references the AGB model, the second part the Type II SNe model, and any third part references model variations. K10 refers to Karakas (2010), whose AGB yields are paired with the Type II SNe yields of Kobayashi et al. (2006, K06), Limongi and Chieffi (2018, C18), and NuGrid (Pignatari et al. 2016; Ritter et al. 2018a). The AGB yields of Cristallo et al. (2015, C15) can also be paired with LC18, NuGrid, or Nomoto, Kobayashi, and Tominaga (2013, N13). Both the N13 and K06 Type II SNe models can include a mixture of supernova and hypernova yields. The fraction of hypernovae yields in this mixture (when available) can be 0.0, 0.5,

or 1.0. These variations are denoted as 0.0-HNe, 0.5-HNe, and 1.0-HNe respectively. OMEGA+ uses models from set R of LC18 which has rotation velocities of 0, 150, and 300 km s−1, giving rise to the labels R000, R150, and R300. There is also the "Ravg" model, which is a mixture of the rotation velocities (see Figure 4 of Prantzos et al. 2018). For Type II SNe, the NuGrid models treat core-collapse supernovae using the prescriptions from Fryer et al. (2012). These prescriptions treat both "delayed" and "rapid" explosion models, and the "mix" yield model refers to a half-and-half mixture of the two. There is also a version of the delayed models with pre-SNe winds (dubbed "delay-winds"; Ritter et al., in prep) and a "Ye" model that adjusts the location inside the massive star from which the explosion is launched based on the electron fraction Y_e (Côté et al. 2017a). NuGrid can also supply AGB models, which may be paired with K06, N13, or its own "delay" Type II SNe models.

All together, we have 20 stellar yield models that, with OMEGA+, allow for 20 non-Solar abundance patterns for each halo and redshift combination. For this preliminary work, this large set of models will help us assess the scale of variation induced by 1) the use of a non-Solar abundance pattern and 2) the propagation of uncertainties inherent to generating our alternative models. The results that follow serve as a proof of concept that will allow us to scale up our analysis and make our conclusions more statistically robust.

4.4 Preliminary Results from Modifying the Abundance Pattern

The results that follow focus on the ionization states of six elements that are commonly observed in the CGM: C, N, O, Mg, Si, and S. The ionization states considered span C II–IV, N II–V, O II–VI, Mg II, Si II–IV, and S II–VI.

Given the wide variety of AGB and Type II SNe yield models available to OMEGA+ (Section 4.3.3), we characterize their impact by determining the median and median absolute deviation (MAD)[7] of the ionic column density across all non-Solar models for each superclump. These statistics are applied in log space such that we will be presenting med($\log_{10} N_{X_i}/(gcm^{-2})$ and MAD($\log_{10} N_{X_i}/(gcm^{-2})$). For more concise notation we will drop the units in the denominator

[7]Defined as med($|X_i - \tilde{X}|$) where $\tilde{X}$ is the median of $\{X_i\}$

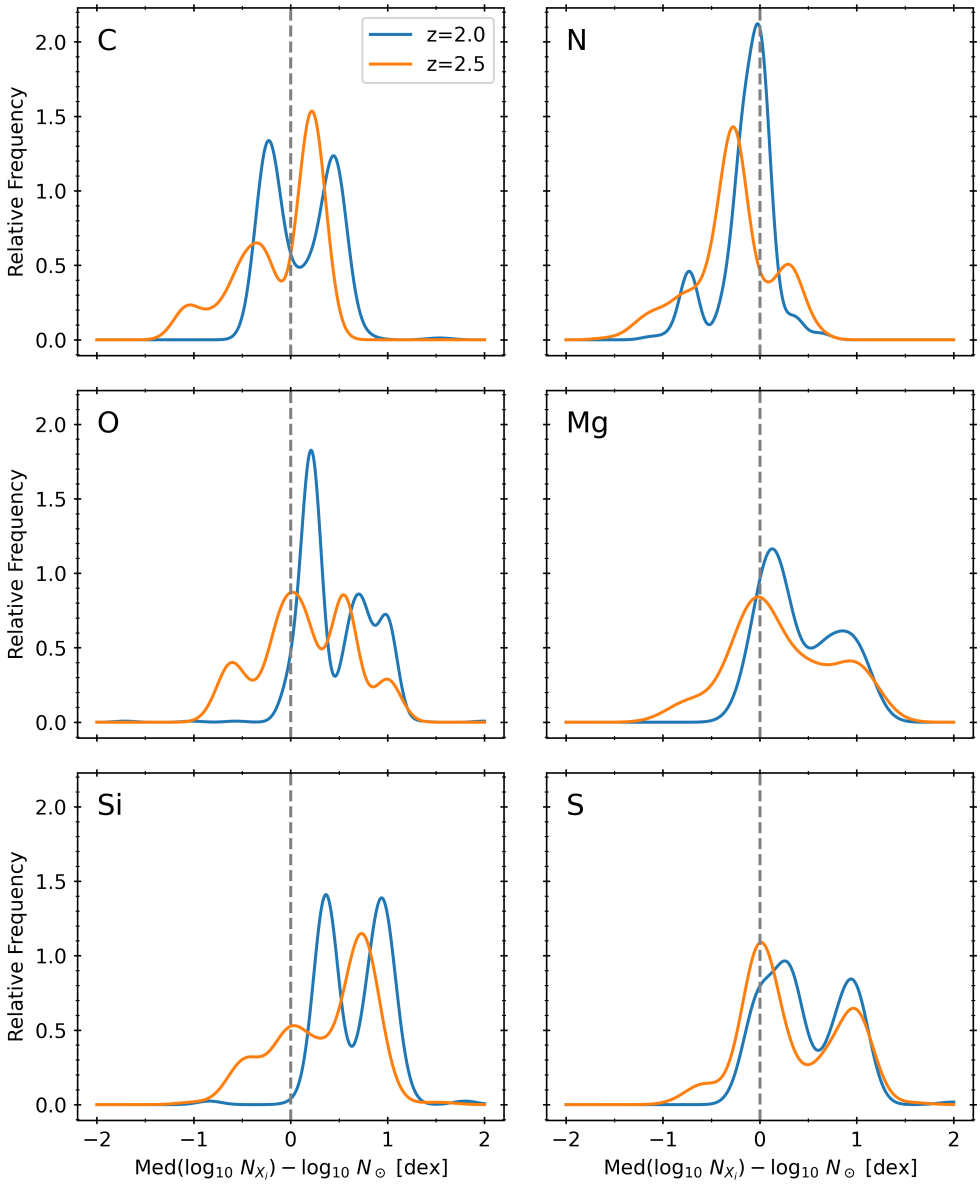

Figure 4.3 Kernel density estimators (KDEs) for the distribution of $\mathrm{med}(\log_{10} N_{X_i}) - \log_{10} N_{X_i}$, which is the difference between the median non-Solar column density for a superclump and the column density of that same superclump given Solar abundances. These differences are shown for six elements—C, N, O, Mg, Si, and S—at two redshifts. Redshift 2 is in blue and 2.5 is in orange. Data from all halos and all considered ionization states (see text) are compiled together at each redshift. A vertical dashed line marks a difference of zero.

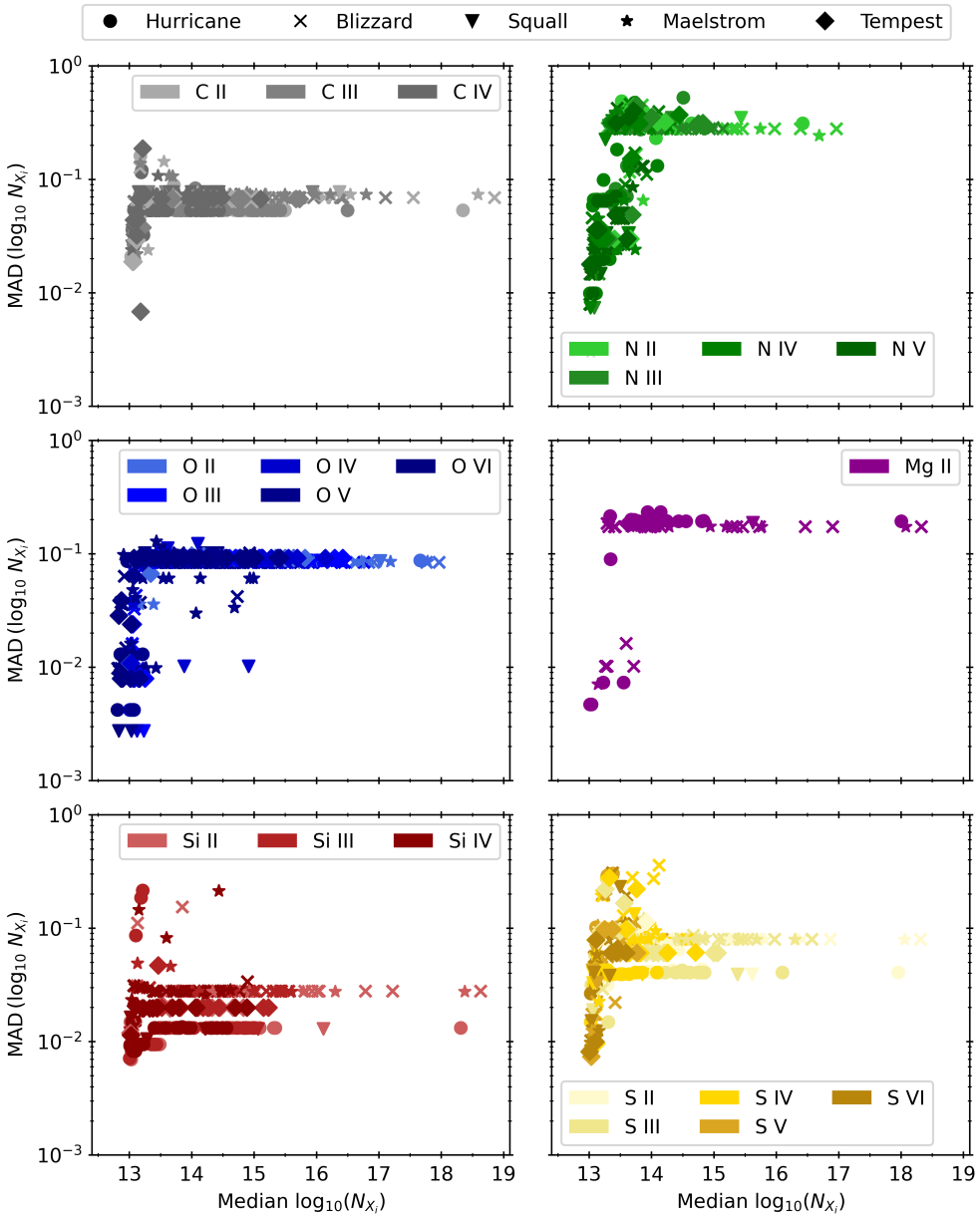

Figure 4.4 Variation in log column density $\log_{10} N_{X_i}$ within a superclump (as quantified through MAD) versus the median column density for that same superclump. Each panel shows ions for the six elements in Figure 4.3 with darker colors indicating higher ionization states. Superclump data is shown for the five FOGGIE halos (designated with symbols) at redshift $z = 2.0$. The column density variation has almost no dependence on the column density of the superclump itself, being largely constant except at the lowest column densities. This trend hold at $z = 2.5$.

moving forward. There are also other quantities of interest associated with the absorbers in each superclump such as density, temperature, and distance from the galaxy center. In order to assign these auxiliary quantities to our superclumps, we average together the values for each constituent absorber weighted by that absorbers column density. Therefore, absorbers that more closely match the superclump have greater weight as the absorber column density necessarily decreases if absorbers are split or shorter than their superclump.

Figure 4.3 compares med($\log_{10} N_{X_i}$) of all non-Solar abundances to the $\log_{10} N_{X_i}$ derived using Solar abundances. This comparison is made at both at $z = 2.0$ and $z = 2.5$. The distribution of differences are presented using a kernel density estimator for data from all of the ionization states and FOGGIE halos. Importantly, since the abundances for these target elements almost always exceed Solar (see Figure 4.2), a superclump may sometimes not have a partner when using Solar abundances because the overall ionic number density will be lower (see the superclump explanation in Section 4.3.2). The frequency of this depends on redshift, being slightly more frequent at $z = 2.0$ than at $z = 2.5$. For C, N, O, and Mg the frequency of lacking a Solar-abundance absorber is about 25–33% at $z = 2.0$ and 20–30% at $z = 2.5$. For Si the frequency is 53% and 46% at these two redshifts, and 66% and 57% for S. Si and S are also the elements with the largest deviations from Solar as demonstrated in Figure 4.2. The general tendency of the non-Solar abundances to be higher also means that the differences in Figure 4.3 tend to be positive. The exception is N, which in Figure 4.2 can be seen to have sub-Solar abundance for several models. Differences tend to be at most 1–1.5 dex.

In Figure 4.4 we look at the variation in column density across the 20 non-Solar abundance patterns for each FOGGIE halo at $z = 2.0$. The variation MAD($\log_{10} N_{X_i}$) is plotted against med($\log_{10} N_{X_i}$) to uncover any possible correlation between the median column density of a superclump and the variation induced by the abundance pattern. The same six elements are in Figure 4.3 are shown with multiple non-neutral ionization states for each. The five FOGGIE halos—Hurricane, Blizzard, Squall, Maelstrom, and Tempest—are distinguished using symbols. The column density MAD appears to have some variation with absorber column density at low

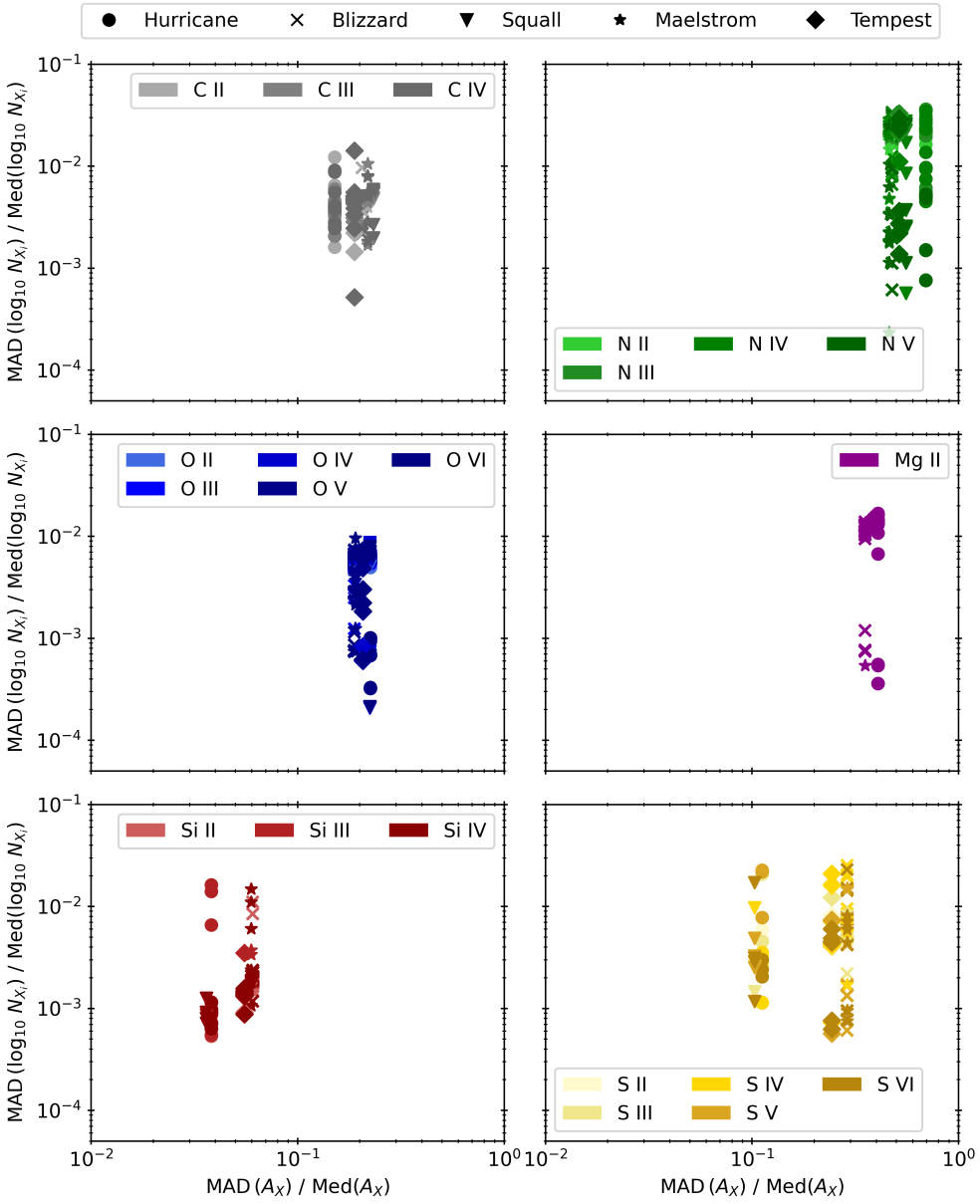

Figure 4.5 Relative variation in log column density $\log_{10} N_{X_i}$ within a superclump versus the relative variation in non-Solar elemental abundance A_X. Both variations are quantified using the MAD and presented relative to their median value. Results are presented for the same ions and simulation data as in Figure 4.4. The relative variation in input abundance A_X generally leads to a decreased fractional variation in column density. There is no correlation between the two quantities. These results also hold for $z = 2.5$.

values of $\log_{10}(N_{X_i}/(g\ cm^{-2})) \sim 13$–$15$ but is otherwise largely constant with median superclump column density. This is true even across ionization state. The constant $\mathrm{MAD}(\log_{10} N_{X_i})$ varies with halo but generally falls around ~ 0.1 dex and $\mathrm{MAD}(\log_{10} N_{X_i})$ is never greater than 1 dex. These trends hold for redshift $z = 2.5$ as well. Additionally, $\mathrm{MAD}(\log_{10} N_{X_i})$ shows no dependence on gas density, temperature, or distance from the galaxy halo.

The variation in column density $\mathrm{MAD}(\log_{10} N_{X_i})$ is an output that results from an input variation in elemental abundance $\mathrm{MAD}(A_X)$. Figure 4.5 explores how these two variations are linked for the abundance patterns modelled at $z = 2.0$. The variation in abundances and column densities are presented relative to their medians for easier comparison across elements. Each halo has a fixed $\mathrm{MAD}(A_X)/A_{X_\odot}$ of $\sim 10\%$ due to their unique histories of stellar and halo mass growth, but these result in a spread of $\mathrm{MAD}(\log_{10} N_{X_i})$ of a few percent or less. The variation in $\log_{10} N_{X_i}$ across non-Solar models is independent of the variance in A_X, and these results also hold true at $z = 2.5$.

4.5 Discussion & Conclusions

In order to compare with observations, it is common for simulations of the CGM to calculate number densities for a number of metal ionization states. Given that simulations track most if not all of the metal elements in a single density field, this must be done as a post-processing step that requires multiple assumptions.

For the preliminary investigation presented in this work, we explore how the assumption of Solar abundances affects the column density of simulated absorbers. We used the chemical evolution code OMEGA+ (Côté et al. 2018) to develop plausible alternative abundance patterns. These models are tuned to the halo and stellar growth experienced by five of the FOGGIE cosmological simulations. These simulations then serve as the test bed for our uncertainty quantification. In order to come up with a suite of non-Solar models, we vary the AGB and Type II SNe yields used by OMEGA+, as these yields have the largest impact on the elements commonly observed in the CGM. This allows us to address two questions: what is the impact of adopting a non-Solar abundance pattern, and how does the uncertainty within those alternative abundance pattern models propagate

to absorbers in the CGM?

Though we have so far only processed four lines of sight, our initial results show that adopting a non-Solar abundance pattern has a larger impact on absorber column density $\log_{10} N_{X_i}$ than picking any one particular OMEGA+ model. The spread in column densities across all possible OMEGA+ models tends to be 10^{-2}–10^{-1} dex, which equates to a relative difference of a few percent or less. On the other hand, the differences from Solar abundances are not uncommonly ±1 dex. Scaling up our proof-of-concept tests will help fill out the KDEs in Figure 4.3 and thereby allow us to more precisely quantify these differences, but we don't expect our conclusions to be dramatically affected. Even with this preliminary analysis, we can provide this estimate of the uncertainty in absorber column density for those that post-process their CGM simulations.

The spread in absorber column density across models—as characterized through the MAD—appears to be independent of the variation in elemental abundance or absorber properties like density, temperature, and distance from the galaxy. This apparent non-correlation could be better quantified if we extended our analysis to more lines of sight.

Our initial findings have interesting implications for simulation post-processing. As described in Section 4.2, adopting Solar abundances is not physically plausible. Chemical evolution models make it possible to tie the abundance pattern to the growth history of the simulated halo, allowing for greater theoretical self-consistency. Chemical evolution introduces additional uncertainties including parameterized models, stellar yields, and the underlying core assumption that metals instantaneous mix uniformly throughout the CGM.

In Section 4.3.3 we explained that many of the free parameters in OMEGA+ have little affect on the resulting abundance pattern. Our results in Section 4.4 demonstrate that uncertainty in the yield models translates to negligible variation in column density. Moreover, there is very good agreement in $MAD(\log_{10} N_{X_i})$ between the FOGGIE halos. While each of the five halos has a unique environment and merger history, they were all chosen to both resemble the Milky Way at $z = 0$ as well as to resemble its growth history. Therefore, uncertainty due to modelling choices within OMEGA+ and even variation in the growth history of Milky Way-like halos has minimal

impact on the resulting column densities of simulated absorbers. This is very reassuring for anyone wishing to use chemical evolution modelling to replace the Solar abundance pattern, as the details of the model contribute negligible uncertainty.

The one uncertainty of chemical evolution modelling that we *cannot* address here is the assumption of instantaneous mixing. Quantifying this uncertainty would require tracking individual elements within a simulation. There would undoubtedly be dependencies on quantities such as density and temperature given that galactic outflows are the primary source of CGM enrichment. Yet we highlight that this assumption is *also* inherent to adopting Solar abundances as is currently the common practice. A possible remedy would be to adopt different abundances based on the underlying gas properties, but in general, addressing this core assumption strains the limits of what simulation post-processing can accomplish.

CHAPTER 5

SUMMARY AND CONTINUING WORKS

In this final chapter, we briefly summarize each of the preceding scientific projects (Chapters 2–4) before describing future research directions. Each chapter is considered in order.

5.1 Chapter 2, Wherein We Investigated Simulated Analogs to the Observed breakBRD Galaxies

In Chapter 2 my coauthors and I analyzed data from the IllustrisTNG simulation (Pillepich et al. 2018b) in an attempt to understand an unusual population of disk galaxies seen in observations (Tuttle and Tonnesen 2020). These unusual galaxies were named the "breakBRDs" after their observational signatures; signatures that indicated they had recent star-formation in their centers but red disks. As we talked about in Section 1.2.1, a red color is an indicator of little-to-no star formation. Usually, galaxies are believed to cease their star formation (aka "quench") from the inside-out. The breakBRDs were therefore intriguing because they appeared to quench from the outside-in.

In an effort to understand the observed breakBRDs we applied similar selection cuts to galaxies within the IllustrisTNG-100 (TNG100) dataset—where the "100" indicates the size of the simulation domain, $(100\ \mathrm{cMpc})^3$—in order to find sets of "breakBRD analogs". We looked for these analogs at multiple redshifts $x \leq 0.5$ in order to get a sense of their evolution but focused on those at $z = 0$. Rather than explicitly limit our search based on morphology, we restricted galaxies to stellar mass $10 < \log_{10}(M_*/\mathrm{M}_\odot) < 12$ assuming that giant elliptical galaxies would naturally be excluded. We also placed a requirement on physical size for resolution considerations, and these two requirements gave us the "parent" population from which the breakBRD analogs would be selected. The breakBRD analogs, in turn, were selected using spectral and photometric cuts that mimicked those used to define the observed breakBRDs. For comparison, we weighted the parent sample to match the stellar mass distribution of the breakBRD analogs in order to remove confounding mass-dependent effects (like those in Section 1.2.2). We also further divided both

parent and analog samples into central and satellite galaxies.

Just as with the observed population, the breakBRD analogs are a small fraction ($< 5\%$) of their parent sample. While not quenched, the analogs also have lower sSFR than their parent sample. This is also consistent with the observed breakBRDs whose sSFRs classifies them as green valley galaxies (that is, they have sSFRs between the star-forming and quenched populations). Additionally, the breakBRD analogs exhibit centrally-concentrated star formation and dense gas—confirmation that the breakBRD selection criteria perform similarly in both observations and the IllustrisTNG simulation.

In particular, we found that the concentration of dense, star-forming gas in the analog's center was due to gas stripping at the outskirts. This is peculiar for central galaxies in particular (since satellites can undergo a number of processes, such a ram pressure stripping, that remove their gas) but we found no clear evidence for why the breakBRD analogs might have acquired their structure. The fraction of satellites and splashbacks (that is, galaxies that were temporarily satellites) is higher among the analogs, and though not statistically significant, the central breakBRD analogs have had less dark matter, stellar, and central black hole mass growth than the parent sample since $z = 0.5$. These findings imply the influence of more subtle environmental effects than we were able to investigate, possible acting over a long period of time. By applying the breakBRD selection criteria at multiple redshifts and comparing the overlap in samples, we were able to estimate that galaxies stay in the "breakBRD state" for between a few hundred Myr and ~ 2 Gyr before fully quenching their star formation.

As stated at the end of Chapter 2, my co-authors and I recommended that followups to the original breakBRD observations should investigate their gas distribution in more detail to see if real breakBRD galaxies also show evidence of a gas deficit in their outskirts and any signs of future quenching. Additionally, I began to investigate the CGM of the breakBRD galaxies on the basis that the CGM could be influencing the galaxy's gas accretion. To that end, Figure 5.1 shows the CGM entropy profiles of the breakBRD analogs compared to their parents. First, I took either the mass-weighted average (top row) or the median (bottom row) of each galaxy's scaled entropy; that

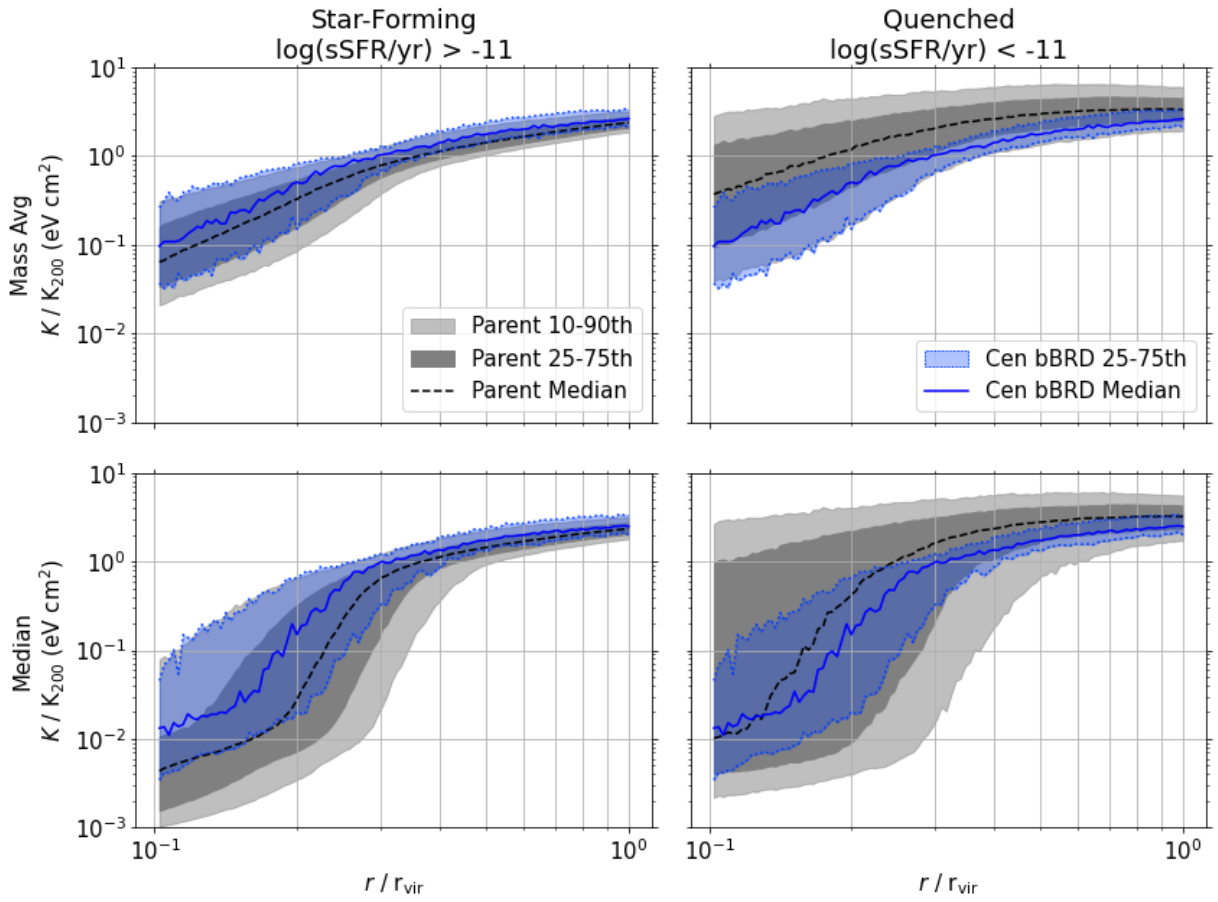

Figure 5.1 Scaled CGM entropy profiles for the central breakBRD analog galaxies (blue), compared to their star-forming ($\log_{10}(\mathrm{sSFR}) > -11$; left) and quenched ($\log_{10}(\mathrm{sSFR}) < -11$; right) parent galaxies (gray). Each galaxy has its scaled entropy (K/K_{200}) profile described by either a mass-weighted average (top) or via the median (bottom). These profiles are binned in r/r_{200} and percentiles of each radial bin are shown. The solid blue line and dashed black line show the 50th percentile (median) of each bin, blue and dark gray shading the 25–75th percentiles, and light gray the 10–90th percentiles (for the parent only).

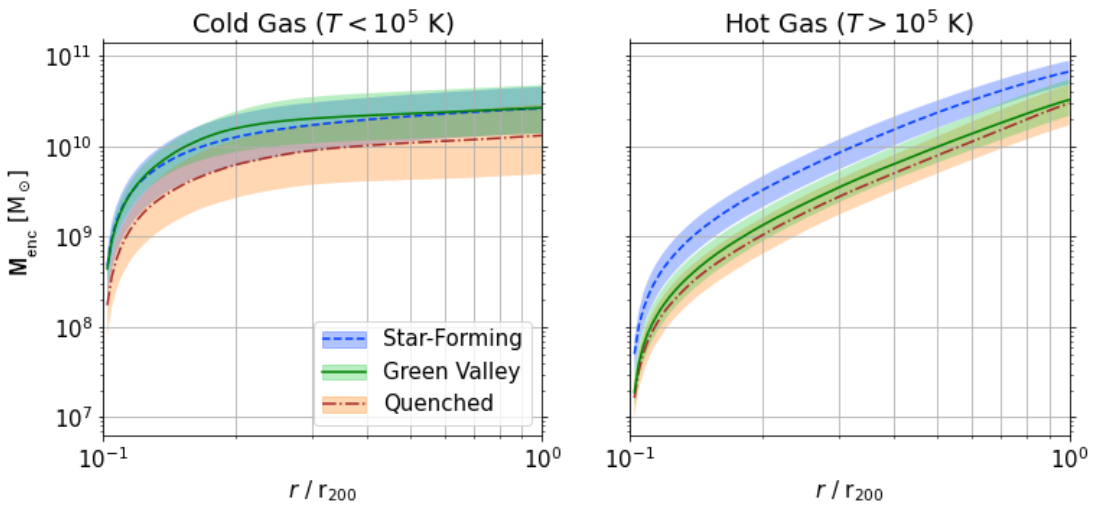

Figure 5.2 Mass enclosed within different radii r/r_{200} for cold ($T < 10^5$ K; left) and hot ($T > 10^5$ K; right) CGM gas around TNG100 galaxies with $10^{12} \leq M_{\rm vir} \leq 10^{12.5}$ $M_\odot$. These galaxies are divided into star-forming ($\log_{10}({\rm sSFR}) > -10.5$; blue), green valley ($-11.5 < \log_{10}({\rm sSFR}) < -10.5$; green), and quenched ($\log_{10}({\rm sSFR}) < -11.5$; orange) populations. Lines show the population median in each bin, while shading shows the 25th–75th percentiles.

is, the entropy relative to the virial entropy K/K_{200}. For each aggregation method, the resulting radial profile is binned in r/r_{200}. By scaling the entropy and radius to the (approximate) virial values for each halo, I can remove any dependence on halo mass. Figure 5.1 shows percentiles for these sets of binned radial profiles and compares the breakBRD analogs in blue to their star-forming and quenched parent samples in gray (left and right, respectively). The parent sample is divided on $\log_{10}({\rm sSFR}) = -11$. We can see that the overall entropy of the CGM tends to increase as galaxies transition from star-forming to quenched, with the breakBRD analogs appearing to fall in between the two populations.

This investigation was eventually expanded to also look at all green valley galaxies in TNG100 with $10^{12} \leq M_{\rm vir} \leq 10^{12.5}$ $M_\odot$. We defined the green valley by $-11.5 < \log_{10}({\rm sSFR}) < -10.5$. The breakBRD analogs and more general green valley populations exhibited somewhat different properties; for example, the 50th percentile profiles for the green valley galaxies was below that for the star-forming galaxies within $\sim 0.3r_{200}$ and above for $r \gtrsim 0.3r_{200}$ while the same profiles for the breakBRD galaxies are consistently higher than their star-forming parent (Figure 5.1). Figure

5.2 shows some results from this broader investigation, comparing the green valley galaxies to star-forming and quenched galaxies with $10^{12} \leq M_{\rm vir} \leq 10^{12.5}$ $M_\odot$. The CGM mass enclosed at a given radius is split between two temperature regimes, cold ($T < 10^5$ K; left) and hot ($T > 10^5$ K; right). As with Figure 5.1, what is plotted are the percentiles within each scaled radial bin. Interestingly, the mass profile for cold green valley gas matches that of the star-forming galaxies, while for the hot gas is matches the quenched galaxies. These similarities may be indicative of how the CGM in TNG100 changes as galaxies quench. Notably the star-forming CGM has more gas overall, including hot gas.

While there is clear evidence of a transitional CGM state, the more meaningful scientific question concerns whether a change in the CGM caused the changes to galaxy star formation concentration or was the result of it. This question is significantly harder to untangle. Around this time, Zinger et al. (2020) published their analysis of the average CGM entropy for both TNG100 and IllustrisTNG-300 (TNG300) galaxies. The TNG300 dataset uses the same physics as the TNG100 dataset but simulates a larger volume—$(300\,\text{cMpc})^3$ instead of $(100\,\text{cMpc})^3$—and therefore includes a larger sample of galaxies. Instead of looking at radial profiles as I had done, Zinger et al. (ibid.) average over all non-star-forming gas cells that fall within the radii they associate with the CGM (see text for more details). They also find that there is an increase in entropy as galaxies move from star-forming to quenched (which they also divide using $\log_{10}(\text{sSFR}) = -11$) but find that this transition is strongly correlated with the mass of the black hole. Around $M_{\rm BH} = 10^{8.3}$ $M_\odot$, the energy injected by the black hole's kinetic mode begins to dominate over that injected by the thermal mode (see Section 1.3.2.5), which lowers the galaxy's sSFR (Terrazas et al. 2020). This is also the black hole mass around which the CGM entropy experiences a jump and at which galaxies become quenched (see also Weinberger et al. 2018).

Rather than solving the "chicken-and-egg" problem between the state of the CGM and quenching, the results from Zinger et al. (2020) indicate that quenching and changes to the CGM are *both* the result of black hole feedback (at least for simulations using the IllustrisTNG model). Though the question of "which came first" is by no means settled in terms of the drivers of quenching—and

as Chapter 2 showed, the breakBRD galaxies are not typical galaxies—I set aside this particular line of inquiry. If I were to pick it back up again with the IllustrisTNG simulations, I would switch to using the IllustrisTNG-50 dataset (Nelson et al. 2019a; Pillepich et al. 2019), which has fewer galaxies overall but better resolution within each individual galaxy. In my preliminary analysis I had difficulty analyzing the CGM very close to the galaxies in TNG100 due to limited resolution. Alternatively, it would be prudent to look at other cosmological simulations for breakBRD analogs and green valley galaxies in general, as the circumstances and evolutionary drivers for each may be model dependent. At the very least, quenching in IllustrisTNG appears sensitive to their implementation of AGN feedback.

5.2 Chapter 3, Wherein We Used Idealized Galaxy Simulations to Explore the Self-Regulation of Star Formation

In Chapter 3 we used a set of idealized simulations of isolated, Milky Way-like galaxies to explore the ability of galaxies to self-regulate their star formation. In particular, we focused on the "precipitation" theory for self-regulation (Voit et al. 2015). Simulations of idealized disk galaxies are common in the literature, but they often do not include a CGM. On the other hand there have also been idealized simulations focused on the behavior of the CGM like Fielding et al. (2017) and Li and Tonnesen (2020), but while these simulations include models for galactic outflows, they do not explicitly model star formation as is common in simulations of galactic disks. Our work therefore represents a mixture of these two approaches, modelling a disk galaxy with explicit star formation but also including the CGM. We ran a total of six models, varying the initial CGM structure (based on the initial ratio of $t_{\rm cool}/t_{\rm ff}$), the rotation profile of the CGM (which is often not accounted for in idealized simulations), and completely disabling stellar feedback. Each variation experienced different amounts of gas accretion and star formation in line with their CGM properties.

Idealized simulations let us study the long-term behavior of galaxy in isolation, but as noted in Section 1.3.2.1 their initial conditions can be a big source of uncertainty. Our simulations have an initial galactic disk that is constructed in a way that is similar to other idealized galaxy simulations, but issues with these initial conditions reveal themselves when also considering the CGM. The

disk experiences a large initial burst of star formation whose feedback quickly disrupts the CGM with hot, low-density bubbles. We attempted to mitigate the impact of this initial, transient burst by starting the simulation with a lower feedback efficiency that was gradually ramped after 1 Gyr of evolution. The goal was to give time for the disk and CGM to interact and settle into a state of equilibrium that is dictated by the simulated physics rather than the limitations of the initial conditions.

While our ramp did give time for the disk and CGM to interact, giving rise to the observed variations in gas accretion and star formation, feedback began to once again disrupt the CGM and carve large, hot cavities upon reaching its full strength. The maximum efficiency is notably *lower* than that used in the zoom simulations of Peeples et al. (2019) and Oh et al. (2020)—works which use the same simulation code and star formation and feedback implementations—but these works do *not* see the same large-scale CGM disruption. The simulations of Fielding et al. (2017) and Li and Tonnesen (2020), which do not model star formation, also don't see this disruption. We therefore conclude that the feedback-driven cavities are a consequence of modelling the *combination* of typical isolated galaxy initial conditions, the CGM, and explicit star formation while *omitting* larger scale "cosmological" effects that are naturally included in zoom simulations. The ultimate conclusion of this work, then, is that some omitted physical process(es) at large radii must also be essential for self-regulation in galaxies on the scale of the Milky Way, in addition to the CGM.

Driven by this conclusion, I have been implementing a series of modifications to our idealized galaxy simulations. These modifications include: adding isobaric entropy perturbations to the initial CGM, which was previously smooth and spherically symmetric unlike the multiphase medium of observations; adjusting the simulation boundary conditions to model inflowing IGM gas, either as a continuous "filament" or discrete "blobs" that serve as an abstraction for satellite galaxies; including the pre-supernova feedback model of Keller, Kruijssen, and Chevance (2022) in an attempt to locally disrupt star formation; and modifying the initial radial profile for gas in the CGM and IGM. With the exception of the pre-supernova feedback model, all of these adjustments are in line with our conclusion that our original simulations lacked some physical process at large radii

($r \sim r_{\rm vir}$). The additional inclusion of pre-supernova feedback was chosen out of the hope it would be a more organic way of limiting star formation (especially the initial burst) than by only adjusting the feedback efficiency.

I'll discuss modifications to the CGM/IGM profile in more detail, since this change is the most fundamental of all the modifications at large radii. As described in Section 3.3.1.2, the CGM in our original simulation was described by adopting the entropy profile of Voit (2019) in conjunction with hydrostatic equilibrium (Equation 1.11). This description is valid within $r_{200} \approx r_{\rm vir}$. Beyond r_{200}, we switch to fixing $\mathrm{d}\log_{10} P / \mathrm{d}\log_{10} r$ and using a temperature profile. This temperature profile is constructed to smoothly connect the CGM's temperature profile with a floor of 4×10^4 K, which is the temperature expected from the influence of the metagalactic UV background; however, as seen in Figure 3.1, the simulation never actually reaches this floor. Additionally, the choice to switch to a fixed pressure derivative and temperature profile were driven by convenience rather than being physically motivated.

I sought to adopt new constraints for the gas profile beyond r_{200} by looking at Milky Way-like galaxies in the FOGGIE (Peeples et al. 2019) and IllustrisTNG-50 (Nelson et al. 2019a; Pillepich et al. 2019) cosmological simulations. Figure 5.3 shows radial profiles of entropy, pressure, density, and temperature for the CGM around 74 TNG50 galaxies with $10^{11.9} < M_{200} < 10^{12.1}$ $\mathrm{M}_\odot$, four FOGGIE halos ($M_{200} = 10^{11.78}$, $10^{12.04}$, $10^{12.06}$, and $10^{12.13}$ $\mathrm{M}_\odot$), and the initial profiles from (Kopenhafer, O'Shea, and Voit 2022, Chapter 3 herein). The Kopenhafer, O'Shea, and Voit (ibid.) and FOGGIE halos are at $z = 0$, while the TNG50 galaxies are at $z = 0.01$.[1] The FOGGIE and TNG50 profiles represent the mass-weighted median (that is, the profiles trace the thermodynamic quantities of the bulk of the gas by mass), whereas the initial profiles from Kopenhafer, O'Shea, and Voit (ibid.) are spherically symmetric. We attempt to remove the influence of the ISM in both FOGGIE and TNG50. For the TNG50 halos, the galaxy is defined as $r < 2R_{1/2}$, where $R_{1/2}$ is the stellar half-mass radius. This is a common definition used when studying the CGM of TNG

[1] While there is also a publicly available TNG50 dataset for $z = 0$, it contains additional particle information that is not needed for this analysis and makes the file size substantially larger. Therefore $z = 0.01$ was chosen as a matter of temporal and storage efficiency.

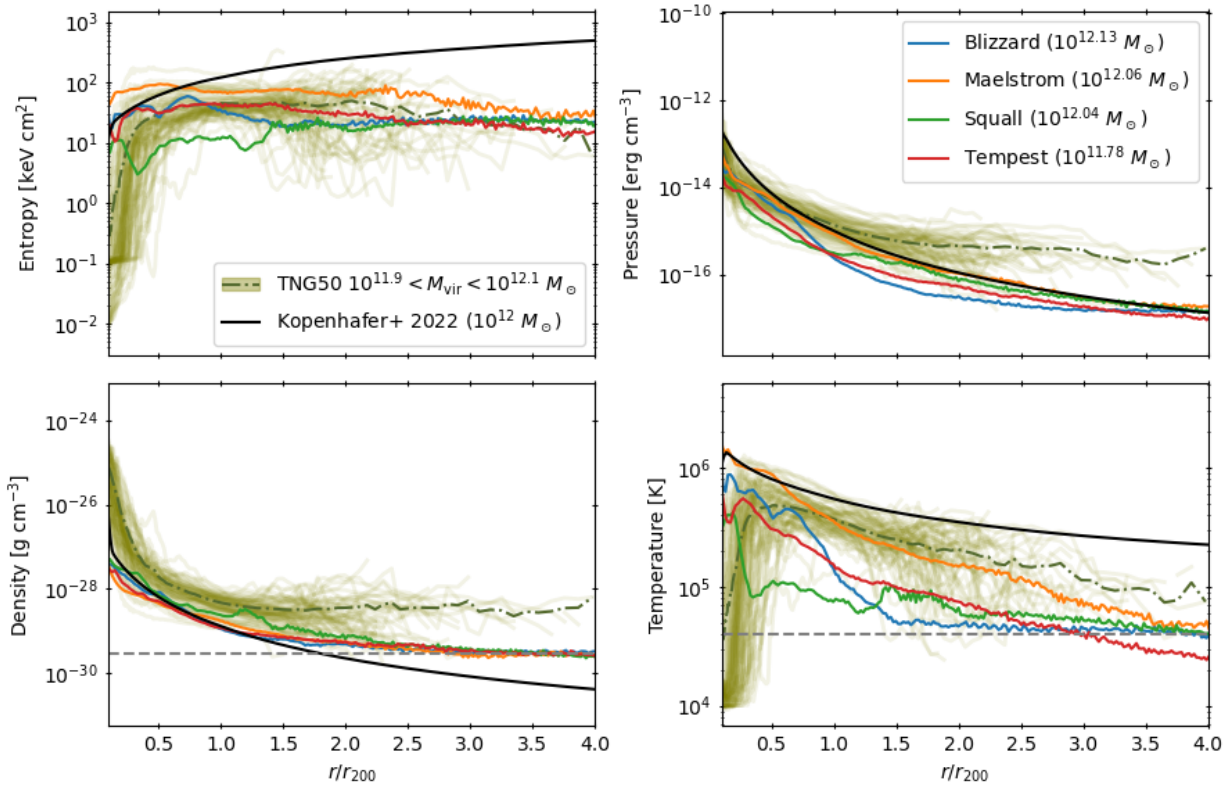

Figure 5.3 Radial profiles of entropy, pressure, temperature, and density (clockwise from upper left) for the CGM of halos in the FOGGIE and IllustrisTNG-50 cosmological simulations and initial conditions of the Kopenhafer, O'Shea, and Voit (2022) idealized simulations. Four FOGGIE halos at $z = 0$ are shown as solid, opaque colored lines with their halo masses are indicated in the legend. The CGM ICs from Kopenhafer, O'Shea, and Voit (2022) are shown as opaque black lines, which target at 10^{12} $M_\odot$ halo. Translucent green lines show 74 halos from TNG50 with $10^{11.9} < M_{200} < 10^{12.1}$ $M_\odot$, while the green dot-dashed line shows their average. The radial profiles are binned in r/r_{200} for comparison across halo mass. Gray dashed horizontal lines mark the approximate density and temperature assymptotes of the FOGGIE simulations at 3×10^{-30} g cm^{-3} and 4×10^4 K, respectively.

galaxies; see e.g. DeFelippis et al. (2020) and Zinger et al. (2020). For FOGGIE, the galaxy ISM is removed using a density cut of $\rho < 2.0 \times 10^{-27}$ g cm^{-3} as detailed in Lochhaas et al. (2022).

Despite differences that are in large part due to variations in stellar and AGN feedback models and resolution, the FOGGIE and TNG50 profiles agree reasonably well. The CGM density in TNG50 is overall higher, which may be due to its poorer spatial resolution compared to FOGGIE. The temperature is, on average, strongly dependent on halo mass within TNG50. This is expected from virial arguments (see Section 1.1.2). The FOGGIE galaxies don't display the expected temperature dependence (that is, increasing CGM temperature with increasing halo mass) but there are also only four galaxies represented.

While the idealized simulations from Kopenhafer, O'Shea, and Voit (2022) agree passably well with the FOGGIE simulations inside r_{200} (and in particular with the Maelstrom halo), their density at $r > r_{200}$ is too low and the temperature in this same region is too high. Indeed, even within r_{200} the CGM temperature is on the high end of agreement with the cosmological profiles. As a result of these density and temperature discrepancies, the entropy profile is not as flat as it should be (though the pressure profile shows reasonable agreement with the FOGGIE halos).

Recent work with FOGGIE, Lochhaas et al. (2022),[2] has found that the CGM within these simulations is *not* in hydrostatic equilibrium. Instead, the CGM is in a dynamic, "emergent" equilibrium that is supported by a wide range of forces in additional to the thermal pressure assumed by hydrostatic equilibrium. In contrast, hydrostatic equilibrium was one of the key assumptions in my idealized galaxy simulations (Kopenhafer, O'Shea, and Voit 2022 and Section 3.3.1.2). It is an assumption that lends itself nicely to idealized simulations, as it is both a simple prescription and leads to a gas configuration that is relatively stable.[3] Given the comparison in Figure 5.3 and the results of Lochhaas et al. (2022), I have decided to test a new set of CGM initial conditions that do *not* assume hydrostatic equilibrium.

My new initial conditions are based on the four FOGGIE halos presented in Figure 5.3. In

[2] I am a contributing author on this paper.

[3] Cooling will deferentially affect the thermal pressure support of the gas because of its nonlinear dependence on temperature in particular; see Figure 1.8.

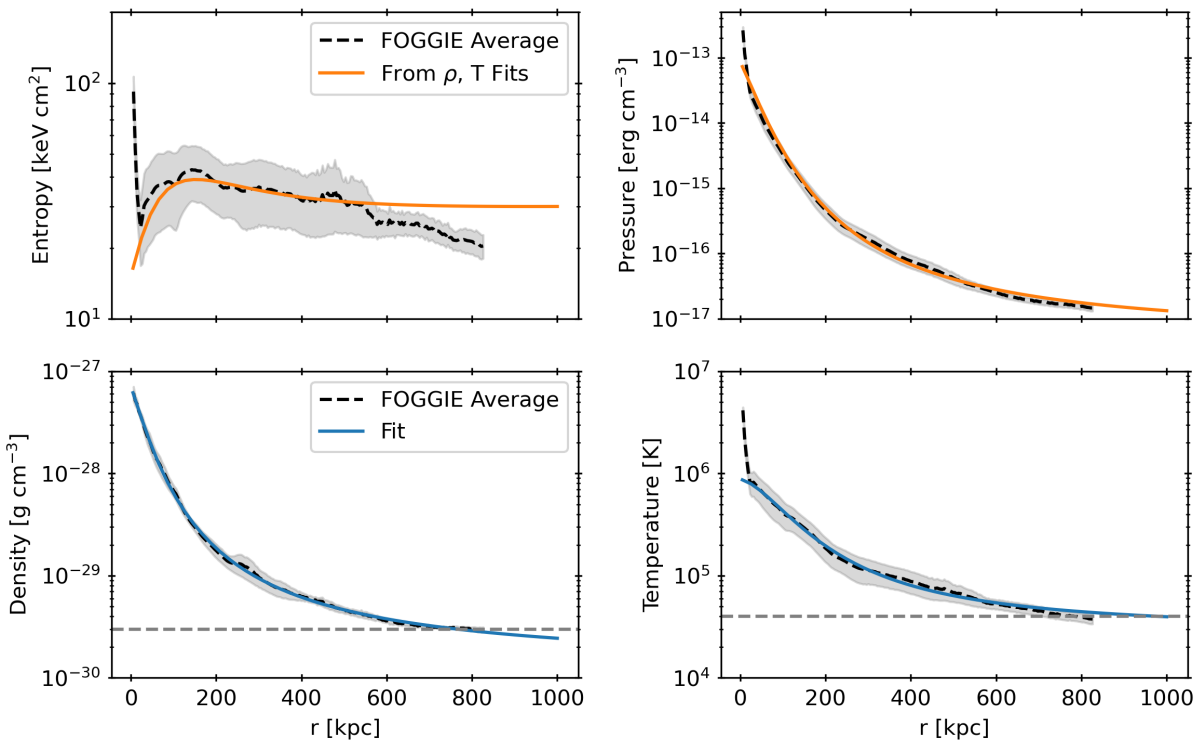

Figure 5.4 Similar to Figure 5.3 but showing the average radial profiles of the four FOGGIE halos over the last 500 Myr (black dashed lines), fits to those profiles in density and temperature (blue lines; bottom row), and the result of those fits in entropy and pressure (orange lines; top row). Gray shading shows one standard deviation for the averaged profiles while the gray horizontal dashed lines mark the approximate density and temperature assymptotes from Figure 5.3. The target idealized halo for these fitted profiles has $r_{200} = 206$ kpc.

particular, I average together the mass-weighted median profiles for all of the halos over the last 11 snapshots (a lookback time of 500 Myr). Over this time the CGM profiles are generally quite stable, so that averaging over multiple simulation snapshots helps reduce small scale variations. Since each halo was processed with a slightly different radial binning, I also average together the radial bins in r/r_{200} space before scaling the profiles to a uniform $r_{200} = 206$ kpc. The temperature profile was modified in two ways: first, the temperature was flattened within $r \lesssim 22$ kpc to a uniform temperature of $T \approx 8.3 \times 10^5$ K. This choice was made because at these small radii the FOGGIE temperature rises sharply due to supernova-driven outflows. Second, the profile is extended by ≈ 410 kpc at large radii with constant $T = 4 \times 10^4$ K to ensure that the temperature profile captures the temperature floor expected from the metagalactic UV background. I then fit the averaged density

and modified temperature profiles with sigmoid functions $e^r/(1+e^r)$. The resulting fits are able to reproduce well the average pressure and entropy profiles, though the latter experiences much more variation. The density and temperature fits, as well as the resulting entropy and pressure profiles, are compared to the average FOGGIE profiles in Figure 5.4. Note that, for calculating the pressure $P = \rho/(\mu m_{\rm H}) k_{\rm B} T$ we assume $\mu = 0.6$ for primordial hydrogen and helium gas and for the entropy $K = k_{\rm B} T n_e^{-2/3}$ we assume the gas is charge neutral and fully ionized; that is, that $n_e \approx n_i$ such that $n \approx 2 n_e$.

These new initial conditions may necessitate removing the ramp in star formation efficiency because the new pressure profiles is *not* in hydrostatic equilibrium. While it matches the pressure of the FOGGIE halos, Lochhaas et al. (2022) showed that dynamical factors were necessary to support the CGM against gravity. Therefore, supernovae feedback may need to drive these dynamical forces earlier than the efficiency ramp allows.

5.3 Chapter 4, Wherein We Quantified Some of the Uncertainties Involved In Synthetic CGM Observations

Chapter 4 presented a set of preliminary results for quantifying the uncertainties inherent to post-processing simulations for column densities. Specifically, these column densities are derived for individual metal ions by assuming an elemental abundance pattern and an incident ionizing background. The former is necessary because simulations usually track all elements heavier than helium with a single "metal" density field. The latter is required by the assumption of photoionization equilibrium. Deriving these ionic column densities is valuable for comparing simulations of the CGM to observations. In Chapter 4, we presented preliminary results quantifying the uncertainty due to the abundance pattern. We used five of the six FOGGIE zoom cosmological simulations at redshifts $z = 2.0$ and 2.5 as the basis of our analysis (Peeples et al. 2019; Simons et al. 2020). For each halo at each redshift we used four lines of sight for 40 lines of sight total. Having proven the capabilities of our analysis pipeline, we intend to scale up the analysis to cover more lines of sight through each halo as well as to add the sixth FOGGIE halo (Cyclone) and include all FOGGIE halos at redshift $z = 1.5$.

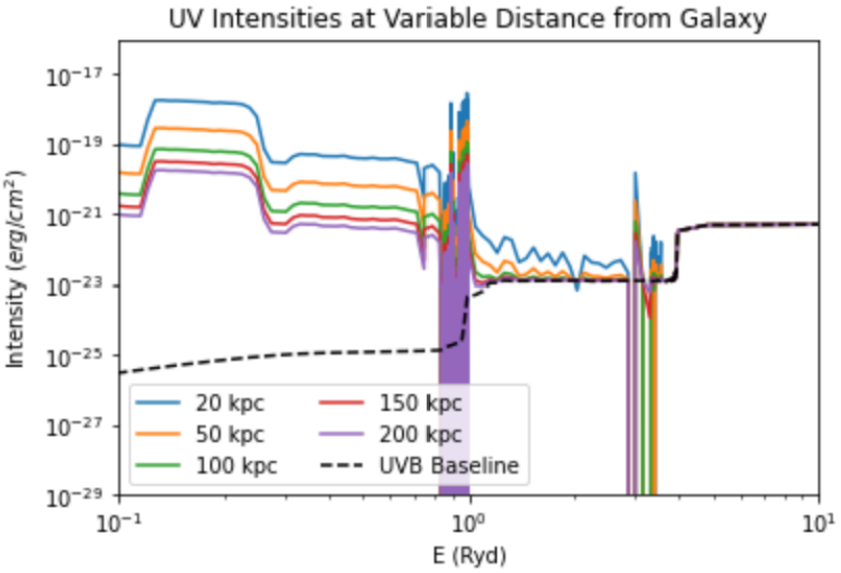

Figure 5.5 Example of galaxy emission spectra at variable distance (colored lines) being added to the metagalactic UV background (black dashed lines). The galaxy emission spectra are calculated for $z = 2.649$ using the star formation history of the Hurricane FOGGIE halo. The UVB is from Puchwein et al. (2019), and $z = 2.649$ is one of the redshifts for which they supply a spectrum. Energy is in Ryd, where 1 Ryd = 13.6 eV.

Typically, simulation post-processing assumes elements follow the Solar abundance pattern. This pattern is well measured but there is little reason to believe it matches the elemental distribution of our own Milky Way CGM, much less all galaxies. We turned to chemical evolution modelling to develop plausible alternatives for the CGM. In order to create a variety of models, we adjusted the yields of AGB and massive stars. These yields have the biggest impact on elements commonly observed in the CGM. We found that just switching from Solar abundances to one developed via chemical evolution modelling had the largest impact on CGM absorbers, adjusting their column density by ±1 dex. The variety of yields only affected CGM column densities by 10^{-2}–10^{-1} dex and this was true across halos and redshifts independent of gas properties or absorber location.

Not presented in Chapter 4 was the second prong of this project: quantifying uncertainties due to the metagalactic UV background (UVB). As noted in Section 4.2, uncertainties due to the UVB have been quantified for observations but not for simulations. This distinction is important because the methods for obtaining column densities are very different. In future work we will investigate

the variation in absorber column density caused by adjusting the UVB. We plan to test either the Faucher-Giguère et al. (2009) and Haardt and Madau (2012) UVB models, which are commonly used in simulation, or their recent respective updates, Faucher-Giguère (2020) and Puchwein et al. (2019). We may also include one or more of the models of Khaire and Srianand (2019), who provide multiple options for the portion of the UVB dominated by quasars.

As alluded to in Section 4.2, we also want to investigate the impact of UV emission from the host galaxy. The metagalactic UVB models assume one is far from any individual galaxy, but of course absorbers in the CGM violate this assumption by definition. To do this, we've been working with the Flexible Stellar Population Synthesis code (FSPS; Conroy, Gunn, and White 2009; Conroy and Gunn 2010; Foreman-Mackey, Sick, and Johnson 2014). This code will allow us to take the star formation histories of the FOGGIE galaxies and calculate their emission spectra at our target redshifts. FSPS can also model the impact of ISM dust.

Figure 5.5 shows an example of this process, where the colored lines represents the emission at various distances from the galactic center added to the Puchwein et al. (2019) UV background. The galaxy spectra is calculated using the Hurricane FOGGIE halo at redshift $z = 2.649$, which is one of the redshifts for which Puchwein et al. (ibid.) provide a spectrum. FSPS does not separate stellar populations spatially so all are treated as if they lie at the galaxy center. A distance of 20 kpc roughly corresponds to the edge of the galactic disk. The black dashed line shows the Puchwein et al. (ibid.) background without a galaxy contribution. Energy is presented in Ryd, where 1 Ryd = 13.6 eV is the ionization energy of hydrogen. Higher energies are relevant for the metal ionization states under investigation, though we can see that emission from the galaxy has the largest impact below 1 Ryd. Dust absorption is also visible. In future work these combined galaxy and UVB spectra will be incorporated into our uncertainty quantification analysis.

BIBLIOGRAPHY

Abazajian, K. N., J. K. Adelman-McCarthy, M. A. Agüeros, et al. (2009). *The Astrophysical Journal Supplement Series* 182.2, p. 543. DOI: 10.1088/0067-0049/182/2/543.

Abohalima, A. and A. Frebel (2018). *The Astrophysical Journal Supplement Series* 238.2, p. 36. DOI: 10.3847/1538-4365/aadfe9.

Abramson, L. E., D. D. Kelson, A. Dressler, et al. (2014). *The Astrophysical Journal* 785.2, L36, p. L36. DOI: 10.1088/2041-8205/785/2/L36.

Acharya, A. and V. Khaire (2022). *Monthly Notices of the Royal Astronomical Society* 509.4, p. 5559. DOI: 10.1093/mnras/stab3316.

Adhikari, S., N. Dalal, and R. T. Chamberlain (2014). *Journal of Cosmology and Astroparticle Physics* 2014.11, 019, p. 019. DOI: 10.1088/1475-7516/2014/11/019.

Aihara, H., C. A. Prieto, D. An, et al. (2011). *The Astrophysical Journal Supplement Series* 193.2, 29, p. 29. DOI: 10.1088/0067-0049/193/2/29.

Alexander, D. M. and R. C. Hickox (2012). *New Astronomy Reviews* 56.4, p. 93. DOI: 10.1016/j.newar.2011.11.003.

Almgren, A. S., V. E. Beckner, J. B. Bell, et al. (2010). *The Astrophysical Journal* 715.2, p. 1221. DOI: 10.1088/0004-637X/715/2/1221.

Anglés-Alcázar, D., R. Davé, C.-A. Faucher-Giguère, et al. (2017). *Monthly Notices of the Royal Astronomical Society* 464.3, p. 2840. DOI: 10.1093/mnras/stw2565.

Anglés-Alcázar, D., F. Özel, and R. Davé (2013). *The Astrophysical Journal* 770.1, p. 5. DOI: 10.1088/0004-637X/770/1/5.

Angulo, R. E., V. Springel, S. D. M. White, et al. (2012). *Monthly Notices of the Royal Astronomical Society* 426.3, p. 2046. DOI: 10.1111/j.1365-2966.2012.21830.x.

Astropy Collaboration, A. M. Price-Whelan, B. M. Sipőcz, et al. (2018). *The Astronomical Journal* 156.3, p. 123. DOI: 10.3847/1538-3881/aabc4f.

Babyk, I. V., B. R. McNamara, P. E. J. Nulsen, et al. (2018). *The Astrophysical Journal* 862.1, p. 39. DOI: 10.3847/1538-4357/aacce5.

Bacchini, C., F. Fraternali, G. Pezzulli, et al. (2020). *Astronomy and Astrophysics* 644, A125. DOI: 10.1051/0004-6361/202038962.

Bagla, J. S. (2002). *Journal of Astrophysics and Astronomy* 23.3, p. 185. DOI: 10.1007/BF02702282.

Baker, W. M., R. Maiolino, A. F. L. Bluck, et al. (2022). *Monthly Notices of the Royal Astronomical Society* 510, p. 3622. DOI: 10.1093/mnras/stab3672.

Baldry, I. K., K. Glazebrook, and S. P. Driver (2008). *Monthly Notices of the Royal Astronomical Society* 388.3, p. 945. DOI: 10.1111/j.1365-2966.2008.13348.x.

Baldry, I. K., K. Glazebrook, J. Brinkmann, et al. (2004). *The Astrophysical Journal* 600.2, p. 681. DOI: 10.1086/380092.

Balogh, M. L., S. L. Morris, H. K. C. Yee, et al. (1999). *The Astrophysical Journal* 527.1, p. 54. DOI: 10.1086/308056.

Bamford, S. P., R. C. Nichol, I. K. Baldry, et al. (2009). *Monthly Notices of the Royal Astronomical Society* 393.4, p. 1324. DOI: 10.1111/j.1365-2966.2008.14252.x.

Barnes, J. and P. Hut (1986). *Nature* 324.6096 (6096), p. 446. DOI: 10.1038/324446a0.

Barrera-Ballesteros, J. K., T. Heckman, S. F. Sánchez, et al. (2021). *The Astrophysical Journal* 909.2, p. 131. DOI: 10.3847/1538-4357/abd855.

Behroozi, P., R. H. Wechsler, A. P. Hearin, et al. (2019). *Monthly Notices of the Royal Astronomical Society* 488.3, p. 3143. DOI: 10.1093/mnras/stz1182.

Behroozi, P. S., R. H. Wechsler, and C. Conroy (2013a). *The Astrophysical Journal Letters* 762.2, p. L31. DOI: 10.1088/2041-8205/762/2/L31.

— (2013b). *The Astrophysical Journal* 770.1, p. 57. DOI: 10.1088/0004-637X/770/1/57.

Behroozi, P. S., R. H. Wechsler, and H.-Y. Wu (2013). *The Astrophysical Journal* 762.2, p. 109. DOI: 10.1088/0004-637X/762/2/109.

Belfiore, F., R. Maiolino, K. Bundy, et al. (2018). *Monthly Notices of the Royal Astronomical Society* 477.3, p. 3014. DOI: 10.1093/mnras/sty768.

Belfiore, F., R. Maiolino, C. Tremonti, et al. (2017). *Monthly Notices of the Royal Astronomical Society* 469.1, p. 151. DOI: 10.1093/mnras/stx789.

Bell, E. F., A. van der Wel, C. Papovich, et al. (2012). *The Astrophysical Journal* 753.2, 167, p. 167. DOI: 10.1088/0004-637X/753/2/167.

Bell, E. F., C. Wolf, K. Meisenheimer, et al. (2004). *The Astrophysical Journal* 608.2, p. 752. DOI: 10.1086/420778.

Bell, E. F., X. Z. Zheng, C. Papovich, et al. (2007). *The Astrophysical Journal* 663.2, p. 834. DOI: 10.1086/518594.

Bender, R., D. Burstein, and S. M. Faber (1992). *The Astrophysical Journal* 399, p. 462. DOI: 10.1086/171940.

Benincasa, S. M., J. Wadsley, H. M. P. Couchman, et al. (2016). *Monthly Notices of the Royal Astronomical Society* 462.3, p. 3053. DOI: 10.1093/mnras/stw1741.

Benson, A. J. (2010). *Physics Reports* 495.2-3, p. 33. DOI: 10.1016/j.physrep.2010.06.001.

Berg, M. A., J. C. Howk, N. Lehner, et al. (2019). *The Astrophysical Journal* 883.1, p. 5. DOI: 10.3847/1538-4357/ab378e.

Berger, M. J. and P. Colella (1989). *Journal of Computational Physics* 82.1, p. 64. DOI: 10.1016/0021-9991(89)90035-1.

Bernardi, M., F. Shankar, J. B. Hyde, et al. (2010). *Monthly Notices of the Royal Astronomical Society* 404.4, p. 2087. DOI: 10.1111/j.1365-2966.2010.16425.x.

Bertschinger, E. (1985). *The Astrophysical Journal Supplement Series* 58, p. 39. DOI: 10.1086/191028.

Binney, J. (1977). *The Astrophysical Journal* 215, p. 483. DOI: 10.1086/155378.

Birnboim, Y. and A. Dekel (2003). *Monthly Notices of the Royal Astronomical Society* 345.1, p. 349. DOI: 10.1046/j.1365-8711.2003.06955.x.

Bish, H. V., J. K. Werk, J. Peek, et al. (2021). *The Astrophysical Journal* 912.1, p. 8. DOI: 10.3847/1538-4357/abeb6b.

Blanton, M. R., J. Dalcanton, D. Eisenstein, et al. (2001). *The Astronomical Journal* 121.5, p. 2358. DOI: 10.1086/320405.

Blanton, M. R., D. W. Hogg, N. A. Bahcall, et al. (2003). *The Astrophysical Journal* 592.2, p. 819. DOI: 10.1086/375776.

Blanton, M. R., D. J. Schlegel, M. A. Strauss, et al. (2005). *The Astronomical Journal* 129.6, p. 2562. DOI: 10.1086/429803.

Bluck, A. F. L., J. T. Mendel, S. L. Ellison, et al. (2014). *Monthly Notices of the Royal Astronomical Society* 441.1, p. 599. DOI: 10.1093/mnras/stu594.

Blumenthal, K. A. and J. E. Barnes (2018). *Monthly Notices of the Royal Astronomical Society* 479.3, p. 3952. DOI: 10.1093/mnras/sty1605.

Bondi, H. (1952). *Monthly Notices of the Royal Astronomical Society* 112, p. 195. DOI: 10.1093/mnras/112.2.195.

Bondi, H. and F. Hoyle (1944). *Monthly Notices of the Royal Astronomical Society* 104, p. 273. DOI: 10.1093/mnras/104.5.273.

Booth, C. M. and J. Schaye (2009). *Monthly Notices of the Royal Astronomical Society* 398.1, p. 53. DOI: 10.1111/j.1365-2966.2009.15043.x.

Bordoloi, R., J. Tumlinson, J. K. Werk, et al. (2014). *The Astrophysical Journal* 796.2, p. 136. DOI: 10.1088/0004-637X/796/2/136.

Boselli, A. and G. Gavazzi (2006). *Publications of the Astronomical Society of the Pacific* 118.842, p. 517. DOI: 10.1086/500691.

Bouché, N., A. Dekel, R. Genzel, et al. (2010). *The Astrophysical Journal* 718.2, p. 1001. DOI: 10.1088/0004-637X/718/2/1001.

Boyd, B. I., D. W. Silvia, B. W. O'Shea, et al. (2020). *Journal of Open Source Software* 5.52, p. 2581. DOI: 10.21105/joss.02581.

Brammer, G. B., K. E. Whitaker, P. G. van Dokkum, et al. (2011). *The Astrophysical Journal* 739.1, p. 24. DOI: 10.1088/0004-637X/739/1/24.

Brinchmann, J., S. Charlot, S. D. M. White, et al. (2004). *Monthly Notices of the Royal Astronomical Society* 351.4, p. 1151. DOI: 10.1111/j.1365-2966.2004.07881.x.

Bromm, V. and N. Yoshida (2011). *Annual Review of Astronomy and Astrophysics* 49.1, p. 373. DOI: 10.1146/annurev-astro-081710-102608.

Brüggen, M. and E. Scannapieco (2020). *The Astrophysical Journal* 905.1, p. 19. DOI: 10.3847/1538-4357/abc00f.

Brummel-Smith, C., G. Bryan, I. Butsky, et al. (2019). *Journal of Open Source Software* 4.42, p. 1636. DOI: 10.21105/joss.01636.

Bryan, G. L. and M. L. Norman (1998). *The Astrophysical Journal* 495.1, p. 80. DOI: 10.1086/305262.

Bryan, G. L., M. L. Norman, B. W. O'Shea, et al. (2014). *The Astrophysical Journal Supplement Series* 211.2, p. 19. DOI: 10.1088/0067-0049/211/2/19.

Bryant, J. J., M. S. Owers, A. S. G. Robotham, et al. (2015). *Monthly Notices of the Royal Astronomical Society* 447.3, p. 2857. DOI: 10.1093/mnras/stu2635.

Buck, T., A. V. Macciò, A. A. Dutton, et al. (2019). *Monthly Notices of the Royal Astronomical Society* 483.1, p. 1314. DOI: 10.1093/mnras/sty2913.

Buie II, E., M. Fumagalli, and E. Scannapieco (2020). *The Astrophysical Journal* 890.1, p. 33. DOI: 10.3847/1538-4357/ab65bc.

Buie II, E., W. J. Gray, E. Scannapieco, et al. (2020). *The Astrophysical Journal* 896.2, p. 136. DOI: 10.3847/1538-4357/ab9535.

Buie II, E., E. Scannapieco, and G. Mark Voit (2022). *The Astrophysical Journal* 927.1, p. 30. DOI: 10.3847/1538-4357/ac4bc2.

Bundy, K., M. A. Bershady, D. R. Law, et al. (2014). *The Astrophysical Journal* 798.1, 7, p. 7. DOI: 10.1088/0004-637X/798/1/7.

Bundy, K., C. Scarlata, C. M. Carollo, et al. (2010). *The Astrophysical Journal* 719.2, p. 1969. DOI: 10.1088/0004-637X/719/2/1969.

Burchett, J. N., T. M. Tripp, J. X. Prochaska, et al. (2019). *The Astrophysical Journal* 877.2, p. L20. DOI: 10.3847/2041-8213/ab1f7f.

Burkert, A., J. W. Truran, and G. Hensler (1992). *The Astrophysical Journal* 391, p. 651. DOI: 10.1086/171378.

Burstein, D., R. Bender, S. Faber, et al. (1997). *The Astronomical Journal* 114, p. 1365. DOI: 10.1086/118570.

Butsky, I. S., D. B. Fielding, C. C. Hayward, et al. (2020). *The Astrophysical Journal* 903.2, p. 77. DOI: 10.3847/1538-4357/abbad2.

Butsky, I. S. and T. R. Quinn (2018). *The Astrophysical Journal* 868.2, p. 108. DOI: 10.3847/1538-4357/aaeac2.

Butsky, I. S., J. K. Werk, K. Tchernyshyov, et al. (2022). *The Astrophysical Journal* 935.2, p. 69. DOI: 10.3847/1538-4357/ac7ebd.

Byrd, G. and M. Valtonen (1990). *The Astrophysical Journal* 350, p. 89. DOI: 10.1086/168362.

Cadiou, C., Y. Dubois, and C. Pichon (2022). *Monthly Notices of the Royal Astronomical Society* 514.4, p. 5429. DOI: 10.1093/mnras/stac1663.

Cassata, P., M. Giavalisco, Y. Guo, et al. (2010). *The Astrophysical Journal* 714.1, p. L79. DOI: 10.1088/2041-8205/714/1/L79.

Catinella, B., D. Schiminovich, G. Kauffmann, et al. (2010). *Monthly Notices of the Royal*

Astronomical Society 403.2, p. 683. DOI: 10.1111/j.1365-2966.2009.16180.x.

Cavagnolo, K. W., M. Donahue, G. M. Voit, et al. (2008). *The Astrophysical Journal* 683.2, p. L107. DOI: 10.1086/591665.

Cen, R. and J. P. Ostriker (1992). *The Astrophysical Journal Letters* 399, p. L113. DOI: 10.1086/186620.

Chabrier, G. (2003). *Publications of the Astronomical Society of the Pacific* 115.809, p. 763. DOI: 10.1086/376392.

Charlot, S. and S. M. Fall (2000). *The Astrophysical Journal* 539.2, p. 718. DOI: 10.1086/309250.

Chen, H.-W., F. S. Zahedy, E. Boettcher, et al. (2020). *Monthly Notices of the Royal Astronomical Society* 497.1, p. 498. DOI: 10.1093/mnras/staa1773.

Chen, Y.-M., Y. Shi, V. Wild, et al. (2019). *Monthly Notices of the Royal Astronomical Society* 489.4, p. 5709. DOI: 10.1093/mnras/stz2494.

Cheung, E., S. M. Faber, D. C. Koo, et al. (2012). *The Astrophysical Journal* 760.2, p. 131. DOI: 10.1088/0004-637X/760/2/131.

Chevance, M., J. M. D. Kruijssen, M. R. Krumholz, et al. (2022). *Monthly Notices of the Royal Astronomical Society* 509.1, p. 272. DOI: 10.1093/mnras/stab2938.

Chiappini, C. and a. R. Gratton (1997). *The Astrophysical Journal* 477.2, p. 765. DOI: 10.1086/303726.

Choi, E., T. Naab, J. P. Ostriker, et al. (2014). *Monthly Notices of the Royal Astronomical Society* 442.1, p. 440. DOI: 10.1093/mnras/stu874.

Choi, E., J. P. Ostriker, T. Naab, et al. (2012). *The Astrophysical Journal* 754.2, p. 125. DOI: 10.1088/0004-637X/754/2/125.

Choi, E., J. P. Ostriker, T. Naab, et al. (2017). *The Astrophysical Journal* 844.1, p. 31. DOI: 10.3847/1538-4357/aa7849.

Choi, J., A. Dotter, C. Conroy, et al. (2016). *The Astrophysical Journal* 823.2, p. 102. DOI: 10.3847/0004-637X/823/2/102.

Chomiuk, L. and M. S. Povich (2011). *The Astronomical Journal* 142.6, p. 197. DOI: 10.1088/0004-6256/142/6/197.

Cole, S. and C. Lacey (1996). *Monthly Notices of the Royal Astronomical Society* 281.2, p. 716. DOI: 10.1093/mnras/281.2.716.

Conroy, C. and J. E. Gunn (2010). *The Astrophysical Journal* 712.2, p. 833. DOI: 10.1088/0004-637X/712/2/833.

Conroy, C., J. E. Gunn, and M. White (2009). *The Astrophysical Journal* 699.1, p. 486. DOI: 10.1088/0004-637X/699/1/486.

Corlies, L., M. S. Peeples, J. Tumlinson, et al. (2020). *The Astrophysical Journal* 896.2, p. 125. DOI: 10.3847/1538-4357/ab9310.

Cosentino, G., I. Jiménez-Serra, J. C. Tan, et al. (2022). *Monthly Notices of the Royal Astronomical Society* 511.1, p. 953. DOI: 10.1093/mnras/stac070.

Côté, B., B. W. O'Shea, C. Ritter, et al. (2017a). *The Astrophysical Journal* 835.2, p. 128. DOI: 10.3847/1538-4357/835/2/128.

Côté, B., C. Ritter, F. Herwig, et al. (2017b). *Proceedings of the 14th International Symposium on Nuclei in the Cosmos (NIC2016)*. DOI: 10.7566/JPSCP.14.020203.

Côté, B., C. Ritter, B. W. O'Shea, et al. (2016). *The Astrophysical Journal* 824.2, p. 82. DOI: 10.3847/0004-637X/824/2/82.

Côté, B., D. W. Silvia, B. W. O'Shea, et al. (2018). *The Astrophysical Journal* 859.1, p. 67. DOI: 10.3847/1538-4357/aabe8f.

Courteau, S., A. A. Dutton, F. C. van den Bosch, et al. (2007). *The Astrophysical Journal* 671.1, p. 203. DOI: 10.1086/522193.

Cox, T. J., P. Jonsson, R. S. Somerville, et al. (2008). *Monthly Notices of the Royal Astronomical Society* 384.1, p. 386. DOI: 10.1111/j.1365-2966.2007.12730.x.

Crain, R. A., J. Schaye, R. G. Bower, et al. (2015). *Monthly Notices of the Royal Astronomical Society* 450.2, p. 1937. DOI: 10.1093/mnras/stv725.

Cristallo, S., O. Straniero, L. Piersanti, et al. (2015). *The Astrophysical Journal Supplement Series* 219.2, p. 40. DOI: 10.1088/0067-0049/219/2/40.

Croom, S. M., J. S. Lawrence, J. Bland-Hawthorn, et al. (2012). *Monthly Notices of the Royal Astronomical Society* 421.1, p. 872. DOI: 10.1111/j.1365-2966.2011.20365.x.

Dale, D. A., G. D. Beltz-Mohrmann, A. A. Egan, et al. (2016). *The Astronomical Journal* 151.1, 4, p. 4. DOI: 10.3847/0004-6256/151/1/4.

Dalla Vecchia, C. and J. Schaye (2012). *Monthly Notices of the Royal Astronomical Society* 426.1, p. 140. DOI: 10.1111/j.1365-2966.2012.21704.x.

Das, S., S. Mathur, A. Gupta, et al. (2021). *The Astrophysical Journal* 918.2, p. 83. DOI: 10.3847/1538-4357/ac0e8e.

Davé, R., D. Anglés-Alcázar, D. Narayanan, et al. (2019). *Monthly Notices of the Royal Astronomical Society* 486.2, p. 2827. DOI: 10.1093/mnras/stz937.

Davé, R., K. Finlator, and B. D. Oppenheimer (2012). *Monthly Notices of the Royal Astronomical Society* 421.1, p. 98. DOI: 10.1111/j.1365-2966.2011.20148.x.

Davé, R., M. H. Rafieferantsoa, and R. J. Thompson (2017). *Monthly Notices of the Royal Astronomical Society* 471.2, p. 1671. DOI: 10.1093/mnras/stx1693.

Davis, M., G. Efstathiou, C. S. Frenk, et al. (1985). *The Astrophysical Journal* 292, p. 371. DOI: 10.1086/163168.

De los Reyes, M. A. C. and R. C. Kennicutt (2019). *The Astrophysical Journal* 872.1, p. 16. DOI: 10.3847/1538-4357/aafa82.

Deason, A. J., A. Fattahi, C. S. Frenk, et al. (2020). *Monthly Notices of the Royal Astronomical Society* 496, p. 3929. DOI: 10.1093/mnras/staa1711.

DeBuhr, J., E. Quataert, and C.-P. Ma (2011). *Monthly Notices of the Royal Astronomical Society* 412.2, p. 1341. DOI: 10.1111/j.1365-2966.2010.17992.x.

— (2012). *Monthly Notices of the Royal Astronomical Society* 420.3, p. 2221. DOI: 10.1111/j.1365-2966.2011.20187.x.

DeBuhr, J., E. Quataert, C.-P. Ma, et al. (2010). *Monthly Notices of the Royal Astronomical Society* 406.1, p. L55. DOI: 10.1111/j.1745-3933.2010.00881.x.

DeFelippis, D., N. F. Bouché, S. Genel, et al. (2021). *The Astrophysical Journal* 923.1, p. 56. DOI: 10.3847/1538-4357/ac2cbf.

DeFelippis, D., S. Genel, G. L. Bryan, et al. (2020). *The Astrophysical Journal* 895.1, p. 17. DOI: 10.3847/1538-4357/ab8a4a.

Dehnen, W. (2000). *The Astrophysical Journal* 536.1, p. L39. DOI: 10.1086/312724.

Dekel, A., Y. Birnboim, G. Engel, et al. (2009). *Nature* 457, p. 451. DOI: 10.1038/nature07648.

Dekel, A. and J. Silk (1986). *The Astrophysical Journal* 303, p. 39. DOI: 10.1086/164050.

Di Teodoro, E. M. and J. E. G. Peek (2021). *The Astrophysical Journal* 923.2, p. 220. DOI: 10.3847/1538-4357/ac2cbd.

Diemand, J., M. Kuhlen, and P. Madau (2007). *The Astrophysical Journal* 667.2, p. 859. DOI: 10.1086/520573.

Diemer, B. (2020). *The Astrophysical Journal Supplement Series* 251.2, arXiv:2007.09149, p. 17. DOI: 10.3847/1538-4365/abbf51.

— (2021). *The Astrophysical Journal* 909.2, arXiv:2007.10992, p. 112. DOI: 10.3847/1538-4357/abd947.

Diemer, B., P. Mansfield, A. V. Kravtsov, et al. (2017). *The Astrophysical Journal* 843.2, 140, p. 140. DOI: 10.3847/1538-4357/aa79ab.

Diemer, B., S. More, and A. V. Kravtsov (2013). *The Astrophysical Journal* 766.1, p. 25. DOI: 10.1088/0004-637X/766/1/25.

Ding, X., J. Silverman, T. Treu, et al. (2020). *The Astrophysical Journal* 888.1, 37, p. 37. DOI: 10.3847/1538-4357/ab5b90.

Djorgovski, S. and M. Davis (1987). *The Astrophysical Journal* 313, p. 59. DOI: 10.1086/164948.

Dolag, K., S. Borgani, G. Murante, et al. (2009). *Monthly Notices of the Royal Astronomical Society* 399.2, p. 497. DOI: 10.1111/j.1365-2966.2009.15034.x.

Donahue, M. and G. M. Voit (2022). *Physics Reports* 973, p. 1. DOI: 10.1016/j.physrep.2022.04.005.

Donnari, M., A. Pillepich, D. Nelson, et al. (2021). *Monthly Notices of the Royal Astronomical Society* 506.4, p. 4760. DOI: 10.1093/mnras/stab1950.

Dotter, A. (2016). *The Astrophysical Journal Supplement Series* 222.1, p. 8. DOI: 10.3847/0067-0049/222/1/8.

Draine, B. T. (2011). Princeton Series in Astrophysics. Princeton University Press. ISBN: 978-0-691-12214-4.

Dubois, Y. and R. Teyssier (2008). *Astronomy and Astrophysics* 477.1, p. 79. DOI: 10.1051/0004-6361:20078326.

Eckart, C. (1960). *Physics of Fluids* 3.3, p. 421. DOI: 10.1063/1.1706053.

Einasto, J. (1965). *Trudy Astrofizicheskogo Instituta Alma-Ata* 5, p. 87.

Ekström, S., C. Georgy, P. Eggenberger, et al. (2012). *Astronomy and Astrophysics* 537, A146. DOI: 10.1051/0004-6361/201117751.

Ellison, S. L., A. Viswanathan, D. R. Patton, et al. (2019). *Monthly Notices of the Royal Astronomical Society* 487.2, p. 2491. DOI: 10.1093/mnras/stz1431.

Ellison, S. L., L. Lin, M. D. Thorp, et al. (2021). *Monthly Notices of the Royal Astronomical Society* 501.4, p. 4777. DOI: 10.1093/mnras/staa3822.

Ellison, S. L., D. R. Patton, J. T. Mendel, et al. (2011). *Monthly Notices of the Royal Astronomical Society* 418.3, p. 2043. DOI: 10.1111/j.1365-2966.2011.19624.x.

Ellison, S. L., S. F. Sánchez, H. Ibarra-Medel, et al. (2018). *Monthly Notices of the Royal Astronomical Society* 474.2, p. 2039. DOI: 10.1093/mnras/stx2882.

Evans, F. A., L. C. Parker, and I. D. Roberts (2018). *Monthly Notices of the Royal Astronomical Society* 476.4, p. 5284. DOI: 10.1093/mnras/sty581.

Evrard, A. E., C. A. Metzler, and J. F. Navarro (1996). *The Astrophysical Journal* 469, p. 494. DOI: 10.1086/177798.

Faber, S. M., A. Dressler, R. L. Davies, et al. (1987). *Nearly Normal Galaxies. From the Planck Time to the Present*. The Eighth Santa Cruz Summer Workshop in Astronomy and Astrophysics. Ed. by S. M. Faber. Lick Observatory: Springer, p. 175. ISBN: 0-387-96521-1.

Faber, S. M. and R. E. Jackson (1976). *The Astrophysical Journal* 204, p. 668. DOI: 10.1086/154215.

Faber, S. M., C. N. A. Willmer, C. Wolf, et al. (2007). *The Astrophysical Journal* 665.1, p. 265. DOI: 10.1086/519294.

Falcón-Barroso, J., P. Sánchez-Blázquez, A. Vazdekis, et al. (2011). *Astronomy and Astrophysics* 532, A95. DOI: 10.1051/0004-6361/201116842.

Faucher-Giguère, C.-A. (2020). *Monthly Notices of the Royal Astronomical Society* 493.2, p. 1614. DOI: 10.1093/mnras/staa302.

Faucher-Giguère, C.-A., A. Lidz, M. Zaldarriaga, et al. (2009). *The Astrophysical Journal* 703.2, p. 1416. DOI: 10.1088/0004-637X/703/2/1416.

Ferland, G. J., M. Chatzikos, F. Guzmán, et al. (2017). *Revista Mexicana de Astronomia y Astrofisica* 53, p. 385.

Ferland, G. J., K. T. Korista, D. A. Verner, et al. (1998). *Publications of the Astronomical Society of the Pacific* 110, p. 761. DOI: 10.1086/316190.

Ferland, G. J., R. L. Porter, P. A. M. van Hoof, et al. (2013). *Revista Mexicana de Astronomia y Astrofisica* 49, p. 137.

Ferramacho, L. D., A. Blanchard, and Y. Zolnierowski (2009). *Astronomy and Astrophysics* 499.1, p. 21. DOI: 10.1051/0004-6361/200810693.

Fielding, D., E. Quataert, M. McCourt, et al. (2017). *Monthly Notices of the Royal Astronomical Society* 466.4, p. 3810. DOI: 10.1093/mnras/stw3326.

Fielding, D. B., S. Tonnesen, D. DeFelippis, et al. (2020). *The Astrophysical Journal* 903.1, p. 32. DOI: 10.3847/1538-4357/abbc6d.

Foreman-Mackey, D., J. Sick, and B. Johnson (2014). Zenodo. DOI: 10.5281/zenodo.12157.

Frankel, N., J. Sanders, H.-W. Rix, et al. (2019). *The Astrophysical Journal* 884.2, 99, p. 99. DOI: 10.3847/1538-4357/ab4254.

Frenk, C. S. and S. D. M. White (2012). *Annalen der Physik* 524.9-10, p. 507. DOI: 10.1002/andp.201200212.

Frenk, C. S., S. D. M. White, M. Davis, et al. (1988). *The Astrophysical Journal* 327, p. 507. DOI: 10.1086/166213.

Frenk, C. S., S. D. M. White, G. Efstathiou, et al. (1985). *Nature* 317.6038 (6038), p. 595. DOI: 10.1038/317595a0.

Frisbie, R. L. S., M. Donahue, G. M. Voit, et al. (2020). *The Astrophysical Journal* 899.2, p. 159. DOI: 10.3847/1538-4357/aba8a8.

Fryer, C. L., K. Belczynski, G. Wiktorowicz, et al. (2012). *The Astrophysical Journal* 749.1, p. 91. DOI: 10.1088/0004-637X/749/1/91.

Fujita, Y. and M. Nagashima (1999). *The Astrophysical Journal* 516.2, p. 619. DOI: 10.1086/307139.

Fumagalli, M., J. M. O'Meara, and J. X. Prochaska (2016). *Monthly Notices of the Royal Astronomical Society* 455.4, p. 4100. DOI: 10.1093/mnras/stv2616.

Gallart, C., P. B. Stetson, I. P. Meschin, et al. (2008). *The Astrophysical Journal* 682.2, p. L89. DOI: 10.1086/590552.

Gaspari, M., F. Brighenti, and P. Temi (2015). *Astronomy and Astrophysics* 579, A62. DOI: 10.1051/0004-6361/201526151.

Gaspari, M., M. Ruszkowski, and S. P. Oh (2013). *Monthly Notices of the Royal Astronomical Society* 432.4, p. 3401. DOI: 10.1093/mnras/stt692.

Gaspari, M., M. Ruszkowski, and P. Sharma (2012). *The Astrophysical Journal* 746.1, p. 94. DOI:

10.1088/0004-637X/746/1/94.

Genel, S., G. L. Bryan, V. Springel, et al. (2019). *The Astrophysical Journal* 871.1, p. 21. DOI: 10.3847/1538-4357/aaf4bb.

Genel, S., S. M. Fall, L. Hernquist, et al. (2015). *The Astrophysical Journal* 804.2, p. L40. DOI: 10.1088/2041-8205/804/2/L40.

Genel, S., M. Vogelsberger, V. Springel, et al. (2014). *Monthly Notices of the Royal Astronomical Society* 445.1, p. 175. DOI: 10.1093/mnras/stu1654.

Gensior, J., J. M. D. Kruijssen, and B. W. Keller (2020). *Monthly Notices of the Royal Astronomical Society* 495.1, p. 199. DOI: 10.1093/mnras/staa1184.

Genzel, R., N. M. F. Schreiber, P. Lang, et al. (2014). *The Astrophysical Journal* 785.1, 75, p. 75. DOI: 10.1088/0004-637X/785/1/75.

Gibson, J. L., N. Lehner, B. D. Oppenheimer, et al. (2022). *The Astronomical Journal* 164.1, p. 9. DOI: 10.3847/1538-3881/ac69d0.

Girichidis, P., S. Walch, T. Naab, et al. (2016). *Monthly Notices of the Royal Astronomical Society* 456.4, p. 3432. DOI: 10.1093/mnras/stv2742.

Glines, F. W., B. W. O'Shea, and G. M. Voit (2020). *The Astrophysical Journal* 901.2, p. 117. DOI: 10.3847/1538-4357/abb08c.

Godunov, S. K. (1959). *Matematičeskij sbornik* 47(89).3, p. 271.

González Delgado, R. M., R. C. Fernandes, E. Pérez, et al. (2016). *Astronomy and Astrophysics* 590, A44, A44. DOI: 10.1051/0004-6361/201628174.

Goulding, A. D., J. E. Greene, R. Bezanson, et al. (2018). *Publications of the Astronomical Society of Japan* 70, S37 (SP1), S37. DOI: 10.1093/pasj/psx135.

Grand, R. J. J., F. A. Gómez, F. Marinacci, et al. (2017). *Monthly Notices of the Royal Astronomical Society* 467.1, p. 179. DOI: 10.1093/mnras/stx071.

Greengard, L. and V. Rokhlin (1987). *Journal of Computational Physics* 73.2, p. 325. DOI: 10.1016/0021-9991(87)90140-9.

Gunn, J. E. (1977). *The Astrophysical Journal* 218, p. 592. DOI: 10.1086/155715.

Gupta, A., J. Kingsbury, S. Mathur, et al. (2021). *The Astrophysical Journal* 909.2, p. 164. DOI: 10.3847/1538-4357/abdbb6.

Haardt, F. and P. Madau (2001). *Clusters of Galaxies and the High Redshift Universe Observed in X-rays*. XXIst Moriond Astrophysics Meeting. Ed. by D. M. Neumann and J. T. V. Tran. eprint: arXiv:astro-ph/0106018, p. 64.

Haardt, F. and P. Madau (2012). *The Astrophysical Journal* 746.2, p. 125. DOI: 10.1088/0004-637X/746/2/125.

Habouzit, M., Y. Li, R. S. Somerville, et al. (2020).

Hafen, Z., J. Stern, J. Bullock, et al. (2022). *Monthly Notices of the Royal Astronomical Society* 514.4, p. 5056. DOI: 10.1093/mnras/stac1603.

Haggar, R., M. E. Gray, F. R. Pearce, et al. (2020). *Monthly Notices of the Royal Astronomical Society* 492.4, p. 6074. DOI: 10.1093/mnras/staa273.

Hahn, O. and T. Abel (2011). *Monthly Notices of the Royal Astronomical Society* 415.3, p. 2101. DOI: 10.1111/j.1365-2966.2011.18820.x.

Haislmaier, K. J., T. M. Tripp, N. Katz, et al. (2020). *Monthly Notices of the Royal Astronomical Society* 502.4, p. 4993. DOI: 10.1093/mnras/staa3544.

Hamilton, A. J. S., P. Kumar, E. Lu, et al. (1991). *The Astrophysical Journal* 374, p. L1. DOI: 10.1086/186057.

Hamilton, D. (1985). *The Astrophysical Journal* 297, p. 371. DOI: 10.1086/163537.

Hani, M. H., H. Gosain, S. L. Ellison, et al. (2020). *Monthly Notices of the Royal Astronomical Society* 493.3, p. 3716. DOI: 10.1093/mnras/staa459.

Harris, C. R., K. J. Millman, S. J. van der Walt, et al. (2020). *Nature* 585.7825, p. 357. DOI: 10.1038/s41586-020-2649-2.

Heckman, T., S. Borthakur, V. Wild, et al. (2017). *The Astrophysical Journal* 846.2, p. 151. DOI: 10.3847/1538-4357/aa80dc.

Heckman, T. M. and P. N. Best (2014). *Annual Review of Astronomy and Astrophysics* 52, p. 589. DOI: 10.1146/annurev-astro-081913-035722.

Heitmann, K., D. Higdon, M. White, et al. (2009). *The Astrophysical Journal* 705.1, p. 156. DOI: 10.1088/0004-637X/705/1/156.

Heitmann, K., M. White, C. Wagner, et al. (2010). *The Astrophysical Journal* 715.1, p. 104. DOI: 10.1088/0004-637X/715/1/104.

Henriques, B. M. B., P. A. Thomas, S. Oliver, et al. (2009). *Monthly Notices of the Royal*

Astronomical Society 396.1, p. 535. DOI: 10.1111/j.1365-2966.2009.14730.x.

Hernquist, L. and J. C. Mihos (1995). *The Astrophysical Journal* 448, p. 41. DOI: 10.1086/175940.

Hinshaw, G., D. Larson, E. Komatsu, et al. (2013). *The Astrophysical Journal Supplement Series* 208.2, p. 19. DOI: 10.1088/0067-0049/208/2/19.

Hirschmann, M., T. Naab, R. S. Somerville, et al. (2012). *Monthly Notices of the Royal Astronomical Society* 419.4, p. 3200. DOI: 10.1111/j.1365-2966.2011.19961.x.

Ho, S. H., C. L. Martin, and J. Schaye (2021). *The Astrophysical Journal* 923.2, p. 137. DOI: 10.3847/1538-4357/ac2c73.

Ho, S. H., C. L. Martin, and M. L. Turner (2019). *The Astrophysical Journal* 875.1, p. 54. DOI: 10.3847/1538-4357/ab0ec2.

Hockney, R. W. and J. W. Eastwood (1981). Advanced Book Program. New York: McGraw-Hill International Book Co. ISBN: 978-0-07-029108-9.

Hodges-Kluck, E. J., M. J. Miller, and J. N. Bregman (2016). *The Astrophysical Journal* 822.1, p. 21. DOI: 10.3847/0004-637X/822/1/21.

Hopkins, P. F. (2015). *Monthly Notices of the Royal Astronomical Society* 450.1, p. 53. DOI: 10.1093/mnras/stv195.

Hopkins, P. F., D. Kereš, J. Oñorbe, et al. (2014). *Monthly Notices of the Royal Astronomical Society* 445.1, p. 581. DOI: 10.1093/mnras/stu1738.

Hopkins, P. F. and E. Quataert (2011). *Monthly Notices of the Royal Astronomical Society* 415.2, p. 1027. DOI: 10.1111/j.1365-2966.2011.18542.x.

Hopkins, P. F., E. Quataert, and N. Murray (2012a). *Monthly Notices of the Royal Astronomical Society* 421.4, p. 3522. DOI: 10.1111/j.1365-2966.2012.20593.x.

— (2012b). *Monthly Notices of the Royal Astronomical Society* 421.4, p. 3488. DOI: 10.1111/j.1365-2966.2012.20578.x.

Hopkins, P. F., P. Torrey, C.-A. Faucher-Giguère, et al. (2016). *Monthly Notices of the Royal Astronomical Society* 458.1, p. 816. DOI: 10.1093/mnras/stw289.

Hopkins, P. F., A. Wetzel, D. Keres, et al. (2018a). *Monthly Notices of the Royal Astronomical Society* 480.1, p. 800. DOI: 10.1093/mnras/sty1690.

Hopkins, P. F., A. Wetzel, D. Kereš, et al. (2018b). *Monthly Notices of the Royal Astronomical Society* 477.2, p. 1578. DOI: 10.1093/mnras/sty674.

Hopkins, P. F., A. Wetzel, C. Wheeler, et al. (2022). DOI: 10.48550/arXiv.2203.00040.

Hoyle, F. and R. A. Lyttleton (1939). *Proceedings of the Cambridge Philosophical Society* 35.3, p. 405. DOI: 10.1017/S0305004100021150.

Hubble, E. P. (1925). *Popular Astronomy* 33, p. 252.

Hummels, C. B., G. L. Bryan, B. D. Smith, et al. (2013). *Monthly Notices of the Royal Astronomical Society* 430.3, p. 1548. DOI: 10.1093/mnras/sts702.

Hummels, C. B., B. D. Smith, P. F. Hopkins, et al. (2019). *The Astrophysical Journal* 882.2, p. 156. DOI: 10.3847/1538-4357/ab378f.

Hummels, C. B., B. D. Smith, and D. W. Silvia (2017). *The Astrophysical Journal* 847.1, p. 59. DOI: 10.3847/1538-4357/aa7e2d.

Hunter, J. D. (2007). *Computing in Science & Engineering* 9.3, p. 90. DOI: 10.1109/MCSE.2007.55.

Ibarra-Medel, H. J., S. F. Sánchez, V. Avila-Reese, et al. (2016). *Monthly Notices of the Royal Astronomical Society* 463.3, p. 2799. DOI: 10.1093/mnras/stw2126.

Jeans, J. H. (1902). *Philosophical Transactions of the Royal Society of London. Series A, Containing Papers of a Mathematical or Physical Character* 199.312-320, p. 1. DOI: 10.1098/rsta.1902.0012.

Jenkins, A., C. S. Frenk, S. D. M. White, et al. (2001). *Monthly Notices of the Royal Astronomical Society* 321.2, p. 372. DOI: 10.1046/j.1365-8711.2001.04029.x.

Jetley, P., F. Gioachin, C. Mendes, et al. (2008). 2008 IEEE International Parallel & Distributed Processing Symposium. IEEE Computer Society, p. 1. ISBN: 978-1-4244-1693-6. DOI: 10.1109/IPDPS.2008.4536319.

Jetley, P., L. Wesolowski, F. Gioachin, et al. (2010). SC Conference. IEEE Computer Society, p. 1. ISBN: 978-1-4244-7559-9. DOI: 10.1109/SC.2010.49.

Ji, S., T. K. Chan, C. B. Hummels, et al. (2020). *Monthly Notices of the Royal Astronomical Society* 496.4, p. 4221. DOI: 10.1093/mnras/staa1849.

Karakas, A. I. (2010). *Monthly Notices of the Royal Astronomical Society* 403.3, p. 1413. DOI: 10.1111/j.1365-2966.2009.16198.x.

Katsianis, A., G. Blanc, C. P. Lagos, et al. (2017). *Monthly Notices of the Royal Astronomical Society* 472.1, p. 919. DOI: 10.1093/mnras/stx2020.

Katsianis, A., X. Zheng, V. Gonzalez, et al. (2019). *The Astrophysical Journal* 879.1, 11, p. 11. DOI: 10.3847/1538-4357/ab1f8d.

Katz, N. (1992). *The Astrophysical Journal* 391, p. 502. DOI: 10.1086/171366.

Kaviraj, S. (2014). *Monthly Notices of the Royal Astronomical Society* 440.4, p. 2944. DOI: 10.1093/mnras/stu338.

Keller, B. W., J. Wadsley, S. M. Benincasa, et al. (2014). *Monthly Notices of the Royal Astronomical Society* 442.4, p. 3013. DOI: 10.1093/mnras/stu1058.

Keller, B. W., J. M. D. Kruijssen, and M. Chevance (2022). *Monthly Notices of the Royal Astronomical Society* 514.4, p. 5355. DOI: 10.1093/mnras/stac1607.

Kennicutt Jr., R. C. (1989). *The Astrophysical Journal* 344, p. 685. DOI: 10.1086/167834.

Kepner, J. V. (1999). *The Astrophysical Journal* 520.1, p. 59. DOI: 10.1086/307419.

Kereš, D., N. Katz, D. H. Weinberg, et al. (2005). *Monthly Notices of the Royal Astronomical Society* 363.1, p. 2. DOI: 10.1111/j.1365-2966.2005.09451.x.

Khaire, V. and R. Srianand (2019). *Monthly Notices of the Royal Astronomical Society* 484.3, p. 4174. DOI: 10.1093/mnras/stz174.

Khokhlov, A. M. (1998). *Journal of Computational Physics* 143.2, p. 519. DOI: 10.1006/jcph.1998.9998.

Kim, C.-G. and E. C. Ostriker (2015). *The Astrophysical Journal* 802.2, p. 99. DOI: 10.1088/0004-637X/802/2/99.

— (2017). *The Astrophysical Journal* 846.2, p. 133. DOI: 10.3847/1538-4357/aa8599.

Kim, J.-h., T. Abel, O. Agertz, et al. (2014). *The Astrophysical Journal Supplement Series* 210.1, p. 14. DOI: 10.1088/0067-0049/210/1/14.

Kim, J.-h., O. Agertz, R. Teyssier, et al. (2016). *The Astrophysical Journal* 833.2, p. 202. DOI: 10.3847/1538-4357/833/2/202.

Kimm, T. and R. Cen (2014). *The Astrophysical Journal* 788.2, p. 121. DOI: 10.1088/0004-637X/788/2/121.

Klypin, A. A. and S. F. Shandarin (1983). *Monthly Notices of the Royal Astronomical Society* 204.3, p. 891. DOI: 10.1093/mnras/204.3.891.

Knebe, A., S. R. Knollmann, S. I. Muldrew, et al. (2011a). *Monthly Notices of the Royal Astro-*

nomical Society 415.3, p. 2293. DOI: 10.1111/j.1365-2966.2011.18858.x.

Knebe, A., N. I. Libeskind, S. R. Knollmann, et al. (2011b). *Monthly Notices of the Royal Astronomical Society* 412.1, p. 529. DOI: 10.1111/j.1365-2966.2010.17924.x.

Kobayashi, C., H. Umeda, K. Nomoto, et al. (2006). *The Astrophysical Journal* 653.2, p. 1145. DOI: 10.1086/508914.

Koopmann, R. A. and J. D. P. Kenney (2004). *The Astrophysical Journal* 613.2, p. 866. DOI: 10.1086/423191.

Kopenhafer, C., B. W. O'Shea, and G. M. Voit (2022). DOI: 10.48550/arXiv.2206.04706.

Kopenhafer, C., T. K. Starkenburg, S. Tonnesen, et al. (2020). *The Astrophysical Journal* 903.2, p. 143. DOI: 10.3847/1538-4357/abbd9c.

Kormendy, J. (1977). *The Astrophysical Journal* 218, p. 333. DOI: 10.1086/155687.

Kormendy, J. and L. C. Ho (2013). *Annual Review of Astronomy and Astrophysics* 51.1, p. 511. DOI: 10.1146/annurev-astro-082708-101811.

Kravtsov, A. V. (2003). *The Astrophysical Journal* 590.1, p. L1. DOI: 10.1086/376674.

Kravtsov, A. V., A. A. Klypin, and A. M. Khokhlov (1997). *The Astrophysical Journal Supplement Series* 111.1, p. 73. DOI: 10.1086/313015.

Kretschmer, M. and R. Teyssier (2020). *Monthly Notices of the Royal Astronomical Society* 492.1, p. 1385. DOI: 10.1093/mnras/stz3495.

Kroupa, P. (2001). *Monthly Notices of the Royal Astronomical Society* 322.2, p. 231. DOI: 10.1046/j.1365-8711.2001.04022.x.

Krumholz, M. R., A. Dekel, and C. F. McKee (2012). *The Astrophysical Journal* 745.1, p. 69. DOI: 10.1088/0004-637X/745/1/69.

Lacey, C. and S. Cole (1993). *Monthly Notices of the Royal Astronomical Society* 262.3, p. 627. DOI: 10.1093/mnras/262.3.627.

Lackner, C. N. and J. E. Gunn (2012). *Monthly Notices of the Royal Astronomical Society* 421.3, p. 2277. DOI: 10.1111/j.1365-2966.2012.20450.x.

Lagos, C. d. P., A. R. H. Stevens, R. G. Bower, et al. (2018). *Monthly Notices of the Royal Astronomical Society* 473.4, p. 4956. DOI: 10.1093/mnras/stx2667.

Lang, P., S. Wuyts, R. S. Somerville, et al. (2014). *The Astrophysical Journal* 788.1, 11, p. 11.

DOI: 10.1088/0004-637X/788/1/11.

Larson, R. B. (1976). *Monthly Notices of the Royal Astronomical Society* 176.1, p. 31. DOI: 10.1093/mnras/176.1.31.

Larson, R. B. (1974). *Monthly Notices of the Royal Astronomical Society* 169, p. 229. DOI: 10.1093/mnras/169.2.229.

Leavitt, H. S. and E. C. Pickering (1912). *Harvard College Observatory Circular* 173, p. 1.

Lee, N., D. B. Sanders, C. M. Casey, et al. (2015). *The Astrophysical Journal* 801.2, p. 80. DOI: 10.1088/0004-637X/801/2/80.

Lehner, N., J. M. O'Meara, A. J. Fox, et al. (2014). *The Astrophysical Journal* 788.2, p. 119. DOI: 10.1088/0004-637X/788/2/119.

Lehner, N., S. C. Berek, J. C. Howk, et al. (2020). *The Astrophysical Journal* 900.1, p. 9. DOI: 10.3847/1538-4357/aba49c.

Lehner, N., C. Kopenhafer, J. M. O'Meara, et al. (2022). *The Astrophysical Journal* 936.2, p. 156. DOI: 10.3847/1538-4357/ac7400.

Lehner, N., J. M. O'Meara, J. C. Howk, et al. (2016). *The Astrophysical Journal* 833.2, p. 283. DOI: 10.3847/1538-4357/833/2/283.

Lehner, N., C. B. Wotta, J. C. Howk, et al. (2018). *The Astrophysical Journal* 866.1, p. 33. DOI: 10.3847/1538-4357/aadd03.

Leitherer, C., D. Schaerer, J. D. Goldader, et al. (1999). *The Astrophysical Journal Supplement Series* 123.1, p. 3. DOI: 10.1086/313233.

Leroy, A. K., F. Walter, E. Brinks, et al. (2008). *The Astronomical Journal* 136.6, p. 2782. DOI: 10.1088/0004-6256/136/6/2782.

LeVeque, R. J. (2007). Philadelphia: Society for Industrial and Applied Mathematics. ISBN: 978-0-89871-629-0.

Li, C., E. Wang, L. Lin, et al. (2015). *The Astrophysical Journal* 804.2, 125, p. 125. DOI: 10.1088/0004-637X/804/2/125.

Li, M. and S. Tonnesen (2020). *The Astrophysical Journal* 898.2, p. 148. DOI: 10.3847/1538-4357/ab9f9f.

Li, Y. and G. L. Bryan (2014a). *The Astrophysical Journal* 789.1, p. 54. DOI: 10.1088/0004-637X/789/1/54.

Li, Y. and G. L. Bryan (2014b). *The Astrophysical Journal* 789.2, p. 153. DOI: 10.1088/0004-637X/789/2/153.

Li, Y., M. Ruszkowski, and G. L. Bryan (2017). *The Astrophysical Journal* 847.2, p. 106. DOI: 10.3847/1538-4357/aa88c1.

Licquia, T. C. and J. A. Newman (2015). *The Astrophysical Journal* 806.1, p. 96. DOI: 10.1088/0004-637X/806/1/96.

Limongi, M. and A. Chieffi (2018). *The Astrophysical Journal Supplement Series* 237.1, p. 13. DOI: 10.3847/1538-4365/aacb24.

Lin, L., B.-C. Hsieh, H.-A. Pan, et al. (2019). *The Astrophysical Journal* 872.1, 50, p. 50. DOI: 10.3847/1538-4357/aafa84.

Lochhaas, C., G. L. Bryan, Y. Li, et al. (2020). *Monthly Notices of the Royal Astronomical Society* 493.1, p. 1461. DOI: 10.1093/mnras/staa358.

Lochhaas, C., T. A. Thompson, E. Quataert, et al. (2018). *Monthly Notices of the Royal Astronomical Society* 481.2, p. 1873. DOI: 10.1093/mnras/sty2421.

Lochhaas, C., J. Tumlinson, M. S. Peeples, et al. (2022).

Lofthouse, E. K., M. Fumagalli, M. Fossati, et al. (2020). *Monthly Notices of the Royal Astronomical Society* 491.2, p. 2057. DOI: 10.1093/mnras/stz3066.

Longair, M. S. (1998). Astronomy and Astrophysics Library. Berlin: Springer. ISBN: 978-3-540-63785-1.

Lopez, S., N. Tejos, L. F. Barrientos, et al. (2020). *Monthly Notices of the Royal Astronomical Society* 491.3, p. 4442. DOI: 10.1093/mnras/stz3183.

López Fernández, R., R. M. González Delgado, E. Pérez, et al. (2018). *Astronomy and Astrophysics* 615, A27, A27. DOI: 10.1051/0004-6361/201732358.

Lu, Y., H. J. Mo, M. D. Weinberg, et al. (2011). *Monthly Notices of the Royal Astronomical Society* 416.3, p. 1949. DOI: 10.1111/j.1365-2966.2011.19170.x.

Mac Low, M.-M. and R. McCray (1988). *The Astrophysical Journal* 324, p. 776. DOI: 10.1086/165936.

Maeder, A. and G. Meynet (1989). *Astronomy and Astrophysics* 210, p. 155.

Magrini, L., L. Coccato, L. Stanghellini, et al. (2016). *Astronomy and Astrophysics* 588, A91, A91. DOI: 10.1051/0004-6361/201527799.

Maiolino, R. and F. Mannucci (2019). *Astronomy and Astrophysics Review* 27.1, 3, p. 3. DOI: 10.1007/s00159-018-0112-2.

Man, A. and S. Belli (2018). *Nature Astronomy* 2.9, p. 695. DOI: 10.1038/s41550-018-0558-1.

Mandelker, N., F. C. van den Bosch, V. Springel, et al. (2019). *The Astrophysical Journal* 881.1, p. L20. DOI: 10.3847/2041-8213/ab30cb.

Marinacci, F., M. Vogelsberger, R. Pakmor, et al. (2018). *Monthly Notices of the Royal Astronomical Society* 480.4, p. 5113. DOI: 10.1093/mnras/sty2206.

Marra, R., C. W. Churchill, C. Doughty, et al. (2021). *Monthly Notices of the Royal Astronomical Society* 508.4, p. 4938. DOI: 10.1093/mnras/stab2896.

Marra, R., C. W. Churchill, G. G. Kacprzak, et al. (2022).

Marri, S. and S. D. M. White (2003). *Monthly Notices of the Royal Astronomical Society* 345.2, p. 561. DOI: 10.1046/j.1365-8711.2003.06984.x.

Martig, M., F. Bournaud, R. Teyssier, et al. (2009). *The Astrophysical Journal* 707.1, p. 250. DOI: 10.1088/0004-637X/707/1/250.

Martig, M., A. F. Crocker, F. Bournaud, et al. (2013). *Monthly Notices of the Royal Astronomical Society* 432.3, p. 1914. DOI: 10.1093/mnras/sts594.

Martin, G., S. Kaviraj, M. Volonteri, et al. (2018). *Monthly Notices of the Royal Astronomical Society* 476.2, p. 2801. DOI: 10.1093/mnras/sty324.

Masters, K. L., M. Mosleh, A. K. Romer, et al. (2010). *Monthly Notices of the Royal Astronomical Society* 405.2, p. 783. DOI: 10.1111/j.1365-2966.2010.16503.x.

Matteucci, F. and P. Francois (1989). *Monthly Notices of the Royal Astronomical Society* 239.3, p. 885. DOI: 10.1093/mnras/239.3.885.

Matthee, J. and J. Schaye (2019). *Monthly Notices of the Royal Astronomical Society* 484.1, p. 915. DOI: 10.1093/mnras/stz030.

McAlpine, S., C. M. Harrison, D. J. Rosario, et al. (2020). *Monthly Notices of the Royal Astronomical Society* 494.4, p. 5713. DOI: 10.1093/mnras/staa1123.

McCabe, T., S. Borthakur, T. Heckman, et al. (2021). *The Astrophysical Journal* 923.2, p. 189. DOI: 10.3847/1538-4357/ac283c.

McCourt, M., P. Sharma, E. Quataert, et al. (2012). *Monthly Notices of the Royal Astronomical Society* 419.4, p. 3319. DOI: 10.1111/j.1365-2966.2011.19972.x.

McKee, C. F. and J. P. Ostriker (1977). *The Astrophysical Journal* 218, p. 148. DOI: 10.1086/155667.

McKinney, W. (2010). Python in Science Conference. Austin, Texas, p. 56. DOI: 10.25080/Majora-92bf1922-00a.

McPartland, C., D. B. Sanders, L. J. Kewley, et al. (2019). *Monthly Notices of the Royal Astronomical Society: Letters* 482.1, p. L129. DOI: 10.1093/mnrasl/sly202.

Medling, A. M., L. Cortese, S. M. Croom, et al. (2018). *Monthly Notices of the Royal Astronomical Society* 475.4, p. 5194. DOI: 10.1093/mnras/sty127.

Meece, G. R., B. W. O'Shea, and G. M. Voit (2015). *The Astrophysical Journal* 808.1, p. 43. DOI: 10.1088/0004-637X/808/1/43.

Mehlert, D., D. Thomas, R. P. Saglia, et al. (2003). *Astronomy and Astrophysics* 407.2, p. 423. DOI: 10.1051/0004-6361:20030886.

Mendel, J. T., L. Simard, S. L. Ellison, et al. (2013). *Monthly Notices of the Royal Astronomical Society* 429.3, p. 2212. DOI: 10.1093/mnras/sts489.

Méndez-Abreu, J., S. F. Sánchez, and A. de Lorenzo-Cáceres (2019). *Monthly Notices of the Royal Astronomical Society: Letters* 488.1, p. L80. DOI: 10.1093/mnrasl/slz103.

Menon, H., L. Wesolowski, G. Zheng, et al. (2015). *Computational Astrophysics and Cosmology* 2, p. 1. DOI: 10.1186/s40668-015-0007-9.

Mignone, A., G. Bodo, S. Massaglia, et al. (2007). *The Astrophysical Journal Supplement Series* 170.1, p. 228. DOI: 10.1086/513316.

Mignone, A., C. Zanni, P. Tzeferacos, et al. (2012). *The Astrophysical Journal Supplement Series* 198.1, p. 7. DOI: 10.1088/0067-0049/198/1/7.

Mihos, J. C. and L. Hernquist (1994). *The Astrophysical Journal Letters* 425, p. L13. DOI: 10.1086/187299.

Mitchell, P. D. and J. Schaye (2022). *Monthly Notices of the Royal Astronomical Society* 511.2, p. 2948. DOI: 10.1093/mnras/stab3339.

Miyamoto, M. and R. Nagai (1975). *Publications of the Astronomical Society of Japan* 27, p. 533.

Moon, S., W.-T. Kim, C.-G. Kim, et al. (2022). *The Astrophysical Journal* 925.1, p. 99. DOI: 10.3847/1538-4357/ac3a7b.

More, S., A. V. Kravtsov, N. Dalal, et al. (2011). *The Astrophysical Journal Supplement Series*

195.1, 4, p. 4. DOI: 10.1088/0067-0049/195/1/4.

Morselli, L., P. Popesso, A. Cibinel, et al. (2019). *Astronomy and Astrophysics* 626, A61, A61. DOI: 10.1051/0004-6361/201834559.

Moustakas, J., J. Kennicutt Robert C., and C. A. Tremonti (2006). *The Astrophysical Journal* 642.2, p. 775. DOI: 10.1086/500964.

Muzzin, A., D. Marchesini, M. Stefanon, et al. (2013). *The Astrophysical Journal* 777.1, p. 18. DOI: 10.1088/0004-637X/777/1/18.

Naab, T., L. Oser, E. Emsellem, et al. (2014). *Monthly Notices of the Royal Astronomical Society* 444.4, p. 3357. DOI: 10.1093/mnras/stt1919.

Naab, T. and J. P. Ostriker (2017). *Annual Review of Astronomy and Astrophysics* 55.1, p. 59. DOI: 10.1146/annurev-astro-081913-040019.

Naiman, J. P., A. Pillepich, V. Springel, et al. (2018). *Monthly Notices of the Royal Astronomical Society* 477.1, p. 1206. DOI: 10.1093/mnras/sty618.

Navarro, J. F. and S. D. M. White (1993). *Monthly Notices of the Royal Astronomical Society* 265.2, p. 271. DOI: 10.1093/mnras/265.2.271.

Navarro, J. F., C. S. Frenk, and S. D. M. White (1996). *The Astrophysical Journal* 462, p. 563. DOI: 10.1086/177173.

Nelson, D., A. Pillepich, V. Springel, et al. (2018). *Monthly Notices of the Royal Astronomical Society* 475.1, p. 624. DOI: 10.1093/mnras/stx3040.

Nelson, D., A. Pillepich, V. Springel, et al. (2019a). *Monthly Notices of the Royal Astronomical Society* 490.3, p. 3234. DOI: 10.1093/mnras/stz2306.

Nelson, D., V. Springel, A. Pillepich, et al. (2019b). *Computational Astrophysics and Cosmology* 6.1, p. 2. DOI: 10.1186/s40668-019-0028-x.

Nelson, E. J., P. G. van Dokkum, N. M. Förster Schreiber, et al. (2016). *The Astrophysical Journal* 828.1, 27, p. 27. DOI: 10.3847/0004-637X/828/1/27.

Nielsen, N. M., G. G. Kacprzak, S. K. Pointon, et al. (2020). *The Astrophysical Journal* 904.2, p. 164. DOI: 10.3847/1538-4357/abc561.

Nomoto, K., C. Kobayashi, and N. Tominaga (2013). *Annual Review of Astronomy and Astrophysics* 51.1, p. 457. DOI: 10.1146/annurev-astro-082812-140956.

Nonaka, A., A. S. Almgren, J. B. Bell, et al. (2010). *The Astrophysical Journal Supplement Series*

188.2, p. 358. DOI: 10.1088/0067-0049/188/2/358.

Oh, B. K., B. D. Smith, J. A. Peacock, et al. (2020). *Monthly Notices of the Royal Astronomical Society* 497.4, p. 5203. DOI: 10.1093/mnras/staa2318.

Oppenheimer, B. D. (2018). *Monthly Notices of the Royal Astronomical Society* 480.3, p. 2963. DOI: 10.1093/mnras/sty1918.

Pagel, B. E. J. and M. G. Edmunds (1981). *Annual Review of Astronomy and Astrophysics* 19, p. 77. DOI: 10.1146/annurev.aa.19.090181.000453.

Pakmor, R., A. Bauer, and V. Springel (2011). *Monthly Notices of the Royal Astronomical Society* 418.2, p. 1392. DOI: 10.1111/j.1365-2966.2011.19591.x.

Pan, Z., J. Li, W. Lin, et al. (2015). *The Astrophysical Journal Letters* 804.2, L42, p. L42. DOI: 10.1088/2041-8205/804/2/L42.

Paxton, B., L. Bildsten, A. Dotter, et al. (2011). *The Astrophysical Journal Supplement Series* 192.1, p. 3. DOI: 10.1088/0067-0049/192/1/3.

Paxton, B., M. Cantiello, P. Arras, et al. (2013). *The Astrophysical Journal Supplement Series* 208.1, p. 4. DOI: 10.1088/0067-0049/208/1/4.

Paxton, B., P. Marchant, J. Schwab, et al. (2015). *The Astrophysical Journal Supplement Series* 220.1, p. 15. DOI: 10.1088/0067-0049/220/1/15.

Paxton, B., J. Schwab, E. B. Bauer, et al. (2018). *The Astrophysical Journal Supplement Series* 234.2, p. 34. DOI: 10.3847/1538-4365/aaa5a8.

Paxton, B., R. Smolec, J. Schwab, et al. (2019). *The Astrophysical Journal Supplement Series* 243.1, p. 10. DOI: 10.3847/1538-4365/ab2241.

Peacock, J. A. and S. J. Dodds (1996). *Monthly Notices of the Royal Astronomical Society* 280.3, p. L19. DOI: 10.1093/mnras/280.3.L19.

Peebles, P. J. E. (2020). *Monthly Notices of the Royal Astronomical Society* 498.3, p. 4386. DOI: 10.1093/mnras/staa2649.

Peeples, M. S., L. Corlies, J. Tumlinson, et al. (2019). *The Astrophysical Journal* 873.2, p. 129. DOI: 10.3847/1538-4357/ab0654.

Peeples, M. S. and F. Shankar (2011). *Monthly Notices of the Royal Astronomical Society* 417.4, p. 2962. DOI: 10.1111/j.1365-2966.2011.19456.x.

Peeples, M. S., J. K. Werk, J. Tumlinson, et al. (2014). *The Astrophysical Journal* 786.1, p. 54.

DOI: 10.1088/0004-637X/786/1/54.

Percival, W. J., R. C. Nichol, D. J. Eisenstein, et al. (2007). *The Astrophysical Journal* 657.2, p. 645. DOI: 10.1086/510615.

Pérez, E., R. Cid Fernandes, R. M. González Delgado, et al. (2013). *The Astrophysical Journal Letters* 764.1, L1, p. L1. DOI: 10.1088/2041-8205/764/1/L1.

Pignatari, M., F. Herwig, R. Hirschi, et al. (2016). *The Astrophysical Journal Supplement Series* 225.2, p. 24. DOI: 10.3847/0067-0049/225/2/24.

Pillepich, A., D. Nelson, L. Hernquist, et al. (2018a). *Monthly Notices of the Royal Astronomical Society* 475.1, p. 648. DOI: 10.1093/mnras/stx3112.

Pillepich, A., D. Nelson, V. Springel, et al. (2019). *Monthly Notices of the Royal Astronomical Society* 490.3, p. 3196. DOI: 10.1093/mnras/stz2338.

Pillepich, A., V. Springel, D. Nelson, et al. (2018b). *Monthly Notices of the Royal Astronomical Society* 473.3, p. 4077. DOI: 10.1093/mnras/stx2656.

Pizzolato, F. and N. Soker (2005). *The Astrophysical Journal* 632.2, p. 821. DOI: 10.1086/444344.

— (2010). *Monthly Notices of the Royal Astronomical Society* 408.2, p. 961. DOI: 10.1111/j.1365-2966.2010.17156.x.

Planck Collaboration, P. a. R. Ade, M. Arnaud, et al. (2014). *Astronomy and Astrophysics* 571, A31. DOI: 10.1051/0004-6361/201423743.

Planck Collaboration, N. Aghanim, Y. Akrami, et al. (2020). *Astronomy and Astrophysics* 641, A6. DOI: 10.1051/0004-6361/201833910.

Poetrodjojo, H., B. Groves, L. J. Kewley, et al. (2018). DOI: 10.1093/mnras/sty1782.

Poggianti, B. M., I. Smail, A. Dressler, et al. (1999). DOI: 10.1086/307322.

Popesso, P., A. Concas, G. Cresci, et al. (2022). DOI: 10.48550/arXiv.2203.10487.

Prantzos, N., C. Abia, M. Limongi, et al. (2018). *Monthly Notices of the Royal Astronomical Society* 476.3, p. 3432. DOI: 10.1093/mnras/sty316.

Prasad, D., P. Sharma, and A. Babul (2015). *The Astrophysical Journal* 811, p. 108. DOI: 10.1088/0004-637X/811/2/108.

Prasad, D., G. M. Voit, and B. W. O'Shea (2022). *The Astrophysical Journal* 932.1, p. 18. DOI: 10.3847/1538-4357/ac69ee.

Prasad, D., G. M. Voit, B. W. O'Shea, et al. (2020). *The Astrophysical Journal* 905, arXiv:2006.10809, p. 50. DOI: 10.3847/1538-4357/abc33c.

Press, W. H. and P. Schechter (1974). *The Astrophysical Journal* 187, p. 425. DOI: 10.1086/152650.

Prochaska, J. X., J. N. Burchett, T. M. Tripp, et al. (2019). *The Astrophysical Journal Supplement Series* 243.2, p. 24. DOI: 10.3847/1538-4365/ab2b9a.

Prochaska, J. X., J. K. Werk, G. Worseck, et al. (2017). *The Astrophysical Journal* 837.2, p. 169. DOI: 10.3847/1538-4357/aa6007.

Puchwein, E., F. Haardt, M. G. Haehnelt, et al. (2019). *Monthly Notices of the Royal Astronomical Society* 485.1, p. 47. DOI: 10.1093/mnras/stz222.

Quai, S., L. Pozzetti, M. Moresco, et al. (2019). DOI: 10.1093/mnras/stz2771.

Queyrel, J., T. Contini, M. Kissler-Patig, et al. (2012). DOI: 10.1051/0004-6361/201117718.

Rees, M. J. and J. P. Ostriker (1977). *Monthly Notices of the Royal Astronomical Society* 179, p. 541. DOI: 10.1093/mnras/179.4.541.

Renzini, A. and Y.-j. Peng (2015). *The Astrophysical Journal Letters* 801, p. L29. DOI: 10.1088/2041-8205/801/2/L29.

Retana-Montenegro, E., E. V. Hese, G. Gentile, et al. (2012). *Astronomy and Astrophysics* 540, A70. DOI: 10.1051/0004-6361/201118543.

Rhodin, N. H. P., O. Agertz, L. Christensen, et al. (2019). *Monthly Notices of the Royal Astronomical Society* 488.3, p. 3634. DOI: 10.1093/mnras/stz1479.

Ritter, C., F. Herwig, S. Jones, et al. (2018a). *Monthly Notices of the Royal Astronomical Society* 480.1, p. 538. DOI: 10.1093/mnras/sty1729.

Ritter, C., B. Côté, F. Herwig, et al. (2018b). *The Astrophysical Journal Supplement Series* 237.2, p. 42. DOI: 10.3847/1538-4365/aad691.

Roberts-Borsani, G. W. (2020). *Monthly Notices of the Royal Astronomical Society* 494, p. 4266. DOI: 10.1093/mnras/staa1006.

Robotham, A. S. G., J. Liske, S. P. Driver, et al. (2013). *Monthly Notices of the Royal Astronomical Society* 431.1, p. 167. DOI: 10.1093/mnras/stt156.

Roca-Fàbrega, S., J.-H. Kim, L. Hausammann, et al. (2021). *The Astrophysical Journal* 917, p. 64. DOI: 10.3847/1538-4357/ac088a.

Rosas-Guevara, Y. M., R. G. Bower, J. Schaye, et al. (2015). *Monthly Notices of the Royal Astronomical Society* 454.1, p. 1038. DOI: 10.1093/mnras/stv2056.

Rosdahl, J., J. Schaye, Y. Dubois, et al. (2017). *Monthly Notices of the Royal Astronomical Society* 466.1, p. 11. DOI: 10.1093/mnras/stw3034.

Rowlands, K., T. Heckman, V. Wild, et al. (2018). DOI: 10.1093/mnras/sty1916.

Saintonge, A., G. Kauffmann, C. Kramer, et al. (2011). *Monthly Notices of the Royal Astronomical Society* 415.1, p. 32. DOI: 10.1111/j.1365-2966.2011.18677.x.

Salem, M. and G. L. Bryan (2014). *Monthly Notices of the Royal Astronomical Society* 437.4, p. 3312. DOI: 10.1093/mnras/stt2121.

Salim, S., R. M. Rich, S. Charlot, et al. (2007). *The Astrophysical Journal Supplement Series* 173.2, p. 267. DOI: 10.1086/519218.

Salmon, B., C. Papovich, S. L. Finkelstein, et al. (2015). *The Astrophysical Journal* 799.2, p. 183. DOI: 10.1088/0004-637X/799/2/183.

Salpeter, E. E. and G. L. Hoffman (1995). *The Astrophysical Journal* 441, p. 51. DOI: 10.1086/175334.

Sánchez, A. G., M. Crocce, A. Cabré, et al. (2009). *Monthly Notices of the Royal Astronomical Society* 400.3, p. 1643. DOI: 10.1111/j.1365-2966.2009.15572.x.

Sánchez, S. F., J. K. Barrera-Ballesteros, D. Colombo, et al. (2021). *Monthly Notices of the Royal Astronomical Society* 503.2, p. 1615. DOI: 10.1093/mnras/stab442.

Sánchez, S. F., R. C. Kennicutt, A. Gil de Paz, et al. (2012). *Astronomy and Astrophysics* 538, A8, A8. DOI: 10.1051/0004-6361/201117353.

Sánchez, S. F., F. F. Rosales-Ortega, J. Iglesias-Páramo, et al. (2014). *Astronomy and Astrophysics* 563, A49, A49. DOI: 10.1051/0004-6361/201322343.

Sánchez, S. F. (2020). *Annual Review of Astronomy and Astrophysics* 58.1, arXiv:1911.06925, p. 99. DOI: 10.1146/annurev-astro-012120-013326.

Sánchez-Blázquez, P., R. F. Peletier, J. Jiménez-Vicente, et al. (2006). *Monthly Notices of the Royal Astronomical Society* 371.2, p. 703. DOI: 10.1111/j.1365-2966.2006.10699.x.

Sánchez-Blázquez, P., D. A. Forbes, J. Strader, et al. (2007). *Monthly Notices of the Royal Astronomical Society* 377.2, p. 759. DOI: 10.1111/j.1365-2966.2007.11647.x.

Sánchez-Menguiano, L., S. F. Sánchez, I. Pérez, et al. (2018). *Astronomy and Astrophysics* 609,

A119, A119. DOI: 10.1051/0004-6361/201731486.

Sarkar, K. C., A. Sternberg, and O. Gnat (2022). DOI: 10.48550/arXiv.2203.15814.

Scannapieco, C., P. B. Tissera, S. D. M. White, et al. (2006). *Monthly Notices of the Royal Astronomical Society* 371.3, p. 1125. DOI: 10.1111/j.1365-2966.2006.10785.x.

Schaller, M., P. Gonnet, A. B. G. Chalk, et al. (2016). *Proceedings of the Platform for Advanced Scientific Computing Conference*. Proceedings of the Platform for Advanced Scientific Computing Conference. eprint: arXiv:1606.02738, p. 2. DOI: 10.1145/2929908.2929916.

Schawinski, K., C. M. Urry, B. D. Simmons, et al. (2014). *Monthly Notices of the Royal Astronomical Society* 440.1, p. 889. DOI: 10.1093/mnras/stu327.

Schaye, J. (2004). *The Astrophysical Journal* 609.2, p. 667. DOI: 10.1086/421232.

Schaye, J., R. A. Crain, R. G. Bower, et al. (2015). *Monthly Notices of the Royal Astronomical Society* 446.1, p. 521. DOI: 10.1093/mnras/stu2058.

Schaye, J., C. D. Vecchia, C. M. Booth, et al. (2010). *Monthly Notices of the Royal Astronomical Society* 402.3, p. 1536. DOI: 10.1111/j.1365-2966.2009.16029.x.

Schechter, P. (1976). *The Astrophysical Journal* 203, p. 297. DOI: 10.1086/154079.

Schiminovich, D., T. K. Wyder, D. C. Martin, et al. (2007). *The Astrophysical Journal Supplement Series* 173.2, p. 315. DOI: 10.1086/524659.

Schmidt, M. (1959). *The Astrophysical Journal* 129, p. 243. DOI: 10.1086/146614.

— (1963). *The Astrophysical Journal* 137, p. 758. DOI: 10.1086/147553.

Schneider, E. E., E. C. Ostriker, B. E. Robertson, et al. (2020). *The Astrophysical Journal* 895.1, p. 43. DOI: 10.3847/1538-4357/ab8ae8.

Schneider, E. E. and B. E. Robertson (2015). *The Astrophysical Journal Supplement Series* 217.2, p. 24. DOI: 10.1088/0067-0049/217/2/24.

— (2018). *The Astrophysical Journal* 860.2, p. 135. DOI: 10.3847/1538-4357/aac329.

Schneider, E. E., B. E. Robertson, and T. A. Thompson (2018). *The Astrophysical Journal* 862.1, p. 56.

Sedov, L. I. (1959). New York: Academic Press. ISBN: 978-1-4832-0088-0.

Seljak, U., A. Makarov, P. McDonald, et al. (2005). *Physical Review D* 71.10, p. 103515. DOI:

10.1103/PhysRevD.71.103515.

Serra, P., T. Oosterloo, R. Morganti, et al. (2012). *Monthly Notices of the Royal Astronomical Society* 422.3, p. 1835. DOI: 10.1111/j.1365-2966.2012.20219.x.

Shakura, N. I. and R. A. Sunyaev (1973). *Astronomy and Astrophysics* 24, p. 337.

Sharma, P., M. McCourt, E. Quataert, et al. (2012). *Monthly Notices of the Royal Astronomical Society* 420.4, p. 3174. DOI: 10.1111/j.1365-2966.2011.20246.x.

Shaver, P. A., R. X. McGee, L. M. Newton, et al. (1983). *Monthly Notices of the Royal Astronomical Society* 204.1, p. 53. DOI: 10.1093/mnras/204.1.53.

Shaw, D. J. and D. F. Mota (2008). *The Astrophysical Journal Supplement Series* 174.2, p. 277. DOI: 10.1086/522339.

Shen, S., H. J. Mo, S. D. M. White, et al. (2003). *Monthly Notices of the Royal Astronomical Society* 343.3, p. 978. DOI: 10.1046/j.1365-8711.2003.06740.x.

Sherman, S., S. Jogee, J. Florez, et al. (2021). *Monthly Notices of the Royal Astronomical Society* 505.1, p. 947. DOI: 10.1093/mnras/stab1350.

Shin, E.-J., J.-H. Kim, and B. K. Oh (2021). *The Astrophysical Journal* 917.1, p. 12. DOI: 10.3847/1538-4357/abffd0.

Sijacki, D., V. Springel, T. Di Matteo, et al. (2007). *Monthly Notices of the Royal Astronomical Society* 380.3, p. 877. DOI: 10.1111/j.1365-2966.2007.12153.x.

Silk, J. and M. J. Rees (1998). *Astronomy and Astrophysics* 331, p. L1.

Simons, R. C., M. S. Peeples, J. Tumlinson, et al. (2020). *The Astrophysical Journal* 905.2, p. 167. DOI: 10.3847/1538-4357/abc5b8.

Simpson, C. M., R. Pakmor, F. Marinacci, et al. (2016). *The Astrophysical Journal Letters* 827.2, p. L29. DOI: 10.3847/2041-8205/827/2/L29.

Smith, B. D., G. L. Bryan, S. C. O. Glover, et al. (2017). *Monthly Notices of the Royal Astronomical Society* 466.2, p. 2217. DOI: 10.1093/mnras/stw3291.

Smith, B. D., E. J. Hallman, J. M. Shull, et al. (2011). *The Astrophysical Journal* 731.1, p. 6. DOI: 10.1088/0004-637X/731/1/6.

Smith, M. C., D. Sijacki, and S. Shen (2018). *Monthly Notices of the Royal Astronomical Society* 478.1, p. 302. DOI: 10.1093/mnras/sty994.

Smith, R. E., J. A. Peacock, A. Jenkins, et al. (2003). *Monthly Notices of the Royal Astronomical Society* 341.4, p. 1311. DOI: 10.1046/j.1365-8711.2003.06503.x.

Soltan, A. (1982). *Monthly Notices of the Royal Astronomical Society* 200, p. 115. DOI: 10.1093/mnras/200.1.115.

Somerville, R. S. and R. Davé (2015). *Annual Review of Astronomy and Astrophysics* 53, p. 51. DOI: 10.1146/annurev-astro-082812-140951.

Speagle, J. S., C. L. Steinhardt, P. L. Capak, et al. (2014). *The Astrophysical Journal Supplement Series* 214.2, p. 15. DOI: 10.1088/0067-0049/214/2/15.

Spilker, J. S., R. Bezanson, B. J. Weiner, et al. (2019). *The Astrophysical Journal* 883.1, 81, p. 81. DOI: 10.3847/1538-4357/ab3804.

Springel, V. (2005). *Monthly Notices of the Royal Astronomical Society* 364.4, p. 1105. DOI: 10.1111/j.1365-2966.2005.09655.x.

— (2010a). DOI: 10.1111/j.1365-2966.2009.15715.x.

— (2010b). *Annual Review of Astronomy and Astrophysics* 48.1, p. 391. DOI: 10.1146/annurev-astro-081309-130914.

Springel, V., T. Di Matteo, and L. Hernquist (2005). *The Astrophysical Journal* 620.2, p. L79. DOI: 10.1086/428772.

Springel, V. and L. Hernquist (2003). *Monthly Notices of the Royal Astronomical Society* 339.2, p. 289. DOI: 10.1046/j.1365-8711.2003.06206.x.

Springel, V., R. Pakmor, A. Pillepich, et al. (2018). *Monthly Notices of the Royal Astronomical Society* 475.1, p. 676. DOI: 10.1093/mnras/stx3304.

Springel, V., S. D. M. White, A. Jenkins, et al. (2005). *Nature* 435.7042 (7042), p. 629. DOI: 10.1038/nature03597.

Springel, V., S. D. M. White, G. Tormen, et al. (2001). *Monthly Notices of the Royal Astronomical Society* 328.3, p. 726. DOI: 10.1046/j.1365-8711.2001.04912.x.

Springel, V., N. Yoshida, and S. D. M. White (2001). *New Astronomy* 6.2, p. 79. DOI: 10.1016/S1384-1076(01)00042-2.

Starkenburg, T. K., S. Tonnesen, and C. Kopenhafer (2019). *The Astrophysical Journal* 874.2, L17, p. L17. DOI: 10.3847/2041-8213/ab0f34.

Steinhardt, C. L., J. S. Speagle, P. Capak, et al. (2014). *The Astrophysical Journal* 791.2, p. L25.

DOI: 10.1088/2041-8205/791/2/L25.

Stern, J., C.-A. Faucher-Giguère, D. Fielding, et al. (2021). *The Astrophysical Journal* 911, p. 88. DOI: 10.3847/1538-4357/abd776.

Stinson, G., A. Seth, N. Katz, et al. (2006). *Monthly Notices of the Royal Astronomical Society* 373.3, p. 1074. DOI: 10.1111/j.1365-2966.2006.11097.x.

Stone, J. M., K. Tomida, C. J. White, et al. (2020). *The Astrophysical Journal Supplement Series* 249.1, p. 4. DOI: 10.3847/1538-4365/ab929b.

Su, K.-Y., P. F. Hopkins, C. C. Hayward, et al. (2019). *Monthly Notices of the Royal Astronomical Society* 487.3, p. 4393. DOI: 10.1093/mnras/stz1494.

Su, K.-Y., P. F. Hopkins, C. C. Hayward, et al. (2020). *Monthly Notices of the Royal Astronomical Society* 491.1, p. 1190. DOI: 10.1093/mnras/stz3011.

Suh, H., H. Jeong, K. Oh, et al. (2010). *The Astrophysical Journal Supplement Series* 187.2, p. 374. DOI: 10.1088/0067-0049/187/2/374.

Suresh, J., D. Nelson, S. Genel, et al. (2019). *Monthly Notices of the Royal Astronomical Society* 483.3, p. 4040. DOI: 10.1093/mnras/sty3402.

Sutherland, R. S. and M. A. Dopita (1993). *The Astrophysical Journal Supplement Series* 88, p. 253. DOI: 10.1086/191823.

Tamburri, S., P. Saracco, M. Longhetti, et al. (2014). *Astronomy and Astrophysics* 570, A102, A102. DOI: 10.1051/0004-6361/201424040.

Tange, O. (2020). Zenodo. DOI: 10.5281/zenodo.3996295.

Taylor, G. I. (1950). *Proceedings of the Royal Society of London. Series A. Mathematical and Physical Sciences* 201.1065, p. 159. DOI: 10.1098/rspa.1950.0049.

Tegmark, M., M. R. Blanton, M. A. Strauss, et al. (2004). *The Astrophysical Journal* 606.2, p. 702. DOI: 10.1086/382125.

Tejos, N., S. López, C. Ledoux, et al. (2021). *Monthly Notices of the Royal Astronomical Society* 507.1, p. 663. DOI: 10.1093/mnras/stab2147.

Terrazas, B. A., E. F. Bell, A. Pillepich, et al. (2020). *Monthly Notices of the Royal Astronomical Society* 493.2, p. 1888. DOI: 10.1093/mnras/staa374.

Teyssier, R. (2002). *Astronomy and Astrophysics* 385, p. 337. DOI: 10.1051/0004-6361:20011817.

Teyssier, R. (2015). *Annual Review of Astronomy and Astrophysics* 53.1, p. 325. DOI: 10.1146/annurev-astro-082214-122309.

Teyssier, R., A. Pontzen, Y. Dubois, et al. (2013). *Monthly Notices of the Royal Astronomical Society* 429.4, p. 3068. DOI: 10.1093/mnras/sts563.

Thornton, J. E. (1970). Scott, Foresman. ISBN: 978-0-673-05953-6.

Tinker, J., A. V. Kravtsov, A. Klypin, et al. (2008). *The Astrophysical Journal* 688.2, p. 709. DOI: 10.1086/591439.

Tonnesen, S. and G. L. Bryan (2009). *The Astrophysical Journal* 694.2, p. 789. DOI: 10.1088/0004-637X/694/2/789.

— (2012). *Monthly Notices of the Royal Astronomical Society* 422.2, p. 1609. DOI: 10.1111/j.1365-2966.2012.20737.x.

Toomre, A. (1964). *The Astrophysical Journal* 139, p. 1217. DOI: 10.1086/147861.

Toro, E. F. (2009). 3rd. Berlin: Springer Berlin Heidelberg. ISBN: 978-3-540-49834-6.

Torrey, P., G. F. Snyder, M. Vogelsberger, et al. (2015). *Monthly Notices of the Royal Astronomical Society* 447.3, p. 2753. DOI: 10.1093/mnras/stu2592.

Tozzi, P. and C. Norman (2001). *The Astrophysical Journal* 546.1, p. 63. DOI: 10.1086/318237.

Trapp, C. W., D. Kereš, T. K. Chan, et al. (2022). *Monthly Notices of the Royal Astronomical Society* 509.3, p. 4149. DOI: 10.1093/mnras/stab3251.

Trevisan, M., G. A. Mamon, and D. H. Stalder (2017). *Monthly Notices of the Royal Astronomical Society* 471.1, p. L47. DOI: 10.1093/mnrasl/slx092.

Truong, N., A. Pillepich, D. Nelson, et al. (2021). *Monthly Notices of the Royal Astronomical Society* 508.2, p. 1563. DOI: 10.1093/mnras/stab2638.

Tully, R. B. and J. R. Fisher (1977). *Astronomy and Astrophysics* 54, p. 661.

Tumlinson, J., M. S. Peeples, and J. K. Werk (2017). *Annual Review of Astronomy and Astrophysics* 55.1, p. 389. DOI: 10.1146/annurev-astro-091916-055240.

Tumlinson, J., C. Thom, J. K. Werk, et al. (2013). *The Astrophysical Journal* 777.1, p. 59. DOI: 10.1088/0004-637X/777/1/59.

Turk, M. J., B. D. Smith, J. S. Oishi, et al. (2011). *The Astrophysical Journal Supplement Series* 192.1, p. 9. DOI: 10.1088/0067-0049/192/1/9.

Tuttle, S. E. and S. Tonnesen (2020). *The Astrophysical Journal* 889.2, p. 188. DOI: 10.3847/1538-4357/ab5dbb.

Upton Sanderbeck, P. R., M. McQuinn, A. D'Aloisio, et al. (2018). *The Astrophysical Journal* 869.2, p. 159. DOI: 10.3847/1538-4357/aaeff2.

Van den Bergh, S. (1976). 206, p. 883. DOI: 10.1086/154452.

Van den Bosch, F. C. (1998). *The Astrophysical Journal* 507.2, p. 601. DOI: 10.1086/306354.

Van de Voort, F., R. Bieri, R. Pakmor, et al. (2021). *Monthly Notices of the Royal Astronomical Society* 501.4, p. 4888. DOI: 10.1093/mnras/staa3938.

Van de Voort, F., V. Springel, N. Mandelker, et al. (2019). *Monthly Notices of the Royal Astronomical Society* 482.1, p. L85. DOI: 10.1093/mnrasl/sly190.

Veilleux, S., G. Cecil, and J. Bland-Hawthorn (2005). *Annual Review of Astronomy and Astrophysics* 43.1, p. 769. DOI: 10.1146/annurev.astro.43.072103.150610.

Vila-Costas, M. B. and M. G. Edmunds (1992). *Monthly Notices of the Royal Astronomical Society* 259.1, p. 121. DOI: 10.1093/mnras/259.1.121.

Virtanen, P., R. Gommers, T. E. Oliphant, et al. (2020). *Nature Methods* 17.3 (3), p. 261. DOI: 10.1038/s41592-019-0686-2.

Vishniac, E. T. (1983). *The Astrophysical Journal* 274, p. 152. DOI: 10.1086/161433.

Vishniac, E. T. and D. Ryu (1989). *The Astrophysical Journal* 337, p. 917. DOI: 10.1086/167161.

Vogelsberger, M., S. Genel, D. Sijacki, et al. (2013). *Monthly Notices of the Royal Astronomical Society* 436.4, p. 3031. DOI: 10.1093/mnras/stt1789.

Vogelsberger, M., S. Genel, V. Springel, et al. (2014). *Monthly Notices of the Royal Astronomical Society* 444.2, p. 1518. DOI: 10.1093/mnras/stu1536.

Vogelsberger, M., F. Marinacci, P. Torrey, et al. (2020). *Nature Reviews Physics* 2.1, p. 42. DOI: 10.1038/s42254-019-0127-2.

Voit, G. M. (2019). *The Astrophysical Journal* 880.2, p. 139. DOI: 10.3847/1538-4357/ab2bfd.

Voit, G. M., K. W. Cavagnolo, M. Donahue, et al. (2008). *The Astrophysical Journal* 681.1, p. L5. DOI: 10.1086/590344.

Voit, G. M. (2005). *Reviews of Modern Physics* 77.1, p. 207. DOI: 10.1103/RevModPhys.77.207.

Voit, G. M. (2018). *The Astrophysical Journal* 868.2, p. 102. DOI: 10.3847/1538-4357/aae8e2.

— (2021). *The Astrophysical Journal* 908.1, p. L16. DOI: 10.3847/2041-8213/abe11f.

Voit, G. M., M. L. Balogh, R. G. Bower, et al. (2003). *The Astrophysical Journal* 593.1, p. 272. DOI: 10.1086/376499.

Voit, G. M., G. L. Bryan, B. W. O'Shea, et al. (2015). *The Astrophysical Journal Letters* 808.1, p. L30. DOI: 10.1088/2041-8205/808/1/L30.

Voit, G. M., G. L. Bryan, D. Prasad, et al. (2020). *The Astrophysical Journal* 899.1, arXiv:2006.09381, p. 70. DOI: 10.3847/1538-4357/aba42e.

Voit, G. M. and M. Donahue (2011). *The Astrophysical Journal* 738.2, p. L24. DOI: 10.1088/2041-8205/738/2/L24.

— (2015). *The Astrophysical Journal* 799.1, p. L1. DOI: 10.1088/2041-8205/799/1/L1.

Voit, G. M., M. Donahue, F. Zahedy, et al. (2019). *The Astrophysical Journal Letters* 879.1, p. L1. DOI: 10.3847/2041-8213/ab2766.

Voit, G. M., G. Meece, Y. Li, et al. (2017). *The Astrophysical Journal* 845.1, p. 80. DOI: 10.3847/1538-4357/aa7d04.

Wadsley, J. W., B. W. Keller, and T. R. Quinn (2017). *Monthly Notices of the Royal Astronomical Society* 471.2, p. 2357. DOI: 10.1093/mnras/stx1643.

Wang, X., T. A. Jones, T. Treu, et al. (2019). *The Astrophysical Journal* 882.2, 94, p. 94. DOI: 10.3847/1538-4357/ab3861.

Wechsler, R. H. and J. L. Tinker (2018). *Annual Review of Astronomy and Astrophysics* 56, p. 435. DOI: 10.1146/annurev-astro-081817-051756.

Weinberger, R., V. Springel, L. Hernquist, et al. (2017). *Monthly Notices of the Royal Astronomical Society* 465.3, p. 3291. DOI: 10.1093/mnras/stw2944.

Weinberger, R., V. Springel, and R. Pakmor (2020). *The Astrophysical Journal Supplement Series* 248.2, p. 32. DOI: 10.3847/1538-4365/ab908c.

Weinberger, R., V. Springel, R. Pakmor, et al. (2018). *Monthly Notices of the Royal Astronomical Society* 479.3, p. 4056. DOI: 10.1093/mnras/sty1733.

Werk, J. K., J. X. Prochaska, J. Tumlinson, et al. (2014). *The Astrophysical Journal* 792.1, p. 8. DOI: 10.1088/0004-637X/792/1/8.

Wetzel, A. R., J. L. Tinker, C. Conroy, et al. (2014). *Monthly Notices of the Royal Astronomical Society* 439.3, p. 2687. DOI: 10.1093/mnras/stu122.

White, S. D. M. and M. J. Rees (1978). *Monthly Notices of the Royal Astronomical Society* 183, p. 341. DOI: 10.1093/mnras/183.3.341.

White, S. D. M. and C. S. Frenk (1991). *The Astrophysical Journal* 379, p. 52. DOI: 10.1086/170483.

Wiener, J., E. G. Zweibel, and M. Ruszkowski (2019). *Monthly Notices of the Royal Astronomical Society* 489.1, p. 205. DOI: 10.1093/mnras/stz2007.

Wiersma, R. P. C., J. Schaye, and B. D. Smith (2009). *Monthly Notices of the Royal Astronomical Society* 393.1, p. 99. DOI: 10.1111/j.1365-2966.2008.14191.x.

Wilde, M. C., J. K. Werk, J. N. Burchett, et al. (2021). *The Astrophysical Journal* 912.1, p. 9. DOI: 10.3847/1538-4357/abea14.

Willett, K. W., K. Schawinski, B. D. Simmons, et al. (2015). *Monthly Notices of the Royal Astronomical Society* 449.1, p. 820. DOI: 10.1093/mnras/stv307.

Williams, B. F., J. J. Dalcanton, A. E. Dolphin, et al. (2009). *The Astrophysical Journal* 695.1, p. L15. DOI: 10.1088/0004-637X/695/1/L15.

Wise, J. H., J. A. Regan, B. W. O'Shea, et al. (2019). *Nature* 566.7742 (7742), p. 85. DOI: 10.1038/s41586-019-0873-4.

Wyder, T. K., D. C. Martin, D. Schiminovich, et al. (2007). *The Astrophysical Journal Supplement Series* 173.2, p. 293. DOI: 10.1086/521402.

Yan, R., K. Bundy, D. R. Law, et al. (2016). *The Astronomical Journal* 152.6, 197, p. 197. DOI: 10.3847/0004-6256/152/6/197.

Yang, J., F. Wang, X. Fan, et al. (2021). *The Astrophysical Journal* 923.2, p. 262. DOI: 10.3847/1538-4357/ac2b32.

Young, L. M., M. Bureau, T. A. Davis, et al. (2011). *Monthly Notices of the Royal Astronomical Society* 414.2, p. 940. DOI: 10.1111/j.1365-2966.2011.18561.x.

Zahedy, F. S., H.-W. Chen, T. M. Cooper, et al. (2021).

Zaragoza-Cardiel, J., J. Fritz, I. Aretxaga, et al. (2019). *Monthly Notices of the Royal Astronomical Society* 487.1, p. L61. DOI: 10.1093/mnrasl/slz093.

Zhang, H.-X., D. A. Hunter, B. G. Elmegreen, et al. (2012). *The Astronomical Journal* 143.2, 47,

p. 47. DOI: 10.1088/0004-6256/143/2/47.

Zinger, E., A. Pillepich, D. Nelson, et al. (2020). *Monthly Notices of the Royal Astronomical Society* 499.1, p. 768. DOI: 10.1093/mnras/staa2607.

Zweibel, E. G. (2013). *Physics of Plasmas* 20.5, p. 055501. DOI: 10.1063/1.4807033.